Università di Bologna

Doctoral Thesis

HIGH-SPEED LASER PROCESSING OF THIN SINGLE AND MULTI-LAYER FILMS

Candidate:
Adrian H. A. Lutey

Supervisor:
Prof. Pier Gabriele Molari

A thesis submitted in fulfilment of the requirements for the degree of Doctor of Philosophy

in the

Dipartimento di Ingegneria Industriale

March 2013

Declaration of Authorship

I, Adrian H. A. Lutey, declare that this thesis titled 'High-Speed Laser Processing of Thin Single and Multi-Layer Films' and the work presented in it are my own. I confirm that:

- This work was done wholly while in candidature for a research degree at this University.
- Where I have consulted the published work of others, this is always clearly attributed.
- Where I have quoted from the work of others, the source is always given.
- I have acknowledged all main sources of help.
- Where the thesis is based on work done by myself jointly with others, I have made clear exactly what was done by others and what I have contributed myself.

Adrian H. A. Lutey
Bologna, 14 March 2013

Abstract

Theoretical models are developed for the continuous-wave and pulsed laser incision and cut of thin single and multi-layer films. A one-dimensional steady-state model establishes the theoretical foundations of the problem by combining a power-balance integral with heat flow in the direction of laser motion. In this approach, classical modelling methods for laser processing are extended by introducing multi-layer optical absorption and thermal properties. The calculation domain is consequently divided in correspondence with the progressive removal of individual layers. A second, time-domain numerical model for the short-pulse laser ablation of metals accounts for changes in optical and thermal properties during a single laser pulse. With sufficient fluence, the target surface is heated towards its critical temperature and homogeneous boiling or "phase explosion" takes place. Improvements are seen over previous works with the more accurate calculation of optical absorption and shielding of the incident beam by the ablation products. A third, general time-domain numerical laser processing model combines ablation depth and energy absorption data from the short-pulse model with two-dimensional heat flow in an arbitrary multi-layer structure. Layer removal is the result of both progressive short-pulse ablation and classical vaporisation due to long-term heating of the sample. At low velocity, pulsed laser exposure of multi-layer films comprising aluminium-plastic and aluminium-paper are found to be characterised by short-pulse ablation of the metallic layer and vaporisation or degradation of the others due to thermal conduction from the former. At high velocity, all layers of the two films are ultimately removed by vaporisation or degradation as the average beam power is increased to achieve a complete cut. The transition velocity between the two characteristic removal types is shown to be a function of the pulse repetition rate. An experimental investigation validates the simulation results and provides new laser processing data for some typical packaging materials.

Acknowledgements

The task of completing a doctorate outside my country of origin has presented challenges and rewards well beyond those that I initially anticipated. I would like to gratefully acknowledge the assistance and support of the following colleagues and friends who have contributed to this ultimately fulfilling experience:

To Professor Pier Gabriele Molari, for having accepted a foreign Ph.D. student who began with little knowledge of the Italian language, academic system or culture at large. Your willingness to communicate in English for the first year of my study made integration into the university environment a much simpler process. Your instruction has taught me the intricacies of life in Italy from both academic and personal points of view.

To G.D, for having provided the scholarship for this doctorate and for having given me the freedom to pursue the research in the direction that I wished to go. I would particularly like to thank *Ing. Luca Cerati* for his general support and assistance.

To Professor Stefano Selleri and *Doctor Michele Sozzi* at the Group of Applied Electromagnetics, Università degli studi di Parma, for having provided much-needed assistance and collaboration for the experimental part of this project. Without this input, the experimental results would not have been possible.

To Simone Carmignato at the Laboratorio di Metrologia Geometrica e Industriale, Università degli studi di Padova, for having undertaken high resolution profile measurements at short notice.

To the NEXPRESSO program (Network for EXchange and PRototype Evaluation of photonicS componentS and Optical systems), for purchasing the Helios IR (Innolight GmbH) picosecond laser.

To my parents, for having willingly accepted my departure and absence for the best part of three years with the knowledge that this would ultimately lead to my own personal fulfilment. You have provided me with the greatest opportunities that I could have hoped for.

To Maria Merlo, for her unwavering support, patience and enthusiasm in the face of my continual sacrifice of our time together to complete this thesis. I am very lucky to have

met you and I hope that I will have the opportunity to reciprocate these actions to you in the future.

To Carlo Peressini, for his companionship, support and assistance in all areas, both work-related and personal, during the entire course of this doctorate. The time and energy that you have dedicated to helping me resolve countless problems, from immigration issues right through to planning cycling routes, has been enormous and I hope that one day I may return the favour.

To Andrew Guzzomi, for his friendship and assistance before and during the first year of this doctorate. Your help in completing a large number of tasks, from the initial application to the negotiation of Italian bureaucracy, made integration into life in Italy the least complicated that it could have been.

To my colleagues with whom I have had the pleasure of sharing our sunny office with each day, for your friendship, conversation and collaboration over the past three years. I would like to particularly thank *Ana Pavlovic* and *Francesco Meoni* for use of their computers for the best part of a year, sometimes at the expense of their own work, so that I could produce the simulation results presented in this thesis.

To the Italian and Turkish friends who I have had the good fortune of meeting while living in Bologna. I hope that, wherever our paths lead, we may continue the good times that we have shared so far.

Contents

Physical Constants

Avogadro's number	N_A	=	6.022×10^{23}
Boltzmann constant	k_B	=	$1.3807 \times 10^{-23} \mathrm{m^2\,kg\,s^{-2}\,K^{-1}}$
charge of one electron	e	=	$1.6022 \times 10^{-19} \mathrm{C}$
mass of one electron	m	=	$9.1094 \times 10^{-31} \mathrm{kg}$
speed of light in vacuum	c	=	$2.998 \times 10^{8} \mathrm{m\,s^{-1}}$
Lorenz number	L	=	$2.44 \times 10^{-8} \mathrm{W\,\Omega\,K^{-2}}$
vacuum permeability	μ_0	=	$1.2566 \times 10^{-6} \mathrm{V\,s\,A^{-1}\,m^{-1}}$

Nomenclature

C	specific heat capacity	$\mathrm{J\,kg^{-1}\,K^{-1}}$
d	ablation depth	m
d_a	depth of expanding plume	m
E_p	pulse energy	J
f_{rep}	laser repetition rate	$\mathrm{s^{-1}}$
F	laser fluence	$\mathrm{J\,cm^{-2}}$
F_a	absorbed fluence	$\mathrm{J\,cm^{-2}}$
F_{th}	phase explosion / threshold fluence	$\mathrm{J\,cm^{-2}}$
h	thickness	m
H	two-dimensional thermal energy density	$\mathrm{J\,m^{-2}}$
H^-	thermal energy density range minimum	$\mathrm{J\,m^{-2}}$
H^+	thermal energy density range maximum	$\mathrm{J\,m^{-2}}$
H_a	ambient thermal energy density	$\mathrm{J\,m^{-2}}$
H_m	enthalpy of fusion	$\mathrm{J\,kg^{-1}}$
H_v	enthalpy of vaporisation	$\mathrm{J\,kg^{-1}}$
i	discrete $x-$position index	
$\hat{i}$	number of calculation points in the $x-$direction	
I_0	on-axis incident laser intensity	$\mathrm{W\,m^{-2}}$
I	laser intensity profile	$\mathrm{W\,m^{-2}}$
I_a	layer-specific absorbed intensity	$\mathrm{W\,m^{-2}}$
I_A	absorbed intensity in complete multi-layer	$\mathrm{W\,m^{-2}}$
I_c	equivalent continuous-wave absorbed intensity	$\mathrm{W\,m^{-2}}$
I_{pk}	peak laser intensity	$\mathrm{W\,m^{-2}}$
j	discrete $y-$position index	
$\hat{j}$	number of calculation points in the $y-$direction	

k	wavenumber	m^{-1}
K	thermal conductivity	$\mathrm{W\,m^{-1}\,K^{-1}}$
$\hat{n}$	complex refractive index	
n	real part of refractive index	
M	molar mass	$\mathrm{g\,mol^{-1}}$
N	electron number density	m^{-3}
p	discrete layer / $z-$position index	
$\hat{p}$	number of layers / calculation points in the $z-$direction	
p_{atm}	atmospheric pressure	torr
p_{sat}	saturation pressure	torr
P	laser beam power	W
q	section index	
$\hat{q}$	number of sections	
$\dot{q}$	heat equation source term	$\mathrm{W\,m}^{-3}$
R	reflectivity of complete multi-layer structure	
R_p	reflectivity according to Fresnel formulae	
s	cut width	m
Δt	time-step size	s
T	temperature	K
T_a	ambient temperature	K
T_c	critical temperature	K
T_I	initial temperature	K
T_m	melting temperature	K
T_s	surface temperature	K
T_v	vaporisation temperature	K
U^+	forward travelling energy flux	$\mathrm{W\,m}^{-2}$
U^-	backward travelling energy flux	$\mathrm{W\,m}^{-2}$
x_c	cut location	m
$x_{\hat{i}}$	maximum discrete $x-$position	m
x_q	phase change location	m
Δx_+	forward mesh spacing size in $x-$direction	m
Δx_-	backward mesh spacing size in $x-$direction	m
V	cut / translation velocity	$\mathrm{m\,s}^{-1}$

Δy_+	forward mesh spacing size in $y-$direction	m
Δy_-	backward mesh spacing size in $y-$direction	m
$y_{\hat{j}}$	maximum discrete $y-$position	m
Δz	mesh spacing size in $z-$direction	m
Δz_{pe}	calculated phase explosion depth	m
Δz_v	calculated vaporisation depth	m
$z_{\hat{p}}$	maximum discrete $z-$position	m

α_a	absorption coefficient of expanding plume	m^{-1}
β	electron collision frequency	$\mathrm{rad\,s}^{-1}$
α_{sh}	shielding coefficient	m^{-1}
Γ	transmissivity of complete multi-layer structure	
η	discrete time-position index	
$\hat{\eta}$	number of time-steps	
κ	complex part of refractive index (extinction coefficient)	
λ	wavelength	m
θ	propagation angle	rad
ν	surface recession velocity	$\mathrm{m\,s}^{-1}$
ξ	mesh spacing proportionality factor	
ρ	density	$\mathrm{kg\,m}^{-3}$
σ	electrical conductivity	$\mathrm{S\,m}^{-1}$
τ	full width at half maximum (FWHM) pulse duration	s
ω	angular frequency	$\mathrm{rad\,s}^{-1}$
ω_0	Gaussian beam waist radius	m

Chapter 1

Introduction

1.1 General Motivation

Despite the maturity of laser technology for industrial materials processing, both in terms of research development and widespread adoption, application of the device to the high-speed incision and cut of thin single and multi-layer films remains a relatively new field with opportunity for growth. It includes, amongst other applications, high-speed packaging machinery and solar panel scribing; the former immersed in a complex, rapidly changing market-place in terms of materials; the latter of increasing importance for the cost reduction and efficiency improvement of renewable energy technologies. The application of laser-based systems within these industries finds motivation in the elevated levels of precision and flexibility that are offered by such devices, as well as their potential for reduction in long-term manufacturing costs. Variable incision and cut form, selective layer removal and fast, micro-scale material modification without the use of consumables or lengthy etching procedures are but some of the advantages that an optimised laser system can offer over other material removal techniques. The introduction of laser technology in the present field is therefore a natural evolution of industries seeking optimisation of process efficiency.

Use of laser light for the incision and cut of multi-layer films introduces a unique complexity that places it apart from other industrial applications: processing of composite films with layers of largely different thermal and optical properties sees different physical responses take place in each. Thorough experimental investigation is made difficult,

except in specific cases, by the large number of materials and laser sources available, as well as their rate of development. Understanding the complete system behaviour is therefore fundamental for the effective and full exploitation of laser technology in this field. A generalised modelling approach provides not only a clear indicator of the driving parameters, but also a flexible pre-prototype platform with which laser selection and control schemes may be developed. It is the creation of such a tool for the packaging industry and, more broadly, the accurate replication of the physical chain of events taking place that form the bases of this work.

1.2 Previous Research

The use of laser sources for materials processing is common and widespread. Such expansive application has required investment into the understanding of laser-material interactions and material transformations under a large range of conditions. Any further growth into new fields finds natural footing on this knowledge. Large-scale industrial materials processing and micro-scale laser ablation are well-established fields that find their bases on similar, but fundamentally different, physical phenomena. The former typically utilises high-power sources, often in the kW range, for bulk material removal or transformation on relatively long time-scales ($> 10^{-6}$s); the latter relies almost exclusively on physical phenomena that occur during, or immediately following, laser pulses with durations in the nanosecond (10^{-9}s), picosecond (10^{-12}s) or femtosecond (10^{-15}s) range. The processing of thin single and multi-layer films finds middle ground between these two fields; the use of pulsed laser sources without assist gas leads to material removal taking place due to short-pulse ablation in some layers and long-term heating effects in others. As such, both will be discussed in light of the present work with emphasis, where necessary, on studies relating to the following typical packaging materials: aluminium, polypropylene, polyethylene and paper.

1.2.1 Industrial Laser Processing of Metals

Industrial materials processing by laser irradiation is essentially a thermal process by which a work piece is heated via optical absorption of a laser beam. The precise, confined delivery of large quantities of energy allows various useful processes to be undertaken;

welding, fusion cutting with assist gas and evaporative cutting are a few examples. While some industrial applications have seen introduction of short-pulse laser sources, the field has historically been dominated by continuous-wave (CW) lasers. Noting that short-pulse ablation will be discussed in sections 1.2.3 and 1.2.4, the following dialogue will be restricted to cases in which such ablation does not take place, or is not the predominant underlying physical mechanism of material removal.

The phenomena of primary interest to laser materials processing are optical absorption of the laser beam, heating of the work-piece, phase transformation and plasma formation; all of which are presented by Von Allmen [1] in what remains one of the principal elementary texts on laser processing. This work presents the fundamentals of optical absorption in both metallic and dielectric media, heat flow for stationary and moving heat sources, melting and evaporation phase change kinetics and the theory of self-regulating plasma at very high irradiance. Further attention to these topics, as well as more specific concepts such as the fundamentals of laser physics, types and components, fluid dynamics, stress and distortion and applications such as heat treatment, cutting, drilling, welding, deposition and rapid prototyping, is given in the handbooks of Ready (ed.) [2] and Kannatey-Asibu [3]. Despite a current tendency to rely on numerical approaches, elegant theoretical discussions of laser cutting, drilling, welding, cladding and forming, such as that of Dowden (ed.) [4], provide fundamental insight into physical system behaviour.

Modelling of energy absorption, heat conduction and material transformations are central to the effective understanding of laser processing of metals. Analytical solutions provide useful insight into the driving physical parameters, forming the basis of more complex computational approaches. CW laser cutting is essentially a three-dimensional free boundary problem that, when posed in its full form, presents a confronting mathematic obstacle. One methodology for simplification of analysis is the variational formulation developed by Biot & Daughaday [5] and applied to laser materials processing by Schulz *et al.* [6, 7]. The method introduces a heat displacement vector field that plays the role of thermal potential. The variation in temperature field resulting from an arbitrary variation in heat displacement is considered in accordance with the law of conservation of energy. The variational formulation has the advantage of allowing approximate verification of the heat conduction law while maintaining exact energy conservation. Schulz

et al. define the approximate temperature field in terms of characteristic dynamic variables: the absorption front position, the spatially integrated temperature and the surface temperature. They subsequently define an ODE approximation of the cutting problem, the solution of which allows closed-form investigation into the formation of ripples along the cut kerf and energy loss due to thermal conduction.

A laser cutting model based on mass and momentum balances in a control volume is presented by Kaplan [8], whose results explain several experimentally observed effects: changes in kerf width and cutting front angle with work piece thickness and process speed, onset of evaporation at high speed and dependence of the oxygen reaction rate on process speed and gas pressure. Solana *et al.* [9] develop an analytical model for laser drilling that includes optical absorption within the vapour. Their results indicate that the logarithmic dependence of hole depth on laser energy may be approximated theoretically by considering an average absorption coefficient within the vapour. A more recent work by Duan, Man & Yue [10] develops a stationary model for laser fusion cutting based on a balance of energy with local heat conduction losses, accounting for additional laser absorption due to multiple reflections at the cutting front. A simple model for laser welding is proposed by Lampa *et al.* [11], based on the heat flow problem with a moving line source. The model is utilised for the prediction of the top and bottom weld widths and the weld penetration depth.

The importance of optical absorption, heat flow and phase changes in laser materials processing are clearly portrayed in the aforementioned works. These factors are accounted for, in the context of thin single and multi-layer films, in models presented in Chapters 2 and 4. The first is an analytical solution to the one-dimensional evaporative CW laser cutting problem; the second is a numerical solution to the two-dimensional laser cutting problem for both CW and pulsed irradiation.

Numerical approaches allow modelling of laser processes where geometry or process complexities make the derivation of exact solutions prohibitive. Early numerical approaches focused on development and optimisation of such methods. Kim, Chen & Majumdar [12] present a finite element model of evaporative laser cutting, applying their work to a parametric study of transient and steady state material removal rates. Picasso & Hoadley [13] develop a numerical model for laser remelting and cladding of material

surfaces, considering both heat transfer and fluid motion in the melt pool. A three-dimensional numerical model for CW and pulsed evaporative cutting is presented by Modest [14]. He demonstrates that material removal rates are greatly improved with the use of nanosecond-pulsed laser irradiation over both CW beams and microsecond pulses. A later work by Kim & Zhang [15] presents an unsteady heat transfer model for evaporative pulsed laser cutting using an iterative scheme to deal with the melt region. They identify threshold values for satisfactory material removal rates and groove shapes, suggesting the use of such a method for the optimisation of laser process planning. Solana & Ocaña [16] present a complete model of laser keyhole welding by combining details that had previously been studied in separation: balance of pressure, heat conduction, ablation and variations in optical absorption due to plasma formation in the keyhole. They use a discrete mesh and iterative procedure to find the free boundary location under steady state conditions. Ki *et al.* [17] present a comprehensive model of the same process that includes simulation of fluid flow, heat transfer and the solid-liquid and liquid-vapour interfaces. They conclude that complex interface phenomena play a critical role in the process, leading to inaccuracies in simpler models. Cho *et al.* [18] model high-power disk laser welding with a volume-of-fluid method for the single-phase problem, considering regions of gas and plasma as voids. They are able to estimate the weld fusion zone shape and analyse the effects of beam profile, vapour shear stress and steel sulphur content on process outcome.

Of recent, numerical methods find widespread use in diverse applications such as laser shock peening (Braisted & Brockman [19], Ocaña *et al.* [20], Tani *et al.* [21]), surface hardening (Tani *et al.* [22]), forming (Edwardson *et al.* [23]) and laser-assisted machining (Ding, Shen & Shin [24]). Thermal stresses are specifically considered by Arif & Yilbas [25] and melt depth by Shidfar, Alinejadmofrad & Garshasbi [26]. Modern computer calculations are now capable of obtaining detailed information about complete process dynamics (Otto *et al.* [27]). Such multi-physics simulations consider the combined effects of laser absorption, melt and vapour dynamics, heat conduction and phase transition at each computational time step.

Extending the range of laser applications to which numerical methods are applied, a generalised numerical simulation of the incision and cutting processes for thin multi-layer films is presented in Chapter 4. This approach solves the two-dimensional heat flow problem, including phase changes, using a simple numerical approach.

Despite the physical insight gained by theoretical approaches, experimental studies often lead the development of laser applications. Precise evaluation of process quality is often possible by experimental means well before process models are presented. An early example is the work of Lunau *et al.* [28], who investigates the now widespread use of a gas jet to enhance high-power laser cutting. A number of subsequent works focus on quality assessment and optimisation of industrial metal cutting and welding processes using CO_2 lasers. Chen [29] studies the influence of gas composition on the cut quality of mild steel. Small impurity levels in the oxygen assist gas are found to markedly reduce cut quality and cut speed. Man, Duan & Yue [30] study the dynamic characteristics of gas flow inside the laser cut kerf for supersonic and conical nozzle tips using shadowgraphy. Further studies into the effects of gas flow are presented by Chen, Yao & Modi [31], who find that the material removal rate is greatly influenced by the shock structure of the impinging gas jet interacting with the work piece. Rajaram, Sheikh-Ahmad & Cheraghi [32] present a study of the cut quality of sheet steel using a 2kW CO_2 laser, measuring the cut kerf width, surface roughness, striation frequency and heat-affected zone (HAZ) for various combinations of feed rate and laser power. Stournaras *et al.* [33] present an investigation into the cut quality of 5-xxx alloy series aluminium with a pulsed CO_2 laser. They conclude that aluminium may effectively be processed in this manner, the quality dependent on beam power, feed rate and repetition rate.

More recent experimental work in industrial settings has focused on the use of laser sources with wavelengths in the near-infrared (NIR) and visible ranges. The most notable development on the current industrial front is the Yb:YAG fibre laser, which is seeing rapid uptake due to its high efficiency, long operational life, good quality beam and compact physical dimensions. For welding operations, the technology has achieved good results. Quintino *et al.* [34], in a preliminary study into the use of high-power fibre laser irradiation for welding of pipeline steel, observe high melting efficiencies compared to conventional laser sources. Salminen, Piili & Purtonen [35] present further results for stainless steel fibre laser welding, noting that at very high power levels, in the 30kW range, the performance advantages of fibre sources are overwhelming in terms of weld speed and process tolerance. For cutting applications, use of the fibre laser has lead to low quality finishes in some cases for thick sections, due to the formation of striations and surface roughness at cut edges (Kratky, Schuöcker & Liedl [36]). A number of studies have focused on the formation and avoidance of such quality issues. Sobih, Crouse

& Li [37, 38] investigate the dependence of cut edge surface roughness on laser power, cutting speed, oxygen pressure, stand-off distance and focal plane position. They observe that, despite a high sensitivity of striation characteristics to process parameters, a steady state, striation-free cut may be obtained within certain parameter windows. The explanation for this striation-free effect is presented by Powell *et al.* [39], who observe that the smoothest cut edge, never completely free of striations, corresponds to both the steadiest flow of liquid out of the cut zone and the cut front angle corresponding to maximum optical absorption. Wandera, Salminen & Kujanpaa [40] report high quality inert gas cuts of 10mm stainless steel and 4mm aluminium using a fibre laser, noting that surface roughness decreases with increasing assist gas pressure up to 16bar.

Cut quality of thin single and multi-layer films may be considered in an analogous way to the aforementioned works, by measuring the consistency of the cut width and the variation in this parameter between adjacent layers. An experimental investigation into the laser incision and cut of some typical packaging materials is presented in Chapter 5.

1.2.2 Industrial Laser Processing of Polymers

Industrial laser processing of polymers differs from that of metals in both the work piece thermal properties and the way in which optical absorption takes place. Furthermore, material removal may be achieved not only by fusion or vaporisation, but also by thermal degradation. The optical penetration depth in metals is in the order of nanometres across the entire range of laser wavelengths (Born & Wolf [41], Palik (ed.) [42, 43]). Wavelength-dependent optical propagation in polymers, however, greatly affects material response. As a result, optical absorption in metals is often considered a surface phenomena of magnitude $1 - R_p$, where R_p is the Fresnel reflection (Born & Wolf [41]), whilst absorption in a bulk polymer must include propagation and absorption according to the Beer-Lambert law. Atanasov [44], in a study on the welding of plastic cylindrical parts, notes that the penetration depth of CO_2 laser radiation in plastics is greater than the thermal penetration depth. By accounting for optical absorption within the work piece, and by approximating thermal diffusion in a simple manner, he is able to accurately predict the optimum experimental process time and laser parameters for good quality welds of plastic components. A numerical model founded on similar bases is presented by Kneip *et al.* [45] for heating of polymers. Using test sheets of thickness

$1 - 4$mm, infrared (IR) thermography is utilised to experimentally validate this model. The same theoretical approach is applied by Ilie *et al.* [46] to predict the thermal field during laser welding of acrylonitrile butadiene styrene (ABS) components.

In some cases, large optical propagation distances require the introduction of scattering parameters. This scenario is considered by Ilie *et al.* [47, 48], who use Mie theory and the Monte Carlo method to determine light scatter and attenuation due to particles in the process medium. The degree of scattering and the resulting attenuation is found to be a strong function of the particle size, with particle diameters comparable to the laser wavelength leading to the highest levels of scattering and attenuation. They apply the developed theory to prediction of the weldability of an amorphous matrix polymethyl methacrylate (PMMA) with suspended silica micro-particles.

In light of the theory developed in these studies, a complete optical model for multi-layer films is presented in Chapter 2, accounting for reflection and absorption by both plastic and metallic layers. Due to the limited thickness of plastic films, optical penetration and transparency greatly influence the absorbed energy in each layer. The optical model is utilised for the simulations presented in Chapters 2 to 4.

Experimentally, cutting of polyethylene (PE), polypropylene (PP) and polycarbonate (PC) with a CO_2 laser is investigated by Caiazzo *et al.* [49], who determine laser cutting workability on the basis of cut edge surface roughness and the formation of resolidified "fin" on the bottom cut edge. Choudhury & Shirley [50] perform similar experiments on PP, PC and PMMA, assessing cut quality on the basis of HAZ, surface roughness and dimensional accuracy. They develop empirical relationships for the cut quality as a function of the laser power, cutting speed and compressed air pressure. Optimisation of process parameters for the cut of PE with a CO_2 laser is presented by Eltawahni, Olabi & Benyounis [51], who determine optimum parameters for cut speeds up to $1000\text{mm}\,\text{min}^{-1}$ and work piece thicknesses up to 10mm.

Consideration of thin polymeric films and polymeric layers of multi-layer films in an experimental setting represents an extension of the aforementioned works, the undertaking of which is presented in Chapter 5.

Use of shorter wavelength laser sources has seen slower uptake for plastics than for metals, due to the high work piece transparency at 1064nm. Of recent, fibre laser sources

with wavelength 2μm have been investigated as potential substitutes, eliminating the need for additional absorber elements in the work piece. Mingareev *et al.* [52] use a 2μm Tm:YAG fibre laser for the join and weld of similar and dissimilar polymeric materials. They find that high quality butt and transmission welds can be achieved at this wavelength with a beam of power 27W, the resulting joint tensile strengths exceeding 80% of the full material strength.

Despite the advantages of 2μm laser sources in an industrial setting, their use is not considered in the present study due to a focus on short-pulse ablation of single-layer polymeric films (Chapter 5) and inter-layer conductive effects in multi-layer films containing polymers and absorbing metallic layers (Chapters 2 and 4). Nonetheless, laser sources with wavelength $\geq 2\mu$m offer scope for future research in this field.

1.2.3 Short-Pulse Laser Ablation of Metals

The physical mechanisms at play during pulsed laser ablation of metals differ in a number of respects to those of CW exposure. "Laser ablation", in the present context, is considered as material removal or modification due to physical phenomena that occur during, or immediately following, a single laser pulse. That is to say, effects that occur on a time-scale shorter than the inter-pulse temporal spacing. The particular mechanisms responsible for ablation depend on the material under consideration and the laser pulse duration.

When subject to nanosecond laser pulses of sufficiently high intensity, metallic targets may be heated well above the vaporisation temperature, toward the critical temperature (T_c). As the temperature reaches $0.8T_c$, large fluctuations in density occur and a dielectric transition takes place. Electrical conductivity falls by several orders of magnitude, rendering the surface layer partially transparent and of low thermal conductivity. As the temperature continues to rise, approaching $0.9T_c$, the nucleation rate of vapour bubbles rises dramatically and explosive boiling, or "phase explosion", takes place. Normal boiling; that is, heterogeneous bubble formation in the bulk liquid, is subject to major kinetic obstacles and does not occur within 100ns (Kelly & Miotello [53]). Such an event was first proposed by Martynyuk [54] and later advocated by Miotello & Kelly [55] as "the only physically sound thermal mechanism able to explain laser sputtering at high fluences." Subsequent studies by the same authors [53, 56, 57] confirm this supposition

and, on a thorough theoretical basis, differentiate what they term "normal vaporisation" and "normal boiling" from phase explosion.

Several models for the nanosecond pulsed ablation of metallic and semi-conductor materials have been presented. In an early work, Peterlongo, Miotello & Kelly [58] obtain theoretical vaporisation rates while considering optical properties as temperature independent. They approximate boiling by increasing the vaporisation rate when the target surface reaches the boiling temperature (T_b), thus restricting further temperature rise. This method yields a large increase in surface recession velocity at the boiling temperature, displaying qualitative agreement with experimental observations above the ablation threshold. Bulgakova & Bulgakov [59] and Bulgakova, Bulgakov & Babich [60] simulate vaporisation for fluences up to the onset of phase explosion, taking into account plasma absorption and considering surface reflection as temperature dependent. They describe phase explosion as a critical phenomena, using experimentally observed phase explosion threshold values to estimate the critical temperatures of some semiconductor materials. Porneala & Willis [61] investigate the effect of the dielectric transition on the onset of phase explosion using a simple optical model while considering thermal conductivity as constant. They find that previously proposed values for the electrical conductivity of metals in the dielectric state, some eight orders of magnitude below that in the metallic state (Prokhorov *et al.* [62], Zhuang *et al.* [63]), do not lead to the experimentally observed onset of phase explosion. A fall in electrical conductivity of two orders of magnitude is instead found to bring about sufficient temperature rise. A subsequent model by Gragossian, Tavassoli & Shokri [64] simulates both the onset of phase explosion and ablation rates by accounting for changes in thermal conductivity, optical reflectivity and density during a single laser pulse. Though claiming to align well with the experimental results of Porneala & Willis [65], their simulations are clearly conducted with a different pulse duration, 10ns instead of 5ns, and the calculated ablation depths are two orders of magnitude greater than the measured values. As such, a new model for the nanosecond pulsed ablation of metals, resolving these discrepancies, is presented in Chapter 3.

Experimentally, a number of studies present nanosecond pulsed laser ablation data for various laser-material combinations. Aluminium (AL), of widespread use in the packaging industry, is of particular interest to the present case. Large variations in the reported ablation depths for this material are present in literature, suggesting a strong dependence on the experimental setup. The number of incident pulses is often increased to

produce craters with measureable depths; however, as will be shown in Chapter 5, this leads to a reduction in the ablation depth per pulse due to shielding of the incident beam by the ablation products. Colina *et al.* [66] present data for aluminium exposed to single pulses of duration 35ns and 10ns at wavelengths 1064nm and 532nm, respectively. They report ablation depths in the low micron range for fluences $6 - 50\mathrm{J\,cm^{-2}}$ at 1064nm and $9 - 20\mathrm{J\,cm^{-2}}$ at 532nm. Porneala & Willis [65, 67] present data for aluminium exposed to groups of 100 pulses of duration 5ns and wavelength 1064nm, together with time-resolved photos of the phase explosion process. In this work, the reported ablation depths per pulse are in the tens of nanometres range for fluences $6 - 12\mathrm{J\,cm^{-2}}$, whilst the observed phase explosion threshold is between $4.3\mathrm{J\,cm^{-2}}$ and $5.2\mathrm{J\,cm^{-2}}$. Stafe *et al.* [68] present data for aluminium exposed to groups of 200 pulses of duration 4.5ns and wavelength 1064nm and groups of 10 pulses of duration 4.5ns and wavelength 532nm. They report ablation depths per pulse in the hundreds of nanometres range for fluences $8 - 22\mathrm{J\,cm^{-2}}$ at 1064nm and the low micron range for fluences $10 - 120\mathrm{J\,cm^{-2}}$ at 532nm. Horn, Guillong & Günther [69] present aluminium ablation data for groups of 12ns and 6ns pulses at 193nm and 266nm, respectively. They report ablation rates per pulse in the range $0.8 - 1.3\mu\mathrm{m}$ for fluences $5 - 23\mathrm{J\,cm^{-2}}$ with both sources. The variation in reported values, particularly those obtained with similar pulse characteristics (e.g. Porneala & Willis and Stafe *et al.*), yields quantitative comparison between the various studies somewhat difficult. Nonetheless, the relationships between fluence and ablation depth per pulse serve as useful data for verification of the short-pulse ablation model presented in Chapter 3. Additional experimental data for the nanosecond pulsed laser ablation of aluminium is presented in Chapter 5.

When a metal is subject to picosecond or femtosecond laser pulses, the pulse duration may be of the same order as, or shorter than, the electron-phonon relaxation time of the target. This gives rise to electron thermal diffusion, a process by which electrons transport energy deep into the target while simultaneously heating the lattice. The so-called two-temperature model (Anisimov, Kapeliovich & Perel'man [70]) accounts for electron heat transfer and its coupling to the lattice temperature. The model is found to be well suited to the description of hot electron diffusion, provided that corrections for ballistic electron motion are incorporated (Hohlfeld *et al.* [71]). Yilbas [72] presents an electron kinetic theory approach for short-pulse target heating that yields temperature distributions similar to those of the two-temperature model.

Where the pulse duration is shorter than the mechanical equilibration time, ablation takes place in the stress confinement regime and non-thermal photomechanical stress fragmentation becomes the dominant physical mechanism responsible for material removal (Zhigilei & Garrison [73], Yang, Zhao & Zhu [74]). A work presented by Schäfer, Urbassek & Zhigilei [75] develops a hybrid simulation that combines the two-temperature heat conduction model with a molecular dynamics simulation to cover all physical aspects of the laser ablation process: strong superheating, pressure effects and phase transitions. They simulate 0.5ps pulsed laser exposure of a copper target, demonstrating that ablation in the stress confinement regime takes place due to a compression wave induced by thermal expansion. Crater formation and plume expansion dynamics are considered for nanosecond, picosecond and femtosecond laser pulses by Perez & Lewis [76], Bouilly, Perez & Lewis [77] and Lewis & Perez [78] using molecular dynamics simulations. Four mechanisms of ablation are demonstrated: spallation, phase explosion, vaporisation and fragmentation; the latter of which is found to be most important in the femtosecond regime. Nedialkov *et al.* [79] investigate the $0.1 - 5$ps pulsed laser ablation of several metals using molecular dynamics simulations. They identifying a dependence of the expulsion mechanism on the incident fluence. At fluences near the ablation threshold, the process is governed by thermo-elastic stress development, whilst at higher fluences, strong superheating leads to phase explosion. Zhang *et al.* [80] present an experimental investigation into the ejection dynamics of femtosecond laser ablation of aluminium using time-resolved shadowgraphy. They find that with a laser fluence of $40\mathrm{J\,cm^{-2}}$, material removal is due to both phase explosion and a thermoelastic wave. In a recent work, Sonntag *et al.* [81] use molecular dynamics simulations with huge sample sizes (6×10^7 atoms) and a cluster algorithm to determine the cluster size distribution of femtosecond ablated aluminium. They are able to calculate the phase diagram, leading to derivation of the ablation threshold and the velocity, angular and size distribution functions of the expanding plume. They note that despite the simulation sample size being one order of magnitude smaller than the smallest experiments, the results align well with measured distribution functions.

Experimentally, several studies demonstrate high levels of ablation precision and efficiency with sub-nanosecond pulsed laser sources. An early work by Pronko *et al.* [82] demonstrates the machining of 300nm holes in a metal target using a 200fs Ti:sapphire

laser. Momma *et al.* [83] and Nolte *et al.* [84] compare nanosecond, picosecond and femtosecond pulsed laser ablation of metal targets. They demonstrate clear improvements in precision with use of femtosecond pulses, producing sharp, well-defined structures up to the diffraction limit with a 150fs source. Semerok *et al.* [85] study the efficiency of nanosecond, picosecond and femtosecond pulsed laser ablation of several different metals, observing highest efficiency with femtosecond pulses. Zhao, Huettner & Menschig [86] manufacture arrays in silicon and aluminium with holes of approximately 1μm diameter using variable pulse lengths in the range $0.1 - 10$ps. Yalizay *et al.* [87] generate structures on thin metal films with resolution down to 200nm using femtosecond laser pulses with Bessel beam profiles.

Despite the advantages offered by sub-nanosecond laser pulses, durations < 0.5ns are not considered in the present work due to prohibitive realisation costs in the context of high-speed packaging machinery. Given reductions in cost, the use of ultrashort-pulse lasers could offer substantial opportunities for development in the field.

1.2.4 Short-Pulse Laser Ablation of Polymers

A large body of literature exists for the pulsed laser ablation of polymers. The process differentiates itself from that of metals by the onset of chemical change, the exact nature of which dependents on the material and laser parameters. In some cases, there is still no general agreement as to whether the predominant mechanism of material removal is photothermal or photochemical (Lippert [88]). The ablation mechanism and rate of material removal in polymers is a function of the laser wavelength, beam intensity and the number of pulses. The ablation rate of polymeric materials under a given set of conditions is usually expressed as a logarithmic function of fluence with an effective absorption coefficient, itself a function of the fluence range considered. The theoretical basis of pulsed laser ablation of polymers is discussed by Lippert [88], Lippert & Dickinson [89] and Dyer [90]. Modelling of both photochemical and photothermal ablation is presented by Bityurin *et al.* [91], who incorporate the features of polymers within the framework of models developed for other materials. They conclude that the dependence of etch depth on laser fluence is insensitive to the mechanism of ablation.

Experimentally, a study of the nanosecond, picosecond and femtosecond pulsed laser ablation of thin PP films is presented by Sohn *et al.* [92], who conclude that high pulse

numbers and pulse energies lead to the onset of both thermal and photochemical effects. They provide PP ablation depth and width data for femtosecond laser pulses. In a recent work by Leme *et al.* [93], the effects of pulse repetition rate and the number of pulses are investigated for PP and PE with nanosecond pulses of wavelength 1064nm. They provide data for various pulse numbers in the range $10-50$, demonstrating a sharp increase in ablated mass per pulse with repetition rate and a decrease in ablated mass per pulse with the number of pulses. An investigation into the ablation behaviour of PMMA subject to infrared (IR) and ultraviolet (UV) nanosecond and picosecond laser pulses is presented by Hahn, Lippert & Wokaun [94], who conclude that etching in the UV is mainly the result of photochemical processes, whilst that in the IR is mainly the result of thermal processes. Luk'yanchuk *et al.* [95] observe that UV laser ablation of polyimide (PI) appears to be thermal for microsecond pulses and photophysical for picosecond and femtosecond pulses, whilst nanosecond pulses display characteristics of both. Baudach, Bonse & Kautek [96] and Baudach *et al.* [97] investigate the femtosecond IR ablation of PI, PC and PMMA, establishing the dependence of ablation depth per pulse on both the fluence and number of pulses.

Due to the complex chemical nature of short-pulse laser ablation of polymers, inclusion of such effects in the general simulation presented in Chapter 4 is based on the experimental results for single-layer plastic films presented in Chapter 5.

1.2.5 Industrial Laser Processing of Thin Films

To the author's knowledge, only a limited number of studies have investigated the laser processing of thin packaging films. The high-speed laser weld and cut of PP and PE films is studied by Coelho, Abreu & Rodrigues [98, 99]. Despite very low levels of laser absorption due to material transparency and low film thickness, welds with tensile strengths exceeding 80% of the full material strength are reported at up to $14\,\mathrm{m\,s^{-1}}$ using a 2.7kW CO_2 laser.

Of recent, interest has grown in the use of pulsed laser irradiation for improvement of the cell efficiency of photovoltaics and the reduction of their production cost. The majority of research in this field is experimental, demonstrating a number of innovative applications that have been made possible with the development of new laser sources with shorter pulse durations and higher average power levels. Engelhart *et al.* [100]

demonstrate picosecond pulsed laser ablation of thermally grown SiO_2 layers, yielding a simplification of the cell process while achieving diode saturation currents identical to those obtained with hydrofluoric acid (HF) etching. Halbwax *et al.* [101] and Lee *et al.* [102] produce so-called "black silicon" by irradiating the material surface with femtosecond laser pulses to produce micro-spikes that strongly reduce surface reflectivity. This process has been found by others to induce damage in the form of sub-surface phase transformations that ultimately reduce cell performance. A subsequent study by Smith *et al.* [103] identifies the cause of this phenomenon as resolidification-induced stress. Müller-Meskamp *et al.* [104] achieve increases in organic solar cell efficiency by direct laser interference patterning (DLIP) of polyethylene terephthalate (PET) substrates, elongating the light path through the absorbing layer.

Use of pulsed laser irradiation for the P1, P2 and P3 scribing processes of thin-film photovoltaic manufacturing is also seeing a strong research focus. The nature of these processes depends on the solar absorber film under consideration and the choice of substrate or superstrate configuration; however, in general, P1 sees parallel line removal of an electrical contact film deposited on a glass substrate, P2 sees parallel line removal of a solar absorber film deposited on this electrical contact and P3 sees parallel line removal of the same absorber film, plus a second contact film deposited on the absorber film. A number of studies present results for these tasks using laser sources with pulse durations ranging from nanoseconds to femtoseconds (Selleri *et al.* [105, 106], Hernandez *et al.* [107], Gečys *et al.* [108], Schoonderbeek *et al.* [109], Bovatsek *et al.* [110]). These works highlight a strong dependence of quality on the pulse duration for the P2 and P3 processes, where the front contact and/or active layers must be removed while leaving the back contact intact. Application of the full process simulation presented in Chapter 4 to thin-film photovoltaic scribing is an opportunity for future research.

A number of applications utilise short-pulse laser sources for the micromachining of specific thin components in a number of different fields; for example, optics, electronics, chemistry and biology. While some of these may broadly be considered industrial applications, they differ from the present study in nature and throughput, focused on precision manufacturing of often complex structures instead of high-speed materials processing. Due to this contrast they will not be discussed here.

1.3 Thesis Content

The present thesis develops and tests a generalised model for the high-speed laser incision and cut of thin single and multi-layer films. The scope of this model is to provide a tool for laser source selection and process quality prediction in the packaging industry. "High-speed", in this context, is considered to be the range $50\text{mm}\,\text{s}^{-1} - 1\text{m}\,\text{s}^{-1}$; in line with the operating requirements of high-speed packaging machinery. Though this velocity range is considered for all of the results presented, the theory developed here within is generally not restricted in this respect.

Chapter 2 establishes the theoretical foundations of the problem by extending the classical theory of industrial laser materials processing to thin multi-layer films. Optical absorption and thermal behaviour are generalised for arbitrary thin multi-layers, following which models based on power balance and steady state heat conduction are introduced. The effects of translation velocity and film composition on minimum CW laser power and cut width are investigated theoretically. Despite limited agreement with the results of Chapters 4 and 5, due to lateral heat conduction losses, the ideas introduced in this section illustrate the foundations upon which later work is developed.

Chapter 3 presents a numerical simulation for the nanosecond pulsed laser ablation of metals, considering one-dimensional heat flow with temperature dependent material properties. A finite-element optical calculation is utilised to determine energy absorption during the pulse and a simplified method is introduced to account for shielding of the incident beam by the ablation products. The simulation is applied to the $0.5 - 20\text{ns}$ pulsed laser ablation of aluminium, with the effects of laser wavelength, pulse duration and sample thickness on the phase explosion threshold comprehensively investigated, as well as the influence of initial temperature on the ablation depth and absorbed fluence. The model is found to be in good agreement with several published works, as well as the experimental results presented in Chapter 5.

Chapter 4 develops a complete numerical process simulation for the laser incision and cut of thin multi-layer films. The physical mechanisms at play are simplified by dividing the chain of events according to time-scale. During and immediately following each pulse, layer profiles are updated based on the beam exposure of each layer and the ablation depth calculated by the single-pulse model. Two-dimensional forward/backward and

lateral heat flow in the complete multi-layer is calculated continuously based on combined material properties and the total absorbed energy as calculated by the single-pulse model. The resulting material removal is a function of both short-pulse ablation and normal vaporisation/degradation due to long-term heating. Where CW laser irradiation is considered, only two-dimensional heat flow and normal vaporisation/degradation are accounted for. The model is applied to the laser exposure of two multi-layer packaging films with three different laser sources at various translation velocities. The effects of repetition rate and focused spot diameter are investigated for one laser source so as to demonstrate the effects of repetition rate and beam diameter on film cut quality.

Chapter 5 presents an experimental investigation into the pulsed laser incision and cut of thin single-layer aluminium (20μm), PP (20μm) and PE (50μm) films as well as multi-layer Triplex (PP 20μm – AL 9μm – PP 20μm), Duplex (PP 20μm – AL $\sim$ 0.1μm – PP 20μm), Metallised Paper (AL 7μm – paper $\sim$ 60μm) and Alufoil (AL $\sim$ 0.1μm – paper $\sim$ 60μm). Two different lasers are utilised for the tests; one emitting pulses of duration $500 - 800$ps at wavelength 1064nm and the other emitting pulses of duration $10 - 16$ns at wavelength 515nm. A 3D optical profiler and optical microscope are used to determine the phase explosion threshold and ablation depth of the single-layer films, as well as the interaction and cut widths of the multi-layer films. The results of this study are utilised to verify the models presented in Chapters 3 and 4.

Chapter 6 summarises the key findings of the thesis, proposing future work for further improvement and expansion of laser technology in this field.

Chapter 2

A One-Dimensional Steady State Model for Continuous-Wave Evaporative Laser Cutting of Thin Single and Multi-Layer Films

The following chapter presents a simple theoretical representation of the thin-film evaporative laser cutting problem. A classical modelling approach for industrial laser processing is generalised to include thin multi-layer structures, leading to cut geometry approximations under steady state conditions. The model serves as a fast calculation for cut effectiveness with arbitrary laser-film combinations. The concepts that are introduced will be utilised in later chapters.

2.1 Optical Absorption in a Multi-Layer Structure

The optical absorption in multi-layer films is a function of the component materials and laser characteristics. A general calculation for this parameter therefore forms the basis of any theoretical representation of the laser cutting problem. Efficient matrix methods for electromagnetic plane wave propagation and absorption in coherent and incoherent

multi-layer media are well-established in literature (Wait [111], Yeh, Yariv & Hong [112], Prentice [113, 114], Centurioni [115]). For cases of coherent propagation, these are based on continuity of the tangential components of the electric field and magnetic vector at layer interfaces; for incoherent propagation, they apply continuity of energy flux. A brief summary of the latter is provided here for application to the current setting.

For incoherent interfaces, the forward and backward travelling waves in each layer may be considered separately without allowance for interference. For an incident transverse electric (TE) plane wave with energy flux U_0^+, the resulting flux at the surface of layer p has forward and backward travelling components, U_p^+ and U_p^-:

$$\begin{pmatrix} U_p^+ \\ U_p^- \end{pmatrix} = \mathbf{T}_{t,p} \begin{pmatrix} U_0^+ \\ U_0^- \end{pmatrix},$$

$$\mathbf{T}_{t,p} = \mathbf{T}_p \mathbf{T}_{p-1} \dots \mathbf{T}_1,$$

$$\mathbf{T}_p = \begin{pmatrix} t_{p,11} & t_{p,12} \\ t_{p,21} & t_{p,22} \end{pmatrix},$$

$$\begin{aligned} t_{p,11} &= \frac{1-2R_p}{1-R_p} \left| e^{ik_{p-1}h_{p-1}\cos(\theta_{p-1})} \right|^2, \\ t_{p,12} &= \frac{R_p}{1-R_p} \left| e^{-ik_{p-1}h_{p-1}\cos(\theta_{p-1})} \right|^2, \\ t_{p,21} &= -\frac{R_p}{1-R_p} \left| e^{ik_{p-1}h_{p-1}\cos(\theta_{p-1})} \right|^2, \\ t_{p,22} &= \frac{1}{1-R_p} \left| e^{-ik_{p-1}h_{p-1}\cos(\theta_{p-1})} \right|^2 \end{aligned} \tag{2.1}$$

Where:

$$R_p = \left| \frac{\hat{n}_p \cos\theta_p - \hat{n}_{p-1}\cos\theta_{p-1}}{\hat{n}_p \cos\theta_p + \hat{n}_{p-1}\cos\theta_{p-1}} \right|^2$$

Where R_p is the reflectivity of layer p according to the Fresnel formula for a TE plane wave, $\hat{n}_p$ is its complex refractive index and h_p its thickness, $k_p = \omega\hat{n}_p/c$ is the propagation wave number in layer p and θ_p the propagation angle as given by Snell's Law with complex values. The angular frequency is $\omega = 2\pi c/\lambda$, the wavelength λ and the speed of light in vacuum c. There is no backward travelling wave in the medium proceeding the final layer, $\hat{p}$:

$$U_{\hat{p}+1}^- = 0 \tag{2.2}$$

This allows resolution of the reflected energy flux U_0^- and therefore U^+ and U^- at any position as functions of U_0^+. The reflectivity, R, and transmissivity, Γ, of the complete multi-layer structure are:

$$R = \frac{U_0^-}{U_0^+}, \qquad \Gamma = \frac{U_{\hat{p}+1}^+}{U_0^+} \tag{2.3}$$

The absorbed intensity in any particular layer is the sum of the change in forward and backward travelling energy fluxes between subsequent interfaces:

$$I_{a,p} = U_p^+ \left[1 - \left|e^{ik_p h_p \cos(\theta_p)}\right|^2\right] + U_p^- \left[\left|e^{-ik_p h_p \cos(\theta_p)}\right|^2 - 1\right] \tag{2.4}$$

That of the complete structure is:

$$I_A = \sum_{p=1}^{\hat{p}} I_{a,p} = U_0^+ - U_0^- - U_{\hat{p}+1}^+ = U_0^+(1 - R - \Gamma) \tag{2.5}$$

Where $\hat{p}$ is the number of layers. For an incident transverse magnetic (TM) plane wave, the expression for reflectivity must be altered according to the corresponding Fresnel formula, noting that for normal incidence, propagation is independent of polarisation. Full equations for optical propagation in arbitrary multi-layer structures with both coherent and incoherent interfaces may be found in the work of Centurioni [115].

In the present Chapter, the incident beam is taken as the continuous-wave (CW) on-axis laser intensity, I_0:

$$U_0^+ = I_0 \tag{2.6}$$

A MATLAB script for coherent and incoherent plane wave propagation and absorption in an arbitrary multi-layer structure is presented in Appendix B.4. The program was developed by the author for use in the models of this chapter and Chapters 3 and 4.

2.2 Power Balance

A power balance is the simplest way in which the minimum CW laser intensity for the complete cut of a thin film may be calculated. Optical absorption is taken as that of the complete multi-layer structure and heat flow is neglected. Given the absence of assist gas, the power required to achieve a complete cut is that necessary to continuously heat all layers to their respective vaporisation/degradation temperatures and to complete

both melting and vaporisation at the given translation velocity. The laser intensity profile is taken as the on-axis beam intensity masked by a Gaussian distribution in the $x-$direction:

$$I(x) = I_0 \exp\left[-2\frac{x^2}{\omega_0^2}\right] \tag{2.7}$$

Where ω_0 is the Gaussian beam waist radius. The on-axis beam intensity is related to the laser beam power, P, by:

$$I_0 = \frac{2P}{\pi\omega_0^2} \tag{2.8}$$

The absorption profile resulting from $I(x)$ is integrated from the cut location, x_c, to ∞ and equated to the necessary cut power:

$$\int_{x_c}^{\infty} I_A \exp\left[-2\frac{x^2}{\omega_0^2}\right] dx = \sum_{p=1}^{\hat{p}} \{((T_{m,p} - T_a)\, C_{s,p} + H_{m,p} + (T_{v,p} - T_{m,p})\, C_{l,p} + H_{v,p})\, \rho_p h_p V\} \tag{2.9}$$

Where V is the cut velocity, $T_{m,p}$ is the melting temperature of layer p, $T_{v,p}$ is its vaporisation temperature, $H_{m,p}$ its enthalpy of fusion, $H_{v,p}$ its enthalpy of vaporisation, $C_{s,p}$ its specific heat capacity in solid state, $C_{l,p}$ its specific heat capacity in liquid state, ρ_p its density and h_p its thickness. I_A is the absorbed intensity of the complete multi-layer structure according to Eqn. (2.5). The equation may be expressed in terms of the cut location:

$$x_c = \frac{\omega_0}{\sqrt{2}} \operatorname{erf}^{-1}[1 - \frac{2\sqrt{\frac{2}{\pi}}}{\omega_0 I_A} \sum_{p=1}^{\hat{p}} \{((T_{m,p} - T_a)\, C_{s,p} + H_{m,p} + (T_{v,p} - T_{m,p})\, C_{l,p} + H_{v,p})\, \rho_p h_p V\} \tag{2.10}$$

The existence of x_c is subject to the following condition:

$$I_A \geq \check{I}_A = \frac{\sqrt{\frac{2}{\pi}}}{\omega_0} \sum_{i=1}^{\hat{p}} \{((T_{m,p} - T_a)\, C_{s,p} + H_{m,p} + (T_{v,p} - T_{m,p})\, C_{l,p} + H_{v,p})\, \rho_p h_p V\} \tag{2.11}$$

Where the minimum on-axis absorbed intensity, $\check{I}_A$, corresponds to the integral in Eqn. (2.9) taken from $-\infty$ to ∞. Practically speaking, any further reduction in I_A does not result in a complete cut. To determine the cut width, the incident beam is further

masked by a Gaussian distribution in the $y-$direction:

$$I(x,y) = I_0 \exp\left[-2\frac{x^2+y^2}{\omega_0^2}\right] \tag{2.12}$$

Equation (2.9) becomes:

$$\int_{x_c(y)}^{\infty} I_A \exp\left[-2\frac{x^2+y^2}{\omega_0^2}\right] dx = \sum_{p=1}^{\hat{p}} \{((T_{m,p}-T_a)\,C_{s,p} + H_{m,p} + (T_{v,p}-T_{m,p})\,C_{l,p} + H_{v,p})\,\rho_p h_p V\} \tag{2.13}$$

The cut width, s, is twice the largest value of y for which $x_c(y)$ exists; that is:

$$I_A \exp\left[-2\frac{(s/2)^2}{\omega_0^2}\right] = \check{I}_A \tag{2.14}$$

Therefore:

$$s = \sqrt{-2\omega_0^2 \ln\left(\frac{\check{I}_A}{I_A}\right)} \tag{2.15}$$

Or:

$$s = \sqrt{-2\omega_0^2 \ln\left(\frac{\check{P}}{P}\right)} \tag{2.16}$$

Where the minimum cut power, $\check{P}$, gives on-axis absorbed intensity $\check{I}_A$.

2.3 Steady State Heat Conduction Model

Aside from thermal conduction losses, the main limitation of the power balance for multi-layer films is that the actual optical absorption may not be that of the complete multi-layer structure. Complex layer combinations lead to difficulty in determining which layers are actually present under the laser spot. A one-dimensional steady state heat conduction model effectively yields the same useful information as the power balance, but with allowance for variable optical absorption. Lateral heat flow, addressed in the complete time-domain model presented in Chapter 4, is neglected in the present simplified approach. The problem is divided into sections $q = 1 \ldots (\hat{q}-1)$, that individually contain all combinations of layer states attained throughout heating from ambient temperature to the onset of vaporisation/degradation of the final remaining layer. An additional section, $\hat{q}$, sees vaporisation of this final layer at constant temperature. As the

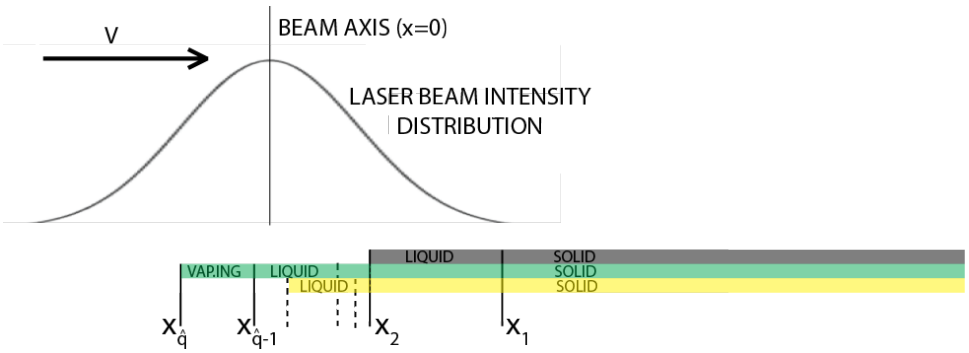

FIGURE 2.1: Schematic of steady state heat conduction model for $\hat{p} = 3$.

material approaches the laser axis from the positive $x-$direction, phase changes in each layer progress in the order of the corresponding phase change temperatures. The points at which these occur are denoted $x_1 \ldots x_{\hat{q}-2}$, with $x_{q-1} > x_q$. The point at which the layer of highest vaporisation temperature begins to vaporise is $x_{\hat{q}-1}$ and that at which its vaporisation is complete (i.e. the cut position) is $x_{\hat{q}}$. A schematic of the model for a three-layer film is presented in Fig. 2.1. Points x_1, x_2, $x_{\hat{q}-1}$ and $x_{\hat{q}}$ are shown explicitly, whilst the intermediate transition points are indicated by dashed lines.

2.3.1 Material Properties

Thermal behaviour in each section is determined by considering the complete structure as a single material. The properties of this equivalent material are chosen such that the energy flux for a given temperature gradient is the sum of the contributions of all layers:

$$h_q = \sum_{p=1}^{\hat{p}} h_p, \qquad K_q = \frac{1}{h_q} \sum_{p=1}^{\hat{p}} \{K_p h_p\},$$
$$\rho_q = \frac{1}{h_q} \sum_{p=1}^{\hat{p}} \{\rho_p h_p\}, \qquad C_q = \frac{1}{h_q \rho_q} \sum_{p=1}^{\hat{p}} \{C_{s/l,p} \rho_p h_p\} \tag{2.17}$$

Where h_q, K_q, ρ_q and C_q are the equivalent thickness, thermal conductivity, density and specific heat capacity of section q, comprising layers 1 to $\hat{p}$, *where present*. These properties depend on the materials present and their states in the section of interest, but are otherwise considered constant with temperature.

2.3.2 Heat Flow

Under the thin-film approximation, temperature throughout film thickness is considered constant. A coordinate system is chosen that translates with the laser beam axis at velocity V in the $x-$direction. Employing the same laser intensity distribution (Eqn. (2.7)), the steady state one-dimensional heat flow equation is, for temperature T_q in the domain $x_{q-1} < x \leq x_q$:

$$\frac{\partial^2 T_q}{\partial x^2} + \frac{VC_q\rho_q}{K_q}\frac{\partial T_q}{\partial x} = -\frac{I_{A,q}\exp\left[-2\frac{x^2}{\omega_0^2}\right]}{K_q h_q} \tag{2.18}$$

Optical absorption is calculated based on the layers present in each section; $I_{A,q}$ is the total absorbed intensity according to Eqn. (2.5) for section q. The global domain for the heat flow problem is:

$$x_{\hat{q}-1} < x < \infty$$

At distances far from the laser beam axis the film is at ambient temperature, T_a, whilst at $x_{\hat{q}-1}$ the film is at the vaporisation temperature of the final remaining layer, r, which has the highest vaporisation/degradation temperature. The global boundary conditions are therefore:

$$T_1|_{x\to\infty} = T_a, \quad T_{\hat{q}-1}|_{x=x_{\hat{q}-1}} = T_{v,r} \tag{2.19}$$

Compatibility conditions maintain continuity of temperature across section, or "local", boundaries and account for enthalpies of phase change by enforcing abrupt changes in energy flux:

$$\begin{aligned} T_q|_{x=x_{q-1}} &= T_{q-1}|_{x=x_{q-1}}\,, \\ K_q h_q \left.\frac{\partial T_q}{\partial x}\right|_{x=x_{q-1}} + H_{m/v,l}\rho_l h_l V &= K_{q-1}h_{q-1}\left.\frac{\partial T_{q-1}}{\partial x}\right|_{x=x_{q-1}} \end{aligned} \tag{2.20}$$

Where l is the layer under transformation at x_{q-1} and $H_{m/v,l}$ is the corresponding enthalpy of phase change. The general solution to (2.18) is:

$$T_q = A_{1,q} + A_{2,q}e^{\lambda_q x} + u_q(x) + v_q(x)e^{\lambda_q x} + T_a \tag{2.21}$$

Where $A_{1,q}$ and $A_{2,q}$ are chosen to satisfy Eqns. (2.19) and (2.20), and:

$$\lambda_q = -\frac{VC_q\rho_q}{K_q},$$

$$\begin{aligned} u_q(x) &= -\frac{1}{\lambda_q}\int -\frac{I_{A,q}\exp\left[-2\frac{x^2}{\omega_0^2}\right]}{K_q h_q}dx \\ &= \sqrt{\frac{\pi}{2}}\frac{I_{A,q}\omega_0}{2K_q h_q \lambda_q}\mathrm{erf}\left[\frac{\sqrt{2}x}{\omega_0}\right], \end{aligned}$$

$$\begin{aligned} v_q(x) &= \frac{1}{\lambda_q}\int -\frac{I_{A,q}\exp\left[-2\frac{x^2}{\omega_0^2}\right]}{K_q h_q \exp\left[\lambda_q x\right]}dx \\ &= -\sqrt{\frac{\pi}{2}}\frac{I_{A,q}\omega_0}{2K_q h_q \lambda_q}\exp\left[\frac{\lambda_q^2\omega_0^2}{8}\right]\mathrm{erf}\left[\frac{\lambda_q\omega_0^2 + 4x}{2\sqrt{2}\omega_0}\right] \end{aligned}$$

The temperature, $T_{\hat{q}}$, in the final section whose domain is $x_{\hat{q}} < x \leq x_{\hat{q}-1}$, is constant at the vaporisation temperature of the final remaining layer, r:

$$T_{\hat{q}} = T_{v,r} \tag{2.22}$$

Points $x_{\hat{q}-1}$ and $x_{\hat{q}}$ must satisfy the following power balance equations:

$$\begin{aligned} \int_{x_{\hat{q}-1}}^{\infty} I_A(x)\exp\left[-2\frac{x^2}{\omega_0^2}\right]dx = & \sum_{p=1}^{\hat{p}} \{((T_{m,p} - T_a)\,C_{s,p} + H_{m,p} + \\ & (T_{v,p} - T_{m,p})\,C_{l,p} + H_{v,p})\,\rho_p h_p V\} - H_{v,r}\rho_r h_r V \\ \int_{x_{\hat{q}}}^{\infty} I_A(x)\exp\left[-2\frac{x^2}{\omega_0^2}\right]dx = & \sum_{p=1}^{\hat{p}} \{((T_{m,p} - T_a)\,C_{s,p} + H_{m,p} + \\ & (T_{v,p} - T_{m,p})\,C_{l,p} + H_{v,p})\,\rho_p h_p V\} \end{aligned} \tag{2.23}$$

Where $I_A(x)$ is constant, equal to $I_{A,q}$ for each section, except for abrupt changes at local boundaries. The problem, stated as such, requires prior knowledge of points $x_1 \ldots x_{\hat{q}-2}$ for resolution. A simple iterative method is introduced:

1. Evaluate locations $x_{\hat{q}-1}$ and $x_{\hat{q}}$ with Eqn. (2.23), setting optical absorption as that of the complete multi-layer (i.e. $I_A(x) = I_{A,1}$). The resulting point $x_{\hat{q}}$ is equal to x_c in Eqn. (2.10) of the power balance.

2. Resolve Eqn. (2.18) as one section by using the global boundary conditions and taking material properties as those of the complete multi-layer (i.e. $h_q = h_1$, $K_q = K_1$, $\rho_q = \rho_1$ and $C_q = C_1$). The problem is a system of two equations for as many coefficients, A.

3. Set transition points $x_1 \dots x_{\hat{q}-2}$ for the next iteration as those at which the evaluated temperature distribution is equal to the respective temperatures of phase change.

4. Evaluate locations $x_{\hat{q}-1}$ and $x_{\hat{q}}$ with Eqn. (2.23), dividing the integral into sections and using the respective optical absorption based on the layers present in each.

5. Resolve Eqn. (2.18) for all sections by using the boundary and compatibility conditions. The problem is a system of $4\hat{p}$ equations for as many coefficients, A.

6. Repeat steps (3), (4) and (5) until the maximum difference in temperature between consecutive iterations is below acceptable limits (< 1K).

If $x_{\hat{q}-1}$ does not exist, the calculation ceases; the final remaining layer does not reach its vaporisation temperature and the domain of the heat flow problem does not exist according to Eqn. (2.19). A solution in this case is no longer sought; the laser power or wavelength must be modified to increase optical absorption. The minimum incident laser power for which a complete cut is attained, $\check{P}$, is the minimum value for which $x_{\hat{q}}$ exists at the final iteration.

To determine the cut width, s, the incident beam is further masked by a Gaussian distribution in the $y-$direction. Noting that the temperature distribution and transition points are decoupled for each $y-$value, the cut width may be expressed in terms of the minimum laser power:

$$s = \sqrt{-2\omega_0^2 \ln\left(\frac{\check{P}}{P}\right)} \tag{2.24}$$

Which is identical to Eqn. (2.16) of the power balance.

A MATLAB script for the one-dimensional steady state model is presented in Appendix B.1. Relevant sub-programs are presented in Appendix B.4 and material properties are presented in Appendix A.

2.4 Results and Discussion

2.4.1 Temperature and State Profiles

The heat flow model yields the steady state temperature distribution and layer cut positions of an arbitrary film subject to CW laser irradiation. These parameters are presented in Figs. 2.2 and 2.3 for a three-layer Triplex film, comprising 9μm aluminium between two 20μm polypropylene (PP) layers, subject to laser radiation of wavelength 515nm and beam waist radius 15μm. The former figure displays interaction during a cut at velocity 50mm s^{-1} with beam power 5W; the latter displays interaction during a cut at velocity 1m s^{-1} with beam power 90W. Layer motion is from right to left, as the system of coordinates follows the laser axis travelling at velocity V in the positive $x-$direction (refer to Fig. 2.1). Both power levels are marginally greater than the respective minimums required for complete cuts. At 50mm s^{-1}, the PP layers are removed some 1300μm ahead of the laser beam axis due to conduction from the absorbing aluminium layer. At 1m s^{-1}, the PP layers are instead removed 75μm ahead of the laser beam axis. In this case, the aluminium layer is still wholly responsible for laser absorption. Abrupt changes in temperature gradient are evident at the melting point of the aluminium layer (923K), whilst such changes at the melting point of the PP layers (441K) are less visible, but still present. The enthalpies of vaporisation of the PP layers are ignored, as the material is taken to undergo chemical degradation at 473K (Appendix A).

Figures 2.4 and 2.5 display the temperature distributions and layer cut positions of a two-layer Alufoil film, comprising 7μm aluminium and 69μm paper, for the same laser wavelength and beam diameter. The former figure displays interaction during a cut at velocity 50mm s^{-1} with beam power 4W; the latter displays interaction during a cut at velocity 1m s^{-1} with beam power 75W. Both power levels are again marginally greater than the minimum required for complete cuts. System behaviour is analogous to the previous case. At 50mm s^{-1}, the paper layer is removed 700μm ahead of the laser beam axis due to conduction from the absorbing aluminium layer, whilst at 1m s^{-1}, it is removed 45μm ahead. In both cases, the aluminium layer is wholly responsible for laser absorption. Abrupt changes in temperature gradient are evident at the melting point of

the aluminium layer. The enthalpies of melting and vaporisation of the paper layer are ignored, as the material is taken to undergo removal at 655K (Appendix A).

2.4.2 Minimum Cut Power and Cut Width

In terms of laser selection, minimum cut power and final cut width are the most useful output parameters of both the power balance and the heat flow model. In the former case, expressions are explicit; in the latter, the calculation must be repeated as necessary to find the corresponding values. The minimum cut power of Triplex and Alufoil, subject to laser radiation of wavelength 515nm and beam waist radius 15μm, are presented in Fig. 2.6 (left), according to both the power balance and the heat flow model. The relationships between minimum cut power and velocity are linear. This is not surprising, as neither model accounts for lateral heat conduction losses, while optical absorption does not change over the velocity range considered (Figs. 2.2–2.5). The difference in gradient between the two curves for Triplex reflects the difference in optical absorption between the complete multi-layer film, as considered by the power balance, and that of aluminium, as considered by the heat flow model. This variation is not observed in the curves for Alufoil, as the aluminium layer is not preceded by another material. The differences between Triplex and Alufoil reflect the variation in minimum absorbed laser power required for complete cuts; that is, differences in the right-hand side of Eqn. (2.9). The complete numerical simulation presented in Chapter 4 indicates a minimum cut power of 50W and 140W for Triplex (Fig. 4.13) and 45W and 120W for Alufoil (Fig. 4.14) at $50\mathrm{mm\,s^{-1}}$ and $1\mathrm{m\,s^{-1}}$, respectively. It is clear that conduction losses lead to poor agreement between the present approximation and more accurate models for low velocity processing of thermally conductive films; the disagreement some one order of magnitude at $50\mathrm{mm\,s^{-1}}$. Alignment is improved at $1\mathrm{m\,s^{-1}}$, as the steady state model indicates a value $55-60\%$ lower than that determined by the complete numerical simulation.

Figure 2.6 (right) presents the cut width of any thin film, according to both the power balance and heat flow model, as a function of minimum cut power for a beam waist of radius 15μm. The cut width approaches zero at the minimum cut power, whilst it is equal to the beam waist radius at approximately 165% of the minimum cut power. This

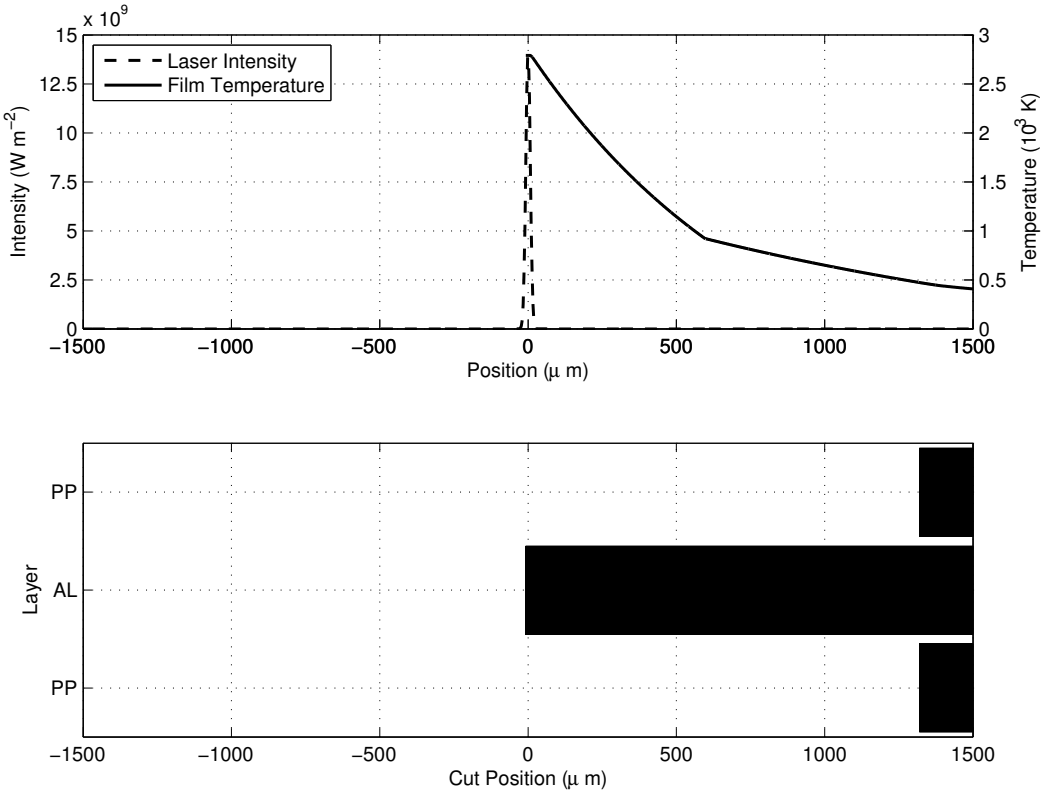

FIGURE 2.2: (Top) Laser intensity, film temperature and (bottom) cut positions of Triplex at $50\text{mm}\,\text{s}^{-1}$ with beam of wavelength 515nm, power 5W and radius 15μm.

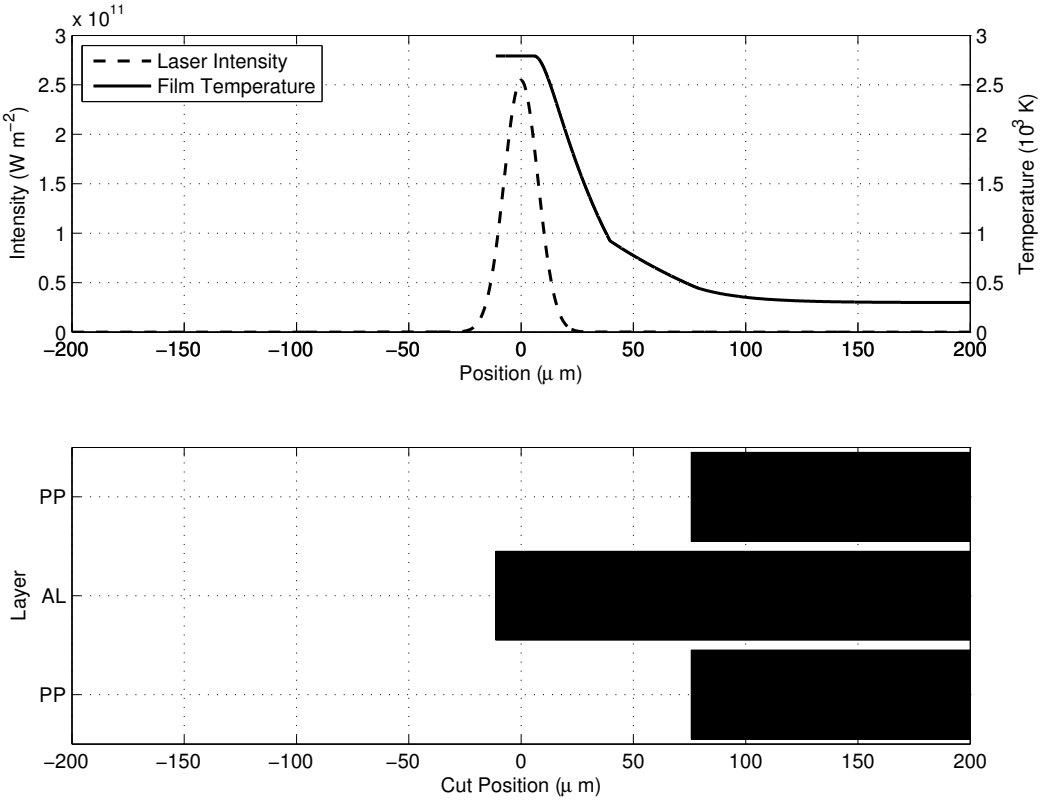

FIGURE 2.3: (Top) Laser intensity, film temperature and (bottom) cut positions of Triplex at $1\text{m}\,\text{s}^{-1}$ with beam of wavelength 515nm, power 90W and radius 15μm.

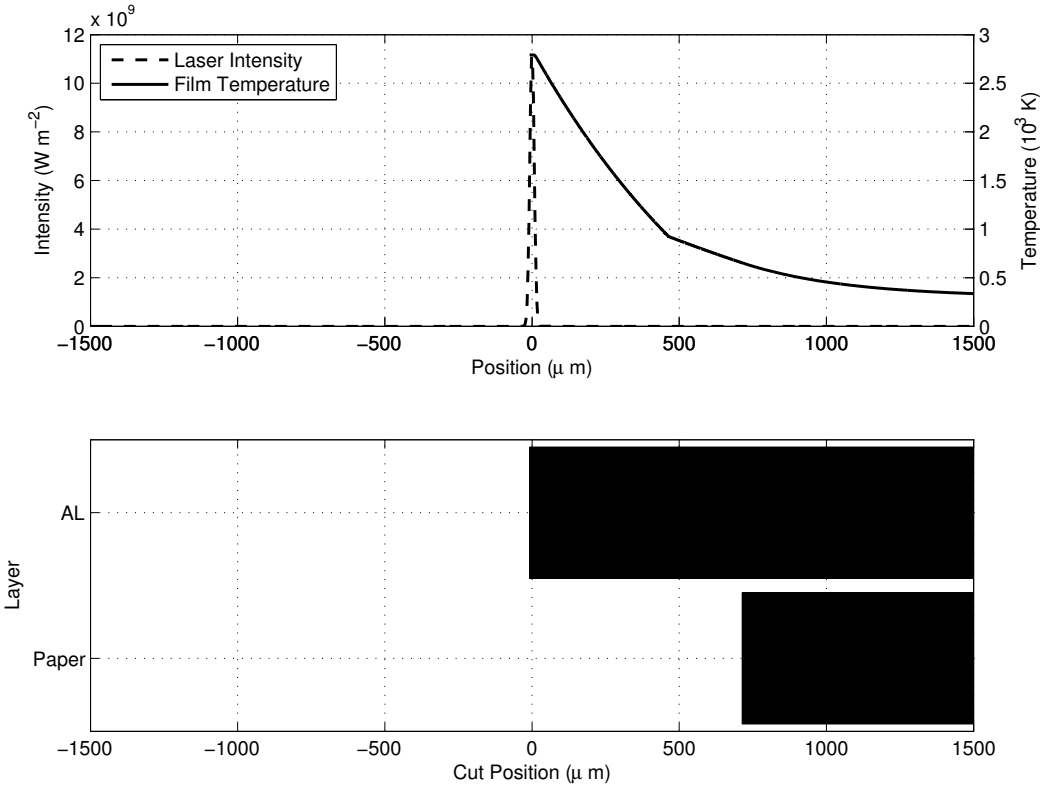

FIGURE 2.4: (Top) Laser intensity, film temperature and (bottom) cut positions of Alufoil at $50\text{mm}\,\text{s}^{-1}$ with beam of wavelength 515nm, power 4W and radius 15μm.

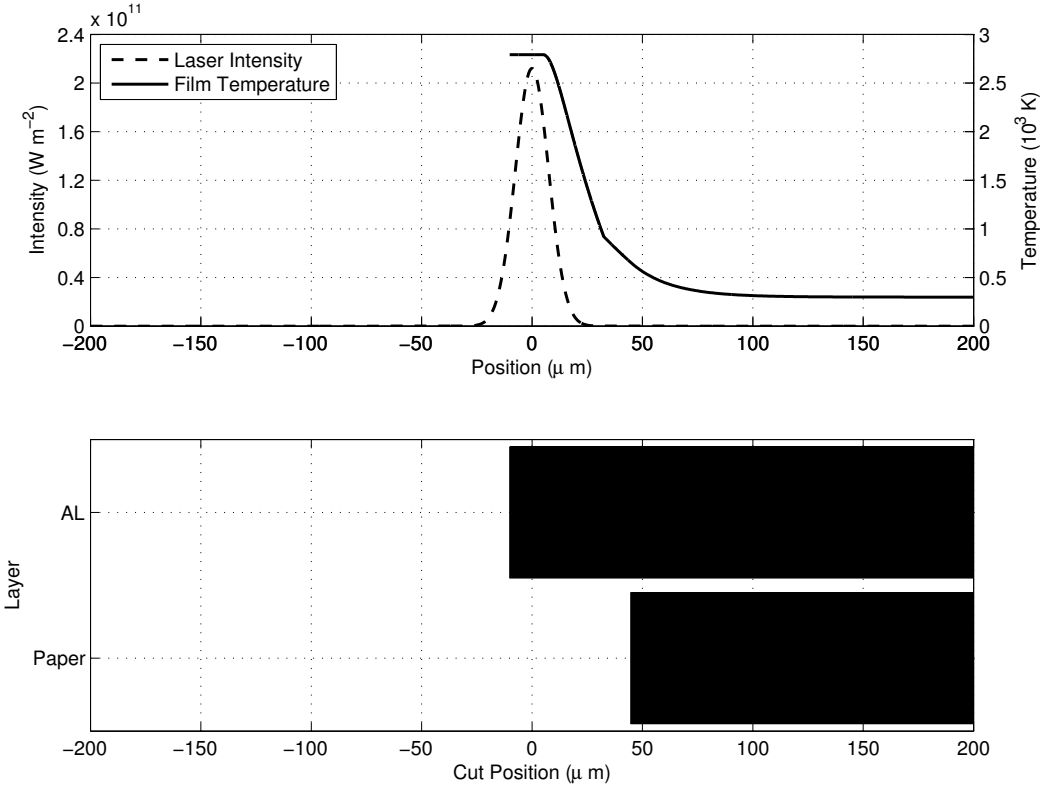

FIGURE 2.5: (Top) Laser intensity, film temperature and (bottom) cut positions of Alufoil at $1\text{m}\,\text{s}^{-1}$ with beam of wavelength 515nm, power 75W and radius 15μm.

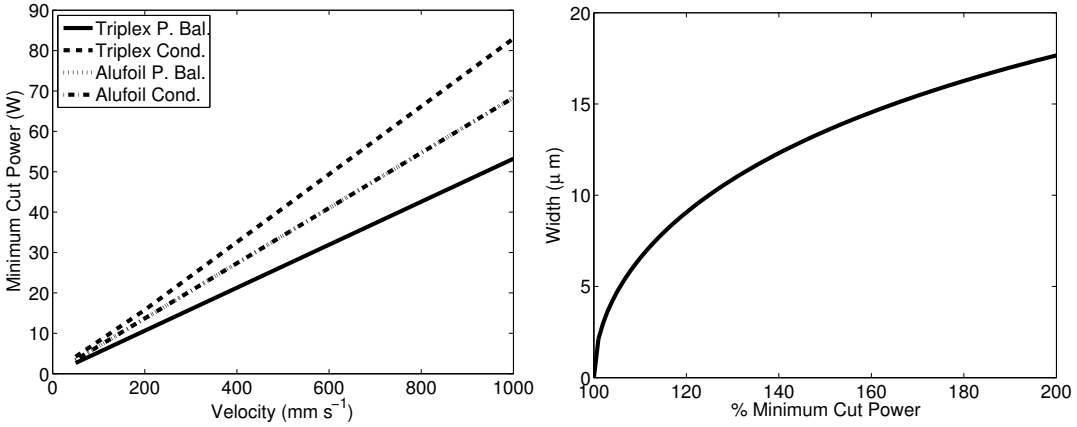

FIGURE 2.6: (Left) Minimum laser power according to the power balance and steady state conduction model for complete cuts of Triplex and Alufoil with a laser of wavelength 515nm and beam waist radius 15μm. (Right) Cut width predicted by both models as a function of minimum laser power for beam waist radius 15μm.

behaviour reflects the relationships given in Eqns. (2.16) and (2.24). The power balance and the heat flow model do not differentiate between the cut widths of separate layers.

2.5 Concluding Remarks

The theory presented in this chapter sets the foundations of the laser cutting problem for thin multi-layer films. Useful insight has been gained into the responses of Triplex and Alufoil packaging films subject to CW laser irradiation. Both the power balance calculation and the heat conduction model predict linear relationships between the velocity and minimum cut power for these materials over the velocity range $50\mathrm{mm\,s^{-1}} - 1\mathrm{m\,s^{-1}}$. The heat conduction model shows that the aluminium layer alone is responsible for optical absorption in each film. This leads to a difference in the predicted minimum cut power between the power balance calculation and the heat conduction model for Triplex. Upon comparison with the numerical simulation presented in Chapter 4, it is clear that lateral heat conduction losses lead to very approximate figures for the minimum cut power in the present case, particularly at low translation speeds. Whilst such conclusions may be obvious for the multi-layer films in question, where the vaporisation temperature and thermal conductivity of one layer is much greater than the others, the models are general and adaptive to more complex scenarios. More importantly, the steady state heat flow calculation represents the closest alternative to a closed-form solution of the evaporative

laser cutting problem for arbitrary thin multi-layer films. The optical calculation presented in section 2.1 will be further utilised in Chapters 3 and 4, while the combination of material properties presented in section 2.3.1 will be employed in Chapter 4.

Chapter 3

A Model for Nanosecond Pulsed Laser Ablation of Metals

The following Chapter presents a one-dimensional model for the nanosecond pulsed laser ablation of metals by vaporisation and phase explosion. The model utilises an approach similar to those of Peterlongo, Miotello & Kelly [58], Bulgakova, Bulgakov & Babich [60], Porneala & Willis [61] and Gragossian, Tavassoli & Shokri [64], applying improvements to the calculation of optical propagation, shielding and absorption. The numerical method is fully developed and the model is verified against several sets of experimental data for aluminium. A comprehensive investigation is undertaken into the effects of laser wavelength, pulse duration and sample thickness on ablation threshold and depth, as well as the influence of initial temperature on absorbed energy and ablation depth. Pulse durations in the range $0.5 - 20$ns are considered, as laser sources in this range may achieve the advantages of efficient short-pulse ablation while presenting realistic investment costs for high-speed packaging machinery.

3.1 Model

3.1.1 Optical Absorption

Optical absorption is calculated in the present model by dividing the material into discrete elements, whose optical properties are considered as constant, and utilising the

method described in section 2.1 for multi-layer optical propagation. The forward and backward travelling components of the energy flux are described by Eqns. (2.1) and (2.2) and the element-specific optical absorption by Eqn. (2.4). The incident on-axis laser energy flux is defined, in this case, as a Gaussian pulse centred at time $t = 0$:

$$I_0(t) = I_{pk}\exp\left[-4\ln(2)\left(\frac{t}{\tau}\right)^2\right] \tag{3.1}$$

Where τ is the full width at half maximum (FWHM) pulse duration and I_{pk} is the peak laser intensity:

$$I_{pk} \approx 0.94\frac{F \cdot 10^4}{\tau} \tag{3.2}$$

Where F is the pulse fluence, in $\mathrm{J\,cm^{-2}}$, related to the pulse energy, E_p, by:

$$F = \frac{2E_p}{\pi\omega_0^2 \cdot 10^4} \tag{3.3}$$

Upon onset of phase explosion, the ablation products, at this point an expanding plume of vapour and liquid, continue to absorb, scatter and reflect the incident laser beam. The corresponding reduction in intensity that reaches the sample surface is calculated in a simplified manner by assuming that, during the laser pulse, the density of ejected material is proportional to the depth of the expanding plume. Justification of this assumption is based on the time-resolved photographs presented by Porneala & Willis [67], which capture the plume dynamics of an aluminium sample subject to 5ns laser pulses. After 22ns, the photographs show ablation products forming a dense expansion front, approximately linear in nature, close to the target surface. Plume expansion becomes less orderly over the time-period $52 - 636$ns; however, for pulses in the range $0.5 - 20$ns, this is no longer of concern when approximating beam shielding. As such, a simulated shielding coefficient, α_{sh}, is introduced to account for scattering, reflection and absorption by the ablation products in a way analogous to that in which Singh & Viatella [116] utilise such a coefficient for plasma absorption:

$$\alpha_a d_a = \Delta z_{pe}\alpha_{sh} \tag{3.4}$$

Where α_a and d_a are the actual absorption coefficient and depth of the expanding plume and Δz_{pe} is the calculated phase explosion depth. The incident intensity reaching the

sample becomes:

$$U_0^+(t) = I_0(t)\exp\left[-\alpha_{sh}\Delta z_{pe}(t)\right] \tag{3.5}$$

Where $U_0^+(t)$ is the source term for the optical calculation. Simplification in this manner allows estimation of the reduction in beam intensity reaching the sample surface without detailed knowledge of the plume dynamics. The shielding coefficient for a given set of laser parameters is determined experimentally by aligning the simulated and measured ablation depth at an arbitrary fluence above the ablation threshold.

In the numerical calculation, the incident on-axis laser intensity at time-step η is expressed as follows, to ensure accurate beam energy regardless of time-step size:

$$\begin{aligned} I_0^\eta &= \frac{I_{pk}}{\Delta t}\int_{t^{\eta-1}}^{t^\eta} \exp\left[-4\ln(2)\left(\frac{t}{\tau}\right)^2\right] \mathrm{dt} \\ &= \frac{I_{pk}\tau}{4\Delta t}\sqrt{\frac{\pi}{\ln(2)}}\left[\mathrm{erf}\left(\frac{2t^\eta\sqrt{\ln(2)}}{\tau}\right) - \mathrm{erf}\left(\frac{2t^{\eta-1}\sqrt{\ln(2)}}{\tau}\right)\right] \end{aligned} \tag{3.6}$$

Where superscript η denotes the index of the corresponding time-step and Δt is the time-step size. The incident on-axis laser intensity, I_0^η, shielding coefficient, α_{sh}, and the calculated phase explosion depth, Δz_{pe}^η, lead to absorbed intensity, $I_{a,p}^\eta$, in element p. Practically speaking, the calculation need only be applied to elements less than $\sim$ 200nm from the target surface due to the small optical absorption depth in metals.

3.1.2 Temperature Dependent Material Properties

The large temperature range traversed by metals under pulse laser irradiation leads to significant changes in their physical properties, particularly near the critical temperature. Unlike continuous-wave (CW) laser cutting, where material properties are often considered as constant, an accurate representation of short-pulse ablation must account for temperature dependent material properties. Aluminium, of widespread use in the packaging industry, will be considered in the present study. Its physical properties have been investigated under a wide range of conditions and a number of experimental laser ablation studies provide data with which model verification may be undertaken.

The electrical resistivity of aluminium is published in literature for temperatures up to 2000K (Desai, James & Ho [117]). The relationship between temperature and electrical resistivity over this range is approximately linear. Under the assumption that this trend

continues above 2000K, the electrical resistivity may be extrapolated for the range 2000K to $0.8T_c$ (5360K), noting that the critical temperature, T_c, of aluminium is 6700K (Morel, Bultel & Chéron [118]). Between $0.8T_c$ and $0.9T_c$ (6030K), the electrical conductivity is presented by Wu & Shin [119]. The relationship between electrical and thermal conductivity is given by the Wiedemann-Franz law:

$$K = LT\sigma \tag{3.7}$$

Where K is the thermal conductivity, L the Lorenz number, T the temperature in Kelvin and σ the electrical conductivity. The relationship between electrical conductivity and refractive index is determined by considering the electron collision frequency, β, according to the Drude model (Born & Wolf [41]):

$$\beta = \frac{Ne^2}{m\sigma}$$

$$\hat{n}^2 = (n + i\kappa)^2 = 1 - \frac{c^2\mu_0 Ne^2}{m\omega(\omega + i\beta)} \tag{3.8}$$

Where N is the electron number density, e the charge of one electron, m the mass of one electron, σ the electrical conductivity and μ_0 vacuum permeability. Using Eqn. (3.8), both the real part of $\hat{n}$, usually termed simply the refractive index, n, and the imaginary part, usually termed the extinction coefficient, κ, may be determined:

$$\begin{aligned} \kappa &= \left(\frac{-A + \sqrt{A^2 - 4B}}{2} \right)^{1/2} \\ n &= \frac{\beta\left(\omega_c^2 + \beta^2\right)}{2\kappa\omega\left(\omega^2 + \beta^2\right)} \end{aligned} \tag{3.9}$$

Where:

$$\begin{aligned} A &= 1 - \frac{\omega_c^2 + \beta^2}{\omega^2 + \beta^2} \\ B &= -\frac{\beta^2\left(\omega_c^2 + \beta^2\right)^2}{4\omega^2\left(\omega^2 + \beta^2\right)^2} \\ \omega_c^2 &= \frac{c^2\mu_0 Ne^2}{m} - \beta^2 \end{aligned}$$

Where ω_c is the critical frequency at which the real part of the dielectric constant changes sign (Born & Wolf [41]). The variation in electrical and thermal conductivity, and the

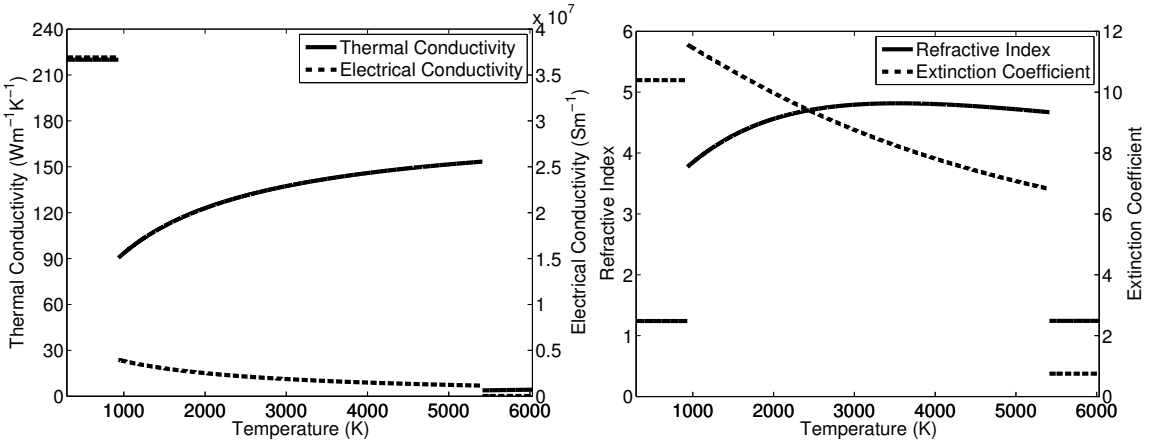

FIGURE 3.1: (Left) Aluminium electrical and thermal conductivities and (right) real and imaginary parts of refractive index at wavelength 1064nm from 298K to 6030K.

real and imaginary parts of the refractive index at wavelength 1064nm, are shown in Fig. 3.1 for aluminium for the temperature range $298 - 6030$K. For temperatures up to the melting point (923K), all parameters are considered as those at room temperature, whilst above $0.8T_c$ (5360K), the electrical conductivity is taken as $2.9 \times 10^4 \mathrm{S\,m^{-1}}$ (Wu & Shin [119]). Abrupt changes in all parameters are evident at 933K and 5360K, corresponding to the melting point and dielectric transition.

3.1.3 Heat-Flow

The optical absorption depth of laser radiation in metals is in the order of nanometres, whilst the beam radius is typically tens of microns. The temperature gradient arising from the heat source is therefore much greater in the $z-$direction than in either the $x-$ or $y-$directions and the problem may be considered one-dimensional:

$$C\rho\frac{\partial T}{\partial t} = \frac{\partial}{\partial z}\left(K(T)\frac{\partial T}{\partial z}\right) + \dot{q} \tag{3.10}$$

Where C is the specific heat capacity, ρ the density and $\dot{q}$ the source term. The surface is considered thermally insulated, whilst at distances far from the surface the target remains at the initial temperature, T_I. Boundary and initial conditions are therefore:

$$\left.\frac{\partial T}{\partial z}\right|_{z=0} = 0, \quad T|_{z\to\infty} = T_I, \quad T|_{t=0} = T_I \tag{3.11}$$

In the numerical calculation, the Crank-Nicolson method (Tannehill, Anderson & Pletcher [120]) is utilised; Eqn. (3.10) becomes:

$$C\rho \quad \frac{T_p^\eta - T_p^{\eta-1}}{\Delta t} = \frac{1}{\Delta z}\left[\left(\frac{K_{p+1}^\eta + K_p^\eta}{2}\right)\left(\frac{T_{p+1}^\eta - T_p^\eta}{2\Delta z}\right) + \left(\frac{K_{p+1}^{\eta-1} + K_p^{\eta-1}}{2}\right)\left(\frac{T_{p+1}^{\eta-1} - T_p^{\eta-1}}{2\Delta z}\right) + \left(\frac{K_{p-1}^\eta + K_p^\eta}{2}\right)\left(\frac{T_{p-1}^\eta - T_p^\eta}{2\Delta z}\right) + \left(\frac{K_{p-1}^{\eta-1} + K_p^{\eta-1}}{2}\right)\left(\frac{T_{p-1}^{\eta-1} - T_p^{\eta-1}}{2\Delta z}\right) + I_{a,p}^\eta\right] \tag{3.12}$$

Where subscript p denotes the index of the corresponding $z-$position and Δz is the mesh spacing size. Equation (3.12) expresses T^η implicitly for each time-step and must be resolved as a system of linear algebraic equations. The averaging of conductivity, K, between adjacent elements is undertaken to ensure continuity of energy flux. At the metal-dielectric interface, where a large discontinuity in thermal conductivity is present (Fig. 3.1), the average conductivity in the negative direction is replaced with K_{p-1} for the element in metallic state and that in the positive direction is replaced with K_p for the element in dielectric state, for both time-steps η and $\eta - 1$. The conductivity at the interface is thus effectively taken as that of the element in dielectric state. This applies the abrupt change in conductivity across one element, the last in metallic state, rather than across the interface between elements.

To satisfy boundary conditions, Eqn. (3.12) is modified for the first and last elements, respectively, as follows:

$$C\rho\frac{T_1^\eta - T_1^{\eta-1}}{\Delta t} = \frac{1}{\Delta z}\left[\left(\frac{K_2^\eta + K_1^\eta}{2}\right)\left(\frac{T_2^\eta - T_1^\eta}{2\Delta z}\right) + \left(\frac{K_2^{\eta-1} + K_1^{\eta-1}}{2}\right)\left(\frac{T_2^{\eta-1} - T_1^{\eta-1}}{2\Delta z}\right) + I_{a,1}^\eta\right] \tag{3.13}$$

$$C\rho\frac{T_{\hat{p}}^\eta - T_{\hat{p}}^{\eta-1}}{\Delta t} = \frac{1}{\Delta z}\left[\left(\frac{K_{\hat{p}-1}^\eta + K_{\hat{p}}^\eta}{2}\right)\left(\frac{T_{\hat{p}-1}^\eta - T_{\hat{p}}^\eta}{2\Delta z}\right) + \left(\frac{K_{\hat{p}-1}^{\eta-1} + K_{\hat{p}}^{\eta-1}}{2}\right)\left(\frac{T_{\hat{p}-1}^{\eta-1} - T_{\hat{p}}^{\eta-1}}{2\Delta z}\right) + I_{a,\hat{p}}^\eta\right] \tag{3.14}$$

Where $\hat{p}$ is the number of elements. The condition $T|_{z\to\infty} = T_I$ is effectively replaced with $\partial T/\partial z|_{z=z_{\hat{p}}} = 0$. This has the practical advantage of allowing adequacy of the calculation domain size to be assessed by checking the difference between $T_{\hat{p}}$ and T_I at the final time-step. The domain size is chosen to be sufficiently large so as to ensure negligible temperature change at this point, approximating the corresponding condition

in Eqn. (3.11). The initial condition is satisfied by setting $T^1 = T_I$ for all elements. Mesh-spacing size is constant for all elements.

3.1.4 Material Removal

Material removal by both vaporisation and phase explosion is considered. The velocity of surface recession due to vaporisation, in $\mathrm{cm\,s^{-1}}$, is given by the Hertz-Knudsen equation (Herman, Richter & Sitter [121], Xu & Yan [122]):

$$\nu = \frac{0.82 \cdot p_{sat}}{\sqrt{2\pi M k_B N_A T_s}} \left(\frac{M}{\rho}\right) \tag{3.15}$$

Where the sticking coefficient is taken as 1, coefficient 0.82 accounts for back-flow of vapour to the surface, M is the molar mass in $\mathrm{g\,mol^{-1}}$, k_B the Boltzmann constant, N_A Avogadro's number, T_s the surface temperature in Kelvin, ρ the density in $\mathrm{g\,cm^{-3}}$ and p_{sat} the saturation pressure given by the Clausius-Clapeyron equation:

$$p_{sat} = p_{atm} \exp\left[\frac{H_v M}{k_B N_A}\left(\frac{1}{T_v} - \frac{1}{T_s}\right)\right] \tag{3.16}$$

Where p_{atm} is atmospheric pressure in torr, H_v the enthalpy of vaporisation in $\mathrm{J\,g^{-1}}$ and T_v the vaporisation temperature in Kelvin. Equations (3.15) and (3.16) are presented in their conventional forms that do not use SI units. In the numerical calculation, the discrete vaporisation depth, Δz_v^η, is determined as follows for surface temperatures above the vaporisation temperature:

$$\Delta z_v^\eta = \begin{cases} 0, & \text{if } \eta = 1, \\ \Delta z_v^{\eta-1} + \Delta z, & \text{if } \epsilon^\eta > \Delta z, \\ \Delta z_v^{\eta-1}, & \text{otherwise} \end{cases} \tag{3.17}$$

Where:

$$\epsilon^\eta = \begin{cases} 0, & \text{if } \eta = 1, \\ \epsilon^{\eta-1} - \Delta z + \nu^\eta \cdot \Delta t, & \text{if } \epsilon^{\eta-1} > \Delta z, \\ \epsilon^{\eta-1} + \nu^\eta \Delta t, & \text{otherwise} \end{cases}$$

The thermal and optical calculations are updated at each time-step to account for changes in surface position. Elements are removed due to phase explosion when they reach $0.9T_c$. The corresponding phase explosion depth is Δz_{pe}^η, which contributes to

beam shielding according to Eqn. (3.5). The discrete ablation depth, d^{η}, is the sum of the vaporisation and phase explosion depths:

$$d^{\eta} = \Delta z_v^{\eta} + \Delta z_{pe}^{\eta} \tag{3.18}$$

Vaporisation is no longer considered once phase explosion has initiated.

A MATLAB script for the single-pulse model is presented in Appendix B.2. Relevant sub-programs are presented in Appendix B.4 and additional material properties are presented in Appendix A.

3.2 Results and Discussion

3.2.1 Temperature Profiles

The model yields metallic target temperature distribution and surface position as functions of time for single laser pulses. These parameters are presented in Fig. 3.2, together with surface reflectivity, for an aluminium target subject to pulses of wavelength 515nm and duration 1ns, below and above the phase explosion threshold. Figure 3.3 displays the same information for 10ns pulses of the same wavelength. The computational $z-$domain in each case is 4μm, twice that displayed in the figures, while the temporal profile of each pulse is centred about $t = 0$s according to Eqn. (3.1). White space in each continuous temperature distribution represents recession of the target surface. In all cases, $T_{\hat{p}}^{\hat{\eta}}$, the temperature of the furthest element from the surface at the final time step, is less than 1K greater than the initial temperature (298K). Abrupt changes in temperature gradient are visible at the melting temperature (923K) and at the dielectric transition (5360K), corresponding to abrupt changes in thermal conductivity at these points (Fig. 3.1). Abrupt changes in target reflectivity are also evident as the surface reaches both the melting temperature and $0.8T_c$, corresponding to abrupt changes in surface optical properties at these points. The observed singularities are due to the propagation of these abrupt changes into the sample. For pulses of duration 1ns, $1\,\mathrm{J\,cm^{-2}}$ raises the surface temperature to 2180K, insufficient for vaporisation or phase explosion on the given time-scale, whilst $2\,\mathrm{J\,cm^{-2}}$ sees attainment of $0.9T_c$ and subsequent onset of material removal due to phase explosion. For pulses of duration 10ns, $3\,\mathrm{J\,cm^{-2}}$ is again below the

ablation threshold, with the surface reaching 2080K, whilst $6\,\mathrm{J\,cm^{-2}}$ sees strong onset of material removal due to phase explosion. The continuous temperature distributions display constant surface temperature at 6030K during the period in which phase explosion takes place. Thermal penetration into the work piece is notably greater for 10ns pulses than for 1ns pulses, leading to a more elevated phase explosion threshold fluence in the former case. Optical reflectivity falls to less than 50% during the period in which the target surface is in dielectric state; an almost seven-fold increase in optical absorption compared to the room temperature value at 515nm (7.7%). This increase is due to improved optical coupling between the preceding medium (assumed to be vacuum) and the metallic substrate via the dielectric layer.

3.2.2 Ablation Depth

The relationship between ablation depth and fluence is fundamental to the full theoretical representation of nanosecond pulsed laser ablation of metals, as well as the practical implementation of pulsed laser sources for the incision and cut of metallic films. Curves for the ablation depth as a function of fluence are derived within the present framework by incrementing the fluence over the desired range and repetitively executing the calculation. These decoupled calculations may be simultaneously assigned to all processors made available to the task.

The effect of the shielding coefficient on ablation depth is first and foremost of interest. It is the choice of this parameter that allows alignment of simulation results with experimental data. Figure 3.4 presents the relationship between ablation depth and fluence up to $23.3\,\mathrm{J\,cm^{-2}}$ for an aluminium target subject to pulses of wavelength 1064nm and duration 4.5ns, with various shielding coefficients. The choice of coefficient has no influence on the calculated phase explosion threshold fluence, as onset of shielding coincides with phase explosion. Below threshold fluence, no material removal takes place, whilst for high fluences, the rate of increase in ablation depth decreases with fluence. Sharp onset of ablation due to phase explosion is observed at threshold fluence. The maximum depth attained at $23.3\,\mathrm{J\,cm^{-2}}$ is 570nm, corresponding to $\alpha_{sh} = 0.5 \times 10^{7}\mathrm{m}^{-1}$, and the minimum is 251nm, corresponding to $\alpha_{sh} = 1.25 \times 10^{7}\mathrm{m}^{-1}$. The curve corresponding to $\alpha_{sh} = 1 \times 10^{7}\mathrm{m}^{-1}$ is in good agreement with the results of Stafe *et al.* [68], obtained experimentally over the range $7.5 - 22\,\mathrm{J\,cm^{-2}}$ using the same laser parameters.

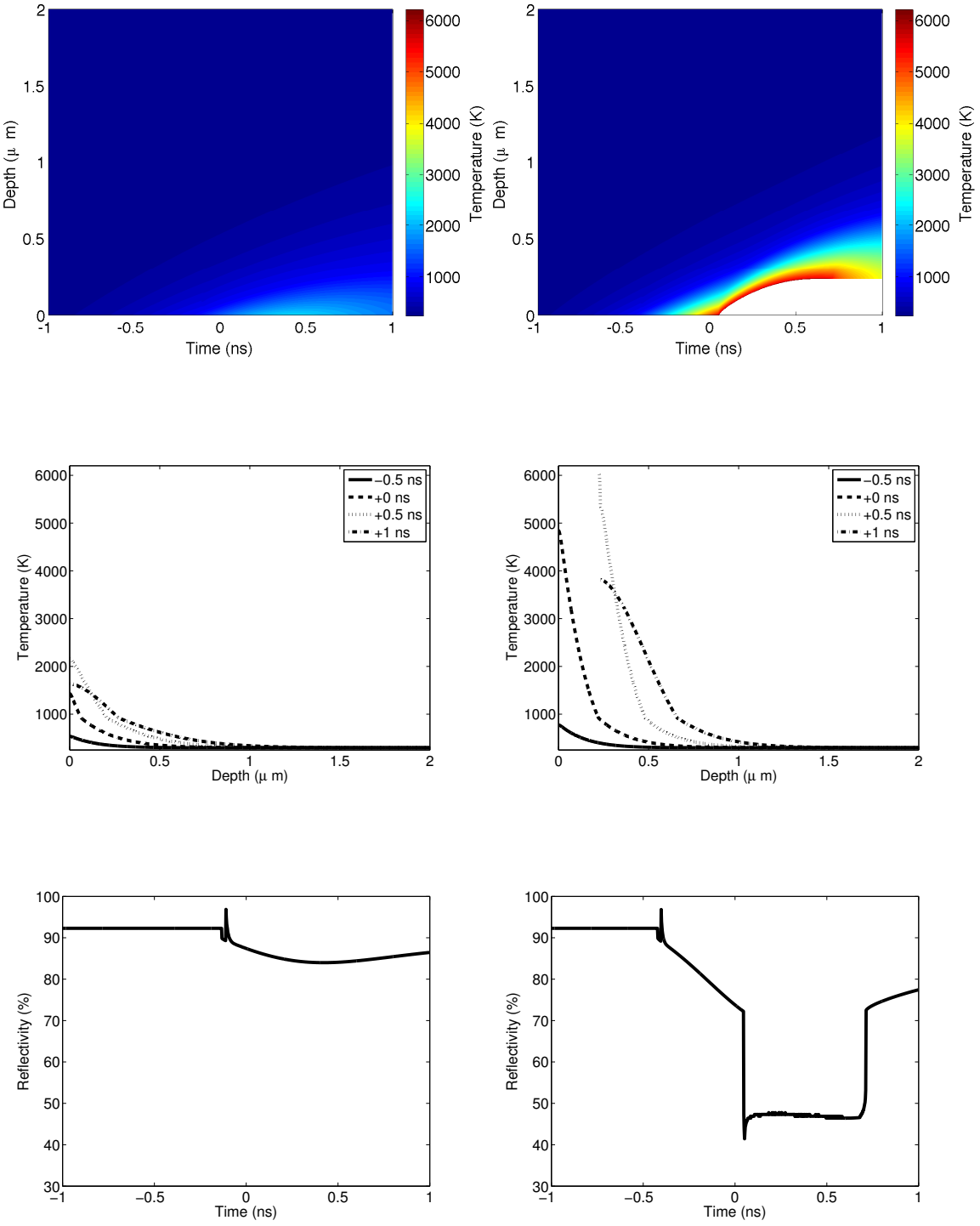

FIGURE 3.2: (Top) Continuous temperature distribution, (middle) temperature distribution at selected times and (bottom) reflectivity of an aluminium target exposed to single (left) $1\,\mathrm{J\,cm^{-2}}$ and (right) $2\,\mathrm{J\,cm^{-2}}$ pulses of duration 1ns and wavelength 515nm.

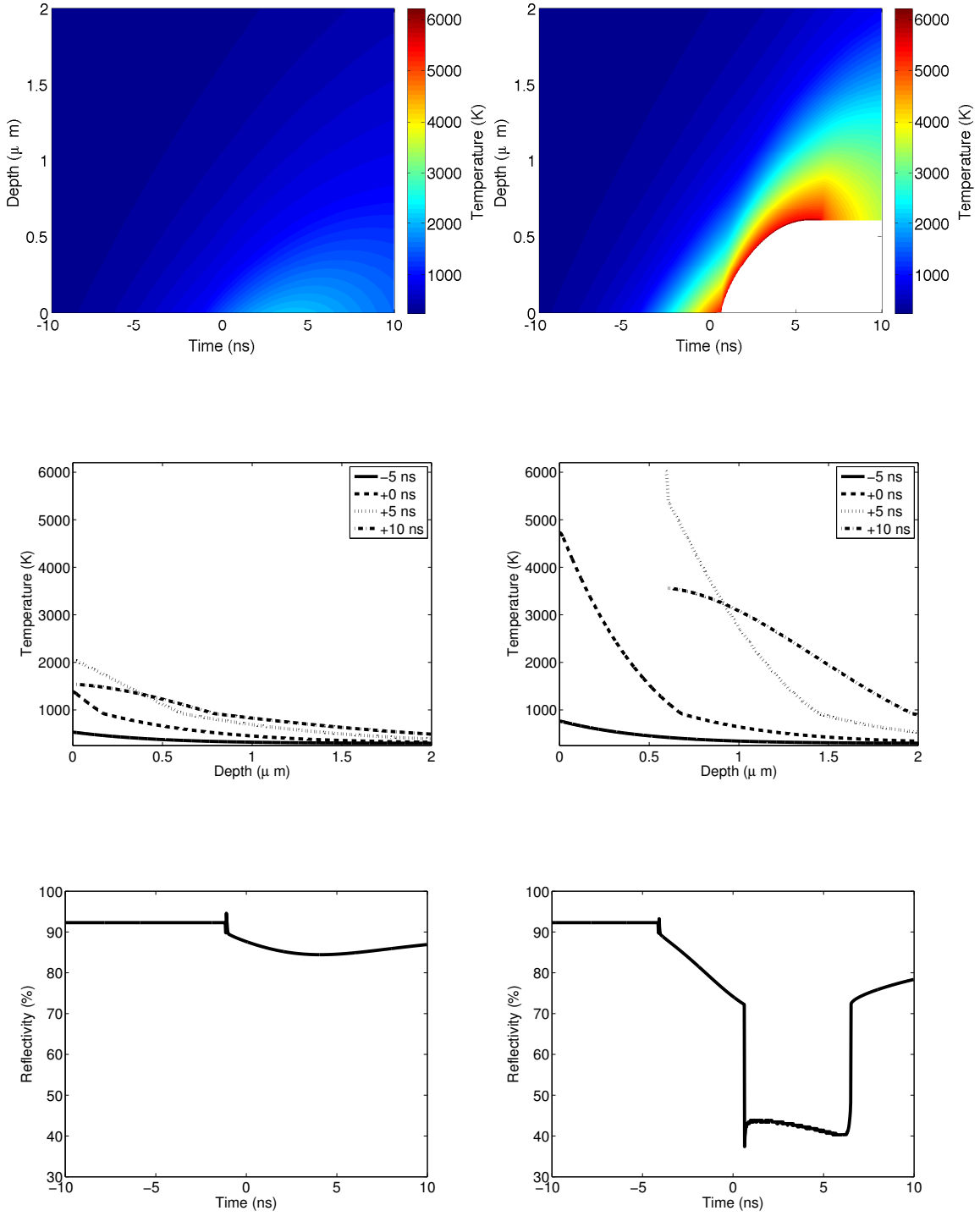

FIGURE 3.3: (Top) Continuous temperature distribution, (middle) temperature distribution at selected times and (bottom) reflectivity of an aluminium target exposed to single (left) $3\,\mathrm{J\,cm^{-2}}$ and (right) $6\,\mathrm{J\,cm^{-2}}$ pulses of duration 10ns and wavelength 515nm.

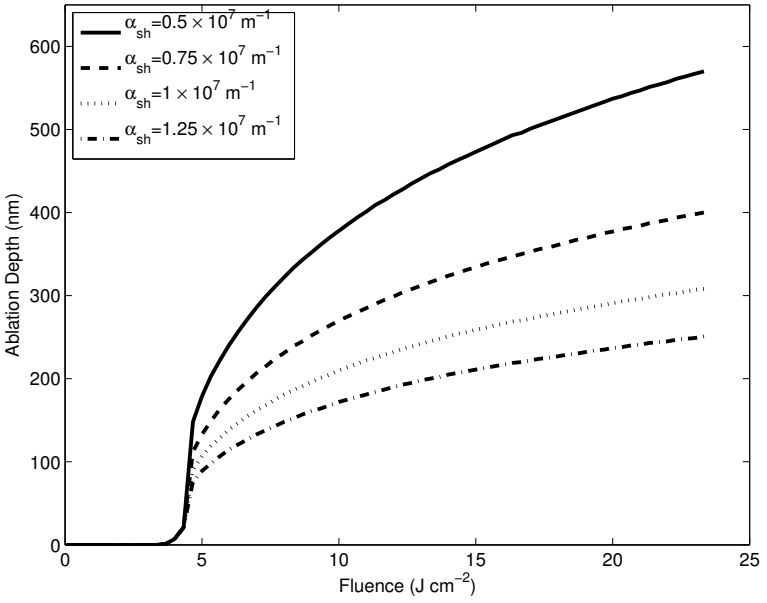

FIGURE 3.4: Calculated ablation depth of aluminium for wavelength 1064nm and pulse duration 4.5ns with various shielding coefficients.

Several sets of experimental data have been published for nanosecond pulsed laser ablation of aluminium. Alignment of simulation and experimental data is achieved in each case by choosing a suitable shielding coefficient. Figure 3.5 (left) presents simulation results for pulses of wavelength 1064nm and duration 5ns for fluences up to $23.3\,\mathrm{J\,cm^{-2}}$, with a shielding coefficient of $8\times10^{7}\,\mathrm{m^{-1}}$. The experimental results of Porneala & Willis [67], obtained with the same parameters over the fluence range $2-12.5\,\mathrm{J\,cm^{-2}}$, are presented in the same figure[1]. The simulated curve displays a small peak in ablation depth at $5\,\mathrm{J\,cm^{-2}}$, corresponding to a brief window of combined vaporisation and phase explosion prior to significant onset of, and shielding from, the latter. Good agreement with the experimental results is attained over the tested fluence range, both in terms of ablation threshold and depth. The simulated ablation depth overestimates the experimental values to a small extent from $4.6\,\mathrm{J\,cm^{-2}}$, the calculated onset of phase explosion, to $7\,\mathrm{J\,cm^{-2}}$. The observed onset of phase explosion by Porneala & Willis is $4.3-5.2\,\mathrm{J\,cm^{-2}}$.

Figure 3.5 (right) presents simulation results for pulses of wavelength 1064nm and duration 4.5ns for fluences up to $23.3\,\mathrm{J\,cm^{-2}}$, with a shielding coefficient of $1\times10^{7}\,\mathrm{m^{-1}}$. The experimental results of Stafe *et al.* [68], obtained with the same parameters over the fluence range $7.5-22\,\mathrm{J\,cm^{-2}}$, are presented in the same figure. Good agreement with the experimental results is attained over the tested fluence range. Figure 3.6 (left) displays

[1] All experimental values presented in Figs. 3.5 and 3.6 are not tabulated within the cited works. They have therefore been measured from the relevant figures.

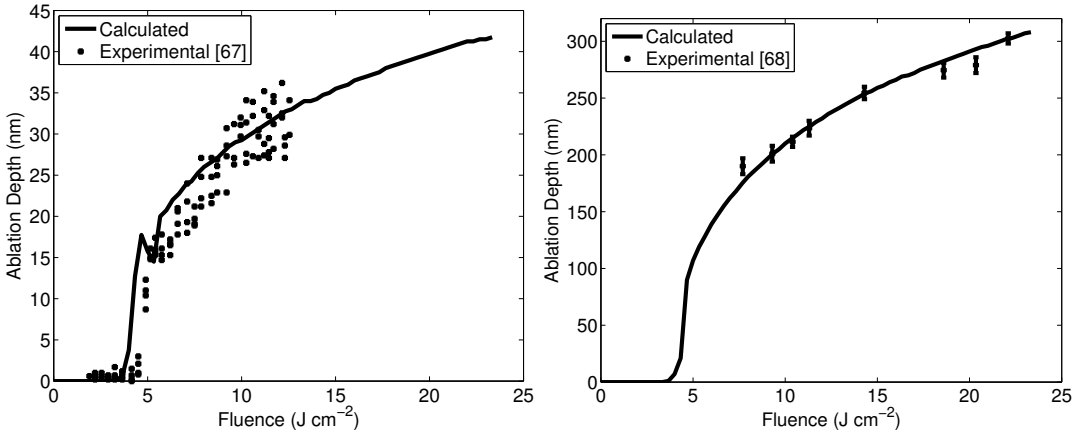

FIGURE 3.5: (Left) Calculated ablation depth of aluminium for wavelength 1064nm and pulse duration 5ns ($\alpha_{sh} = 8 \times 10^7 \mathrm{m}^{-1}$) with experimental results of Porneala & Willis [67]. (Right) Calculated ablation depth of aluminium for wavelength 1064nm and pulse duration 4.5ns ($\alpha_{sh} = 1 \times 10^7 \mathrm{m}^{-1}$) with experimental results of Stafe *et al.* [68].

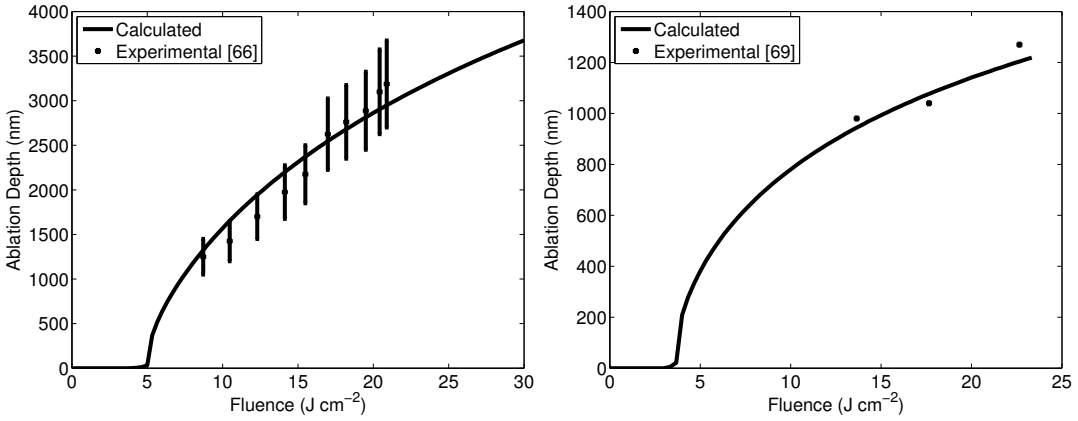

FIGURE 3.6: (Left) Calculated ablation depth of aluminium for wavelength 532nm and pulse duration 10ns ($\alpha_{sh} = 4.25 \times 10^5 \mathrm{m}^{-1}$) with experimental results of Colina *et al.* [66]. (Right) Calculated ablation depth of aluminium for wavelength 266nm and pulse duration 6ns ($\alpha_{sh} = 2 \times 10^6 \mathrm{m}^{-1}$) with experimental results of Horn, Guillong & Günther [69].

the calculated ablation depth for pulses of wavelength 532nm and duration 10ns for fluences up to $30\mathrm{J\,cm}^{-2}$, with a shielding coefficient of $4.25 \times 10^5 \mathrm{m}^{-1}$. The experimental results of Colina *et al.* [66], obtained with the same parameters over the fluence range $8.5 - 21\mathrm{J\,cm}^{-2}$, are presented in the same figure. Fair alignment with the experimental results is attained. The simulated ablation depth overestimates the experimental values to a small extent over the range $10 - 16\mathrm{J\,cm}^{-2}$. Figure 3.6 (right) presents the simulated ablation depth for pulses of wavelength 266nm and duration 6ns for fluences up to $23.3\mathrm{J\,cm}^{-2}$, with a shielding coefficient of $2 \times 10^6 \mathrm{m}^{-1}$. The experimental results of Horn, Guillong & Günther [69], obtained with the same parameters over the fluence

range $13.5 - 22.5\,\mathrm{J\,cm^{-2}}$, are presented in the same figure. The simulation provides a reasonable representation of the few experimental data points available.

Figure 5.11 (right) in Chapter 5 presents the simulated ablation depth per pulse of aluminium for eight different scenarios that are tested experimentally in the present work. Four test parameter groups are considered (Tab. 5.2), at two different translation velocities, $50\mathrm{mm\,s^{-1}}$ and $1\mathrm{m\,s^{-1}}$. By considering pulse overlap under translating conditions (section 5.3), good agreement between simulated and experimental results is attained in all cases (Figs. 5.10 (right) and 5.11 (left)). This particular investigation demonstrates an increase in beam shielding by the ablation products for 1064nm over 515nm, as well as for multi-pulse exposure over single-pulse exposure (Tab. 5.4).

All of the above cases display similar behaviour: sharp onset of ablation at the phase explosion threshold followed by a gradual reduction in the rate of increase of ablation depth with fluence. Vaporisation plays no significant part in material removal for the pulse durations considered. Introduction of the absorption coefficient allows accurate alignment with experimental results over a wide range of laser parameters. The variation in shielding coefficient between data sets reflects the variation in published experimental figures. The ablation depths reported by Stafe *et al.* [68], for example, are one order of magnitude greater than those of Porneala & Willis [67], despite the use of similar laser sources. Correspondingly, the shielding coefficient employed for theoretical representation of the former is one order of magnitude less than that of the latter. The number of pulses and repetition rate are clearly of importance when considering the total effective shielding of the laser beam by the ablation products. While no attempt has been made to model plume dynamics, the shielding coefficient provides simple equivalence and accurate calculation of ablation depth where at least one experimental result is known.

3.2.3 Phase Explosion Threshold

The phase explosion threshold is of both practical and theoretical interest, as onset of this phenomenon sees abrupt changes take place in terms of material removal rate and ablation quality. The ablation efficiency, defined as the ratio of removed material to fluence, is greatest shortly above threshold fluence. It is therefore an important parameter for the optimisation of laser processing systems. Given the resources required to experimentally obtain the phase explosion threshold, prediction through simulation

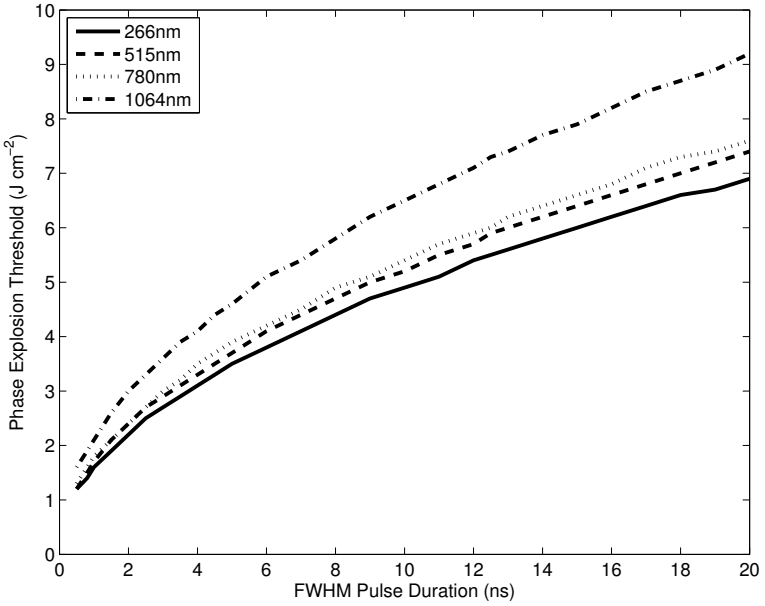

FIGURE 3.7: Phase explosion threshold of aluminium as a function of pulse duration for wavelengths 266nm, 515nm, 780nm and 1064nm.

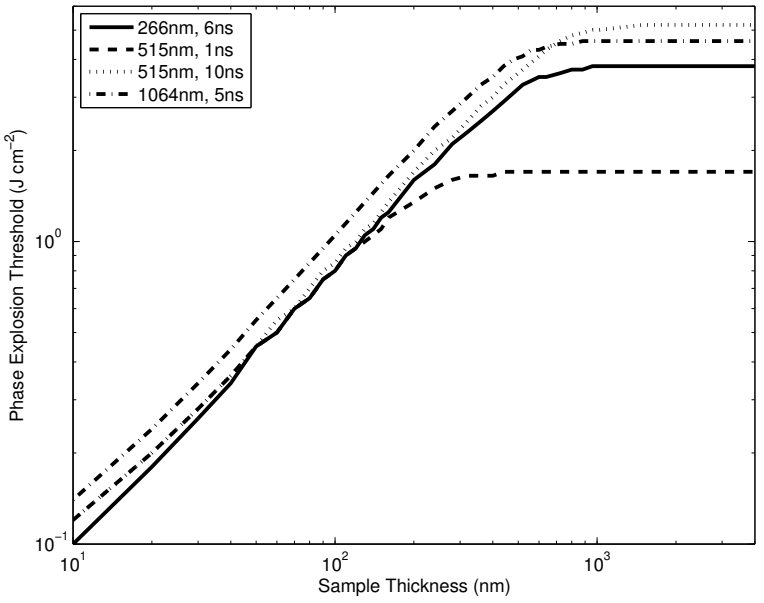

FIGURE 3.8: Phase explosion threshold of aluminium as a function of sample thickness for various laser sources.

offers advantages in terms of time and cost. In light of the simulation results, the phase explosion threshold may be considered analogous to the ablation threshold for pulses of duration $<$ 20ns.

The ablation threshold is a strong function of laser wavelength and pulse duration, as the onset of phase explosion is dictated by optical absorption of the laser beam and thermal energy transport away from the sample surface. Simulated values have been determined

for aluminium by incrementing the fluence near the threshold and establishing the value at which the surface temperature first reaches $0.9T_c$. Figure 3.7 displays the calculated ablation thresholds for pulse durations in the range $0.5 - 20$ns and laser wavelengths of 266nm, 515nm, 780nm and 1064nm. All curves tend to zero as the pulse duration tends to zero, though accurate representation of the ablation threshold in this manner is only expected for pulses of duration $\geq$ 1ns (Martynyuk [54]). For pulses of duration 1ns, ablation thresholds of $1.6\mathrm{J\,cm^{-2}}$, $1.7\mathrm{J\,cm^{-2}}$, $1.8\mathrm{J\,cm^{-2}}$ and $2.1\mathrm{J\,cm^{-2}}$ are calculated for 266nm, 532nm, 780nm and 1064nm, respectively. For pulses of duration 20ns, the same wavelengths yield calculated ablation thresholds of $6.9\mathrm{J\,cm^{-2}}$, $7.4\mathrm{J\,cm^{-2}}$, $7.6\mathrm{J\,cm^{-2}}$ and $9.2\mathrm{J\,cm^{-2}}$. A fourfold difference is seen over the pulse duration range considered.

The variation in ablation threshold with sample thickness is seldom discussed; yet, it is of practical interest for thin-film applications where layers are of thickness $< 1\mu$m. Such values, for example, are typically of thin-film photovoltaics (Bovatsek *et al.* [110]). Thin metallic layers of thickness $< 0.1\mu$m are also present in some of the packaging materials considered experimentally in Chapter 5 (Tab. 5.1). The effect of sample thickness is noteworthy only where thermal saturation of the target comes into play. This, in turn, is dependent on the pulse duration, which dictates the degree of thermal penetration. The calculated ablation threshold for four different laser sources is presented in Fig. 3.8 for sample thicknesses in the range $10 - 4000$nm. For extremely thin targets, heat conduction is insignificant and threshold fluence is dependent on optical absorption only. For larger thicknesses, threshold values are identical to those in Fig. 3.7; functions of both laser wavelength and pulse duration. The minimum sample thickness at which this parameter no longer affects the ablation threshold depends on the pulse duration under consideration. This value is approximately 450μm, 900μm, 950μm and 1500μm for the pulses of duration 1ns, 5ns, 6ns and 10ns considered in Fig. 3.8, respectively.

The numerical simulation provides clarity of the factors influencing the ablation threshold. Results are independent of the choice of shielding coefficient and may therefore be generated without reliance on experimental data. The penetration of thermal energy into the work piece is of fundamental importance; the ablation threshold is a function of both the sample and laser characteristics. Any comparison of results without allowance for these factors is therefore misleading.

3.2.4 Energy Absorption and Dependence on Initial Temperature

The total absorbed energy from a single pulse is of interest for the complete process simulation presented in Chapter 4. It will be shown that heating of the work piece in the vicinity of the laser spot over a time-period much longer than a single pulse can be significant and, in some cases, the primary means of layer removal. Under such conditions, individual layers of a film may reach their vaporisation or degradation temperature on a relatively long time-scale and be removed by similar mechanisms to those seen in CW evaporative cutting. The effect of sample temperature on the absorbed energy and ablation depth are of interest under such conditions. The relatively high optical absorption of superheated metals (Figs. 3.2 and 3.3) leads to larger increases in work piece temperature for pulsed laser irradiation than for CW irradiation with the same average beam power.

The absorbed intensity is based on the time-dependent reflectivity of the material surface, $R(t)$, calculated in accordance with section 2.1, Eqn. (2.3), for the discretised target profile. The absorbed fluence is calculated by integrating the absorbed intensity over the pulse duration:

$$F_a = \int_{-\infty}^{\infty} I_0(t)(1 - R(t))dt \tag{3.19}$$

This definition effectively considers all energy absorbed by both the plume and bulk material, while the optical properties are taken as those of the target. Justification of this is based on the time-resolved photographs of Porneala & Willis [67], which capture the plume dynamics of an aluminium sample subject to 5ns laser pulses. After 22ns, these photographs show the ablation products, composed of molten particles, forming a dense expansion front close to the target surface. Additionally, the photographs show the redeposition of large quantities of molten material in the vicinity of the laser spot. For the purposes of calculating the absorbed intensity, it is therefore assumed that these ablation products have the same absorptivity and reflectivity as the bulk material, and that they eventually deposit their thermal energy in the target. The photographs show this redeposition taking place in the time-period of approximately $200 - 600$ns after the laser pulse. It is therefore further assumed that energy deposition by the ablation products is of no influence to the onset and progression of phase explosion itself, as calculated by the single-pulse model.

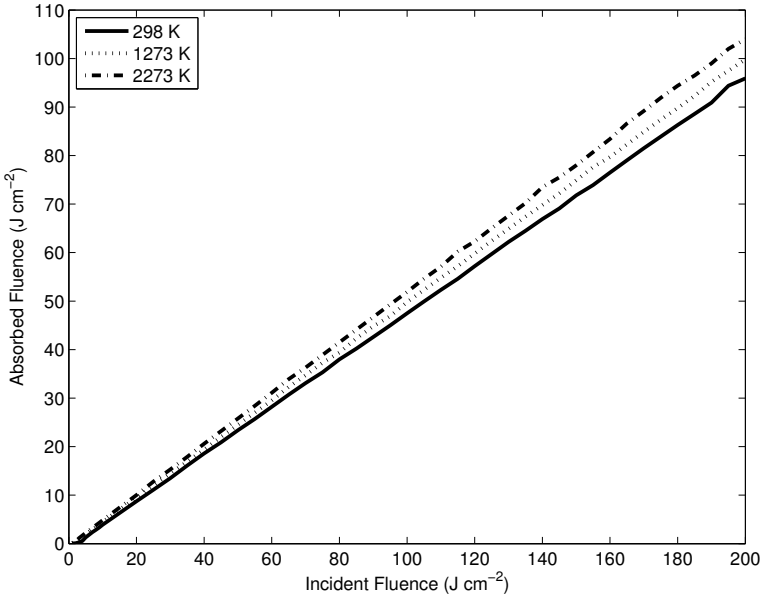

FIGURE 3.9: Absorbed fluence in aluminium as a function of incident fluence for initial temperatures 298K, 1273K and 2273K with 4.5ns pulses of wavelength 1064nm.

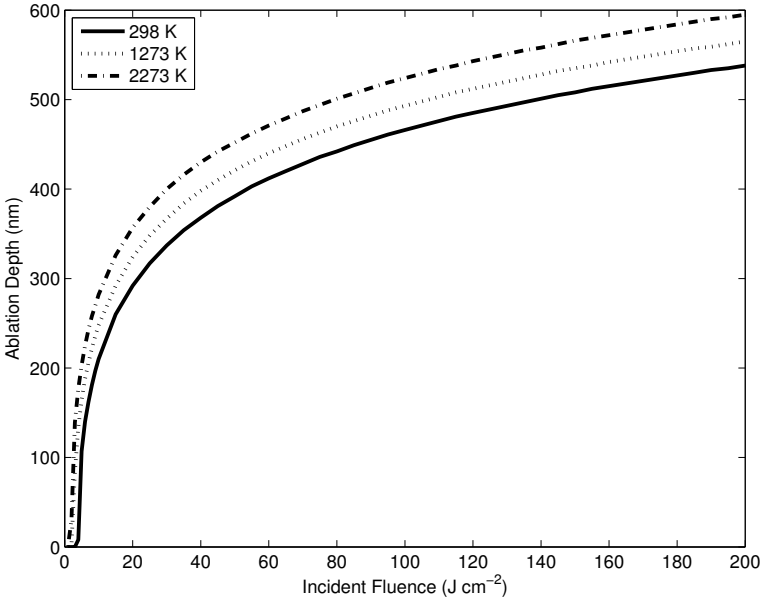

FIGURE 3.10: Ablation depth of aluminium as a function of incident fluence for initial temperatures 298K, 1273K and 2273K with 4.5ns pulses of wavelength 1064nm.

Figures 3.9 and 3.10 present the calculated absorbed fluence and ablation depth of aluminium for pulses of wavelength 1064nm and duration 4.5ns at various initial temperatures. The relationship between absorbed and incident fluence is linear over the best part of the fluence range considered. The absorbed fluence is approximately 50% of the incident fluence. It is useful to note that the room temperature optical absorption of aluminium at 1064nm is approximately 5%. The variation in absorbed fluence between 298K and 2273K is approximately 10% for incident fluences greater than $50\,\mathrm{J\,cm^{-2}}$. At lower fluences, the difference is larger, with a variation of 75% observed at $5\,\mathrm{J\,cm^{-2}}$. A similar trend is seen in ablation depth, with a variation of $10 - 15\%$ observed over the same temperature range for incident fluences greater than $50\,\mathrm{J\,cm^{-2}}$ and a variation of 90% observed at $5\,\mathrm{J\,cm^{-2}}$.

The short-pulse simulation is an integral part of the complete process simulation presented in Chapter 4. The calculation of ablation depth and absorbed energy for each position at every time-step is, however, impractical and unnecessary. To avoid duplicate tasks and to reduce computational time, a library of absorption data is produced and stored separately, from which interpolated values are utilised in the complete process simulation.

3.3 Concluding Remarks

The short-pulse ablation model presents a number of improvements over previously published works. The numerical method with which optical absorption is established allows accurate replication of energy coupling between the laser beam and work piece. As observed in section 3.2.1, energy absorption under short-pulse conditions can be far greater than for CW, or linear, conditions. As such, failure to account for temperature dependent material properties when calculating optical absorption leads to large shortfalls in the calculated work piece temperature. With resolution of these factors in the present model, accurate prediction of ablation depth of aluminium under a wide range of laser parameters has been demonstrated. Introduction of the shielding coefficient provides a simple method of calculating the reduction in incident laser intensity reaching the target surface due to scattering, reflection and absorption by the ablation products without detailed knowledge of the plume dynamics. Though there is clearly scope for further model development – indeed, experimental data is necessary for derivation of

the shielding coefficient – the accuracy of this simplification in the tested fluence ranges proves that it is a computationally light approach for expanding data generated by more detailed methods.

An investigation into the phase explosion threshold of aluminium has demonstrated dependence of this parameter on the sample thickness and laser source. The threshold was found to be a strong, increasing function of both the pulse duration and wavelength, due to thermal energy transport and energy coupling between the laser beam and work piece, respectively. The threshold was further found to decrease with sample thickness for thicknesses less than $\sim 1\mu$m. In this case, the effect was due to the influence of thermal saturation in the sample. In light of the presented model, these conclusions are obvious; however, their importance must not be neglected when comparing experimental data obtained under different conditions.

An investigation into energy absorption and the effects of initial temperature has lead to derivation of some important factors for the complete process simulation presented in Chapter 4. Both the absorbed energy and ablation depth of aluminium were found to increase slightly over the temperature range $298 - 2273$K. The absorbed fluence was found to be approximately 50% of the incident fluence at a wavelength of 1064nm for high fluences. The single-pulse ablation model will further utilised in Chapter 4.

Chapter 4

A General Time-Domain Model for Continuous-Wave and Pulsed Laser Incision and Cut of Thin Single and Multi-Layer Films

The following Chapter describes a complete process model for the laser incision and cut of arbitrary thin multi-layer films. Both short-pulse ablation and two-dimensional heat flow in the forward/backward and lateral directions are considered. The domain is separated into regions of constant material state, within which layer properties are combined to form an equivalent material. The simulation manages local compatibility conditions so as to ensure continuity of energy flux and motion of phase-change boundaries. Layers are removed as a result of progressive short-pulse ablation and normal vaporisation due to long-term heating. An investigation is undertaken into the effects of laser wavelength, repetition rate and beam waist radius on cut efficiency and quality for two multi-layer packaging films.

4.1 Model

4.1.1 Optical Absorption

The calculation of optical absorption is dependent on the type of laser irradiation taking place and the composition of the work piece. For continuous-wave (CW) exposure, absorption is based on the matrix method presented in section 2.1, with allowance for the spatial distribution of the incident beam. The forward and backward travelling components of the energy flux are described by Eqns. (2.1) and (2.2) and the optical absorption of the complete structure by Eqn. (2.5). For pulsed laser exposure, the same matrix method is utilised to determine the effective incident laser fluence for each layer. This effective fluence, different for all layers, is that which would lead to the same absorption profile in each layer without considering the influence of other layers. Optical properties for this calculation are considered as those at room temperature. From the effective incident fluence for each layer, the ablation depth and absorbed fluence per pulse are calculated for metals as per the single-pulse model presented in Chapter 3. The ablation depth per pulse is calculated for plastics as per Eqn. (5.2) in Chapter 5. For non-metal layers, optical absorption is considered linear, calculated with constant optical properties according to the matrix method presented in section 2.1.

The incident beam is taken as the on-axis laser intensity masked by a Gaussian distribution in the $x-$ and $y-$directions:

$$I(x,y,t) = I_0(t)\exp\left[-2\frac{x^2+y^2}{\omega_0^2}\right] \tag{4.1}$$

Where $I_0(t)$ is the on-axis beam intensity (Eqn. (2.8) for CW and Eqn. (3.1) for pulsed irradiation) and ω_0 is the beam waist radius. In the numerical calculation, the incident intensity at point (x_i, y_j) is expressed as follows to ensure accurate beam energy

regardless of element size:

$$
\begin{aligned}
I_{i,j}^{\eta} &= \frac{4I_0(t^{\eta})}{(\Delta x_{i+}+\Delta x_{i-})(\Delta y_{j+}+\Delta y_{j-})}\int_{y_j-\Delta y_{j-}/2}^{y_j+\Delta y_{j+}/2}\int_{x_i-\Delta x_{i-}/2}^{x_i+\Delta x_{i+}/2}\exp\left[-2\frac{x^2+y^2}{\omega_0^2}\right]\mathrm{dx}\,\mathrm{dy} \\
&= \frac{I_0(t^{\eta})\pi\omega_0^2}{2(\Delta x_{i+}+\Delta x_{i-})(\Delta y_{j+}+\Delta y_{j-})}\left[\mathrm{erf}\left(\frac{\sqrt{2}(x_i+\Delta x_{i+}/2)}{\omega_0}\right)-\right. \\
&\quad \left.\mathrm{erf}\left(\frac{\sqrt{2}(x_i-\Delta x_{i-}/2)}{\omega_0}\right)\right]\times\left[\mathrm{erf}\left(\frac{\sqrt{2}(y_j+\Delta y_{j+}/2)}{\omega_0}\right)-\right. \\
&\quad \left.\mathrm{erf}\left(\frac{\sqrt{2}(y_j-\Delta y_{j-}/2)}{\omega_0}\right)\right] \qquad (4.2)
\end{aligned}
$$

Where superscript η denotes the index of the corresponding time-step, subscript i and j denote the indices of the corresponding $x-$ and $y-$positions and Δx_{i+}, Δx_{i-}, Δy_{j+} and Δy_{j-} are the forward and backward element sizes in the $x-$ and $y-$directions, respectively, at point (x_i, y_j). For pulsed laser irradiation of films with metallic layers, the absorbed fluence is distributed continuously between pulses to give an equivalent CW absorbed intensity, I_c:

$$I_c(x,y,t) = \sum_{p=1}^{\hat{p}}\left\{f_{rep}\cdot F_{a,p}(x,y,t)\cdot 10^4\right\} \qquad (4.3)$$

Where f_{rep} is the repetition rate in s^{-1}, $\hat{p}$ the number of layers present and $F_{a,p}(x,y,t)$ the absorbed fluence per pulse, in $\mathrm{J\,cm}^{-2}$, in layer p at position (x,y) (section 3.2.4). The absorbed fluence is updated at each pulse and is therefore also considered a function of time.

4.1.2 Material Properties

Thermal behaviour is determined by considering the complete structure as a single material. The properties of this equivalent material are chosen such that the energy flux for a given temperature gradient is the sum of the contributions of all layers. This method was introduced in section 2.3.1. The equivalent thickness, thermal conductivity, density and specific heat capacity of a section comprising layers 1 to $\hat{p}$, *where present*, are described by Eqn. (2.17). In the present model, these section-specific properties are denoted as simply h, K, ρ and C, respectively. They depend on the materials present and their states at the point of interest, but are otherwise considered as constant with temperature.

4.1.3 Heat Flow

Under the thin-film approximation, temperature throughout film thickness is considered constant and heat flow is two-dimensional. To account for phase changes, the heat flow equation is expressed in terms of two-dimensional thermal energy density, H, in $\mathrm{J\,m^{-2}}$ with respect to solid state at 273K. This parameter is a function of the layers present, their states and the film temperature. A coordinate system is chosen that translates with the laser beam axis at velocity V in the $x-$direction. For regions of constant material state and free of phase changes:

$$\frac{\partial H}{\partial t} = \frac{K}{C\rho}\left[\frac{\partial^2 H}{\partial x^2} + \frac{\partial^2 H}{\partial y^2}\right] + V\frac{\partial H}{\partial x} + I_c, \quad H^- \leq H \leq H^+ \tag{4.4}$$

Where:

$$\begin{aligned} H^- &= \sum_{p=1}^{\hat{p}} \left\{ h_p \rho_p H_{m,p} \middle| T_{m,p} \leq T^- \right\} + h\rho C T^-, \\ H^+ &= \sum_{p=1}^{\hat{p}} \left\{ h_p \rho_p H_{m,p} \middle| T_{m,p} \leq T^- \right\} + h\rho C T^+ \end{aligned}$$

Where T^- is the maximum melting temperature of any layer that will be attained upon cooling, T^+ is the minimum melting or vaporisation temperature of any layer that will be attained upon heating, $H_{m,p}$ is the enthalpy of fusion of layer p, *where present*, and $T_{m,p}$ is the corresponding melting temperature.

For regions where a phase change is underway in one or more layers:

$$\frac{\partial H}{\partial t} = V\frac{\partial H}{\partial x} + I_c, \quad H^- < H < H^+ \tag{4.5}$$

Where:

$$\begin{aligned} H^- &= \sum_{p=1}^{\hat{p}} \left\{ h_p \rho_p H_{m,p} \middle| T_{m,p} < T \right\} + h\rho C T, \\ H^+ &= \sum_{p=1}^{\hat{p}} \left\{ h_p \rho_p H_{m,p} \middle| T_{m,p} \leq T \right\} + \sum_{p=1}^{\hat{p}} \left\{ h_p \rho_p H_{v,p} \middle| T_{v,p} \leq T \right\} + h\rho C T \end{aligned}$$

Where T is the corresponding phase change temperature, $H_{v,p}$ is the enthalpy of vaporisation of layer p, *where present*, and $T_{v,p}$ is the corresponding melting temperature.

Only the translation and source terms are considered in this case. Eqns. (4.4) and (4.5) account for the thermal energy density of layers *that are present in the region under consideration*. As a consequence, H^- does not contain enthalpy of vaporisation terms. In cases where layers are subject to thermal degradation, the temperature at which this occurs is still denoted $T_{v,p}$, whilst the enthalpies of fusion and vaporisation are chosen to reflect the processes taking place (Appendix A). When speaking generally, vaporisation will be taken to include thermal degradation.

Material at distances far from the laser beam axis is at ambient temperature, T_a, whilst, noting that the problem is symmetrical about the $y-$axis, the line $y = 0$ is considered thermally insulated. The domain is therefore reduced to $0 \leq y \leq \infty$, $-\infty \leq x \leq \infty$ and the global boundary and initial conditions are:

$$H|_{x\to\pm\infty} = H_a, \quad \left.\frac{\partial H}{\partial y}\right|_{y=0} = 0, \quad H|_{y\to\infty} = H_a, \quad H|_{t=0} = H_a \tag{4.6}$$

Where H_a is the thermal energy density corresponding to ambient temperature, T_a:

$$H_a = h\rho C T_a \tag{4.7}$$

In the numerical calculation, the Crank-Nicolson method is utilised; Eqn. (4.4) becomes:

$$\begin{aligned}\frac{H^{\eta}_{i,j}-H^{\eta-1}_{i,j}}{\Delta t} = {} & \frac{2K_{i,j}}{C_{i,j}\rho_{i,j}(\Delta x_{i+}+\Delta x_{i-})}\left[\frac{H^{\eta}_{i+1,j}-H^{\eta}_{i,j}+H^{\eta-1}_{i+1,j}-H^{\eta-1}_{i,j}}{2\Delta x_{i+}} + \frac{H^{\eta}_{i-1,j}-H^{\eta}_{i,j}+H^{\eta-1}_{i-1,j}-H^{\eta-1}_{i,j}}{2\Delta x_{i-}}\right] + \\ & \frac{2K_{i,j}}{C_{i,j}\rho_{i,j}(\Delta y_{j+}+\Delta y_{j-})}\left[\frac{H^{\eta}_{i,j+1}-H^{\eta}_{i,j}+H^{\eta-1}_{i,j+1}-H^{\eta-1}_{i,j}}{2\Delta y_{j+}} + \frac{H^{\eta}_{i,j-1}-H^{\eta}_{i,j}+H^{\eta-1}_{i,j-1}-H^{\eta-1}_{i,j}}{2\Delta y_{j-}}\right] + \\ & V\left[\frac{H^{\eta}_{i+1,j}-H^{\eta}_{i,j}+H^{\eta-1}_{i+1,j}-H^{\eta-1}_{i,j}}{2\Delta x_{i+}}\right] + I^{\eta}_{c,i,j}, \quad H^- \leq H^{\eta-1}_{i,j} \leq H^+\end{aligned} \tag{4.8}$$

Equation (4.5) becomes:

$$\frac{H^{\eta}_{i,j} - H^{\eta-1}_{i,j}}{\Delta t} = V\left[\frac{H^{\eta}_{i+1,j} - H^{\eta}_{i,j} + H^{\eta-1}_{i+1,j} - H^{\eta-1}_{i,j}}{2\Delta x_{i+}}\right] + I^{\eta}_{c,i,j}, \quad H^- < H^{\eta-1}_{i,j} < H^+ \tag{4.9}$$

Equations (4.8) and (4.9) express H implicitly for each time-step and must be resolved as a system of algebraic equations. To satisfy global boundary conditions in the $x-$direction, Eqn. (4.8) is modified for elements along the lines $x = x_1$ and $x = x_{\hat{i}}$,

respectively:

$$\frac{H^{\eta}_{1,j}-H^{\eta-1}_{1,j}}{\Delta t} = \frac{K_{1,j}}{C_{1,j}\rho_{1,j}\Delta x_{1+}}\left[\frac{H^{\eta}_{2,j}-H^{\eta}_{1,j}+H^{\eta-1}_{2,j}-H^{\eta-1}_{1,j}}{2\Delta x_{1+}}\right] + \frac{2K_{1,j}}{C_{1,j}\rho_{1,j}(\Delta y_{j+}+\Delta y_{j-})} \times \left[\frac{H^{\eta}_{1,j+1}-H^{\eta}_{1,j}+H^{\eta-1}_{1,j+1}-H^{\eta-1}_{1,j}}{2\Delta y_{j+}} + \frac{H^{\eta}_{1,j-1}-H^{\eta}_{1,j}+H^{\eta-1}_{1,j-1}-H^{\eta-1}_{1,j}}{2\Delta y_{j-}}\right] + V\left[\frac{H^{\eta}_{2,j}-H^{\eta}_{1,j}+H^{\eta-1}_{2,j}-H^{\eta-1}_{1,j}}{2\Delta x_{1+}}\right] + I^{\eta}_{c,1,j} \tag{4.10}$$

$$\frac{H^{\eta}_{\hat{i},j}-H^{\eta-1}_{\hat{i},j}}{\Delta t} = \frac{K_{\hat{i},j}}{C_{\hat{i},j}\rho_{\hat{i},j}\Delta x_{\hat{i}-}}\left[\frac{H^{\eta}_{\hat{i}-1,j}-H^{\eta}_{\hat{i},j}+H^{\eta-1}_{\hat{i}-1,j}-H^{\eta-1}_{\hat{i},j}}{2\Delta x_{\hat{i}-}}\right] + \frac{2K_{\hat{i},j}}{C_{\hat{i},j}\rho_{\hat{i},j}(\Delta y_{j+}+\Delta y_{j-})} \times \left[\frac{H^{\eta}_{\hat{i},j+1}-H^{\eta}_{\hat{i},j}+H^{\eta-1}_{\hat{i},j+1}-H^{\eta-1}_{\hat{i},j}}{2\Delta y_{j+}} + \frac{H^{\eta}_{\hat{i},j-1}-H^{\eta}_{\hat{i},j}+H^{\eta-1}_{\hat{i},j-1}-H^{\eta-1}_{\hat{i},j}}{2\Delta y_{j-}}\right] + I^{\eta}_{c,\hat{i},j} \tag{4.11}$$

Where $\hat{i}$ is the number of calculation points in the $x-$direction. To satisfy global boundary conditions in the $y-$direction, Eqn. (4.8) is modified for elements along the lines $y = y_1$ and $y = y_{\hat{j}}$, respectively:

$$\frac{H^{\eta}_{i,1}-H^{\eta-1}_{i,1}}{\Delta t} = \frac{2K_{i,1}}{C_{i,1}\rho_{i,1}(\Delta x_{i+}+\Delta x_{i-})}\left[\frac{H^{\eta}_{i+1,1}-H^{\eta}_{i,1}+H^{\eta-1}_{i+1,1}-H^{\eta-1}_{i,1}}{2\Delta x_{i+}} + \frac{H^{\eta}_{i-1,1}-H^{\eta}_{i,1}+H^{\eta-1}_{i-1,1}-H^{\eta-1}_{i,1}}{2\Delta x_{i-}}\right] + \frac{K_{i,1}}{C_{i,1}\rho_{i,1}\Delta y_{1+}}\left[\frac{H^{\eta}_{i,2}-H^{\eta}_{i,1}+H^{\eta-1}_{i,2}-H^{\eta-1}_{i,1}}{2\Delta y_{1+}}\right] + V\left[\frac{H^{\eta}_{i+1,1}-H^{\eta}_{i,1}+H^{\eta-1}_{i+1,1}-H^{\eta-1}_{i,1}}{2\Delta x_{i+}}\right] + I^{\eta}_{c,i,1} \tag{4.12}$$

$$\frac{H^{\eta}_{i,\hat{j}}-H^{\eta-1}_{i,\hat{j}}}{\Delta t} = \frac{2K_{i,\hat{j}}}{C_{i,\hat{j}}\rho_{i,\hat{j}}(\Delta x_{i+}+\Delta x_{i-})}\left[\frac{H^{\eta}_{i+1,\hat{j}}-H^{\eta}_{i,\hat{j}}+H^{\eta-1}_{i+1,\hat{j}}-H^{\eta-1}_{i,\hat{j}}}{2\Delta x_{i+}} + \frac{H^{\eta}_{i-1,\hat{j}}-H^{\eta}_{i,\hat{j}}+H^{\eta-1}_{i-1,\hat{j}}-H^{\eta-1}_{i,\hat{j}}}{2\Delta x_{i-}}\right] + \frac{K_{i,\hat{j}}}{C_{i,\hat{j}}\rho_{i,\hat{j}}\Delta y_{\hat{j}-}}\left[\frac{H^{\eta}_{i,\hat{j}-1}-H^{\eta}_{i,\hat{j}}+H^{\eta-1}_{i,\hat{j}-1}-H^{\eta-1}_{i,\hat{j}}}{2\Delta y_{\hat{j}-}}\right] + V\left[\frac{H^{\eta}_{i+1,\hat{j}}-H^{\eta}_{i,\hat{j}}+H^{\eta-1}_{i+1,\hat{j}}-H^{\eta-1}_{i,\hat{j}}}{2\Delta x_{i+}}\right] + I^{\eta}_{c,i,\hat{j}} \tag{4.13}$$

Where $\hat{j}$ is the number of calculation points in the $y-$direction. In the case of a phase changes, equation (4.9) is modified for elements along the line $x = x_{\hat{i}}$:

$$\frac{H^{\eta}_{\hat{i},j} - H^{\eta-1}_{\hat{i},j}}{\Delta t} = I^{\eta}_{c,\hat{i},j} \tag{4.14}$$

At points (x_1, y_1), $(x_{\hat{i}}, y_1)$, $(x_1, y_{\hat{j}})$ and $(x_{\hat{i}}, y_{\hat{j}})$, Eqn. (4.8) is further reduced in the same manner. The conditions $H|_{x\to\pm\infty} = H_a$ and $H|_{y\to\infty} = H_a$ are effectively replaced by $\partial H/\partial x|_{x=x_{1/\hat{i}}} = 0$ and $\partial H/\partial y|_{y=y_{\hat{j}}} = 0$, respectively. This has the practical advantage of allowing adequacy of the calculation domain size to be assessed by checking the difference between H and H_a along the domain boundaries at the final time-step. The domain size is chosen to be sufficiency large so as to ensure negligible temperature change

at these points, approximating the corresponding conditions in Eqn. (4.6).

Local compatibility conditions ensure continuity of temperature and energy flux across discontinuities in material state and presence. Such conditions are present where material phase changes begin and end, or where layers are removed. These "local boundaries" are dealt with by type. Where a region free of phase change is adjacent to one of phase change (type 1), the former sees the corresponding phase change temperature at the boundary for the conduction component, whilst the latter sees the energy gain or loss from the resulting temperature gradient in the region free of phase change. In the latter case, the gain or loss is applied across the whole phase change region. Considering such a boundary across points (x_i, y_j) and (x_{i+1}, y_j), Eqn. (4.8) for point (x_i, y_j) becomes:

$$\begin{aligned}\frac{H^{\eta}_{i,j}-H^{\eta-1}_{i,j}}{\Delta t} = \frac{2K_{i,j}}{C_{i,j}\rho_{i,j}(\Delta x_{i+}+\Delta x_{i-})}\left[\frac{2H^{+/-}-H^{\eta}_{i,j}-H^{\eta-1}_{i,j}}{2\Delta x_{i+}} + \frac{H^{\eta}_{i-1,j}-H^{\eta}_{i,j}+H^{\eta-1}_{i-1,j}-H^{\eta-1}_{i,j}}{2\Delta x_{i-}}\right] + \\ \frac{2K_{i,j}}{C_{i,j}\rho_{i,j}(\Delta y_{j+}+\Delta y_{j-})}\left[\frac{H^{\eta}_{i,j+1}-H^{\eta}_{i,j}+H^{\eta-1}_{i,j+1}-H^{\eta-1}_{i,j}}{2\Delta y_{j+}} + \frac{H^{\eta}_{i,j-1}-H^{\eta}_{i,j}+H^{\eta-1}_{i,j-1}-H^{\eta-1}_{i,j}}{2\Delta y_{j-}}\right] + \\ V\left[\frac{H^{\eta}_{i+1,j}-H^{\eta}_{i,j}+H^{\eta-1}_{i+1,j}-H^{\eta-1}_{i,j}}{2\Delta x_{i+}}\right] + I^{\eta}_{c,i,j}\end{aligned} \tag{4.15}$$

Where $H^{+/-}$ is the thermal energy density range limit corresponding to the phase change in question and its temperature with respect to the adjacent region. Equation (4.9) for point (x_{i+1}, y_j) becomes:

$$\begin{aligned}\frac{H^{\eta}_{i+1,j}-H^{\eta-1}_{i+1,j}}{\Delta t} = V\left[\frac{H^{\eta}_{i+2,j}-H^{\eta}_{i+1,j}+H^{\eta-1}_{i+2,j}-H^{\eta-1}_{i+1,j}}{2\Delta x_{(i+1)+}}\right] + I^{\eta}_{c,i+1,j} + \\ \frac{K_{i,j}(\Delta y_{j+}+\Delta y_{j-})}{2AC_{i,j}\rho_{i,j}}\left[\frac{H^{\eta}_{i,j}+H^{\eta-1}_{i,j}-2H^{+/-}}{2\Delta x_{i+}}\right] + \ldots\end{aligned} \tag{4.16}$$

Where A is the total area of the phase change region and '...' signifies addition of all other contributions along the boundary of this region. All other elements in the phase change region see boundary contributions of analogous form. Where regions free of phase change but with different material states are adjacent (type 2), the corresponding boundary temperatures change in both regions by the same amount according to the combined incident laser energy and the temperature gradient to either side of the boundary. In this way, the elements are effectively grouped as one for the conductive and source terms in the heat flow equation. The translation term remains element specific. Considering such a boundary across points (x_i, y_j) and (x_{i+1}, y_j), Eqn. (4.8) for point

(x_i, y_j) becomes:

$$\frac{H^{\eta}_{i,j}-H^{\eta-1}_{i,j}}{\Delta t} = \Bigg(\frac{(\Delta x_{i+}+\Delta x_{i-})(\Delta y_{j+}+\Delta y_{j-})}{4} I^{\eta}_{c,i,j} + \frac{(\Delta x_{(i+1)+}+\Delta x_{(i+1)-})(\Delta y_{j+}+\Delta y_{j-})}{4} I^{\eta}_{c,i+1,j} + \frac{K_{i+1,j}(\Delta y_{j+}+\Delta y_{j-})}{2C_{i+1,j}\rho_{i+1,j}} \left[\frac{H^{\eta}_{i+2,j}-H^{\eta}_{i+1,j}+H^{\eta-1}_{i+2,j}-H^{\eta-1}_{i+1,j}}{2\Delta x_{(i+1)+}}\right] + \frac{K_{i,j}(\Delta y_{j+}+\Delta y_{j-})}{2C_{i,j}\rho_{i,j}} \left[\frac{H^{\eta}_{i-1,j}-H^{\eta}_{i,j}+H^{\eta-1}_{i-1,j}-H^{\eta-1}_{i,j}}{2\Delta x_{i-}}\right] + \frac{K_{i+1,j}(\Delta x_{(i+1)+}+\Delta x_{(i+1)-})}{2C_{i+1,j}\rho_{i+1,j}} \left[\frac{H^{\eta}_{i+1,j+1}-H^{\eta}_{i+1,j}+H^{\eta-1}_{i+1,j+1}-H^{\eta-1}_{i+1,j}}{2\Delta y_{j+}} + \frac{H^{\eta}_{i+1,j-1}-H^{\eta}_{i+1,j}+H^{\eta-1}_{i+1,j-1}-H^{\eta-1}_{i+1,j}}{2\Delta y_{j-}}\right] + \frac{K_{i,j}(\Delta x_{i+}+\Delta x_{i-})}{2C_{i,j}\rho_{i,j}} \left[\frac{H^{\eta}_{i,j+1}-H^{\eta}_{i,j}+H^{\eta-1}_{i,j+1}-H^{\eta-1}_{i,j}}{2\Delta y_{j+}} + \frac{H^{\eta}_{i,j-1}-H^{\eta}_{i,j}+H^{\eta-1}_{i,j-1}-H^{\eta-1}_{i,j}}{2\Delta y_{j-}}\right]\Bigg) \times \left(\frac{4C_{i,j}\rho_{i,j}h_{i,j}}{(\Delta y_{j+}+\Delta y_{j-})(C_{i,j}\rho_{i,j}h_{i,j}(\Delta x_{i+}+\Delta x_{i-})+C_{i+1,j}\rho_{i+1,j}h_{i+1,j}(\Delta x_{(i+1)+}+\Delta x_{(i+1)-}))}\right) + V\left[\frac{H^{\eta}_{i+1,j}-H^{\eta}_{i,j}+H^{\eta-1}_{i+1,j}-H^{\eta-1}_{i,j}}{2\Delta x_{i+}}\right] \tag{4.17}$$

An analogous modification is seen at point (x_{i+1}, y_j). Boundary type 2 may be further subdivided into those resulting from change of state (type $2a$) and those resulting from material removal (type $2b$). Type $2a$ is an intermediate condition during motion of phase change boundaries; the subsequent rise or fall of temperature in both elements initiates phase change in one, causing a progression to boundary type 1 at the next time step. Type $2b$ simply maintains equal temperature and continuity of energy flux across a boundary of discontinuous material properties. Where an adjacent region has no material present at all (type 3), a zero temperature gradient condition is imposed. Considering such a boundary across points (x_i, y_j) and (x_{i+1}, y_j), Eqn. (4.8) for point (x_i, y_j) becomes:

$$\frac{H^{\eta}_{i,j}-H^{\eta-1}_{i,j}}{\Delta t} = \frac{2K_{i,j}}{C_{i,j}\rho_{i,j}(\Delta x_{i+}+\Delta x_{i-})} \left[\frac{H^{\eta}_{i-1,j}-H^{\eta}_{i,j}+H^{\eta-1}_{i-1,j}-H^{\eta-1}_{i,j}}{2\Delta x_{i-}}\right] + \frac{2K_{i,j}}{C_{i,j}\rho_{i,j}(\Delta y_{j+}+\Delta y_{j-})} \times \left[\frac{H^{\eta}_{i,j+1}-H^{\eta}_{i,j}+H^{\eta-1}_{i,j+1}-H^{\eta-1}_{i,j}}{2\Delta y_{j+}} + \frac{H^{\eta}_{i,j-1}-H^{\eta}_{i,j}+H^{\eta-1}_{i,j-1}-H^{\eta-1}_{i,j}}{2\Delta y_{j-}}\right] + V\left[\frac{H^{\eta}_{i+1,j}-H^{\eta}_{i,j}+H^{\eta-1}_{i+1,j}-H^{\eta-1}_{i,j}}{2\Delta x_{i+}}\right] + I^{\eta}_{c,i,j} \tag{4.18}$$

Point (x_{i+1}, y_j) has zero thermal energy density:

$$H^{\eta}_{i+1,j} = 0 \tag{4.19}$$

The allocation of regions, boundary conditions and material properties is undertaken explicitly in a pre-calculation phase of every time-step. Thermal energy density ranges

for the states of an arbitrary layer, l, are as follows:

$$\textit{Solid:}\quad H_{i,j}^{\eta-1} \leq \left[\sum_{p=1}^{\hat{p}} \{h_p\rho_p\, H_{m,p} |\, T_{m,p} < T_{m,l}\} + \sum_{p=1}^{\hat{p}} \{h_p\rho_p\, H_{v,p} |\, T_{v,p} < T_{m,l}\} + h\rho C T_{m,l}\right]$$

$$\textit{Melting:}\quad \left[\sum_{p=1}^{\hat{p}} \{h_p\rho_p\, H_{m,p} |\, T_{m,p} < T_{m,l}\} + \sum_{p=1}^{\hat{p}} \{h_p\rho_p\, H_{v,p} |\, T_{v,p} < T_{m,l}\} + h\rho C T_{m,l}\right] < H_{i,j}^{\eta-1} < \left[\sum_{p=1}^{\hat{p}} \{h_p\rho_p\, H_{m,p} |\, T_{m,p} \leq T_{m,l}\} + \sum_{p=1}^{\hat{p}} \{h_p\rho_p\, H_{v,p} |\, T_{v,p} \leq T_{m,l}\} + h\rho C T_{m,l}\right]$$

$$\textit{Liquid:}\quad \left[\sum_{p=1}^{\hat{p}} \{h_p\rho_p\, H_{m,p} |\, T_{m,p} \leq T_{m,l}\} + \sum_{p=1}^{\hat{p}} \{h_p\rho_p\, H_{v,p} |\, T_{v,p} \leq T_{m,l}\} + h\rho C T_{m,l}\right] \leq H_{i,j}^{\eta-1} \leq \left[\sum_{p=1}^{\hat{p}} \{h_p\rho_p\, H_{m,p} |\, T_{m,p} < T_{v,l}\} + \sum_{p=1}^{\hat{p}} \{h_p\rho_p\, H_{v,p} |\, T_{v,p} < T_{v,l}\} + h\rho C T_{v,l}\right]$$

$$\textit{Vaporising:}\quad \left[\sum_{p=1}^{\hat{p}} \{h_p\rho_p\, H_{m,p} |\, T_{m,p} < T_{v,l}\} + \sum_{p=1}^{\hat{p}} \{h_p\rho_p\, H_{v,p} |\, T_{v,p} < T_{v,l}\} + h\rho C T_{v,l}\right] < H_{i,j}^{\eta-1} < \left[\sum_{p=1}^{\hat{p}} \{h_p\rho_p\, H_{m,p} |\, T_{m,p} \leq T_{v,l}\} + \sum_{p=1}^{\hat{p}} \{h_p\rho_p\, H_{v,p} |\, T_{v,p} \leq T_{v,l}\} + h\rho C T_{v,l}\right]$$

$$\textit{Removed:}\quad \left[\sum_{p=1}^{\hat{p}} \{h_p\rho_p\, H_{m,p} |\, T_{m,p} \leq T_{v,l}\} + \sum_{p=1}^{\hat{p}} \{h_p\rho_p\, H_{v,p} |\, T_{v,p} \leq T_{v,l}\} + h\rho C T_{v,l}\right] \leq H_{i,j}^{\eta-1} \tag{4.20}$$

Where $T_{m,l}$ and $T_{v,l}$ are the melting and vaporisation temperatures of the layer in question and layer p, taken to include layer l itself, *is present* at the preceding time-step at point (x_i, y_j). When a layer is removed, its thermal energy density is removed:

$$H_{i,j}^{(\eta-1)'} = H_{i,j}^{\eta-1} - h_l\rho_l\,(C_l T_{v,l} + H_{m,l} + H_{v,l}) \tag{4.21}$$

Where l is the removed layer and $H_{i,j}^{(\eta-1)'}$ takes the place of $H_{i,j}^{\eta-1}$ in the heat flow calculation. Mesh spacing is a function of position, with progression from small elements

in the vicinity of the laser beam to large elements at the edges of the domain that are not along the line $y = 0$. Mesh spacing grows proportionally to the factor ξ about the origin:

$$x_i = \begin{cases} \left(x_{i+1} - x_{\hat{i}}\xi^{((\hat{i}+1)/2-i)}\right) \Big/ \sum_{\gamma=1}^{(\hat{i}+1)/2-1} \xi^{\gamma}, & \text{for } i = 1 \ldots (\hat{i}+1)/2 - 1, \\ 0, & \text{for } i = (\hat{i}+1)/2, \\ \left(x_{i-1} + x_{\hat{i}}\xi^{(i-(\hat{i}+1)/2)}\right) \Big/ \sum_{\gamma=1}^{(\hat{i}+1)/2-1} \xi^{\gamma}, & \text{for } i = (\hat{i}+1)/2 + 1 \ldots \hat{i} \end{cases} \tag{4.22}$$

$$y_i = \begin{cases} 0, & \text{for } j = 1, \\ \left(y_{j-1} + y_{\hat{j}}\xi^{(j-1)}\right) \Big/ \sum_{\gamma=1}^{\hat{j}-1} \xi^{\gamma}, & \text{for } j = 2 \ldots \hat{j} \end{cases} \tag{4.23}$$

Where $\hat{i}$ must be odd. In this way, very large domains may be generated without excessive calculation points or loss of resolution near the laser spot.

4.1.4 Material Removal

For pulsed laser irradiation, material removal due to ablation is calculated by progressively reducing the thickness of layers according to the short-pulse model for metals (section 3.2.4) and an empirical formula for plastics (Eqn. (5.2)). These calculations are based on the effective incident intensity of each layer (section 4.1.1) at point (x_i, y_j) and are based on the assumption that the relationship between ablation depth and fluence does not change with the number of pulses. This assumption will be further justified in Chapter 5 (section 5.4.2). Under the laser spot, material translation is accounted for by interpolation:

$$h^{\eta}_{i,j,p} = h^{\eta-1}_{i,j,p} + \frac{V\Delta t}{\Delta x_{i+}}\left(h^{\eta-1}_{i+1,j,p} - h^{\eta-1}_{i,j,p}\right) - d^{\eta}_{i,j,p} \tag{4.24}$$

Where $d^{\eta}_{i,j,p}$ is the calculated ablation depth per pulse of layer p. At distances greater than ω_0 from the origin, such interpolation yields damping of the crater form due to large mesh spacing. To best account for material translation in these regions, discrete transfer is undertaken at specific time intervals:

$$h^{\eta}_{i,j,p} = \begin{cases} h^{\eta-1}_{i+1,j,p} - d^{\eta}_{i,j,p}, & \text{if } \epsilon^{\eta} > \Delta x_{i+}/2, \\ h^{\eta-1}_{i,j,p} - d^{\eta}_{i,j,p}, & \text{otherwise} \end{cases} \tag{4.25}$$

Where:

$$\epsilon^{\eta} = \begin{cases} 0, & \text{if } \eta = 1, \\ \epsilon^{\eta-1} + V\Delta t - \Delta x_{i+}, & \text{if } \epsilon^{\eta-1} > \Delta x_{i+}/2, \\ \epsilon^{\eta-1} + V\Delta t, & \text{otherwise} \end{cases} \tag{4.26}$$

When the thickness is reduced to zero, the layer and its corresponding thermal energy density are removed from the heat flow calculation in accordance with Eqn. (4.21).

For both CW and pulsed laser irradiation, layer removal due to normal vaporisation takes place according to the respective thermal energy density limit in Eqn. (4.20). In this case, the layer height becomes zero at the point in question.

A MATLAB script for the general model is presented in Appendix B.3. Relevant subprograms are presented in Appendix B.4 and material properties are presented in Appendix A.

4.2 Results and Discussion

4.2.1 Temperature, State and Thickness Profiles

The developed model yields the sample temperature, layer states and layer thicknesses of an arbitrary multi-layer structure during CW or pulsed laser exposure. Figures 4.1 and 4.2 present these parameters for a three-layer Triplex film, comprising 9μm aluminium between two 20μm polypropylene (PP) layers, translating at 50mm s^{-1} and subject to 0.14mJ, 10ns pulses of wavelength 515nm and waist radius 15μm at a repetition rate of 30kHz. The figures correspond to exposure times of 0.1ms, 1ms, 10ms and 50ms, respectively. White space in the temperature distributions represents removal of all layers; that is, complete penetration of the film. The calculation $x-$ and $y-$domains are 12mm and 6mm, respectively, whilst the problem is symmetrical about the $x-$axis. The presented plot domains are smaller than the calculation domain so as to highlight the regions of interest. The sample temperature after 0.1ms is already sufficient to begin thermal degradation of the PP layers, whilst a crater may be seen in the aluminium layer directly under the laser spot. At 1ms, the PP layers are removed over a region much larger than the laser spot, whilst the aluminium is completely penetrated. Progression of the cut is evident at 10ms and steady state behaviour is attained at 50ms. Both PP

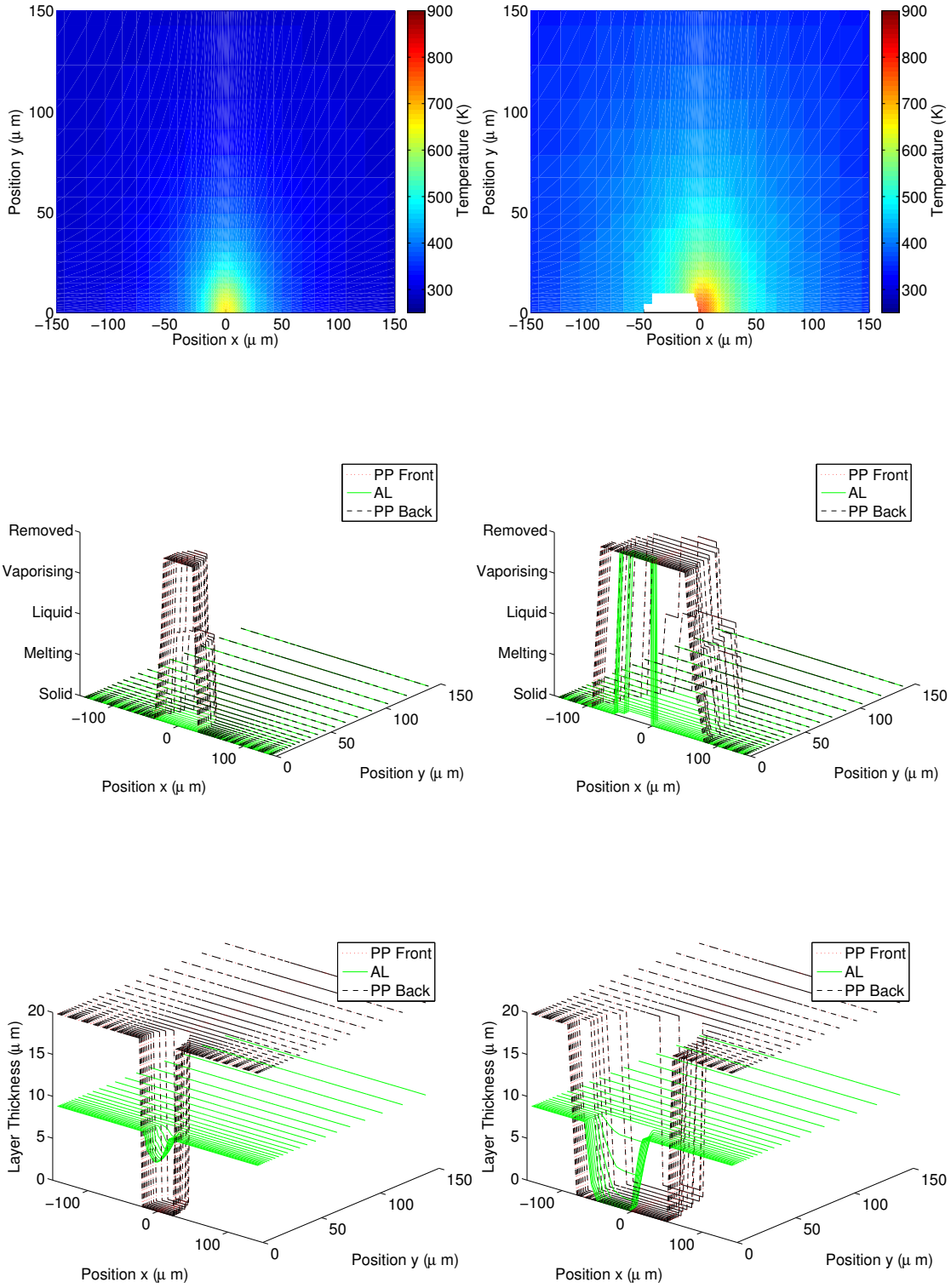

FIGURE 4.1: (Top) Temperature distribution, (middle) layer states and (bottom) layer thicknesses of Triplex after (left) 0.1ms and (right) 1ms at 50mm s^{-1} subject to 0.14mJ, 10ns pulses of wavelength 515nm, repetition rate 30kHz and beam waist radius 15μm.

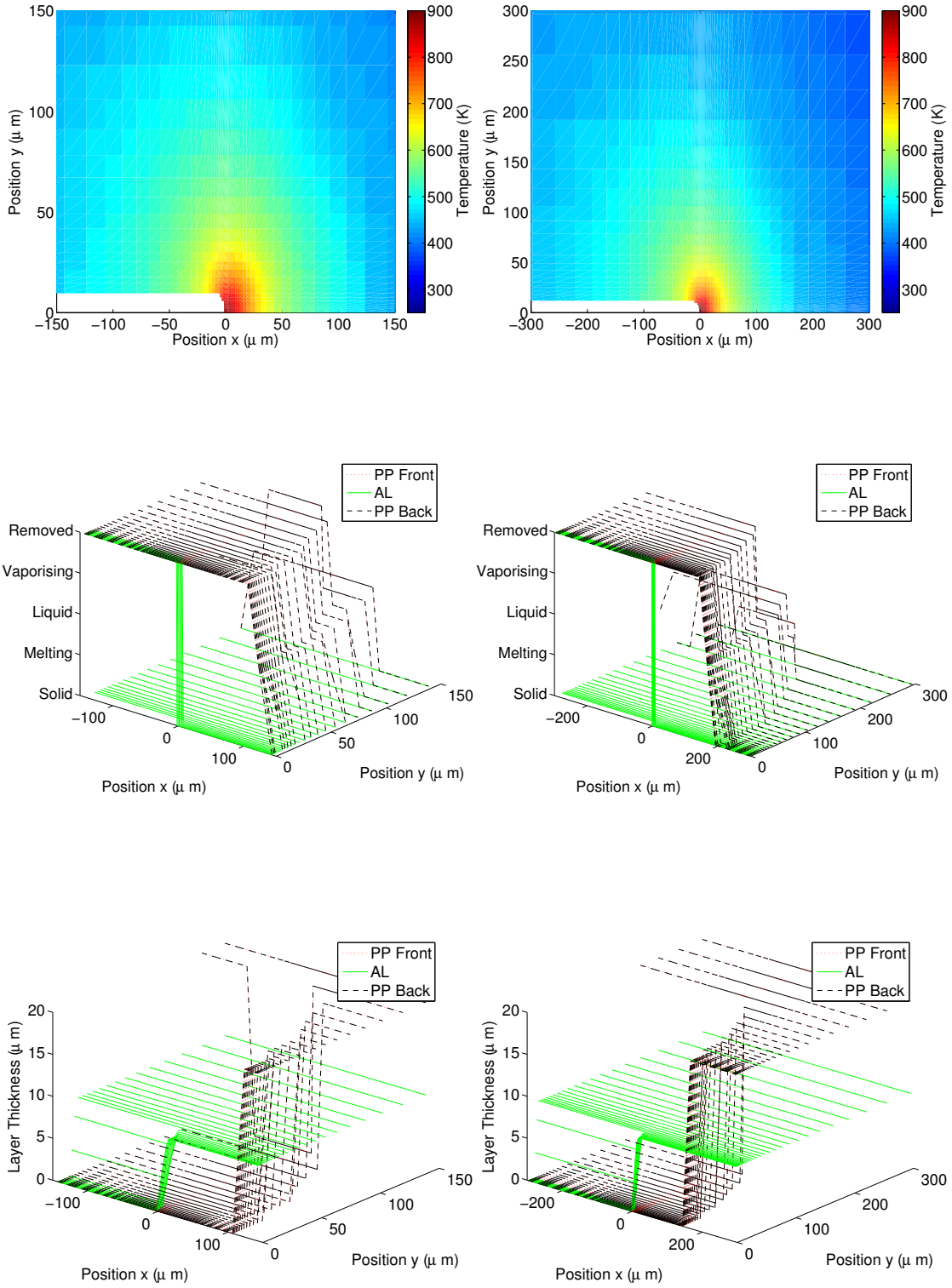

FIGURE 4.2: (Top) Temperature distribution, (middle) layer states and (bottom) layer thicknesses of Triplex after (left) 10ms and (right) 50ms at 50mm s^{-1} subject to 0.14mJ, 10ns pulses of wavelength 515nm, repetition rate 30kHz and beam waist radius 15μm.

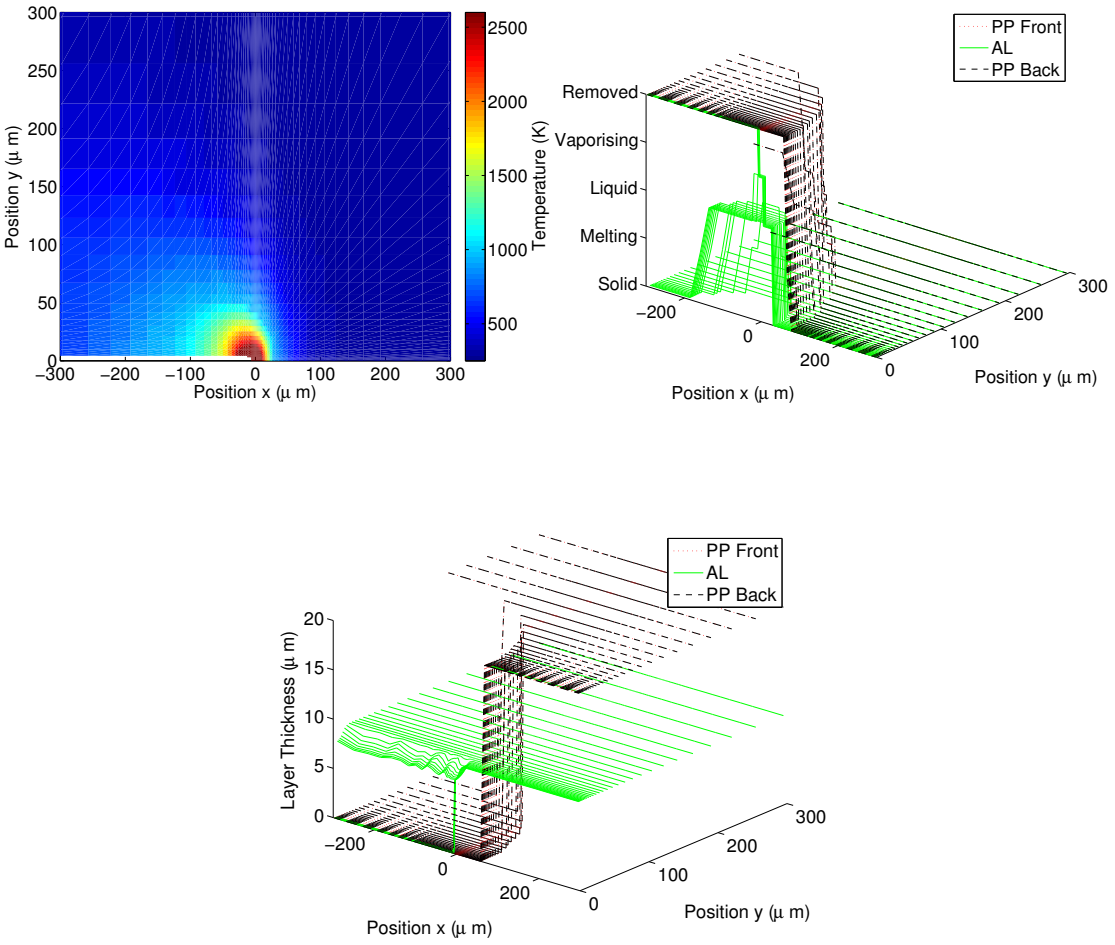

FIGURE 4.3: (Top left) Temperature distribution, (top right) layer states and (bottom) layer thicknesses of Triplex after 1ms at $1\,\mathrm{m\,s^{-1}}$ subject to 0.71mJ, 10ns pulses of wavelength 515nm, repetition rate 30kHz and beam waist radius 15μm.

layers have the same state and thickness at all points displayed, their behaviour driven by the sample temperature that is constant throughout film thickness under the thin-film approximation. An abrupt change in temperature gradient is present at the plastic thermal degradation boundary in all cases, corresponding to abrupt changes in equivalent thermal conductivity and thickness. The steady state cut width of the aluminium layer is approximately 20μm and that of the PP layers is approximately 330μm. No melting of the aluminium takes place between pulses (i.e. aside from short-pulse effects), whilst the melt width of the PP layers is 440μm. From a practical standpoint, it may be said that complete cut of Triplex is possible under these conditions; however, the quality is questionable as there is a substantial difference in the cut and melt widths between the aluminium and PP layers. The enthalpies of vaporisation of the PP layers are ignored,

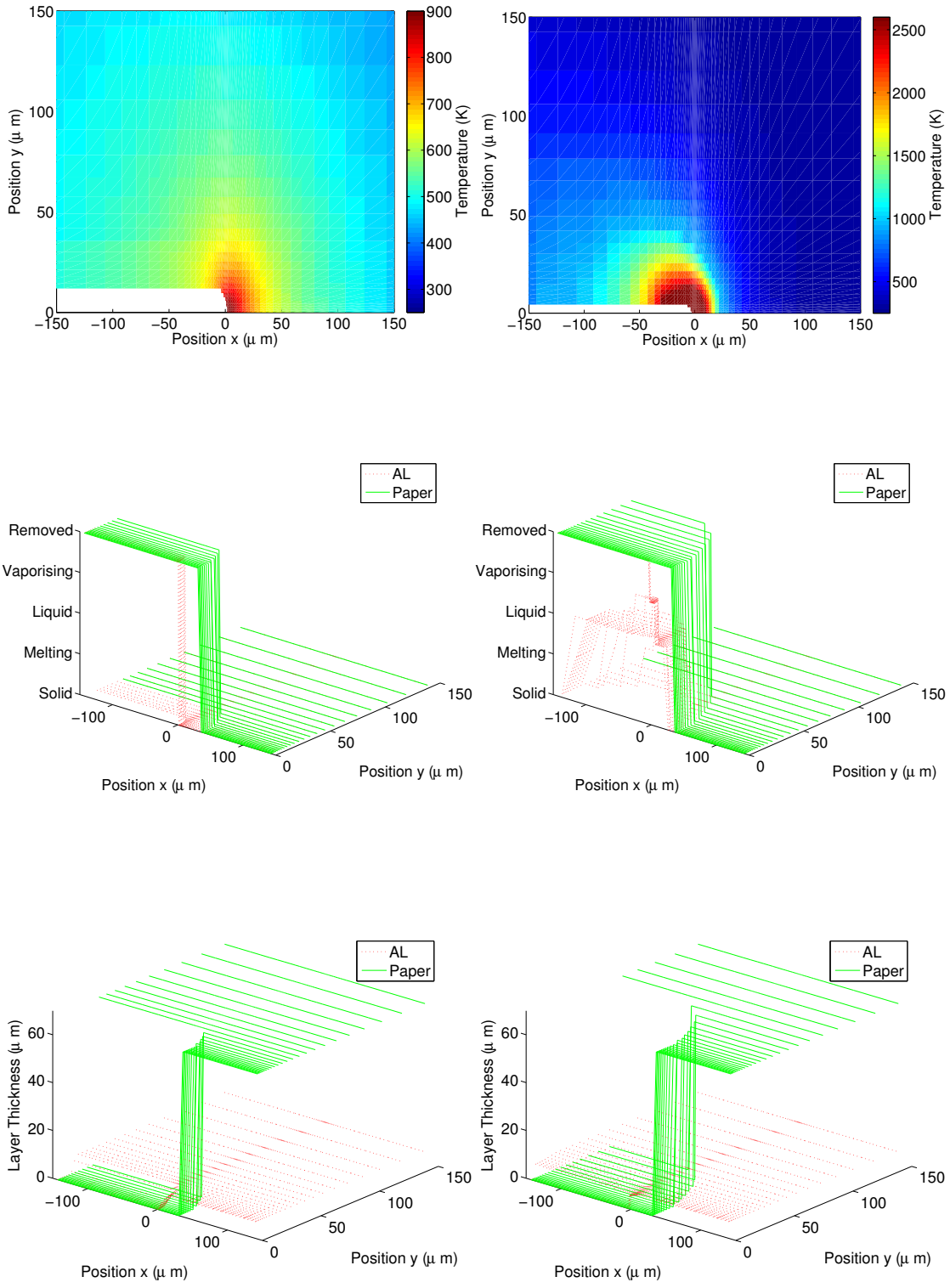

FIGURE 4.4: (Top left) Temperature distribution, (middle left) layer states and (bottom left) layer thicknesses of Alufoil after 50ms at $50\text{mm}\,\text{s}^{-1}$ subject to 0.14mJ, 10ns pulses of wavelength 515nm, repetition rate 30kHz and beam waist radius 15μm. (Top right) Temperature distribution, (middle right) layer states and (bottom right) layer thicknesses of Alufoil after 1ms at $1\text{m}\,\text{s}^{-1}$ subject to 0.71mJ, 10ns pulses of wavelength 515nm, repetition rate 30kHz and beam waist radius 15μm.

as the material is taken to undergo removal at 473K (Appendix A).

Figure 4.3 presents the same parameters for Triplex translating at $1\,\mathrm{m\,s^{-1}}$ and subject to 0.71mJ pulses of the same duration, wavelength, beam waist radius and repetition rate. The figure corresponds to an exposure time of 1ms, within which steady state behaviour is attained. The process characteristics are somewhat different to the previous case: though some removal of aluminium by short-pulse ablation is observed, the complete cut of this layer is also due to vaporisation from long-term heating of the sample. This event comes about due to the reduced ablation efficiency of aluminium at high fluence (Figs. 3.5 and 3.6), while energy absorbed by the ablation products is continually deposited in the work piece according to Eqn. (3.19). The film temperature in the vicinity of the laser spot is 2793K and a small region of vaporisation is present in the aluminium layer. The temperature profile shows greater offset due to translation, reflecting the elevated effects of velocity at $1\,\mathrm{m\,s^{-1}}$. The cut width of the aluminium layer in this case is approximately 6μm and that of the PP layers is approximately 300μm. The melt width of the aluminium layer is 100μm and that of the PP layers is 330μm. Interestingly, the cut width of the PP layers remains similar to the previous case, implying that cut quality does not improve substantially with velocity under these conditions.

Steady state simulation outputs for a two-layer Alufoil film, comprising 7μm aluminium and 69μm paper, are presented in Fig. 4.4 at translation velocities of $50\,\mathrm{mm\,s^{-1}}$ and $1\,\mathrm{m\,s^{-1}}$, with the same respective laser sources as the previous cases. System behaviour is analogous to that of Triplex. At $50\,\mathrm{mm\,s^{-1}}$, the aluminium layer is removed by short-pulse ablation and does not traverse melting or vaporisation phases outside of each pulse. Due to the aluminium thickness of just 7μm, this layer is removed over a greater area at $50\,\mathrm{mm\,s^{-1}}$ than for Triplex. As a result, energy deposition in the sample decreases due to a reduction in absorbing substrate under the laser spot. The total cut width of the aluminium layer is approximately 20μm and that of the paper layer is 60μm. At $1\,\mathrm{m\,s^{-1}}$, removal of the aluminium layer is due to normal vaporisation. The total cut width of the aluminium layer in this case is approximately 6μm and that of the paper layer is 80μm, whilst the aluminium melt width is 20μm. The enthalpy of melting and vaporisation of the paper layer are ignored, as the material is taken to undergo removal at 655K (Appendix A).

4.2.2 Ablation, Interaction and Cut Widths

The interaction and cut widths of all layers in a multi-layer structure are of interest, as comparison of these values is the principle quantitative method with which incision or cut quality may be determined using the generalised simulation. The interaction width is defined within the present section as the maximum of the layer melt or crater widths, whilst the cut width is defined as the span at which no material is present. As will be further discussed in Chapter 5, differences in layer interaction and cut widths lead to incisions or cuts that are non-uniform throughout the section. Where such differences are visible to the naked eye ($> 300\mu$m), the process quality is considered poor. The relationship between laser fluence and these values provides useful information about the characteristic system behaviour. The steady state widths may be established as functions of layer fluence by progressively incrementing parameters and allowing each simulation to run until no further changes are observed.

Figure 4.5 presents the interaction and cut widths of all layers of Triplex for exposures at $50\text{mm}\,\text{s}^{-1}$ and $1\text{m}\,\text{s}^{-1}$ with a laser of wavelength 515nm, pulse duration 10ns, repetition rate 30kHz and beam waist radius 15μm. The fluence range is $5 - 200\text{J}\,\text{cm}^{-2}$, corresponding to a pulse energy range of $0.02 - 0.71$mJ (Eqn. (3.3)). The step-type nature of these plots is the result of practical mesh resolution constraints imposed by the available computing resources. Nonetheless, they give a clear indication of system behaviour: the interaction and cut widths of PP are much larger than those of aluminium, whilst all are generally increasing functions of fluence. The values for PP are lower at $50\text{mm}\,\text{s}^{-1}$ than at $1\text{m}\,\text{s}^{-1}$. They reach limiting values at high fluence, corresponding to the onset of normal vaporisation of the aluminium layer. This effect reflects the constant temperature condition imposed under the laser spot at the onset of aluminium vaporisation. The interaction width of the aluminium layer reaches a constant value at moderate fluence, corresponding to the maximum short-pulse crater width, before increasing again at the onset of melting.

Figure 4.6 provides a comparison between the cut widths of each individual layer under the same conditions at $50\text{mm}\,\text{s}^{-1}$, $200\text{mm}\,\text{s}^{-1}$, $400\text{mm}\,\text{s}^{-1}$ and $1\text{m}\,\text{s}^{-1}$. It is clear that the minimum fluence at which a full cut of the aluminium layer is observed, corresponding to complete film penetration, is an increasing function of velocity. As noted above, the maximum interaction and cut widths of the PP layers for each velocity are attained

at the onset of normal vaporisation of the aluminium layer. The fluence at which this phenomenon is first observed is a non-linear function of velocity. At $50\text{mm}\,\text{s}^{-1}$, short-pulse ablation removes the absorbing aluminium layer quickly, reducing energy coupling between the beam and sample. As a result, normal vaporisation of the aluminium layer occurs at high fluence ($\geq 160\text{J}\,\text{cm}^{-2}$). At $200\text{mm}\,\text{s}^{-1}$, short-pulse ablation is no longer sufficient for complete penetration of the aluminium layer. Thus, vaporisation of the aluminium layer occurs at lower fluence ($\geq 80\text{J}\,\text{cm}^{-2}$). At higher velocities, translational energy transport increases. As a result, vaporisation of the aluminium layer takes place progressively later ($\geq 100\text{J}\,\text{cm}^{-2}$ at $400\text{mm}\,\text{s}^{-1}$ and $\geq 160\text{J}\,\text{cm}^{-2}$ at $1\text{m}\,\text{s}^{-1}$). The minimum fluence at which the maximum cut width of PP takes place is therefore driven by energy coupling at $50\text{mm}\,\text{s}^{-1}$ and translational energy transport at higher velocities. Another consequence of the same physical behaviour is the variation in PP cut width at the minimum film penetration fluence. At $50\text{mm}\,\text{s}^{-1}$, this value is just 100μm, whilst at $200\text{mm}\,\text{s}^{-1}$, $400\text{mm}\,\text{s}^{-1}$ and $1\text{m}\,\text{s}^{-1}$ the respective values are 600μm, 450μm and 300μm. Cut quality is therefore greater at $50\text{mm}\,\text{s}^{-1}$ than at higher velocities due to ablative penetration of the aluminium film, leading to a reduction in energy coupling between the beam and sample.

Figures 4.7 and 4.8 present the same data for Triplex exposed to pulses of wavelength 1064nm, duration 4.5ns, repetition rate 30kHz and beam waist radius 21μm. The fluence range is once more $5-200\text{J}\,\text{cm}^{-2}$, corresponding to a pulse energy range of $0.03-1.39$mJ. The ablation efficiency of aluminium with this laser source is lower than in the previous case and the spot size is larger. Consequently, more energy is deposited in the sample at low velocity and the PP layer interaction and cut widths are larger. Under none of the simulated conditions is short-pulse ablation responsible for complete removal of the aluminium layer. A cut width limit is once more seen in the PP layers due to vaporisation of the aluminium layer, its onset driven by translational energy transport at all velocities. This laser effectively provides selective removal of the PP layers via conduction. For full cuts it provides poor quality with respect to the previous case.

Figure 4.9 presents the interaction and cut widths of all layers of Alufoil for exposures at $50\text{mm}\,\text{s}^{-1}$ and $1\text{m}\,\text{s}^{-1}$ with a laser of wavelength 515nm, pulse duration 10ns, repetition rate 30kHz and beam waist radius 15μm. The cut width of paper is greater than that of aluminium, whilst both are increasing functions of fluence. A cut width limit is observed for the paper layer at $1\text{m}\,\text{s}^{-1}$, whilst this is not the case at $50\text{mm}\,\text{s}^{-1}$. As

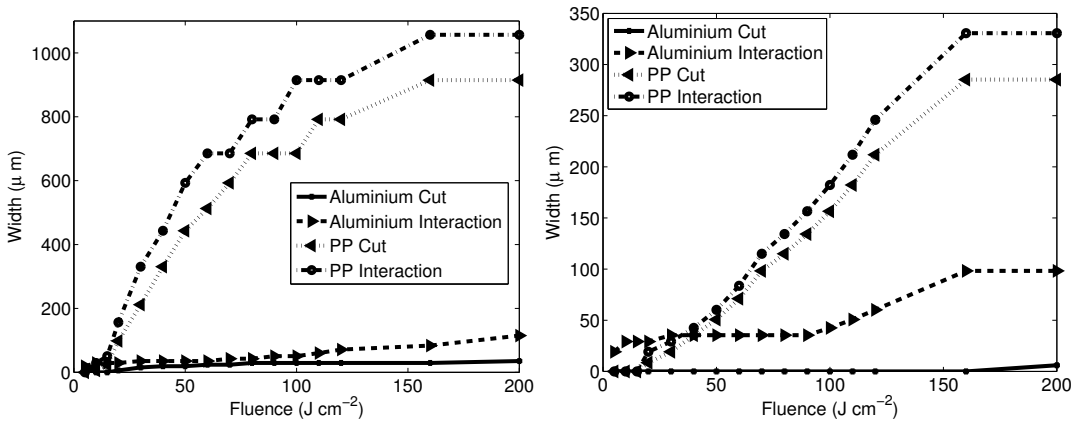

FIGURE 4.5: Interaction and cut widths of Triplex layers at (left) 50mm s^{-1} and (right) 1m s^{-1} with laser of wavelength 515nm, pulse duration 10ns, repetition rate 30kHz and beam waist radius 15μm.

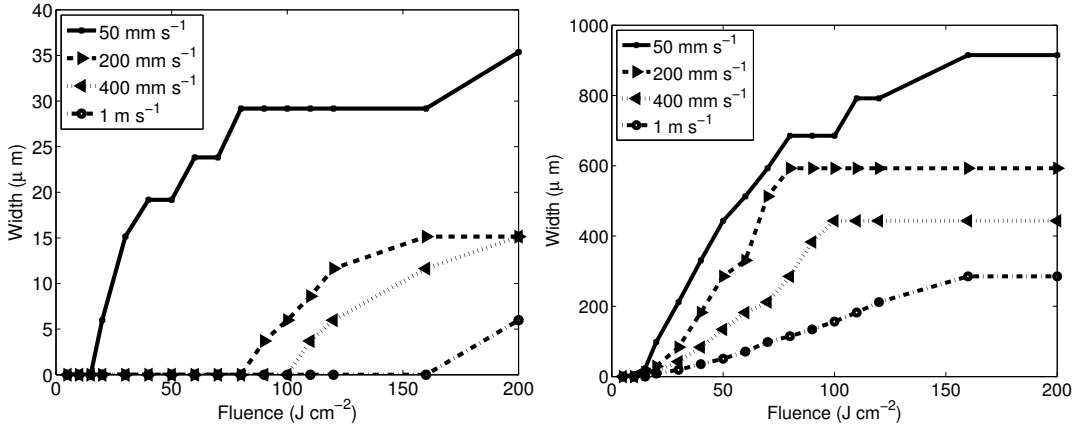

FIGURE 4.6: Cut widths of (left) aluminium and (right) PP layers of Triplex with laser of wavelength 515nm, pulse duration 10ns, repetition rate 30kHz and beam waist radius 15μm.

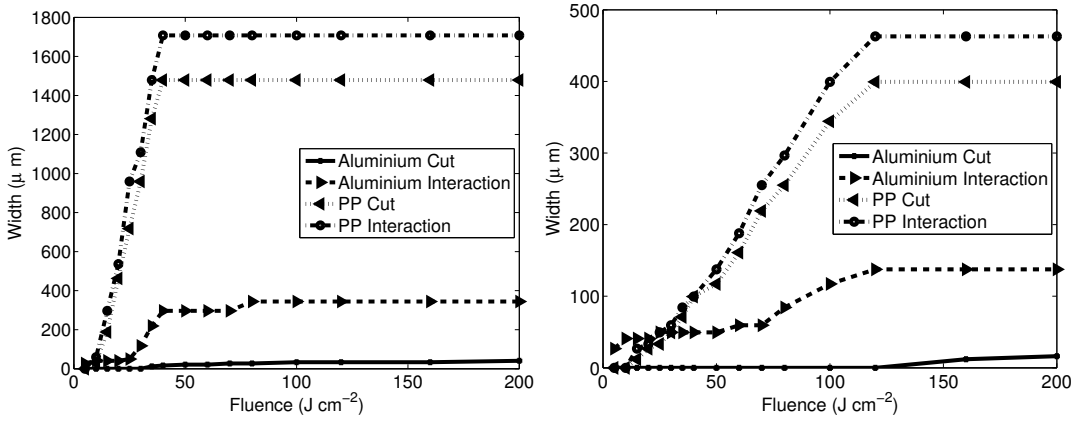

FIGURE 4.7: Interaction and cut widths of Triplex layers at (left) 50mm s^{-1} and (right) 1m s^{-1} with laser of wavelength 1064nm, pulse duration 4.5ns, repetition rate 30kHz and beam waist radius 21μm.

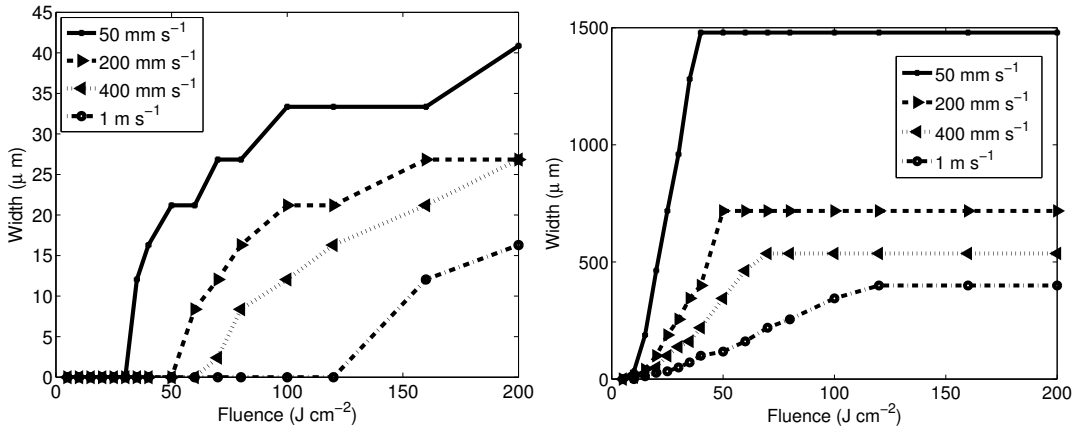

FIGURE 4.8: Cut widths of (left) aluminium and (right) PP layers of Triplex with laser of wavelength 1064nm, pulse duration 4.5ns, repetition rate 30kHz and beam waist radius 21μm.

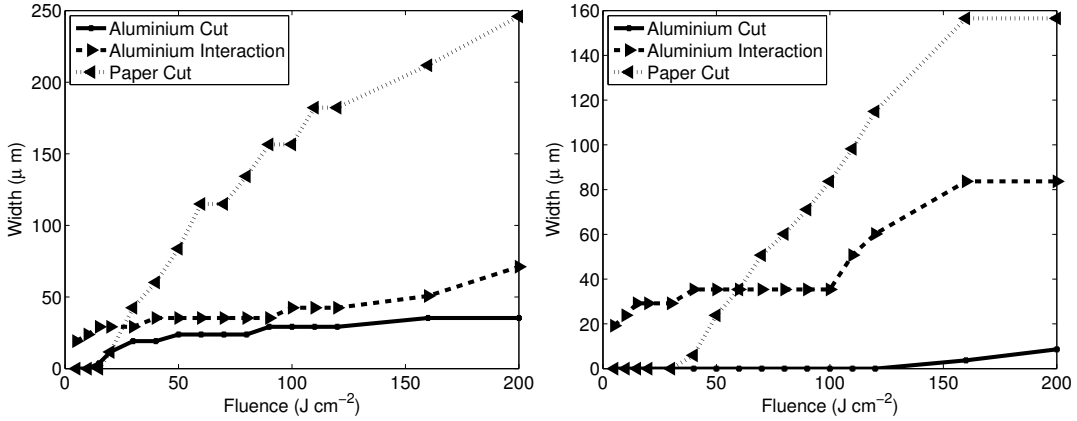

FIGURE 4.9: Interaction and cut widths of Alufoil layers at (left) 50mm s^{-1} and (right) 1m s^{-1} with laser of wavelength 515nm, pulse duration 10ns, repetition rate 30kHz and beam waist radius 15μm.

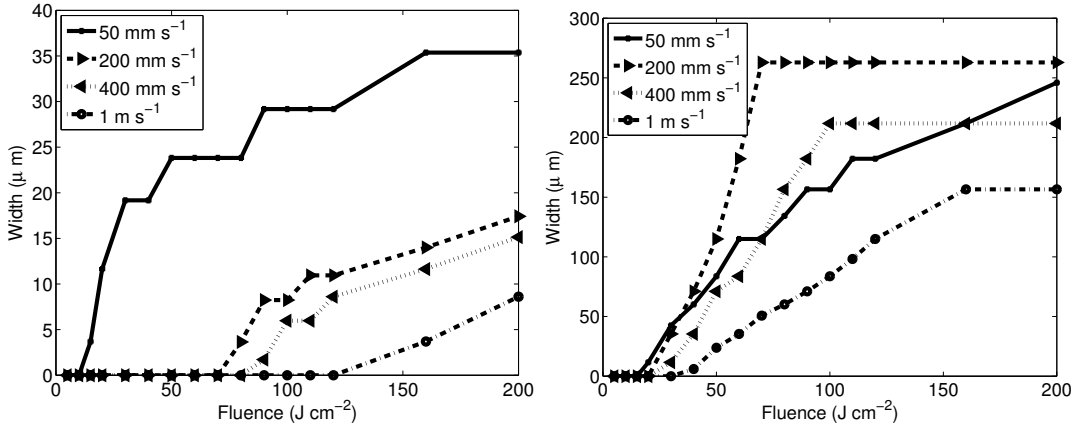

FIGURE 4.10: Cut widths of (left) aluminium and (right) paper layers of Alufoil with laser of wavelength 515nm, pulse duration 10ns, repetition rate 30kHz and beam waist radius 15μm.

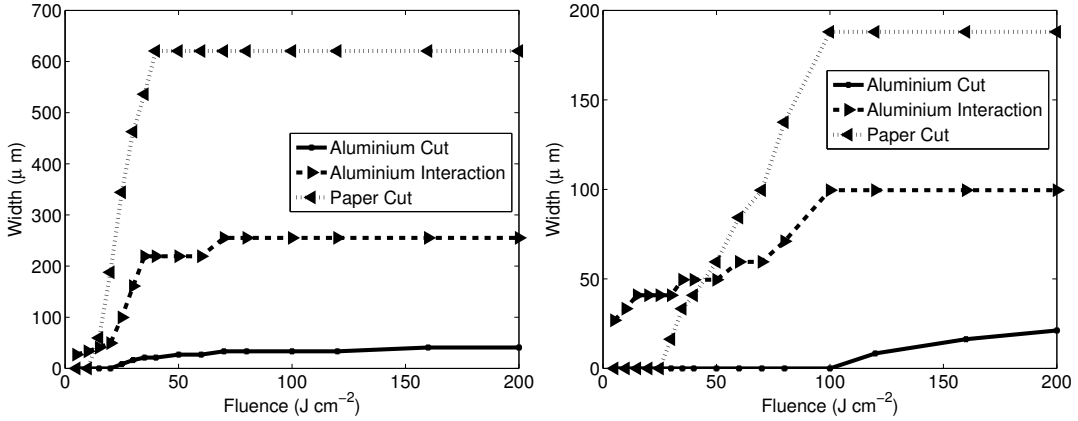

FIGURE 4.11: Interaction and cut widths of Alufoil layers at (left) 50mm s^{-1} and (right) 1m s^{-1} with laser of wavelength 1064nm, pulse duration 4.5ns, repetition rate 30kHz and beam waist radius 21μm.

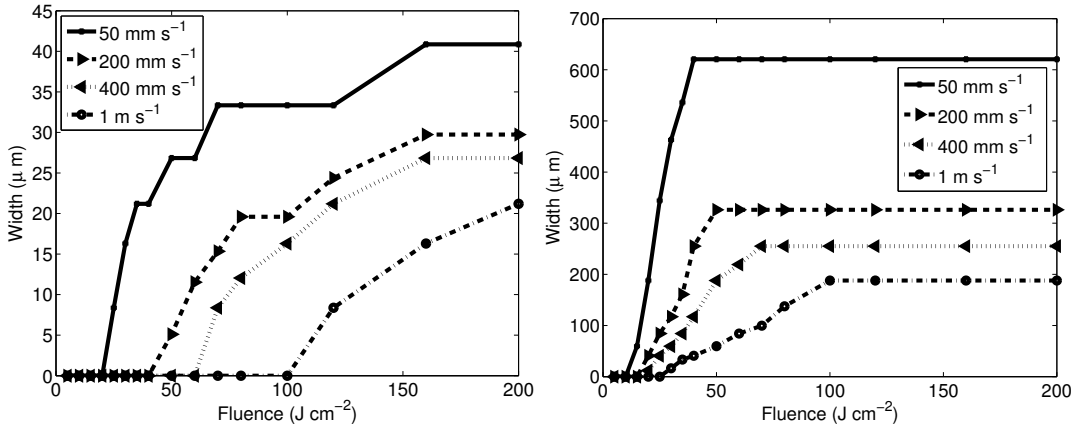

FIGURE 4.12: Cut widths of (left) aluminium and (right) paper layers of Alufoil with laser of wavelength 1064nm, FWHM pulse duration 4.5ns, repetition rate 30kHz and beam waist radius 21μm.

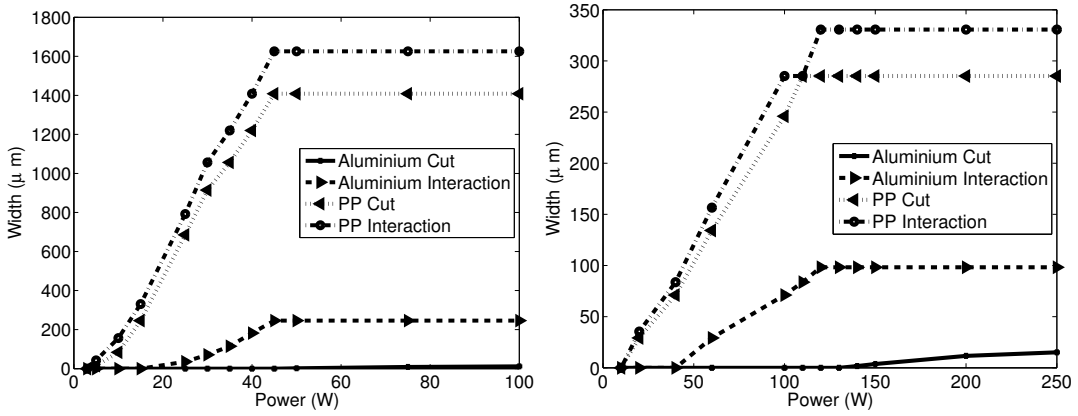

FIGURE 4.13: Interaction and cut widths of Triplex layers at (left) 50mm s^{-1} and (right) 1m s^{-1} with CW laser of wavelength 515nm and beam waist radius 15μm.

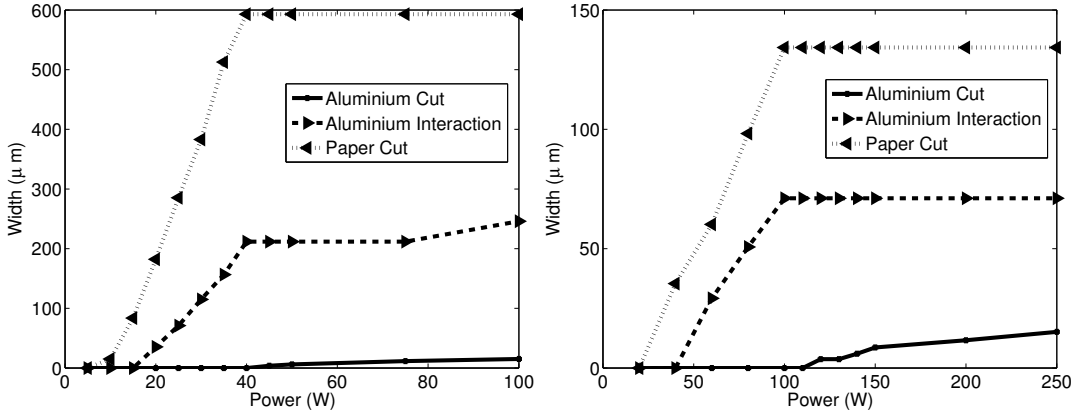

FIGURE 4.14: Interaction and cut widths of Alufoil layers at (left) $50\text{mm}\,\text{s}^{-1}$ and (right) $1\text{m}\,\text{s}^{-1}$ with CW laser of wavelength 515nm and beam waist radius 15μm.

with Triplex, the interaction width of the aluminium layer reaches a constant value at moderate fluence, corresponding to the short-pulse crater width, before increasing again at the onset of melting.

Figure 4.10 provides a comparison between the cut widths of each individual layer at $50\text{mm}\,\text{s}^{-1}$, $200\text{mm}\,\text{s}^{-1}$, $400\text{mm}\,\text{s}^{-1}$ and $1\text{m}\,\text{s}^{-1}$. The full cut of the aluminium layer follows a similar trend to that of Triplex, but with earlier onset due to the reduced layer thickness. At velocities greater than $50\text{mm}\,\text{s}^{-1}$, the cut width of paper displays the same limiting behaviour as that seen with the PP layers of Triplex. At $50\text{mm}\,\text{s}^{-1}$, however, short-pulse ablation removes the absorbing aluminium layer quickly, reducing energy coupling to the film. In this case, the reduction is sufficient enough to bring the paper cut width below that seen at higher velocities, with no limiting behaviour observed within the simulated fluence range. For all other cases, the cut width limit of the paper layer corresponds to the onset of aluminium vaporisation. At $50\text{mm}\,\text{s}^{-1}$, the paper cut width at minimum film penetration fluence is just 12μm, whilst at $200\text{mm}\,\text{s}^{-1}$, $400\text{mm}\,\text{s}^{-1}$ and $1\text{m}\,\text{s}^{-1}$ the respective values are 250μm, 180μm and 160μm. Optimum cut quality is once again greater at $50\text{mm}\,\text{s}^{-1}$ than at higher velocities due to ablative penetration of the aluminium film, leading to a reduction in energy coupling between the beam and sample.

Figures 4.11 and 4.12 present the same data for Alufoil exposed to pulses of wavelength 1064nm, duration 4.5ns, repetition rate 30kHz and beam waist radius 21μm. The reduced ablation efficient of aluminium with this laser increases energy coupling at low velocity and leads to larger paper cut widths with respect to the previous case.

Figures 4.13 and 4.14 display the interaction and cut widths of all layers of Triplex and Alufoil, respectively, for exposures at $50\text{mm}\,\text{s}^{-1}$ and $1\text{m}\,\text{s}^{-1}$ with a CW laser of wavelength 515nm and beam waist radius 15μm. These results allow comparison with the steady state heat flow calculation presented in Chapter 2 (Fig. 2.6 (left)). The minimum calculated cut powers with the present model under the given conditions are 50W and 140W for Triplex, and 45W and 120W for Alufoil, at $50\text{mm}\,\text{s}^{-1}$ and $1\text{m}\,\text{s}^{-1}$, respectively. These values correspond to the minimum power at which a non-zero cut width is reported for the aluminium layers. The interaction and cut widths of the other layers increase linearly before onset of aluminium vaporisation, at which point no further increases in these values are observed.

4.2.3 The Effect of Repetition Rate on Quality

In light of the preceding results, the ablation characteristics of metallic layers are clearly of great influence on process quality when considering multi-layer films. Where ablation efficiency is high, metallic layers are removed with minimal energy deposition in the film. As a result, the cut and interaction widths of other layers are minimised. This is observed at $50\text{mm}\,\text{s}^{-1}$ for both Triplex and Alufoil multi-layer films in the preceding section. At higher velocities, increasing the pulse energy to maintain complete film penetration leads to normal vaporisation of the aluminium layer and, as a result, large interaction widths in the other layers. This effect is due to a reduction in ablation efficiency with fluence; that is, a reduction in the rate of increase of the ablation depth at high fluences (Figs. 3.5 and 3.6). To maintain ablation efficiency, the repetition rate may be raised such that material removal rates are increased while maintaining reasonable ablation efficiency.

Figure 4.15 displays the cut widths of all layers of Triplex subject to pulses of wavelength 515nm, duration 10ns and beam waist radius 15μm. Repetition rates in the range $30-400\text{kHz}$ are considered for velocities in the range $50\text{mm}\,\text{s}^{-1}-1\text{m}\,\text{s}^{-1}$. The cut width is plotted versus average beam power to allow comparison between different repetition rates. The minimum average beam power required for complete penetration of the aluminium layer is an increasing function of repetition rate at low translation speeds. This indicates that, in general, the process becomes less efficient at higher repetition rates. This is due to an increase in the average beam power corresponding to the phase explosion threshold. With increasing repetition rate, however, the cut width of PP

is less strongly influenced by velocity. Increasing the repetition rate has the effect of increasing the minimum velocity at which normal vaporisation of the aluminium layer takes place before complete film penetration is achieved. At 100kHz, this minimum velocity is greater than $200\text{mm}\,\text{s}^{-1}$, while at 200kHz, it is greater than $400\text{mm}\,\text{s}^{-1}$. At 400kHz, the minimum velocity for this effect is still less than $1\text{m}\,\text{s}^{-1}$. Only for velocities below this minimum value is a significant reduction observed, with respect to 30kHz, in the PP cut width at minimum film penetration fluence. Figure 4.17 (left) displays the PP cut widths at minimum film penetration fluence for the parameter range considered. At $200\text{mm}\,\text{s}^{-1}$ and $400\text{mm}\,\text{s}^{-1}$, the cut widths of these layers reduce with increasing repetition rate. At $50\text{mm}\,\text{s}^{-1}$, there is some fluctuation but the values remain low. The cut width at $1\text{m}\,\text{s}^{-1}$ is mostly unaffected by the repetition rate. These results represent a general improvement in cut quality at intermediate velocities and a reduction in the dependence of cut quality on translation velocity with increasing repetition rate up to 400kHz.

Figure 4.16 displays the cut widths of all layers of Alufoil under the same conditions. The behaviour of this film is analogous to the previous case. The minimum average beam power required for complete penetration of the aluminium layer increases with repetition rate at low velocity, whilst the cut width of the paper layer becomes less strongly influenced by velocity. Figure 4.17 (right) displays the paper cut widths at minimum film penetration fluence for the parameter range considered. As with the PP layers of Triplex, the cut width of the paper layer of Alufoil generally reduces with increasing repetition rate at $200\text{mm}\,\text{s}^{-1}$ and $400\text{mm}\,\text{s}^{-1}$. Again, at $50\text{mm}\,\text{s}^{-1}$, there is some fluctuation but the values remain low, while at $1\text{m}\,\text{s}^{-1}$, the cut width is mostly unaffected by the repetition rate. These results represent a general improvement in cut quality at intermediate velocities and a reduction in the dependence of cut quality on translation velocity with increasing repetition rate up to 400kHz.

4.2.4 The Effect of Beam Spot Size on Quality

The laser beam spot size provides another parameter with which multi-layer film cut quality can be investigated. Figure 4.18 displays the cut widths of all layers of Triplex subject to pulses of wavelength 515nm, duration 10ns and repetition rate 30kHz. Beam waist radii in the range $15 - 75\mu\text{m}$ are considered for velocities in the range $50\text{mm}\,\text{s}^{-1} -$

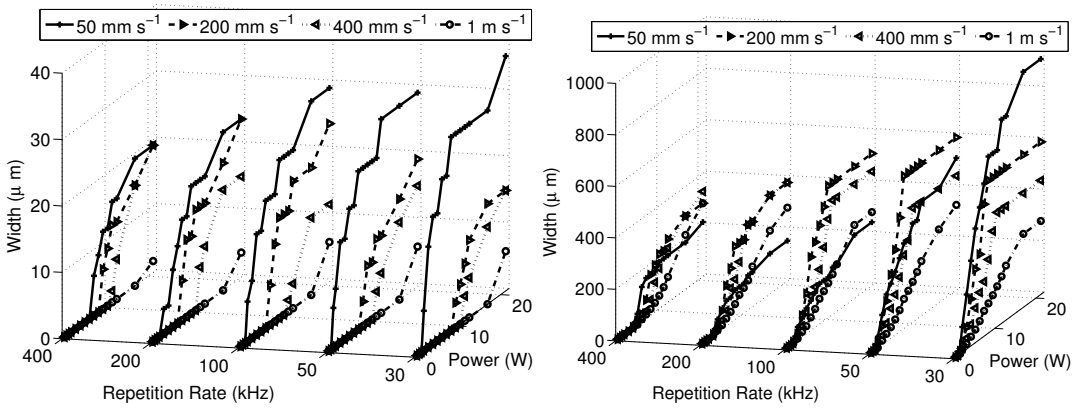

FIGURE 4.15: Cut width of the (left) aluminium and (right) PP layers of Triplex with laser of wavelength 515nm, pulse duration 10ns, beam waist radius 15μm and repetition rate $30 - 400$kHz.

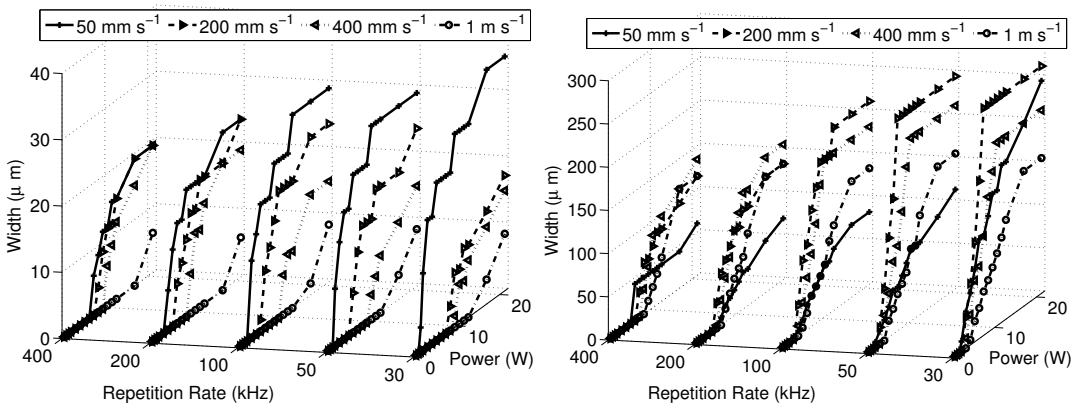

FIGURE 4.16: Cut width of the (left) aluminium and (right) paper layers of Alufoil with laser of wavelength 515nm, pulse duration 10ns, beam waist radius 15μm and repetition rate $30 - 400$kHz.

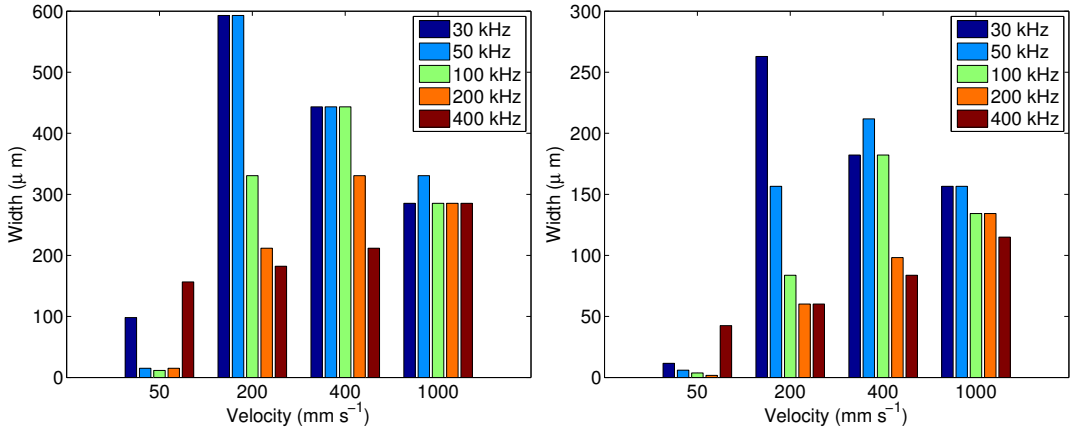

FIGURE 4.17: (Left) PP layer cut widths at minimum film penetration fluence for Triplex as functions of velocity and laser repetition rate. (Right) Paper layer cut widths at minimum film penetration fluence for Alufoil as functions of velocity and laser repetition rate.

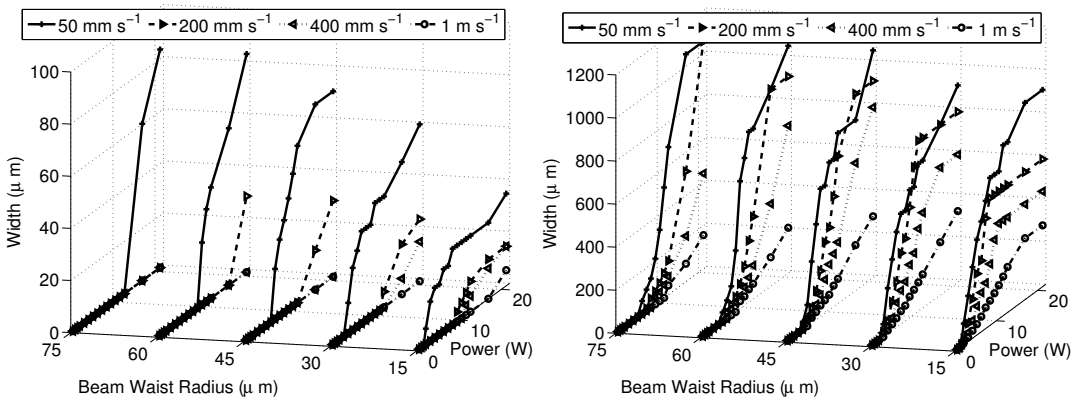

FIGURE 4.18: Cut width of the (left) aluminium and (right) PP layers of Triplex with laser of wavelength 515nm, pulse duration 10ns, repetition rate 30kHz and beam waist radius $15 - 75\mu$m.

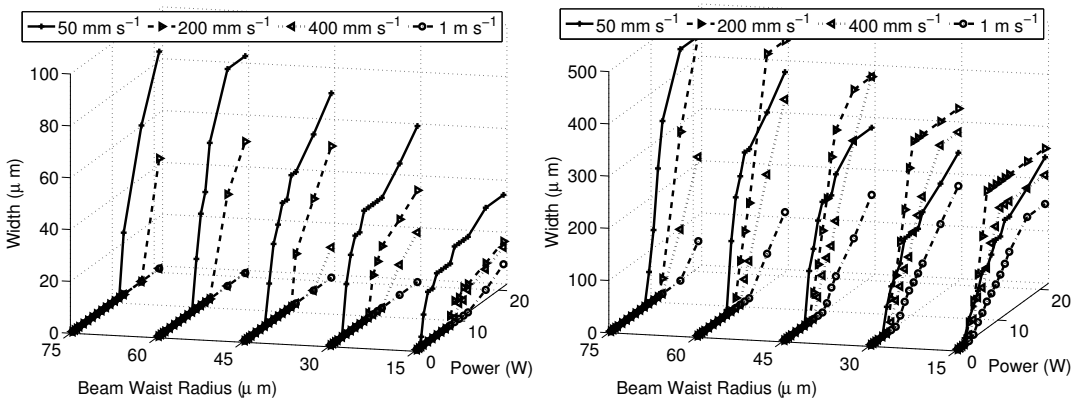

FIGURE 4.19: Cut width of the (left) aluminium and (right) paper layers of Alufoil with laser of wavelength 515nm, pulse duration 10ns, repetition rate 30kHz and beam waist radius $15 - 75\mu$m.

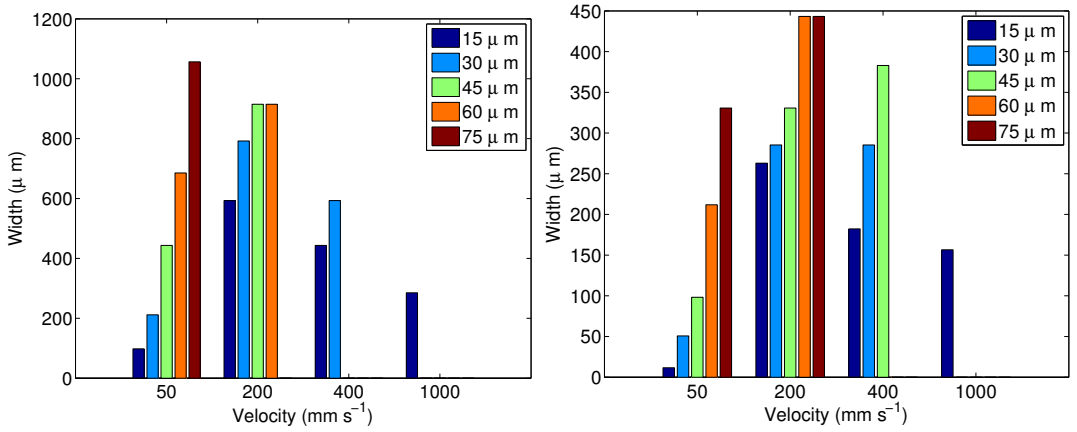

FIGURE 4.20: (Left) PP layer cut widths at minimum film penetration fluence, where achieved, for Triplex as functions of velocity and beam waist radius. (Right) Paper layer cut widths at minimum film penetration fluence, where achieved, for Alufoil as functions of velocity and beam waist radius.

$1\,\mathrm{m\,s^{-1}}$. Increasing the beam waist radius leads to a rapid increase in the minimum average beam power required for complete penetration of the aluminium layer at all velocities. At 75μm, such penetration is only possible at $50\,\mathrm{mm\,s^{-1}}$ within the simulated power range. This indicates a loss of process efficiency with increasing waist radius. Furthermore, the cut width of PP is more strongly influenced by velocity for larger spot sizes. Figure 4.20 (left) displays the PP cut widths at minimum film penetration fluence for the parameter range considered. Where a value is not displayed, complete film penetration is not possible within the parameter range considered. The cut widths of these layers increase rapidly with the beam waist radius. This represents a general decrease in cut quality with increasing beam spot size.

Figure 4.19 displays the cut widths of all layers of Alufoil under the same conditions. System behaviour is analogous to that of Triplex, with rapid decreases in both process efficiency and cut quality with increasing beam spot size. Figure 4.20 (right) displays the paper cut widths at minimum film penetration fluence, where possible within the parameter range considered. As with the PP layers of Triplex, the cut width of the paper layer of Alufoil increases rapidly with the beam waist radius. This represents a general decrease in cut quality with increasing beam spot size.

4.3 Concluding Remarks

The general simulation presents a complete picture of the characteristic behaviour of multi-layer films subject to CW or pulsed laser irradiation. In the latter case, the combination of short-pulse ablation and long-term conduction effects leads to different underlying removal mechanisms for each layer. This is in line with the experimental observations presented in Chapter 5. Detailed insight into the response of Triplex and Alufoil packaging films subject to pulsed laser irradiation has been gained. At low to moderate fluences in the velocity range $50\,\mathrm{mm\,s^{-1}} - 1\,\mathrm{m\,s^{-1}}$, aluminium layer incision is due to short-pulse ablation, whilst PP and paper layer removal is due to thermal degradation as a result of thermal conduction from the aluminium layer. At high fluences, the aluminium layer begins to vaporise on a longer time-scale due to a reduction in ablation efficiency. This effect leads to large interaction and cut widths in the other layers of both films and is generally seen to reduce the process quality. By increasing the repetition rate, it has been demonstrated that the ablation efficiency of the aluminium layer can

be maintained at high translation velocities, leading to lower interaction and cut widths in the other layers. Despite marginal reductions in process efficiency, a repetition rate of 400kHz is found to reduce PP layer cuts widths in Triplex to $\leq 300\mu$m and paper layer cut widths in Alufoil to $\leq 120\mu$m, over the velocity range $50\text{mm}\,\text{s}^{-1} - 1\text{m}\,\text{s}^{-1}$. Increasing the beam spot size was instead found to reduce both the process efficiency and cut quality. As a whole, the results indicate strong dependence of the cut quality on the ablation efficiency of the metallic layer.

The numerical process simulation is limited by the short-pulse ablation and absorption data provided by the short-pulse model presented in Chapter 3. The dependence of cut quality on translation velocity and repetition rate is based on the assumption that the relationship between ablation depth and fluence does not change between cases. A variation in ablation efficiency with the number of pulses has obvious consequences on conclusions regarding cut quality and repetition rate. Whilst the experimental results of Chapter 5 indicate a decrease in ablation efficiency with multiple pulses with respect to single pulses, the variation between pulse numbers in the multiple-pulse regime is shown to be much less significant. For the film thicknesses considered in the present chapter, complete removal of the metallic layers by a single laser pulse is not realistic; multiple-pulse conditions prevail in almost all cases. It may therefore be concluded that the simulation provides a reasonable approximation to the real-world scenario, leading to useful and quantitative conclusions regarding the use of laser sources in the packaging industry.

Chapter 5

An Experimental Investigation into the Pulsed Laser Incision and Cut of Some Typical Packaging Films

The following chapter exhibits testing of three single-layer and four multi-layer packaging materials using two laser sources: a $0.5 - 0.8$ns near-infrared (NIR) laser and a $10 - 12.5$ns green laser. Tests with each material-laser combination have been conducted at translation velocities in the range $50\text{mm}\,\text{s}^{-1} - 1\text{m}\,\text{s}^{-1}$ and fluences in the range $0.4 - 37\text{J}\,\text{cm}^{-2}$. Samples have been analysed using an optical microscope and a 3D optical profiler. Subsequently, the ablation threshold and depth of all single-layer films and the interaction, melt and cut widths of all single and multi-layer films have been determined under the tested conditions. Experimental data has been utilised to verify the numerical models presented in Chapters 3 and 4.

5.1 Tested Films

Single-layer polyethylene (PE), polypropylene (PP) and aluminium (AL) and multi-layer Duplex, Triplex, Metallised Paper and Alufoil packaging films have been tested. Their compositions are giving in Tab. 5.1. These multi-layer films were chosen so as

Name	**Layer 1**	**Thick.**	**Layer 2**	**Thick.**	**Layer 3**	**Thick.**
PE	PE	50μm	-	-	-	-
PP	PP	20μm	-	-	-	-
Aluminium	AL	20μm	-	-	-	-
Duplex	PP	20μm	AL	$< 0.1\mu$m	PP	20μm
Triplex	PP	20μm	AL	9μm	PP	20μm
Metallised Paper	AL	$< 0.1\mu$m	Paper	69μm	-	-
Alufoil	AL	7μm	Paper	69μm	-	-

TABLE 5.1: Tested film compositions and layer thicknesses.

to demonstrate the influence of metallic layer thickness on multi-layer film response to laser irradiation. Duplex and Triplex, and Metallised Paper and Alufoil, are of the same respective structures; however, the former in each case has a much thinner aluminium layer.

5.2 Experimental Setup

A NIR and a green laser source were utilised for the experiments: the Helios IR (Innolight GmbH) and the Boreas G15 (Eolite Systems), respectively. The Helios IR was attenuated externally by a half-wave plate and polariser, whilst the Boreas G15 was attenuated by an internal device provided by the manufacturer. The Boreas G15, customised to emit at both infrared and green wavelengths, was mounted with dichroic and 45° mirrors to separate out the green beam for utilisation and to offset it horizontally from the infrared beam. For both the Helios IR and Boreas G15, the horizontal beam was directed vertically onto the sample by a 45° mirror and focused onto its surface with a lens. The lasers were mounted on two different machines equipped with x-y translation stages on which the samples were mounted. Samples were held horizontally above the stage under a slight tension. No contact between the sample and the stage was present for at least three centimetres in the direction of translation in the tested area of each sample. For the Helios IR, this was achieved by folding the sample around and clamping it beneath two metal rods of precise thickness; for the Boreas G15, this was achieved by clamping the sample between two magnetic rings of precise thickness. Both machines were mounted with fume extraction tubes; the IR system connected to an outside exhaust; the green system connected to a carbon filter. Figures 5.1 - 5.3 present photographs of the experimental setup with each component indicated. All experiments were undertaken by the author at the Università degli Studi di Parma. *Assistance with*

Test Group	A	B	C	D
Laser Model	Helios IR	Helios IR	Boreas G15	Boreas G15
Wavelength	1064nm	1064nm	515nm	515nm
Repetition Rate	30kHz	70kHz	30kHz	100kHz
Pulse Duration	0.5ns	0.8ns	10ns	12.5ns
Beam Quality M^2	< 1.2	< 1.2	< 1.2	< 1.2
Focusing Lens Focal Length	70mm	70mm	75mm	75mm
Calculated Spot Size	42μm	42μm	30μm	30μm
Calculated Rayleigh Range	1300μm	1300μm	1300μm	1300μm
Max. Average Power @ Sample	4.05W	4.83W	3.78W	5.91W
Max. Pulse Energy @ Sample	135μJ	69μJ	126μJ	59μJ
Max. Fluence @ Sample	$20\,\mathrm{J\,cm^{-2}}$	$10\,\mathrm{J\,cm^{-2}}$	$37\,\mathrm{J\,cm^{-2}}$	$17\,\mathrm{J\,cm^{-2}}$
Average Power Range	$2-100\%$	$4-100\%$	$14-100\%$	$14-100\%$

TABLE 5.2: Laser characteristics under test conditions.

the experimental setup was provided by M. Sozzi at the Group of Applied Electromagnetics (GAEM), Università degli Studi di Parma. The Helios IR was provided by the NEXPRESSO program (Network for EXchange and PRototype Evaluation of photonicS componentS and Optical systems), funded by the Seventh Framework Programme of the European Union.

Each laser was operated at two different repetition rates, 30kHz and 70kHz for the Helios IR and 30kHz and 100kHz for the Boreas G15, giving four test groups, $A-D$, for each material. The average power at the sample was measured using a Coherent LabMax-Top power meter. This parameter was then utilised to calculate the pulse energy and fluence at the sample surface. The power meter was also employed to calibrate the attenuation systems. Table 5.2 presents the characteristics of each test group.

Tests to locate the focal point for the Helios IR system were conducted using PP, scanning at $50\mathrm{mm\,s^{-1}}$ with a repetition rate of 30kHz and an attenuated beam. With such an arrangement, clear laser interaction was visible at the focal point, faint interaction at $\pm 400\mu$m (vertically) from the focal point and no interaction at $\pm 500\mu$m. Focal point tests for the Boreas G15 system were conducted using the metallic side of Metallised Paper, scanning at $1\mathrm{m\,s^{-1}}$ with a repetition rate of 30kHz and an attenuated beam. With such an arrangement, clear laser interaction was visible at the focal point, faint interaction at $\pm 800\mu$m (vertically) from the focal point and no interaction at $\pm 1000\mu$m. On the basis of these interactions, the uncertainty in focal position was estimated as being less than $\pm 500\mu$m for all tests, corresponding to a maximum fluence reduction of 13% due to this effect.

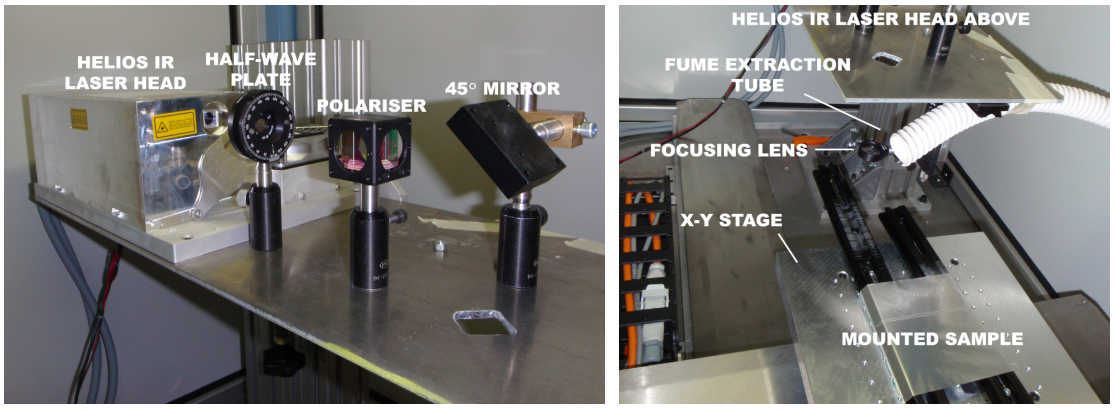

FIGURE 5.1: (Left) Helios IR laser head with half-wave plate, polariser and 45° mirror. (Right) Fume extraction tube, focusing lens, x-y stage and mounted sample of Helios IR system.

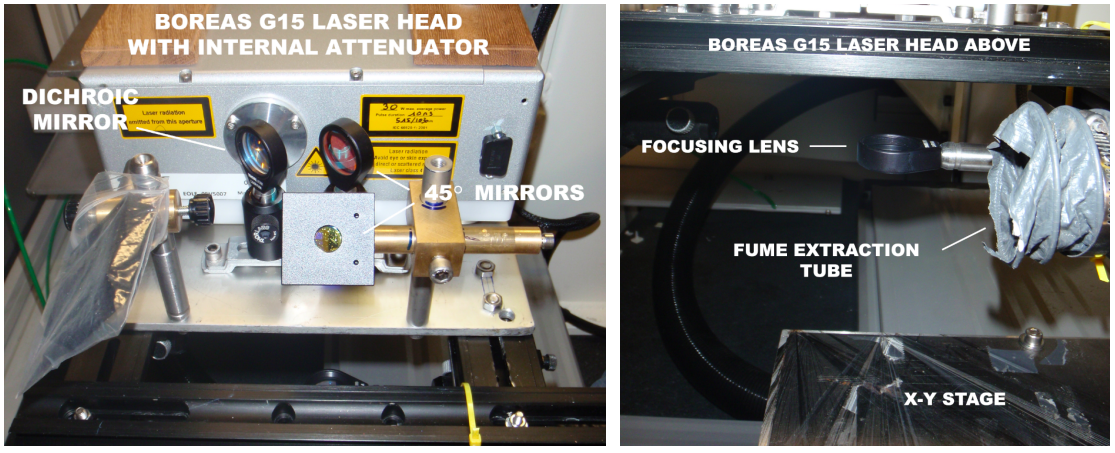

FIGURE 5.2: (Left) Boreas G15 laser head with dichroic mirror and 45° mirrors. (Right) Fume extraction tube, focusing lens and x-y stage of Boreas G15 system.

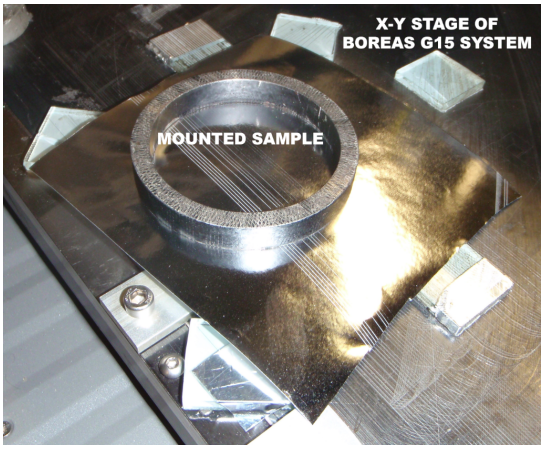

FIGURE 5.3: Mounted sample of Boreas G15 system.

Ablation tests were performed by translating samples under the focused beam and varying the velocity and average beam power with each test. All test groups were utilised at translation velocities of $50\,\mathrm{mm\,s^{-1}}$ and $1\,\mathrm{m\,s^{-1}}$ for aluminium and $50\,\mathrm{mm\,s^{-1}}$, $200\,\mathrm{mm\,s^{-1}}$ and $1\,\mathrm{m\,s^{-1}}$ for PE and PP. The additional tests at $200\,\mathrm{mm\,s^{-1}}$ for the plastic films came about after no interactions were observed at $1\,\mathrm{m\,s^{-1}}$. Group *C* was utilised at translation velocities of $50\,\mathrm{mm\,s^{-1}}$, $200\,\mathrm{mm\,s^{-1}}$ and $1\,\mathrm{m\,s^{-1}}$ for all multi-layer films except for Alufoil, which was only tested at $50\,\mathrm{mm\,s^{-1}}$. Alufoil was limited to the lowest velocity as its ablation behaviour at higher velocities replicated that of single-layer aluminium, with no observed interaction in the paper layer. Groups *A* and *B* were utilised at maximum power for all multi-layer materials at translation velocities of $50\,\mathrm{mm\,s^{-1}}$, $200\,\mathrm{mm\,s^{-1}}$ and $1\,\mathrm{m\,s^{-1}}$. Both Alufoil and Metallised Paper were subject to laser irradiation from the aluminium side only for all tests, as no interaction with paper was observed under any of the tested conditions.

Ablation thresholds and interaction and cut widths were determined by observing the laser incisions under an optical microscope. Ablation depth measurements and 3D images of all incisions made in single-layer films were obtained with an optical profiler. *All depth measurements were undertaken on the tested samples by S. Carmignato at the Laboratorio di Metrologia Geometrica e Industriale, Università di Padova.*

5.3 Pulse Overlap

In light of the aforementioned experimental procedure, a brief discussion of pulse overlap is necessary for the later description of phenomena that are typically reported on a "per-pulse" basis. At low velocities, the proportion of pulse overlap is high. Due to translation of the target relative to the laser beam, a particular point on the surface is subject to several pulses of different fluence. In this case, the total ablation depth may be considered as the sum of the contributions of all incident pulses above the ablation threshold. The discrete distribution of pulse fluence at a particular point is a function of the beam radius, ω_0, repetition rate, f_{rep}, and translation velocity, V, in correspondence with the Gaussian intensity distribution of the laser:

$$F_{\pm i} = F \cdot \exp\left[-2\left(\frac{Vi}{f_{rep}\,\omega_0}\right)^2\right], \qquad i = 0 \ldots n \tag{5.1}$$

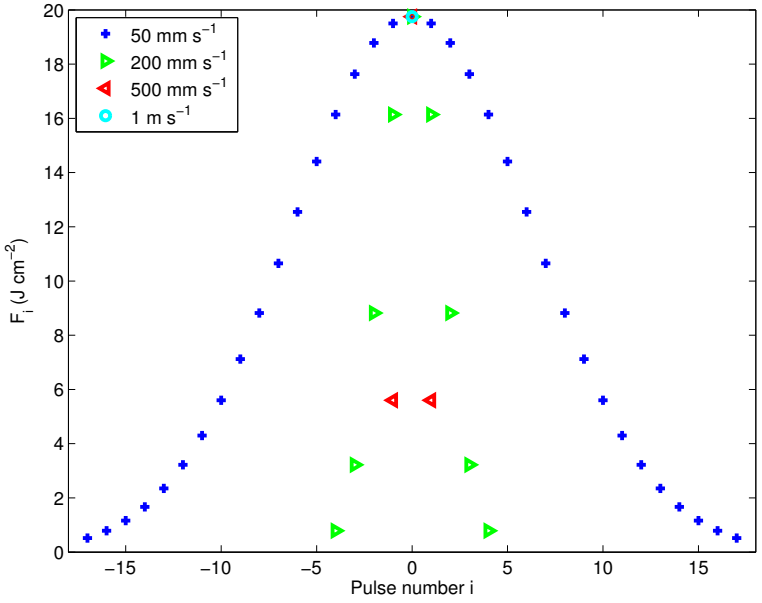

FIGURE 5.4: Fluence distribution of multiple pulses $F_{\pm i}$ ($\geq F_{th} = 0.5\,\mathrm{J\,cm^{-2}}$) for laser fluence $F = 20\,\mathrm{J\,cm^{-2}}$, test group A.

Where $F_{\pm i}$ is the fluence at the point under consideration for pulse numbers i to either side of the central pulse at $i = 0$ (where the laser axis is directly in line with the point of interest). F is the on-axis laser fluence and n is the largest integer for which $F_{\pm n} \geq F_{th}$, where F_{th} is the threshold fluence. The employed notation is restricted to the present discussion only. Such a method allows comparison of per-pulse values for experiments undertaken with single and multiple pulses. As an example, the fluence distribution of test group A with no attenuation (an on-axis fluence of $20\,\mathrm{J\,cm^{-2}}$) and a threshold fluence of $F_{th} = 0.5\,\mathrm{J\,cm^{-2}}$ is given in Fig. 5.4 for translation speeds of $50\,\mathrm{mm\,s^{-1}}$, $200\,\mathrm{mm\,s^{-1}}$, $500\,\mathrm{mm\,s^{-1}}$ and $1\,\mathrm{m\,s^{-1}}$. At $50\,\mathrm{mm\,s^{-1}}$, the target surface is subject to many pulses with an almost continuous distribution. At $200\,\mathrm{mm\,s^{-1}}$, the number of incident pulses above the ablation threshold is reduced, whilst at $500\,\mathrm{mm\,s^{-1}}$ only three such pulses are observed. At $1\,\mathrm{m\,s^{-1}}$, exposure is effectively single-pulse at $i = 0$. An increase in on-axis laser fluence, F, may lead to an increase in the number of pulses above the ablation threshold. This, in turn, leads to abrupt changes in the gradient of the calculated total ablation depth curve as a function of incident on-axis laser fluence (Figs. 5.10 and 5.11 (left)).

5.4 Results

High quality incisions were obtained for all materials under certain conditions. Interaction width at full cut, the principal quantitative measure of cut quality, was generally limited to $< 300\mu$m for all films except Triplex, where values of up to 500μm were observed. Microscopic analysis revealed some variability in interaction at low fluence, particularly for the PP and PE samples. This variation was most likely due to laser instability, its effect accentuated near the ablation threshold of each film. The first interactions seen in PP and PE with increasing fluence were optical modification and intermittent material removal (Fig. 5.5 (left)). Raising the fluence further saw sharp onset of efficient material removal with the Helios IR (Fig. 5.5 (right)). Such ablation was not observed with the Boreas G15, only optical modification. The device therefore yielded no useful results for the plastic single-layer films. Aluminium showed clear evidence of material removal at fluences above the ablation threshold (Fig. 5.6 (left)) for both lasers.

A full cut of Triplex was possible with the Boreas G15, the cut width of the aluminium layer much smaller than that of the PP layers (Fig. 5.6 (right)). The aluminium layer of Duplex could be removed at low fluence with no cut of the PP layers (Fig. 5.7 (left)), whilst a complete cut was only possible at maximum fluence with the Helios IR. The aluminium layer of Metallised Paper could be removed at low fluence with no effect on the paper layer (Fig. 5.7 (left)), whilst a complete cut was not possible under any of the tested conditions. Though selective layer removal was easily achieved for Duplex, the formation of large, irregular bubbles lead to low process quality in some cases. For Metallised Paper, however, high quality selective layer removal could be undertaken at low power. A complete cut of Alufoil was achieved at low velocity with the Boreas G15, the cut width of the paper layer irregular but small, with little charring (Fig. 5.8).

5.4.1 Single-Layer Ablation Thresholds

Optical microscopy was undertaken to analyse the film responses to laser irradiation. The ablation threshold of each single-layer material was calculated by averaging the minimum tested fluence at which ablation was observed and that immediately below. For metals, the ablation threshold was considered analogous to the phase explosion

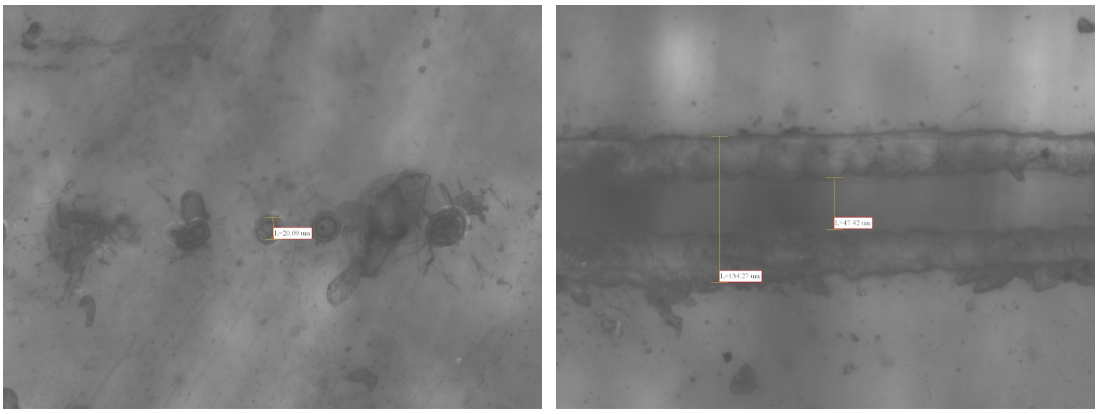

FIGURE 5.5: (Left) PE following $50\text{mm}\,\text{s}^{-1}$ exposure to Helios IR laser, test group A, at $12\text{J}\,\text{cm}^{-2}$. (Right) PP following $50\text{mm}\,\text{s}^{-1}$ exposure to Helios IR laser, test group A, at $14\text{J}\,\text{cm}^{-2}$.

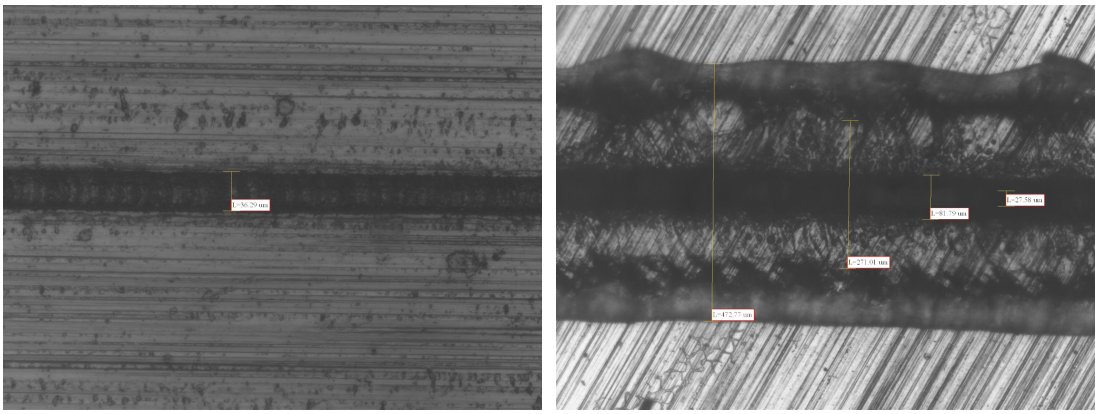

FIGURE 5.6: (Left) Aluminium following $50\text{mm}\,\text{s}^{-1}$ exposure to Helios IR laser, test group A, at $3\text{J}\,\text{cm}^{-2}$. (Right) Triplex following $50\text{mm}\,\text{s}^{-1}$ exposure to Boreas G15 laser, test group C, at $37\text{J}\,\text{cm}^{-2}$.

threshold, due to the pulse durations considered. This mechanism was identified by the presence of large amounts of dislodged material at the crater edges, the result of pressure created by the explosive phase change. The observation of this crater type in correspondence with the onset of phase explosion is presented by Porneala & Willis [67], who directly observe the dynamics of phase explosion for 5ns laser pulses. For plastics, the threshold was considered as the point at which crater-type formations, corresponding to the onset of material removal, were observed. Table 5.3 presents the measured values for each test group where ablation was possible within the maximum pulse energy available.

The measured threshold fluence of all films shows dependence on the beam characteristics and, in some cases, the translation velocity. This implies dependence on the pulse duration, beam wavelength and the number of pulses or average beam power. The

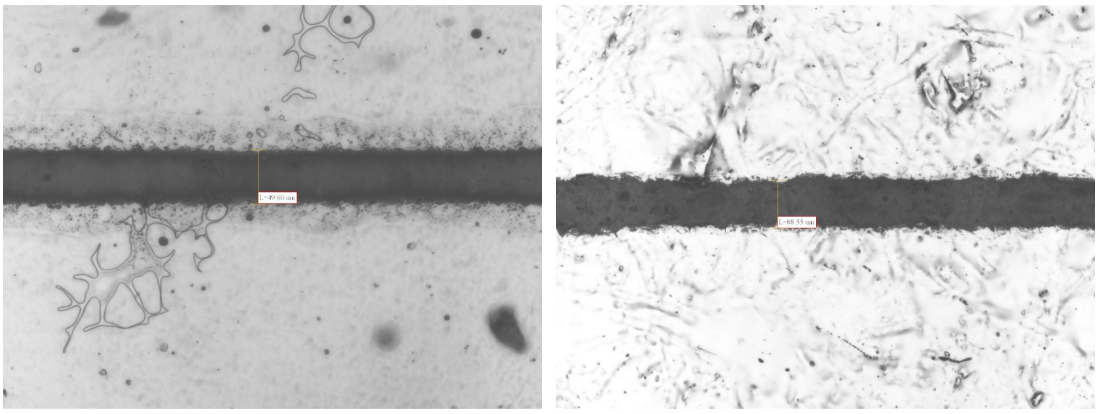

FIGURE 5.7: (Left) Duplex following $1\,\mathrm{m\,s^{-1}}$ exposure to Boreas G15 laser, test group C, at $2.4\,\mathrm{J\,cm^{-2}}$. (Right) Metallised Paper following $1\,\mathrm{m\,s^{-1}}$ exposure to Boreas G15 laser, test group C, at $2.4\,\mathrm{J\,cm^{-2}}$.

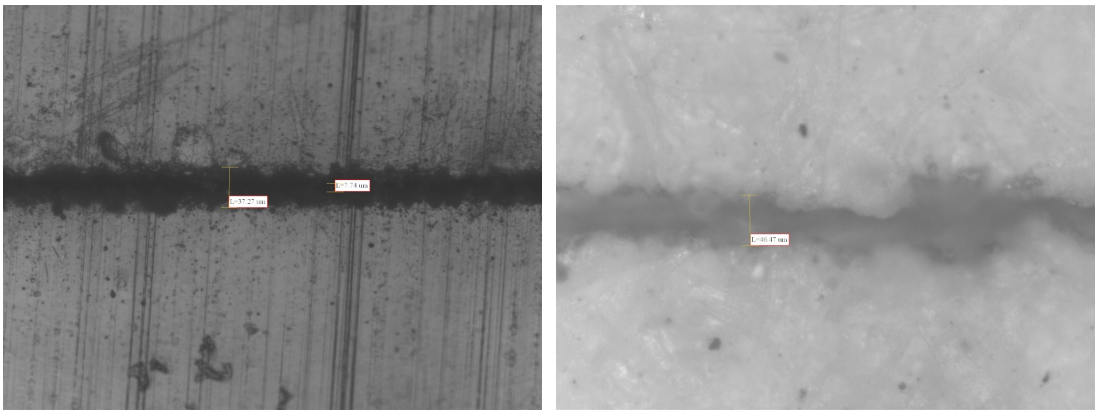

FIGURE 5.8: (Left) Metal side of Alufoil following $50\,\mathrm{mm\,s^{-1}}$ exposure to Boreas G15 laser, test group C, at $37\,\mathrm{J\,cm^{-2}}$. (Right) Paper side of same sample.

Film	**Velocity**	**Test Grp. A**	**Test Grp. B**	**Test Grp. C**	**Test Grp. D**
PE	$50\,\mathrm{mm\,s^{-1}}$	$6.6\,\mathrm{J\,cm^{-2}}$	$7.7\,\mathrm{J\,cm^{-2}}$	-	-
PE	$200\,\mathrm{mm\,s^{-1}}$	$6.6\,\mathrm{J\,cm^{-2}}$	$9.6\,\mathrm{J\,cm^{-2}}$	-	-
PE	$1\,\mathrm{m\,s^{-1}}$	-	-	-	-
PP	$50\,\mathrm{mm\,s^{-1}}$	$6.6\,\mathrm{J\,cm^{-2}}$	$6.2\,\mathrm{J\,cm^{-2}}$	-	-
PP	$200\,\mathrm{mm\,s^{-1}}$	$7.9\,\mathrm{J\,cm^{-2}}$	$9.6\,\mathrm{J\,cm^{-2}}$	-	-
PP	$1\,\mathrm{m\,s^{-1}}$	-	-	-	-
AL	$50\,\mathrm{mm\,s^{-1}}$	$0.5\,\mathrm{J\,cm^{-2}}$	$0.5\,\mathrm{J\,cm^{-2}}$	$6\,\mathrm{J\,cm^{-2}}$	$5.2\,\mathrm{J\,cm^{-2}}$
AL	$1\,\mathrm{m\,s^{-1}}$	$0.5\,\mathrm{J\,cm^{-2}}$	$0.6\,\mathrm{J\,cm^{-2}}$	$6.8\,\mathrm{J\,cm^{-2}}$	$5.8\,\mathrm{J\,cm^{-2}}$

TABLE 5.3: Measured ablation thresholds of single-layer films for all tested translation velocities and laser test groups.

variation in ablation threshold with velocity for the plastic films is due to the dependence of ablation behaviour on the number of pulses; a fact confirmed by the lack of material removal under single-pulse conditions at $1\,\mathrm{m\,s^{-1}}$. The ablation process is therefore one by which optical change occurs during the first pulse(s), leading to subsequent absorption and material removal during later pulses. The variation in phase explosion threshold with

velocity for the aluminium film is instead the result of a long-term target temperature rise in the vicinity of the focused spot at low translation speeds. An increase in target temperature reduces the minimum pulse energy required for the surface to reach $0.9T_c$ (Fig. 3.10). For test groups A and B, the low fluence in question at the threshold leads to low average beam power and minimal temperature rise in the sample at $50\text{mm}\,\text{s}^{-1}$. The differences in threshold between $50\text{mm}\,\text{s}^{-1}$ and $1\text{m}\,\text{s}^{-1}$ are therefore minimal, the sample temperature similar in both cases. For test groups C and D, the higher threshold fluence with respect to the previous case results in greater average beam power and target temperature rise at $50\text{mm}\,\text{s}^{-1}$. There are therefore some differences in threshold between $50\text{mm}\,\text{s}^{-1}$ and $1\text{m}\,\text{s}^{-1}$; the target temperature lower in the latter case.

While the Helios IR induced material removal in the PP and PE films at moderate fluence, the Boreas G15 was not capable of inducing short-pulse ablation in either. This indicates a strong dependence of material removal on pulse duration for these films. Laser wavelength is not considered the primary factor in this case, as such dependence would suggest the opposite behaviour; PP and PE exhibit marginally lower transparency to light of wavelength 515nm than that of wavelength 1064nm (Appendix A). An increase in ablation threshold is also observed in most cases for PP and PE with test group B compared to group A, further indicating dependence on pulse duration. The results also indicate that the increase in number of pulses in group B, due to the higher repetition rate, is of less influence than the pulse duration under constant velocity conditions. For aluminium, the Helios IR was found to induce phase explosion at a fluence approximately 10% of that with the green nanosecond source. This indicates a reduction in thermal energy losses during $0.5 - 0.8$ns pulses compared to those during $10 - 12.5$ns pulses. As with the plastic films, laser wavelength is not considered the primary factor, as dependence on this parameter would suggest the opposite behaviour; light of wavelength 515nm is more readily absorbed by aluminium than that of wavelength 1064nm (Appendix A). A slight increase in ablation threshold is observed at $1\text{m}\,\text{s}^{-1}$ with group B compared to group A, further indicating dependence on pulse duration. The results with the Boreas G15, however, display contrary behaviour. A decrease in ablation threshold is observed with an increase in pulse duration. This effect may be due to large long-term sample temperature increases with test group D, where the average beam power is approximately three times greater than that of group C at threshold fluence, due to the higher repetition rate.

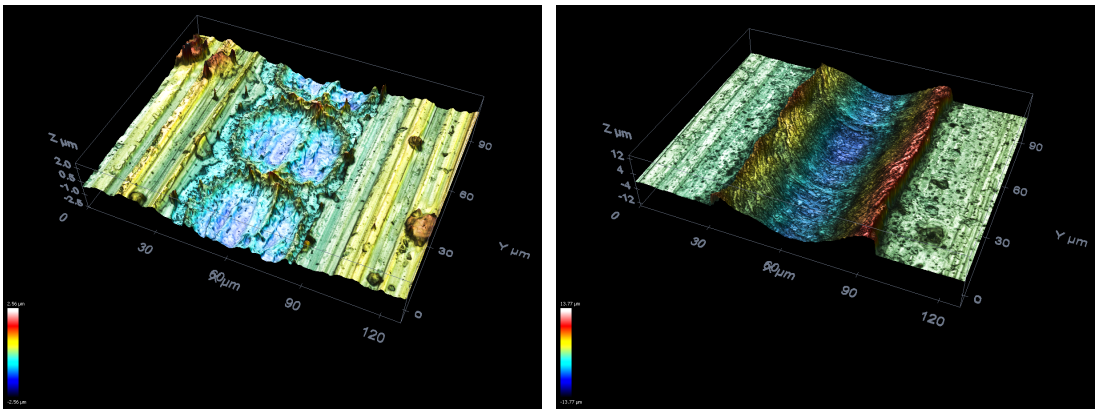

FIGURE 5.9: (Left) 3D profile showing the interaction of single $10\,\mathrm{J\,cm^{-2}}$ pulses, test group *A*, with an aluminium target translating at $1\,\mathrm{m\,s^{-1}}$. (Right) 3D profile showing the interaction of multiple $20\,\mathrm{J\,cm^{-2}}$ pulses, test group *A*, with an aluminium target translating at $50\,\mathrm{mm\,s^{-1}}$. *Images courtesy of S. Carmignato, Laboratorio di Metrologia Geometrica e Industriale, Università di Padova.*

The simulated phase explosion threshold for 515nm laser pulses of duration $10 - 12.5$ns is $5.2 - 5.9\,\mathrm{J\,cm^{-2}}$, whilst that for 1064nm laser pulses of duration $0.5 - 0.8$ns is $1.6 - 1.9\,\mathrm{J\,cm^{-2}}$. The alignment with experimental values in the former case is within 30%. Poor alignment for $0.5 - 0.8$ns pulses is due to limited model accuracy for low fluence pulses of duration $<$ 1ns.

5.4.2 Single-Layer Ablation Depths

The ablation depth is the principle quantitative parameter with which ablative incision or cut efficiency may be determined. A 3D optical profiler was utilised to perform surface analysis of the single-layer samples exposed to both single and multiple pulses. Ablation depth was taken as the difference in measured profile between the lowest section in each cut profile and the level immediately outside the zone of laser interaction. For multiple pulses, ablation depth was measured in a number of sections along the cut axis then averaged. For single pulses, the depth was measured at the lowest section of each crater along the cut axis then averaged. All measurements were averaged across several data points to minimise singularities and experimental error. Nonetheless, some variation in the measured values was observed, primarily due to sample surface roughness. Two profile measurements are presented in Fig. 5.9. *All ablation depth measurements were undertaken by S. Carmignato at the Laboratorio di Metrologia Geometrica e Industriale, Università di Padova.*

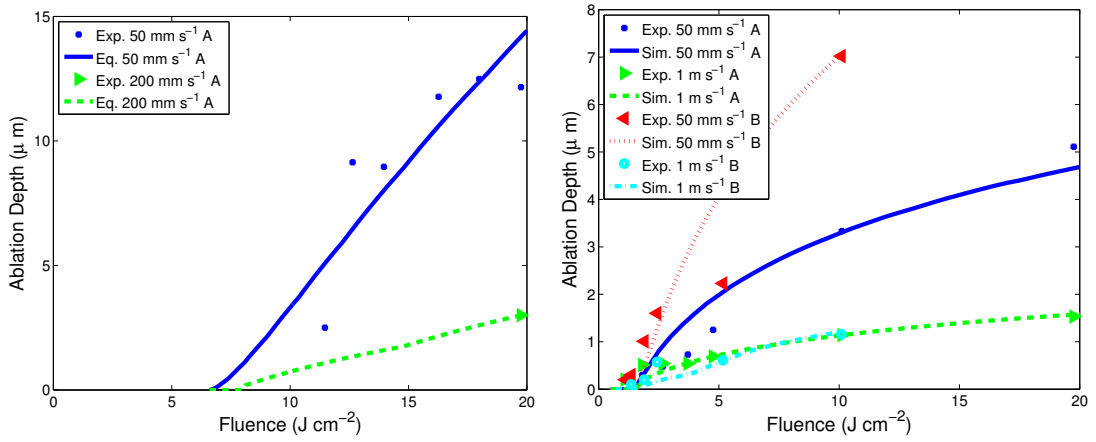

FIGURE 5.10: (Left) Total measured and calculated ablation depth for PE subject to test group *A*. (Right) Total measured and calculated ablation depth for aluminium subject to test groups *A* and *B*. *Experimental depth measurements courtesy of S. Carmignato, Laboratorio di Metrologia Geometrica e Industriale, Università di Padova.*

Figure 5.10 (left) presents the measured and calculated ablation depth of PE as a function of fluence for test group *A*. The following empirical equation has been employed for the calculated ablation depth:

$$d = A \cdot \ln\left(\frac{F}{F_{th}}\right) \tag{5.2}$$

Where d is the ablation depth per pulse, F the fluence, F_{th} the threshold fluence (Tab. 5.3) and A a coefficient derived from experimental data. The theoretical basis of this equation is presented by Lippert [88]. In the present case, the total ablation depth was calculated by summing the values obtained in Eqn. 5.2 *for all pulses* in the fluence distribution given in Eqn. 5.1. Based on the PE ablation depth measurements, coefficient A was calculated as 1.04 and 0.87, respectively, for $50\,\mathrm{mm\,s^{-1}}$ and $200\,\mathrm{mm\,s^{-1}}$. As F_{th} is identical in both cases, the decrease in A with increasing velocity reflects a reduction in ablation efficiency with velocity or, more precisely, with the number of incident pulses. The calculated curves are in reasonable alignment with the experimental data. While interaction was observed with the optical microscope for test group *B*, no measureable ablation depth was obtained with the 3D optical profiler due to low levels of material removal.

Figures 5.10 (right) and 5.11 (left) present the measured and calculated ablation depth of aluminium as a function of fluence for all test groups. The calculated ablation depths per pulse were determined using the simulation presented in Chapter 3. The respective

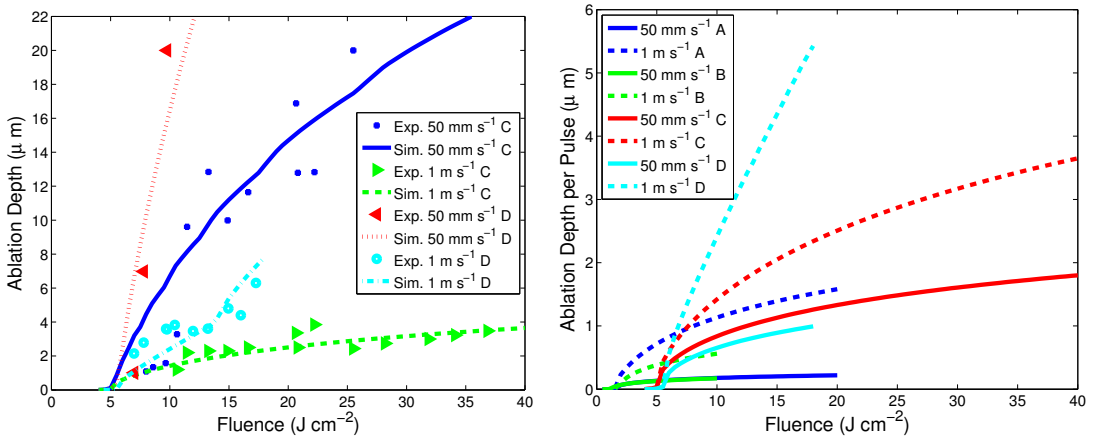

FIGURE 5.11: (Left) Total measured and calculated ablation depth for aluminium subject to test groups C and D. (Right) Calculated ablation depth per pulse for aluminium subject to all test groups. *Experimental depth measurements courtesy of S. Carmignato, Laboratorio di Metrologia Geometrica e Industriale, Università di Padova.*

Test Group	**Velocity**	**Shielding Coefficient (α_{sh})**
A	$50\,\mathrm{mm\,s^{-1}}$	$1.75 \times 10^{7}\,\mathrm{m^{-1}}$
A	$1\,\mathrm{m\,s^{-1}}$	$1.4 \times 10^{6}\,\mathrm{m^{-1}}$
B	$50\,\mathrm{mm\,s^{-1}}$	$1.75 \times 10^{7}\,\mathrm{m^{-1}}$
B	$1\,\mathrm{m\,s^{-1}}$	$4 \times 10^{6}\,\mathrm{m^{-1}}$
C	$50\,\mathrm{mm\,s^{-1}}$	$1.5 \times 10^{6}\,\mathrm{m^{-1}}$
C	$1\,\mathrm{m\,s^{-1}}$	$5.5 \times 10^{5}\,\mathrm{m^{-1}}$
D	$50\,\mathrm{mm\,s^{-1}}$	$2 \times 10^{6}\,\mathrm{m^{-1}}$
D	$1\,\mathrm{m\,s^{-1}}$	0

TABLE 5.4: Shielding coefficients employed in short-pulse simulation (Chapter 3) for the calculated aluminium ablation depths.

shielding coefficients (section 3.1.1), α_{sh}, are given in Tab. 5.4. The total ablation depth was determined by summing the respective values *for all pulses* in the fluence distribution given in Eqn. 5.1. The calculated ablation depths per pulse are presented in Fig. 5.11 (right). The total ablation depth for all test groups is higher at $50\,\mathrm{mm\,s^{-1}}$ than at $1\,\mathrm{m\,s^{-1}}$; however, the calculated ablation depth per pulse is markedly lower. The ablation efficiency is therefore lower for multiple pulses than for single pulses. This is due to shielding of the incident beam by the ablation products, which is reflected by the lower choices of simulated shielding coefficient for the higher velocity tests. Despite the lower threshold fluence of aluminium subject to pulses of duration $< 1\,\mathrm{ns}$, the ablation efficiency is clearly superior with the Boreas G15 for fluences $> 8\,\mathrm{J\,cm^{-2}}$. At $50\,\mathrm{mm\,s^{-1}}$, the test groups with shorter pulse durations for each laser, A and C, lead to greater ablation efficiencies; however, the total ablation depths are lower due to the reduced repetition rate. Despite these differences, the variation in ablation efficiency between

multiple-pulse scenarios is far less pronounced than that between multiple and single-pulse conditions. This has implications for the general model presented in Chapter 4, where the relationship between fluence and ablation depth is assumed to be unaffected by the number of pulses. Provided that multiple-pulse conditions prevail, as is the case for all results presented in Chapter 4, this assumption is therefore reasonable. At $1\,\mathrm{m\,s^{-1}}$, the ablation efficiency of group A is greater than that of group B, while the ablation efficiency of group D is greater than that of group C. The high ablation efficiency of group D may be the result of long-term sample heating, as discussed in section 5.4.1. The simulated ablation depth shows reasonable alignment with the experimental values for all test groups above the ablation threshold.

The measurement of ablation depth was not possible for the PP film, as complete cuts were invoked before measurable ablation depths could be obtained. Complete cuts of this film took place with test group A at velocity $50\,\mathrm{mm\,s^{-1}}$ and fluence $12.5\,\mathrm{J\,cm^{-2}}$, as well as at velocity $200\,\mathrm{mm\,s^{-1}}$ and fluence $18\,\mathrm{J\,cm^{-2}}$.

5.4.3 Single and Multi-Layer Interaction and Cut Widths

The interaction and cut widths are the principle quantitative parameters with which incision or cut quality may be determined. The interaction width is defined within the present section as the maximum of either the optical modification width, crater width or observed melting width, whilst the cut width is defined as the span at which no material is present. Where multi-layer films see large interaction widths in some layers but not in others, the resulting incision or cut is non-uniform throughout the section. Where such differences are visible to the naked eye ($> 300\mu\mathrm{m}$), the process quality is considered poor. The same may be said for large differences between the cut and interaction widths in single-layer films. Minimisation of these differences is of interest for optimisation of cut quality.

Figure 5.12 presents the interaction and cut widths, where observed, of single-layer PE and PP films with test groups A and B. A complete cut of PE was not observed in any of the tests due to its large thickness with respect to the PP film. Above the ablation threshold, the interaction width of PE is of the same order as the beam diameter and rises linearly with fluence for test group A. There is insufficient data to reach such a conclusion for test group B. The interaction width of PP behaves similarly below

the onset of film penetration, at which point a discrete increase in interaction width is observed. Cut widths of 42μm and 51μm are reported for PP at 50mm s^{-1} and 200mm s^{-1}, with test group *A* at fluences of 12.5J cm^{-2} and 18J cm^{-2}, respectively.

The interaction and cut widths, where observed, of single-layer aluminium for all test groups are presented in Fig. 5.13. All interaction curves display logarithmic behaviour, rising sharply at the onset of ablation and less so at high fluence. A reduction in interaction width with velocity may be seen, particularly for fluences > 15J cm^{-2}. Cut widths of 7μm are reported at 50mm s^{-1} for test groups *C* and *D* with fluences of 25.5J cm^{-2} and 7.8J cm^{-2}, respectively.

Figure 5.14 presents the experimental and calculated interaction and cut widths, where observed, of all layers of Triplex for test group *C*. The calculated widths have been determined using the simulation presented in Chapter 4. At low fluences, interaction is only seen in the aluminium layer. At the onset of PP layer removal, the interaction and cut widths of this layer rise quickly, becoming much larger than those of the aluminium layer at high fluence. A full cut of all layers is seen at 50mm s^{-1} for fluences > 25J cm^{-2}, the PP layer cut width approximately 10 times that of the aluminium layer. These cuts are of poor quality to the naked eye. The simulated cut widths of both layers, where present, show reasonable alignment with the experimental results. The calculated interaction widths are underestimated in almost all cases. For PP, this is the result of difficulty in defining the interaction width experimentally; the observed width may not have corresponded precisely to the melted region. For aluminium, this is the result of redeposited material at the edges of the crater that effectively increased the measured interaction width. The simulated onset of interaction in the aluminium layer is at a lower fluence than the experimental result, due to the difference in calculated and experimental threshold fluences for aluminium (section 5.4.1).

The respective interaction and cut widths, where observed, of the same material with the Helios IR at maximum power are presented in Fig. 5.15. Under no conditions is a full cut observed; however, the cut and interaction widths of the PP layer are greater than those seen with test group *C* at both 50mm s^{-1} and 200mm s^{-1}. This is due to the lower ablation efficiency of aluminium using the Helios IR laser.

Figure 5.16 (left) presents the experimental and calculated interaction and cut widths, where observed, of all layers of Alufoil at 50mm s^{-1} with test group *C*. It should be noted

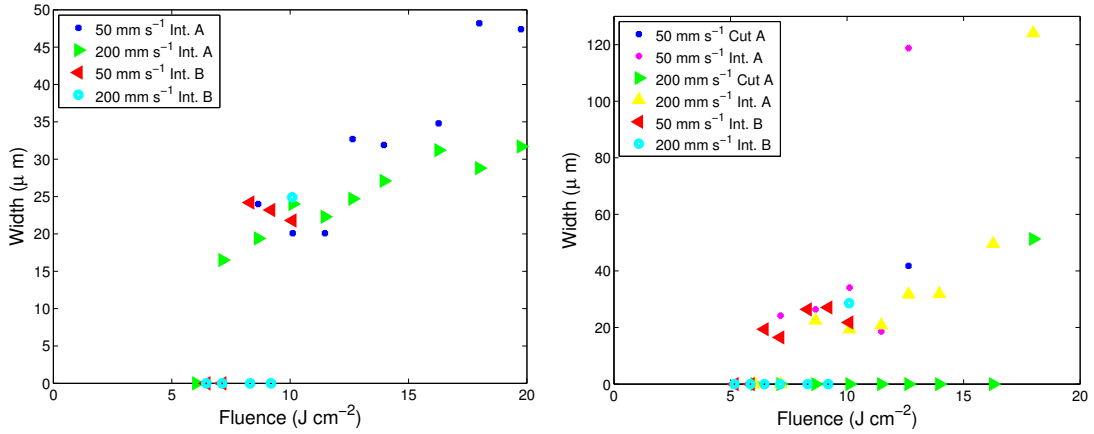

FIGURE 5.12: Interaction and cut widths of (left) PE and (right) PP subject to laser radiation of test groups A and B.

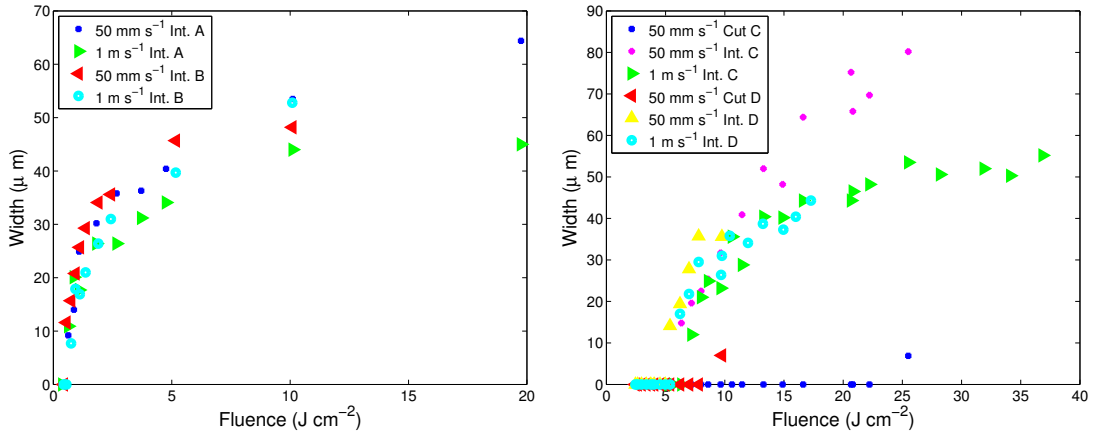

FIGURE 5.13: Interaction and cut width of aluminium subject to laser radiation of (left) test groups A and B and (right) C and D.

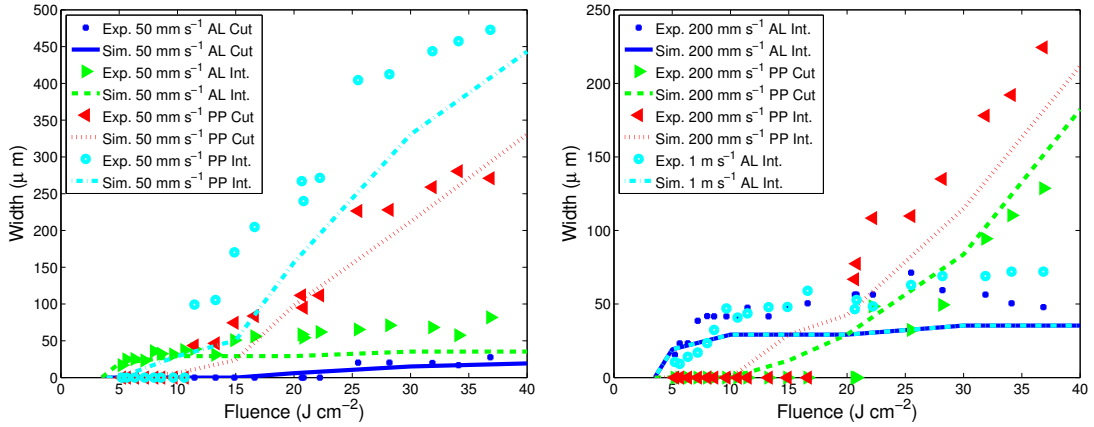

FIGURE 5.14: Interaction and cut widths of Triplex subject to laser radiation of test group C.

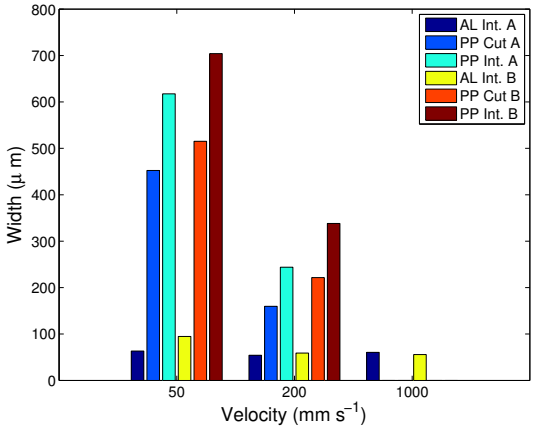

FIGURE 5.15: Interaction and cut widths of Triplex subject to laser radiation of test groups A and B.

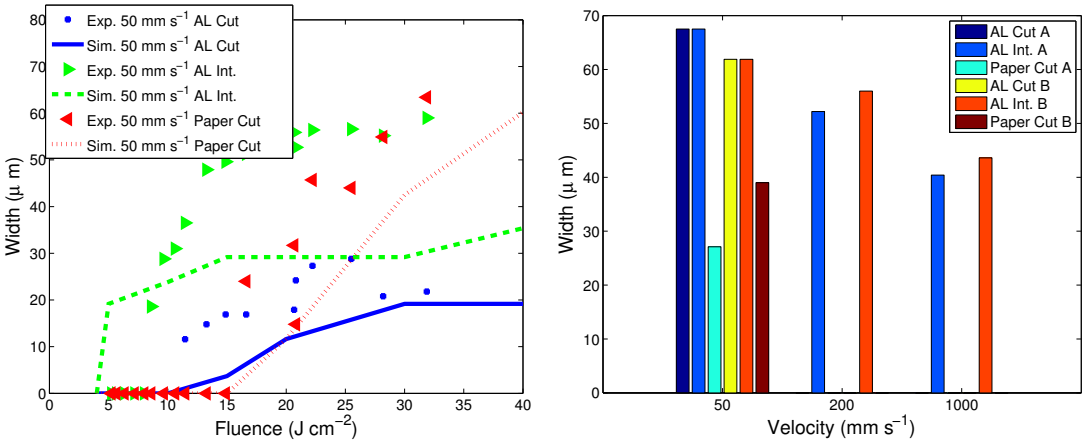

FIGURE 5.16: Interaction and cut widths of Alufoil subject to laser radiation of (left) test groups C and (right) A and B.

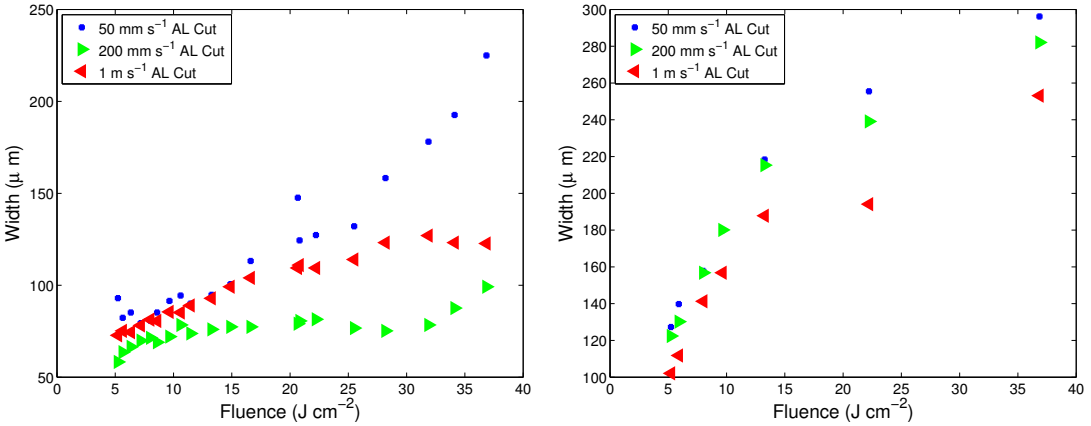

FIGURE 5.17: Interaction and cut widths of (left) Duplex and (right) Metallised Paper subject to laser radiation of test group C.

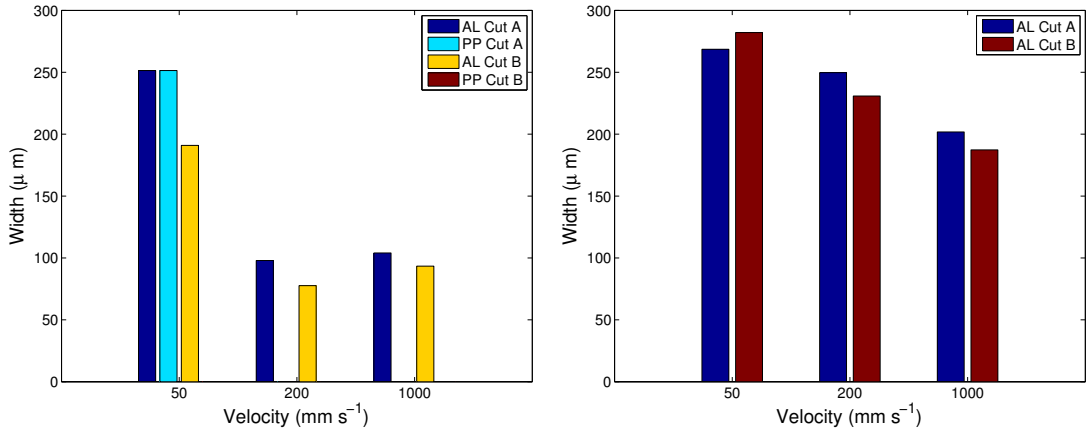

FIGURE 5.18: Interaction and cut widths of (left) Duplex and (right) Metallised Paper subject to laser radiation of test groups A and B.

that the cut width of the paper layer was irregular within the range ±50%. Negligible charring was observed and, as such, the interaction width was taken to be equal to the cut width. The characteristic behaviour of this film is similar to that of Triplex. Interaction is seen in the aluminium layer only at low fluences. At the onset of paper layer removal, the cut width of this layer rises in a linear fashion, approaching the aluminium layer interaction width. The simulated cut widths of both layers, where present, are indicative of system behaviour but are ultimately below the measured values in all cases. The irregular cut width of the paper layer accentuates the differences between the simulated and experimental widths. Furthermore, the natural inhomogeneity of paper leads to difficulties in defining material properties for the simulation. It is also possible that separation of the cut edges lead to larger measured values. The onset of complete film penetration and that of cut in the paper layer are, however, accurately predicted by the model.

The respective interaction and cut widths, where observed, of the same material with the Helios IR at maximum power are presented in Fig. 5.16 (right). A full cut is observed at 50mm s^{-1}, the cut width of the paper layer approximately half that of the aluminium layer. These cuts are of good quality to the naked eye. At all other velocities the film behaves as single-layer aluminium.

The aluminium layer cut widths of Duplex and Metallised Paper subject to test group C are presented in Fig. 5.17. In all cases, the cut width is much larger than the laser spot size and increases with fluence. For Duplex this increase is linear, whilst for Metallised Paper it is logarithmic. Interestingly, the aluminium layer cut width of Duplex is lower

at $200\text{mm}\,\text{s}^{-1}$ than it is at $1\text{m}\,\text{s}^{-1}$. This is also reflected in the maximum power results with test groups A and B, presented in Fig. 5.18. A full cut of Duplex is reported at $50\text{mm}\,\text{s}^{-1}$ with test group A, the cut widths of both the PP and aluminium layers of the same value. Under no conditions is a full cut observed in Metallised Paper. The elevated aluminium layer cut width with respect to the beam diameter for both Duplex and Metallised Paper implies the presence of lateral heat transfer in the single layer. This effect is not accounted for in the simulation presented in Chapter 3, which assumes all layers are of the same temperature between laser pulses.

5.5 Concluding Remarks

The present experimental investigation provides some practical conclusions regarding the laser incision and cut of packaging films. There is no doubt that high quality processing of such materials may be performed. It has been found that 0.5ns pulsed IR laser irradiation at relatively low fluence levels can be used to efficiently remove material in single-layer PP and PE films at velocities in the range $50 - 200\text{mm}\,\text{s}^{-1}$, with a full cut of PP presenting an interaction width of just $\sim 120\mu\text{m}$. While such laser parameters were also found to reduce the ablation threshold of aluminium by one order of magnitude with respect to longer pulses, the efficiency of material removal for fluences $> 8\text{J}\,\text{cm}^{-2}$ was found to be superior with green $10 - 12.5$ns laser pulses. The effectiveness of either exposure type for the cut and incision of multi-layers depended on the thickness of the aluminium layer. Triplex and Alufoil multi-layer structures with aluminium of thickness 9μm and 7μm, respectively, were processed effectively with the green laser, whilst a Duplex multi-layer structure with aluminium of thickness $< 0.1\mu$m required pulses of duration 0.5ns to achieve a complete cut via direction ablation of the PP layers. A Metallised Paper multi-layer structure with aluminium of thickness $< 0.1\mu$m could not be cut by either source due to lack of absorption by the paper layer. The mechanism of material removal in each case was governed by the degree of thermal energy transfer from the aluminium layer to the others.

Verification of both the single-pulse ablation model (Chapter 3) and the general simulation (Chapter 4) has been undertaken. In former case, optimum choice of the simulated shielding coefficient lead to good alignment between the calculated and experimental ablation depths of aluminium for both single and multiple-pulse exposures. Subsequently,

the model allowed comparison of the ablation depths per pulse under these conditions. The ablation efficiency was found to be higher for single pulses than for multiple pulses, whilst the rate of change in this parameter was less pronounced at higher pulse numbers. This observation has implications for the general simulation, which assumes that the ablation depth per pulse is independent of the number of pulses. The simulated phase explosion threshold was found to be within 30% of the experimentally observed values for $10 - 12.5$ns pulses. Poor alignment of this parameter was observed for pulses of duration $0.5 - 0.8$ns due to a reduction in model accuracy for low fluence pulses of duration $<$ 1ns. For the general simulation, alignment between simulation and experimental values of layer cut widths was found to be reasonable for Triplex. For Alufoil, the simulated results were indicative of the experimental system behaviour, accurately predicting the onset of paper layer removal and complete film penetration. The calculated cut widths in this case were, however, below the measured values. This was partly due to the irregular experimental cut width of the paper layer, but also due to difficulty in specifying the simulated material properties for this layer. Nonetheless, the simulation has been shown to provide a reasonable approximation of the real-world scenario.

Chapter 6

Overview and Future Work

The present thesis has established a theoretical basis and modelling approach for industrial laser processing of thin single and multi-layer films. The phenomena taking place in such films during laser exposure are complex and strongly dependent on the thickness and composition of the component materials. The effects of these phenomena have been separated and simplified, leading to a process simulation that replicates the laser incision and cut of packaging films. Single-pulse ablation depth and optical absorption data has been obtained for metals via a numerical model that accounts for temperature dependent material properties and simulates the onset and progression of vaporisation and phase explosion. This data has been subsequently utilised within a two-dimensional heat flow simulation for arbitrary thin multi-layer films, which accounts for both short-pulse effects and normal vaporisation due to heating on a longer time-scale. Both the single-pulse model and the complete simulation have been verified by experimental results divulged here within and, in the former case, with data published in literature. While a general analysis method has been developed and a number of useful conclusions presented for specific types of packaging film, the breadth of this field leads to a number of directions in which the study could be carried forward and optimised for industrial application.

6.1 Short-Pulse Laser Ablation

The model presented in Chapter 3 for the short-pulse laser ablation of metals has allowed accurate prediction of the ablation depth of metals exposed to nanosecond laser pulses. Furthermore, the calculation has been utilised to derive the dependence of the phase explosion threshold on laser parameters, as well as the relationships between the initial work piece temperature and the ablation depth and absorbed fluence. The model has been verified by four different groups of published experimental ablation data for aluminium, as well as several test groups undertaken as part of the present work. An extensive investigation into the phase explosion threshold has demonstrated dependence of this parameter on the laser wavelength, pulse duration and sample thickness. It has been shown that the phase explosion threshold of aluminium is an increasing function of pulse duration and wavelength in the region UV–NIR, while its value decreases with reduced sample thickness for thicknesses less than $\sim 1\mu$m. These results have practical ramifications for industrial applications, as the cut efficiency and quality of multi-layer films is dependent on the ablation efficiency, which is highest for fluences near the threshold.

The accuracy of the short-pulse model is due to the introduction of a number of improvements over previously published models for the same or similar processes (Peterlongo, Miotello & Kelly [58], Bulgakova, Bulgakov & Babich [60], Porneala & Willis [61], Gragossian, Tavassoli & Shokri [64]). A numerical optical calculation has been utilised, based on a matrix method for electromagnetic plane wave propagation in multi-layer media (Centurioni [115]). This has lead to a more accurate representation of the dielectric zone and the optical absorption profile of the target. Additionally, a simulated "shielding coefficient" has been introduced to account for scattering, reflection and absorption by the phase explosion ablation products, analogous to the way in which other studies have used such a coefficient for optical absorption in plasma (Singh & Viatella [116]). Selection of the shielding coefficient for particular cases has been undertaken by aligning the simulated and measured ablation depth at arbitrary fluences above the ablation threshold. The dependence of simulated results on experimental data is a limitation of the single-pulse model and, as a result, the complete process simulation presented in Chapter 4. Nonetheless, the accuracy of the shielding coefficient over the tested fluence range proves it to be a computationally light approach for extrapolating data generated by more complex methods. The addition of a plume dynamics model to the present

approach is an obvious direction for future work, allowing calculation of the ablation depth in a purely theoretical manner.

The focus on aluminium when comparing experimental and simulated results was due, in part, to its importance in the packaging industry, but also to the availability of published physical and experimental ablation depth data. The short-pulse model is general and could be applied to other metals and semi-conductors that must be processed in industrial settings. For the most part, these extensions would require the measurement or estimation of high-temperature material properties, as is undertaken by Wu & Shin [119] for aluminium. On the other hand, the single-pulse model could be utilised to derive these parameters based on experimental ablation data, as proposed by Bulgakova & Bulgakov [59].

Nanosecond pulsed laser ablation of bulk metals is of increasing importance in industrial settings due to the reduced heat-affected zone (HAZ) and increased efficiency of material removal with this process. Reduction in the cost of nanosecond pulsed laser sources has also contributed to their uptake. It is clear that the physical processes taking place do not lead to linear optical absorption in this case (section 3.2.4), as is often assumed when processing with continuous-wave (CW) sources. The short-pulse model, which is not limited to thin-films, could greatly improve the accuracy of industrial laser processing simulations.

Experimentally, the investigation presented in Chapter 4 has highlighted some of the characteristic differences between irradiation of single-layer films with a laser of wavelength 1064nm and pulse duration $0.5-0.8$ns and that with a laser of wavelength 515nm and pulse duration $10-12.5$ns. The phase explosion ablation threshold of aluminium has been found to be lower in the former case due to the reduced pulse duration; in line with conclusions drawn by the short-pulse ablation model presented in Chapter 3. The ablation efficiency, however, has been found to be greater for irradiation at a wavelength of 515nm, due to a reduction in incident beam shielding by the ablation products. The data presented in this study has widened the laser parameter range for which the nanosecond pulsed laser ablation of aluminium is reported experimentally (Stafe *et al.* [68], Porneala & Willis [67], Colina *et al.* [66], Horn, Guillong & Günther [69]). Ablation of single-layer plastic films has been shown to be possible with pulses of duration 0.5ns, while both the ablation threshold and efficiency have been found to be functions of the

number of pulses. The data presented for plastic films widens the parameter range for which the nanosecond pulse laser ablation of polyethylene (PE) and polypropylene (PP) is reported experimentally (Sohn *et al.* [92], Leme *et al.* [93]).

The directions for future experimental work in this field are as numerous as the number of available laser sources and packaging materials. In light of the experimental results, the use of laser pulses in the duration range $0.1 - 1$ns with a wavelength of 515nm would be a logical starting point for investigation into a universal laser source capable of efficiently cutting both metallic and plastic films in the packaging industry. Such a source would allow ablation of plastics, due to the pulse duration, as well as efficient incision of aluminium, due to the wavelength. This pulse duration range could potentially avoid the cost increases associated with ultrashort-pulse laser sources. As an alternative, an investigation into laser irradiation in the wavelength range $1 - 2\mu$m could offer opportunities for higher optical absorption in organic layers, particularly paper. This material could not be processed as a single layer in the present work; however, its absorption profile shows a small peak at 1500nm (Appendix A). Lasers operating in this range offer the same advantages as other short wavelength sources over the CO_2 laser, which is typically employed for organic materials.

6.2 Laser Processing of Thin Single and Multi-Layer Films

The model presented in Chapter 2 has established the principles of CW laser processing of thin multi-layer films. While a general approach for dealing with such materials has been introduced, it has yielded very approximate figures compared to more complex approaches as a result of lateral heat conduction losses in films containing metallic layers. The general simulation presented in Chapter 4, however, accounting for such losses, has been shown to provide a good representation of packaging material response to CW and pulsed laser irradiation. It has allowed observation of transient effects during the early stages of laser exposure, as well as calculation of the steady state interaction and cut widths of individual layers for quantitative prediction of process quality. In general, the cut efficiency and quality of multi-layer films has been found to be strongly influenced by the presence and thickness of metallic layers. This is the result of their influence on the optical absorption and thermal conductivity of the complete multi-layer structure. The model has been verified by experimental interaction and cut width data for two packaging

films, Triplex and Alufoil, presented in Chapter 5. Alignment between simulated and experimental results is reasonable. The further theoretical investigation into Triplex and Alufoil has lead to some useful conclusions regarding the process parameters that drive their cut quality. With increasing velocity, process quality has been shown to improve by increasing the laser repetition rate instead of the pulse fluence. This result is a consequence of the higher ablation efficiency of aluminium near the phase explosion threshold, leading to fast material removal while minimising energy deposition in the film. It has also been shown that at high pulse fluences, where the ablation efficiency of metals is lower, the aluminium layers of both Triplex and Alufoil reach their vaporisation temperatures before a full cut by short-pulse ablation takes place. This leads to large interaction and cut widths in the other layers and a general reduction in process quality. A theoretical investigation into the effects of focused beam spot size has also shown that an increase in this parameter leads to a worsening of process quality for both Triplex and Alufoil.

The general simulation is bounded by the thin-film approximation, which requires the combination of layer properties to form an equivalent material (2.3.1). This simplification is necessary for reduction of the thermal problem to two dimensions, maintaining model complexity within reasonable limits for industrial application. Where very thin metallic layers of thickness $< 0.1\mu$m are combined with thicker non-conductive layers, it has been shown experimentally in Chapter 5 that the cut width of these metallic layers is much greater than the beam diameter. This suggests that thermal conduction within the metallic layer leads to its removal before the film temperature is constant throughout its depth. Investigation into the dependence of temperature homogeneity on layer combination is therefore a possible direction for further study.

The general process simulation is not limited to packaging films. The theoretical model could be utilised for other industrial applications involving thin multi-layer films. Of recent, a number of experimental works have studied the use of pulsed laser irradiation for the improvement of thin-film photovoltaic cell efficiency and the reduction of production costs (Selleri *et al.* [105, 106], Hernandez *et al.* [107], Gečys *et al.* [108], Schoonderbeek *et al.* [109], Bovatsek *et al.* [110]). Development and application of the approach presented in Chapter 4 could lead to a strong theoretical basis for these works with which further process optimisation could take place. The choice of nanosecond-pulsed laser irradiation in the present work has been primarily driven by cost considerations

for application within the packaging industry. In light of the quality improvements seen with picosecond laser sources for thin-film photovoltaic cell production, it is likely that a modified short-pulse modelling approach would be necessary for application of the general model in this field.

The experimental investigation presented in Chapter 5 has provided interaction and cut width data for laser processing of four multi-layer packaging films. It has been shown that, in general, high quality incisions and cuts are possible with optimum selection of laser parameters. For Triplex and Alufoil films, with aluminium layers of thickness $7 - 9\mu$m, pulses of duration $10 - 12.5$ns and wavelength 515nm have been found to be well-suited for incision and full cut procedures. For Duplex and Metallised Paper films, with aluminium of thickness $< 0.1\mu$m, pulses of duration 0.5ns have instead been found to be more appropriate. It has also been shown that the cut of paper layers with these laser sources is only possible via conduction from a metallic layer. As such, Metallised Paper could not be cut by either source due to fast removal of the absorbing substrate. Given the wide range of possible packaging materials and laser sources, there is large scope for further experimental investigation in this field, particularly where optimisation of specific procedures is of interest. As noted previously, use of laser pulses in the duration range $0.1 - 1$ns with a wavelength of 515nm would be a logical starting point for investigation into a universal laser source capable of cutting films typical of the packaging industry.

The number of experimental tests undertaken in the present work has been limited by the materials and laser sources made available during the course of the project. A more complete experimental investigation into the accuracy of the full simulation over the complete parameter range considered theoretically in Chapter 4 is scope for future work. Nonetheless, the process simulation developed here within is general and, to the author's knowledge, the most complete representation of packaging film laser processing developed to date.

Appendix A

Additional Material Properties

The following section contains relevant material properties of some typical packaging materials: aluminium (AL), polyethylene (PE), polypropylene (PP) and paper.

A.1 Optical Properties

The optical properties of aluminium are discussed extensively by Palik (ed.) [42] for wavelengths in the range 17nm $-$ 32μm. Likewise, the optical properties of PE are discussed by Palik (ed.) [43] for wavelengths in the range 13nm $-$ 2mm. As part of the present work, optical transmission and reflectance measurements of PE have been conducted over the wavelength range 250 $-$ 1700nm with an Avantes spectrometer, mounted with an integrating sphere, by the Laboratorio di Micro e Submicro Tecnologie Abilitanti dell'Emilia Romagna, Consiglio Nazionale delle Ricerche (Summonte & Menin [123]). These values have been taken in preference to other published values. Optical transmission and reflectance measurements of PP have been conducted over the wavelength range 250nm $-$ 25μm with an Avantes spectrometer, mounted with an integrating sphere, and a FTIR Nicolet by the same research group (Summonte & Menin [123]). Optical transmission and reflectance measurements of standard office paper for wavelengths in the range 250nm $-$ 2.5μm have been conducted by the author with a Perkin Elmer Lambda 19 UV/Vis/NIR, mounted with an integrating sphere, from which the complex refractive index has been calculated. These values are considered approximate due to

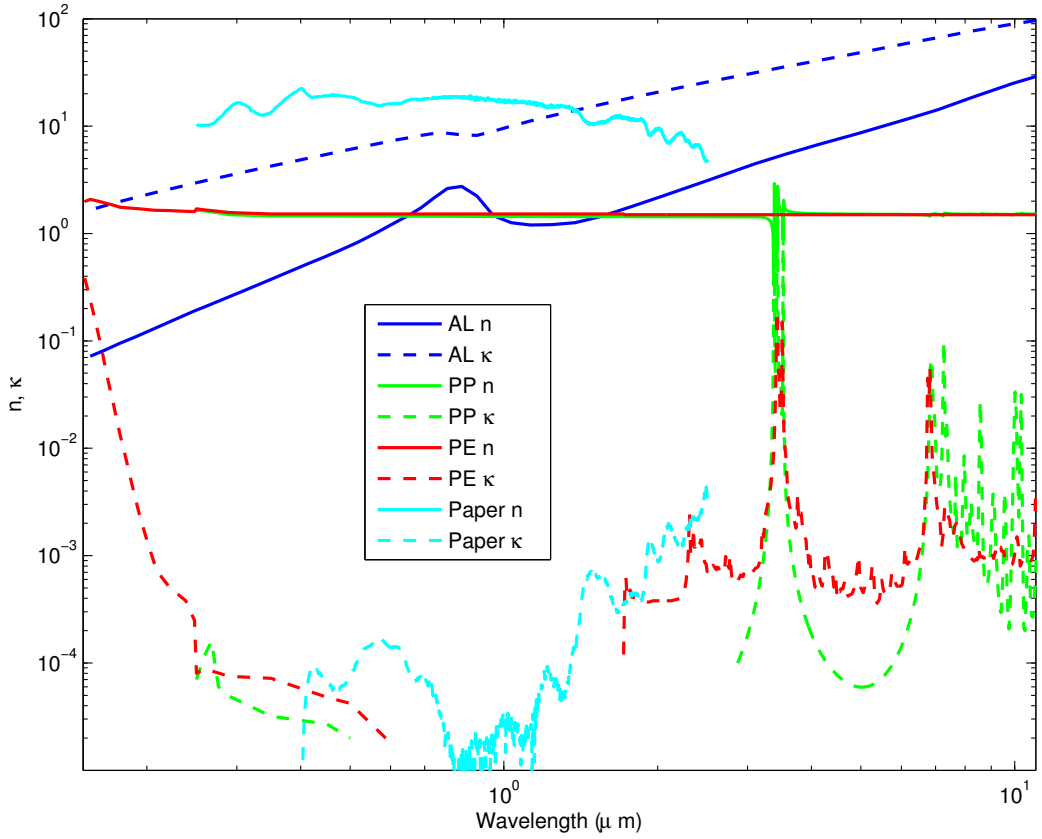

FIGURE A.1: Real (n) and imaginary (κ) parts of the refractive index of aluminium, PP, PE and paper.

the natural inhomogeneity of paper. The real (n) and imaginary (κ) parts of the refractive index for these materials, where available, are presented in Fig. A.1 over the range $150\text{nm} - 11\mu\text{m}$, encompassing all commercially available lasers of interest to the present application. A break in the curve for κ represents a near-zero value.

A.2 Other Physical Properties

In general, the physical properties of aluminium depend on the temperature and the quantity of alloying elements. Constant solid and liquid values have been approximated based on the data presented by Hatch (ed.) [124]. The physical properties of PE and PP depend on the temperature, density and percentage crystallinity of the sample. Based on the work of Kurek *et al.* [125], the crystallinity of PE and PP packaging films have been taken as $\sim 30\%$ and $\sim 45\%$, respectively. The corresponding melting temperatures and enthalpies of fusion are given within the same study. The density of low-density polypropylene is given by Passaglia & Kevorkian [126], together with the specific heat

Physical Property	**AL**	**PE**	**PP**	**Paper**
Thermal Conductivity, Solid ($\mathrm{W\,m^{-1}\,K^{-1}}$)	220	0.32	0.17	0.06
Thermal Conductivity, Liquid ($\mathrm{W\,m^{-1}\,K^{-1}}$)	100	0.32*	0.17*	–
Density* ($\mathrm{kg\,m^{-3}}$)	2700	914	860	800
Specific Heat Capacity, Solid ($\mathrm{J\,kg^{-1}\,K^{-1}}$)	904	2300	2100	1340
Specific Heat Capacity, Liquid ($\mathrm{J\,kg^{-1}\,K^{-1}}$)	904*	2300*	2500	–
Melting Temp. (K)	923	382	441	–
Vaporisation / Degradation Temp. (K)	2792	423	473	655
Enthalpy of Fusion ($\mathrm{J\,kg^{-1}}$)	390×10^3	90×10^3	89×10^3	–
Enthalpy of Vaporisation ($\mathrm{J\,kg^{-1}}$)	10.8×10^6	–	–	–

TABLE A.1: Material properties of aluminium, PP, PE and paper. *Assumed equal for solid and liquid states.

capacity as a function of temperature. The density of low-density polyethylene is given by Kutz (ed.) [127], while the specific heat is given by Askeland, Fulay & Wright [128]. The enthalpies of vaporisation of both PE and PP have been taken as zero, as they are subject to thermal degradation. The temperature at which this takes place in each case has been based on the values given by Beyler & Hirschler [129] for thin PE and PP samples in the presence of oxygen. In light of the low density and crystallinity of plastic wrapping films, the thermal conductivity of both plastics has been taken as the lowest values given by Maier & Calafut [130]. The density of paper has been estimated based on the dimensions and weight of a ream of standard $80\mathrm{g\,m^{-2}}$ office paper. Shivadev [131] represents the thermal degradation of paper by two competitive first-order reactions with Arrhenius kinetics. That with the highest pre-exponential factor is considered relevant to the present application, due to the short exposure time of laser irradiation. As such, the degradation temperature is taken as the minimum temperature for this reaction: 655K. As with the plastic films, the enthalpy of vaporisation has been taken as zero due to thermal degradation. Other physical properties for paper are given by Ashby [132].

A summary of material properties is presented in Tab A.1 for aluminium, PE, PP and paper. Where temperature dependent values are present in literature, constants have been approximated in the present work for solid and liquid states. Unless otherwise stated, these values are utilised for the results presented in Chapters 2 to 4.

Appendix B

MATLAB Scripts

The following section contains MATLAB scripts for the models presented in Chapters 2 to 4. Model-specific scripts are in sections B.1-B.3 and those common to all simulations are in section B.4. The reduced material file "Aluminium.m" is provided in section B.4.4 as an example of physical property allocation within each input file.

B.1 One-Dimensional Steady State Model

B.1.1 Laser.m

```
%%%%%%%%%%%%%%%%%%%%%%%%
%%%%% DESCRIPTION %%%%%
%%%%%%%%%%%%%%%%%%%%%%%%

% One-dimensional steady state model for continuous-wave laser cutting of thin single and multi-layer films.
% Adrian Lutey, University of Bologna, 2013


%%%%%%%%%%%%%%%%%%%
%%%%% INPUTS %%%%%
%%%%%%%%%%%%%%%%%%%

clear
Input


%%%%%%%%%%%%%%%%%%%%%%%%%%%%%%%%%%%
%%%%% CALCULATION CONSTANTS %%%%%
%%%%%%%%%%%%%%%%%%%%%%%%%%%%%%%%%%%

% Physical constants (SI units)
c=299792458;                    % Speed of light in free space
mu00=4e-7*pi;                   % Permeability constant
omega=2*pi*c/(lambda0*1e-6);    % Angular frequency
e0=8.854187817e-12;             % Vacuum permittivity

% Absorption & heat coefficients. Proceed by updating molten and removed
% layers in order of melting and vaporisation temperatures.
q20=ones(1,M-2);    % Layer present
q19=ones(1,M-2);    % Layer solid
m=zeros(1,2*M-4);   % Melting / vaporisation record
Cp=Cps;             % Specific heat capacity initially that of solid
K=Ks;               % Thermal conductivity initially that of solid

% Intensity
IEinc=2*PEinc/pi/(w0*1e-6)^2;
IMinc=2*PMinc/pi/(w0*1e-6)^2;
```

```
for o=1:2*M-4

    % Optical absorption
    Optics
    IABSEq(o)=sum(IABS);

    % Equivalent material properties
    ht(o)=sum(h(2:M-1));
    Kt(o)=sum(K(1:M-2).*h(2:M-1))/ht(o);
    Cprhot(o)=sum(Cp(1:M-2).*rho(1:M-2).*h(2:M-1))/ht(o);
    Ast(o)=-V*Cprhot(o)*1000/Kt(o);

    % Find next lowest melting or vaporisation temperature
    TT=9e9;
    for i=1:M-2
        if q20(i)==1 && Tv(i)<TT
            m(o)=i;
            TT=Tv(i);
        end
        if q19(i)==1 && Tm(i)<TT
            m(o)=i;
            TT=Tm(i);
        end
    end

    % Remove layer of next lowest vaporisation temperature and update
    % properties
    if min(abs(m(o)-m(1:o-1)))==0
        COHERENT(m(o))=0;
        COHERENT(m(o)+1)=0;
        n(m(o)+1)=1;
        kappa(m(o)+1)=0;
        K(m(o))=0;
        rho(m(o))=0;
        Cp(m(o))=0;
        h(m(o)+1)=0;
        q20(m(o))=0;
    else
        Cp(m(o))=Cpl(m(o));
        K(m(o))=Kl(m(o));
        q19(m(o))=0;
    end
end

% Reset material properties
Input


%%%%%%%%%%%%%%%%%%%%%%%%%%%%%%%%%
%%%%% TRANSITION LOCATIONS %%%%%
%%%%%%%%%%%%%%%%%%%%%%%%%%%%%%%%%

% Reset coefficient, coordinate and temperature matrices
C=zeros(itmax,4*M-8);
xxx=zeros(itmax,dstep*(2*M-4));
T=zeros(itmax,dstep*(2*M-4));

% Transition energies
for o=1:4*M-8
    % Heat to first melting temperature
    if o==1
        X(o)=(Tm(m((o+1)/2))-Ta)*Cprhot((o+1)/2)*1000*ht((o+1)/2)*1e-6*V;
        TT=Tm(m((o+1)/2));
    % First layer melting
    elseif o==2
        X(o)=X(o-1)+Hf(m(o/2))*1000*rho(m(o/2))*h(m(o/2)+1)*1e-6*V;
    elseif mod(o,2)==0
    % Layer vaporising
        if min(abs(m(o/2)-m(1:o/2-1)))==0
            X(o)=X(o-1)+Hv(m(o/2))*1000*rho(m(o/2))*h(m(o/2)+1)*1e-6*V;
        % Layer melting
        else
            X(o)=X(o-1)+Hf(m(o/2))*1000*rho(m(o/2))*h(m(o/2)+1)*1e-6*V;
        end
    % Heat to vaporisation
    elseif min(abs(m((o+1)/2)-m(1:(o+1)/2-1)))==0
        X(o)=X(o-1)+(Tv(m((o+1)/2))-TT)*Cprhot((o+1)/2)*1000*ht((o+1)/2)*1e-6*V;
        TT=Tv(m((o+1)/2));
    % Heat to melting
    else
        X(o)=X(o-1)+(Tm(m((o+1)/2))-TT)*Cprhot((o+1)/2)*1000*ht((o+1)/2)*1e-6*V;
        TT=Tm(m((o+1)/2));
    end
end

% Evaluation of transition points
% Main time loop
for IT=1:itmax;

    % Initial transition locations
    if IT==1

        % Final transition location
        x(IT,2*M-4)=erfinv(1-2*sqrt(2/pi)*X(size(X,2)-1)/IABSEq(1)/(w0*1e-6))*(w0*1e-6)/sqrt(2);
        if isnan(x(IT,2*M-4))==1 || x(IT,2*M-4)<-plotw*2*w0*1e-6
            x(IT,2*M-4)=-plotw*2*w0*1e-6;
```

```
        end

        % Termination location
        x(IT,2*M-3)=erfinv(1-2*sqrt(2/pi)*X(size(X,2))/IABSEq(1)/(w0*1e-6))*(w0*1e-6)/sqrt(2);
        if isnan(x(IT,2*M-3))==1 || x(IT,2*M-3)<-plotw*2*w0*1e-6
            x(IT,2*M-3)=-1.2*plotw*2*w0*1e-6;
        end

    % Transition locations based on previous time-step temperature
    % distribution
    else

        for o=1:2*M-5
            x(IT,o)=xxx(IT-1,1);
            for j=1:size(xxx(IT-1,:),2)
                if o==1 && T(IT-1,j)>=Tm(m(o))
                    if j==size(xxx(IT-1,:),2) || abs(T(IT-1,j)-Tm(m(o)))<abs(T(IT-1,j+1)-Tm(m(o)))
                        x(IT,o)=xxx(IT-1,j);
                    else
                        x(IT,o)=xxx(IT-1,j+1);
                    end
                elseif o>1
                    if min(abs(m(o)-m(1:o-1)))==0 && T(IT-1,j)>=Tv(m(o))
                        if j==size(xxx(IT-1,:),2) || abs(T(IT-1,j)-Tv(m(o)))<abs(T(IT-1,j+1)-Tv(m(o)))
                            x(IT,o)=xxx(IT-1,j);
                        else
                            x(IT,o)=xxx(IT-1,j+1);
                        end
                    elseif min(abs(m(o)-m(1:o-1)))~=0 && T(IT-1,j)>=Tm(m(o))
                        if j==size(xxx(IT-1,:),2) || abs(T(IT-1,j)-Tm(m(o)))<abs(T(IT-1,j+1)-Tm(m(o)))
                            x(IT,o)=xxx(IT-1,j);
                        else
                            x(IT,o)=xxx(IT-1,j+1);
                        end
                    end
                end
            end

            % Absorbed energy up to second-last transition point
            if o==1
                J(IT)=1/2*sqrt(pi/2)*w0*1e-6*IABSEq(1)*(1-erf(sqrt(2)*x(IT,1)/(w0*1e-6)));
            else
                J(IT)=J(IT)+1/2*sqrt(pi/2)*w0*1e-6*IABSEq(o)*(erf(sqrt(2)*x(IT,o-1)/(w0*1e-6))-erf(sqrt(2)*x(IT,o)/(w0*1e-6)));
            end
            if isnan(x(IT,o))==1 || x(IT,o)<-plotw*2*w0*1e-6
                x(IT,o)=-plotw*2*w0*1e-6;
            end

        end

        % Final transition location
        x(IT,2*M-4)=erfinv(erf(sqrt(2)*x(IT,2*M-5)/(w0*1e-6))-2*sqrt(2/pi)*(X(size(X,2)-1)-J(IT))/IABSEq(2*M-4)/(w0*1e-6))*(w0*1e-6)/sqrt(2);
        if isnan(x(IT,2*M-4))==1 || x(IT,2*M-4)<-plotw*2*w0*1e-6
            x(IT,2*M-4)=-plotw*2*w0*1e-6;
        end

        % Termination location
        x(IT,2*M-3)=erfinv(erf(sqrt(2)*x(IT,2*M-5)/(w0*1e-6))-2*sqrt(2/pi)*(X(size(X,2))-J(IT))/IABSEq(2*M-4)/(w0*1e-6))*(w0*1e-6)/sqrt(2);
        if isnan(x(IT,2*M-3))==1 || x(IT,2*M-3)<-plotw*2*w0*1e-6
            x(IT,2*M-3)=-1.2*plotw*2*w0*1e-6;
        end

    end


%%%%%%%%%%%%%%%%%%%%%%%%%%%%%%%%%%%%%%%%
%%%%% TEMPERATURE DISTRIBUTION %%%%%
%%%%%%%%%%%%%%%%%%%%%%%%%%%%%%%%%%%%%%%%

    if IT==1
        % Coefficient to infinity
        C(IT,1)=-1/2*sqrt(pi/2)*IABSEq(1)*w0*1e-6/(Kt(1)*ht(1)*1e-6*Ast(1));
        % Left-hand coefficient based on fixed temperature
        if x(IT,2*M-4)>-plotw*2*w0*1e-6
            C(IT,2)=(Tv(m(size(m,2)))-Ta-C(1,1)-1/2*sqrt(pi/2)*IABSEq(1)*w0*1e-6/(Kt(1)*ht(1)*1e-6*Ast(1))*erf(sqrt(2)*x(1,2*M-4)/(w0*1e-6))+
1/2*sqrt(pi/2)*IABSEq(1)*w0*1e-6/(Kt(1)*ht(1)*1e-6*Ast(1))*exp(Ast(1)^2*(w0*1e-6)^2/8)*erf((Ast(1)*(w0*1e-6)^2+4*x(1,2*M-4))/(2*sqrt(2)*
w0*1e-6))*exp(Ast(1)*x(1,2*M-4)))/(exp(Ast(1)*x(1,2*M-4)));
        else
            % Match ambient temperature at boundary
            C(IT,2)=(-C(1,1)-1/2*sqrt(pi/2)*IABSEq(1)*w0*1e-6/(Kt(1)*ht(1)*1e-6*Ast(1))*erf(sqrt(2)*x(1,2*M-4)/(w0*1e-6))+
1/2*sqrt(pi/2)*IABSEq(1)*w0*1e-6/(Kt(1)*ht(1)*1e-6*Ast(1))*exp(Ast(1)^2*(w0*1e-6)^2/8)*erf((Ast(1)*(w0*1e-6)^2+4*x(1,2*M-4))/(2*sqrt(2)*
w0*1e-6))*exp(Ast(1)*x(1,2*M-4)))/(exp(Ast(1)*x(1,2*M-4)));
        end

    else
        % Coefficient to infinity
        F(IT,1,1)=1;
        R(IT,1)=-1/2*sqrt(pi/2)*IABSEq(1)*w0*1e-6/(Kt(1)*ht(1)*1e-6*Ast(1));
        for o=1:2*M-5
            % Coefficients to match temperatures
            F(IT,2*o,2*o-1)=1;
            F(IT,2*o,2*o)=exp(Ast(o)*x(IT,o));
            F(IT,2*o,2*o+1)=-1;
            F(IT,2*o,2*o+2)=-exp(Ast(o+1)*x(IT,o));
            R(IT,2*o)=-1/2*sqrt(pi/2)*IABSEq(o)*w0*1e-6/(Kt(o)*ht(o)*1e-6*Ast(o))*erf(sqrt(2)*x(IT,o)/(w0*1e-6))+1/2*sqrt(pi/2)*
IABSEq(o)*w0*1e-6/(Kt(o)*ht(o)*1e-6*Ast(o))*exp(Ast(o)^2*(w0*1e-6)^2/8)*erf((Ast(o)*(w0*1e-6)^2+4*x(IT,o))/(2*sqrt(2)*w0*1e-6))*
exp(Ast(o)*x(IT,o))+1/2*sqrt(pi/2)*IABSEq(o+1)*w0*1e-6/(Kt(o+1)*ht(o+1)*1e-6*Ast(o+1))*erf(sqrt(2)*x(IT,o)/(w0*1e-6))-1/2*sqrt(pi/2)*
```

```
IABSEq(o+1)*w0*1e-6/(Kt(o+1)*ht(o+1)*1e-6*Ast(o+1))*exp(Ast(o+1)^2*(w0*1e-6)^2/8)*erf((Ast(o+1)*(w0*1e-6)^2+4*x(IT,o))/(2*sqrt(2)*
w0*1e-6))*exp(Ast(o+1)*x(IT,o));

            % Coefficients to match temperature gradients
            if o==1
                F(IT,2*o+1,2*o)=Kt(o)*ht(o)*1e-6*Ast(o)*exp(Ast(o)*x(IT,o));
                F(IT,2*o+1,2*o+2)=-Kt(o+1)*ht(o+1)*1e-6*Ast(o+1)*exp(Ast(o+1)*x(IT,o));
                R(IT,2*o+1)=Hf(m(o))*1000*rho(m(o))*h(m(o)+1)*1e-6*V+Kt(o)*ht(o)*1e-6*(-(1e6*IABSEq(o)*exp(-2e12*x(IT,o)^2/w0^2))/
(Ast(o)*Kt(o)*ht(o))+(1e6*IABSEq(o)*exp(x(IT,o)*(-Ast(o)-2e12*x(IT,o)/w0^2)))/(Ast(o)*Kt(o)*ht(o))*exp(Ast(o)*x(IT,o))+1/2*sqrt(pi/2)*
IABSEq(o)*w0*1e-6/(Kt(o)*ht(o)*1e-6*Ast(o))*exp(Ast(o)^2*(w0*1e-6)^2/8)*erf((Ast(o)*(w0*1e-6)^2+4*x(IT,o))/(2*sqrt(2)*w0*1e-6))*
Ast(o)*exp(Ast(o)*x(IT,o)))+Kt(o+1)*ht(o+1)*1e-6*((1e6*IABSEq(o+1)*exp(-2e12*x(IT,o)^2/w0^2))/(Ast(o+1)*Kt(o+1)*ht(o+1))-(1e6*
IABSEq(o+1)*exp(x(IT,o)*(-Ast(o+1)-2e12*x(IT,o)/w0^2)))/(Ast(o+1)*Kt(o+1)*ht(o+1))*exp(Ast(o+1)*x(IT,o))-1/2*sqrt(pi/2)*IABSEq(o+1)*
w0*1e-6/(Kt(o+1)*ht(o+1)*1e-6*Ast(o+1))*exp(Ast(o+1)^2*(w0*1e-6)^2/8)*erf((Ast(o+1)*(w0*1e-6)^2+4*x(IT,o))/(2*sqrt(2)*w0*1e-6))*
Ast(o+1)*exp(Ast(o+1)*x(IT,o)));
            elseif min(abs(m(o)-m(1:o-1)))==0
                F(IT,2*o+1,2*o)=Kt(o)*ht(o)*1e-6*Ast(o)*exp(Ast(o)*x(IT,o));
                F(IT,2*o+1,2*o+2)=-Kt(o+1)*ht(o+1)*1e-6*Ast(o+1)*exp(Ast(o+1)*x(IT,o));
                R(IT,2*o+1)=Hv(m(o))*1000*rho(m(o))*h(m(o)+1)*1e-6*V+Kt(o)*ht(o)*1e-6*(-(1e6*IABSEq(o)*exp(-2e12*x(IT,o)^2/w0^2))/
(Ast(o)*Kt(o)*ht(o))+(1e6*IABSEq(o)*exp(x(IT,o)*(-Ast(o)-2e12*x(IT,o)/w0^2)))/(Ast(o)*Kt(o)*ht(o))*exp(Ast(o)*x(IT,o))+1/2*sqrt(pi/2)*
IABSEq(o)*w0*1e-6/(Kt(o)*ht(o)*1e-6*Ast(o))*exp(Ast(o)^2*(w0*1e-6)^2/8)*erf((Ast(o)*(w0*1e-6)^2+4*x(IT,o))/(2*sqrt(2)*w0*1e-6))*
Ast(o)*exp(Ast(o)*x(IT,o)))+Kt(o+1)*ht(o+1)*1e-6*((1e6*IABSEq(o+1)*exp(-2e12*x(IT,o)^2/w0^2))/(Ast(o+1)*Kt(o+1)*ht(o+1))-(1e6*
IABSEq(o+1)*exp(x(IT,o)*(-Ast(o+1)-2e12*x(IT,o)/w0^2)))/(Ast(o+1)*Kt(o+1)*ht(o+1))*exp(Ast(o+1)*x(IT,o))-1/2*sqrt(pi/2)*IABSEq(o+1)*
w0*1e-6/(Kt(o+1)*ht(o+1)*1e-6*Ast(o+1))*exp(Ast(o+1)^2*(w0*1e-6)^2/8)*erf((Ast(o+1)*(w0*1e-6)^2+4*x(IT,o))/(2*sqrt(2)*w0*1e-6))*
Ast(o+1)*exp(Ast(o+1)*x(IT,o)));
            else
                F(IT,2*o+1,2*o)=Kt(o)*ht(o)*1e-6*Ast(o)*exp(Ast(o)*x(IT,o));
                F(IT,2*o+1,2*o+2)=-Kt(o+1)*ht(o+1)*1e-6*Ast(o+1)*exp(Ast(o+1)*x(IT,o));
                R(IT,2*o+1)=Hf(m(o))*1000*rho(m(o))*h(m(o)+1)*1e-6*V+Kt(o)*ht(o)*1e-6*(-(1e6*IABSEq(o)*exp(-2e12*x(IT,o)^2/w0^2))/
(Ast(o)*Kt(o)*ht(o))+(1e6*IABSEq(o)*exp(x(IT,o)*(-Ast(o)-2e12*x(IT,o)/w0^2)))/(Ast(o)*Kt(o)*ht(o))*exp(Ast(o)*x(IT,o))+1/2*sqrt(pi/2)*
IABSEq(o)*w0*1e-6/(Kt(o)*ht(o)*1e-6*Ast(o))*exp(Ast(o)^2*(w0*1e-6)^2/8)*erf((Ast(o)*(w0*1e-6)^2+4*x(IT,o))/(2*sqrt(2)*w0*1e-6))*
Ast(o)*exp(Ast(o)*x(IT,o)))+Kt(o+1)*ht(o+1)*1e-6*((1e6*IABSEq(o+1)*exp(-2e12*x(IT,o)^2/w0^2))/(Ast(o+1)*Kt(o+1)*ht(o+1))-(1e6*
IABSEq(o+1)*exp(x(IT,o)*(-Ast(o+1)-2e12*x(IT,o)/w0^2)))/(Ast(o+1)*Kt(o+1)*ht(o+1))*exp(Ast(o+1)*x(IT,o))-1/2*sqrt(pi/2)*IABSEq(o+1)*
w0*1e-6/(Kt(o+1)*ht(o+1)*1e-6*Ast(o+1))*exp(Ast(o+1)^2*(w0*1e-6)^2/8)*erf((Ast(o+1)*(w0*1e-6)^2+4*x(IT,o))/(2*sqrt(2)*w0*1e-6))*
Ast(o+1)*exp(Ast(o+1)*x(IT,o)));
            end
        end

        % Final temperature condition
        if x(IT,2*M-4)>-plotw*2*w0*1e-6
            F(IT,4*M-8,4*M-9)=1;
            F(IT,4*M-8,4*M-8)=exp(Ast(2*M-4)*x(IT,2*M-4));
            R(IT,4*M-8)=Tv(m(size(m,2)))-Ta-1/2*sqrt(pi/2)*IABSEq(2*M-4)*w0*1e-6/(Kt(2*M-4)*ht(2*M-4)*1e-6*Ast(2*M-4))*erf(sqrt(2)*
x(IT,2*M-4)/(w0*1e-6))+1/2*sqrt(pi/2)*IABSEq(2*M-4)*w0*1e-6/(Kt(2*M-4)*ht(2*M-4)*1e-6*Ast(2*M-4))*exp(Ast(2*M-4)^2*(w0*1e-6)^2/8)*
erf((Ast(2*M-4)*(w0*1e-6)^2+4*x(IT,2*M-4))/(2*sqrt(2)*w0*1e-6))*exp(Ast(2*M-4)*x(IT,2*M-4));
        else
            % Match ambient temperature at boundary
            F(IT,4*M-8,4*M-9)=1;
            F(IT,4*M-8,4*M-8)=exp(Ast(2*M-4)*x(IT,2*M-4));
            R(IT,4*M-8)=-1/2*sqrt(pi/2)*IABSEq(2*M-4)*w0*1e-6/(Kt(2*M-4)*ht(2*M-4)*1e-6*Ast(2*M-4))*erf(sqrt(2)*x(IT,2*M-4)/(w0*1e-6))+
1/2*sqrt(pi/2)*IABSEq(2*M-4)*w0*1e-6/(Kt(2*M-4)*ht(2*M-4)*1e-6*Ast(2*M-4))*exp(Ast(2*M-4)^2*(w0*1e-6)^2/8)*erf((Ast(2*M-4)*(w0*1e-6)^2+
4*x(IT,2*M-4))/(2*sqrt(2)*w0*1e-6))*exp(Ast(2*M-4)*x(IT,2*M-4));
        end

        % Solve coefficients
        C(IT,:)=permute(F(IT,:,:),[2 3 1])\R(IT,:)';
    end

    % Generate numerical temperature distribution
    if IT==1
        xxx(1,:)=x(1,2*M-4):(max(plotw*2*w0*1e-6,2*x(1,2*M-4))-x(1,2*M-4))/((2*M-4)*dstep-1):max(plotw*2*w0*1e-6,2*x(1,2*M-4));
        T(1,1:(2*M-4)*dstep)=C(1,1)+1/2.*sqrt(pi/2).*IABSEq(1).*w0.*1e-6./(Kt(1).*ht(1).*1e-6.*Ast(1)).*erf(sqrt(2).*xxx(1,1:(2*M-4)*
dstep)./(w0.*1e-6))+(C(1,2)-1/2.*sqrt(pi/2).*IABSEq(1).*w0.*1e-6./(Kt(1).*ht(1).*1e-6.*Ast(1)).*exp(Ast(1).^2.*(w0.*1e-6).^2./8).*
erf((Ast(1).*(w0.*1e-6).^2+4.*xxx(1,1:(2*M-4)*dstep))./(2.*sqrt(2).*w0.*1e-6))).*exp(Ast(1).*xxx(1,1:(2*M-4)*dstep))+Ta;
    else
        % Temperature distribution is generated from left to right (in
        % opposite direction to other calculations)
        for o=1:2*M-4
            if o==2*M-4
                xxx(IT,dstep*(o-1)+1:dstep*o)=x(IT,1):(max(plotw*2*w0*1e-6,2*x(IT,1))-x(IT,1))/(dstep-1):max(plotw*2*w0*1e-6,2*x(IT,1));
            elseif x(IT,2*M-4-o+1)~=x(IT,2*M-4-o)
                xxx(IT,dstep*(o-1)+1:dstep*o)=x(IT,2*M-4-o+1):(x(IT,2*M-4-o)-x(IT,2*M-4-o+1))/(dstep-1):x(IT,2*M-4-o);
            else
                xxx(IT,dstep*(o-1)+1:dstep*o)=x(IT,2*M-4-o).*ones(1,dstep);
            end
            if (o<2*M-4 && x(IT,2*M-4-o)>-plotw*2*w0*1e-6) || o==2*M-4
                T(IT,dstep*(o-1)+1:dstep*o)=C(IT,4*M-8-2*o+1)+1/2.*sqrt(pi/2).*IABSEq(2*M-4-o+1).*w0.*1e-6./(Kt(2*M-4-o+1).*
ht(2*M-4-o+1).*1e-6.*Ast(2*M-4-o+1)).*erf(sqrt(2).*xxx(IT,dstep*(o-1)+1:dstep*o)./(w0*1e-6))+(C(IT,4*M-8-2*o+2)-1/2.*sqrt(pi/2).*
IABSEq(2*M-4-o+1).*w0.*1e-6./(Kt(2*M-4-o+1).*ht(2*M-4-o+1).*1e-6.*Ast(2*M-4-o+1)).*exp(Ast(2*M-4-o+1).^2.*(w0.*1e-6).^2./8).*
erf((Ast(2*M-4-o+1).*(w0.*1e-6).^2+4.*xxx(IT,dstep*(o-1)+1:dstep*o))./(2.*sqrt(2).*w0.*1e-6))).*exp(Ast(2*M-4-o+1).*
xxx(IT,dstep*(o-1)+1:dstep*o))+Ta;
            else
                T(IT,dstep*(o-1)+1:dstep*o)=NaN.*ones(1,dstep);
            end
        end
    end

    % Calculation termination
    if IT>1
        if max(abs(T(IT,:)-T(IT-1,:)))<tempdiff && x(IT,2*M-4)>-plotw*w0*1e-6 && x(IT,2*M-3)>-1.2*plotw*w0*1e-6;
            disp(['Converged in ' num2str(IT) ' iterations.'])
            break

        elseif max(abs(T(IT,:)-T(IT-1,:)))<tempdiff
            disp(['Converged in ' num2str(IT) ' iterations.'])
            disp('Insufficient laser power to evaporate final layer, check optical absorption > 0 at selected wavelength then increase
power or change wavelength.')
            IABSEq
```

```
            break

        elseif IT==itmax
            disp('Did not converge within maximum number of iterations.')
            disp('Try activating convergence plots to check calculation behaviour.')
            disp(['Plot output is final iteration. Maximum difference in temperature between iterations is: ' num2str(max(abs(T(IT,:)-
T(IT-1,:)))) ' degC'])
            IABSEq
            break
        end
    end


%%%%%%%%%%%%%%%%%%
%%%%% OUTPUT %%%%%
%%%%%%%%%%%%%%%%%%

    % Temporary plot for viewing of convergence path
    if conv==1
        figure('Position',[100 100 800 600]);
        plot(xxx(IT,:),T(IT,:))
        title('Temperature Distribution');
        xlabel('Position (m)');
        ylabel('Temperature (DegC)');

        display(['Iteration number ' num2str(IT)])
    end

end


figure('Position',[100 100 800 600]);

% Laser intensity plot
subplot(3,1,1)
xp=-max(plotw*w0*1e-6,2*x(IT,2*M-4)):(2*max(plotw*w0*1e-6,2*x(IT,2*M-4)))/(dstep+1):max(plotw*w0*1e-6,2*x(IT,2*M-4));
plot(xp,(IEinc+IMinc).*exp(-2.*xp.^2./(w0*1e-6).^2))
title('Laser Intensity Distribution (Total)');
xlim([-max(plotw*w0*1e-6,2*x(IT,2*M-4)) max(plotw*w0*1e-6,2*x(IT,2*M-4))]);
ylim([0 max(IEinc,IMinc)])
xlabel('Position (m)')
ylabel('Intensity (W/m^2)');

% Temperature distribution plot
subplot(3,1,2)
if x(IT,2*M-3)<x(IT,2*M-4) && x(IT,2*M-4)>-plotw*w0*1e-6
    plot([x(IT,2*M-3):(x(IT,2*M-4)-x(IT,2*M-3))/(dstep-1):x(IT,2*M-4) xxx(IT,:)],[ones(1,dstep).*Tv(m(size(m,2))) T(IT,:)])
else
    plot(xxx(IT,:),T(IT,:))
end
title('Temperature Distribution');
xlim([-max(plotw*w0*1e-6,2*x(IT,2*M-4)) max(plotw*w0*1e-6,2*x(IT,2*M-4))]);
ylim([0 Tv(m(2*M-4))*1.1])
xlabel('Position (m)')
ylabel('Temperature (Degrees Celsius)');

% Cut position plot
subplot(3,1,3)
q111=1;
for o=1:2*M-4
    if min(abs(m(o)-m(1:o-1)))==0
        Sus(q111)=m(o);
        Susx(q111)=x(IT,o);
        if o==2*M-4
            Susx(q111)=x(IT,2*M-3);
        end
        q111=q111+1;
    end
end


barh(Sus,Susx,1,'BaseValue',max(plotw*w0*1e-6,2*x(IT,2*M-4)));
title('Layer Cut Positions');
set(gca,'YDir','reverse','YTick',1:M-2)
xlim([-max(plotw*w0*1e-6,2*x(IT,2*M-4)) max(plotw*w0*1e-6,2*x(IT,2*M-4))]);
xlabel('Position (m)');
ylabel('Layer Number');
```

B.1.2 Input.m

```
%%%%%%%%%%%%%%%%%%%%%%%%
%%%%% DESCRIPTION %%%%%
%%%%%%%%%%%%%%%%%%%%%%%%

% Contains all simulation inputs.
% Adrian Lutey, University of Bologna, 2013
```

```
%%%%%%%%%%%%%%%%%%%%%%%%%%%%%%%%%%%%%%%%%%%%%%%%%%%%%%%%%%%%%%%%%%%%%%%%%%%%%%%%
%%%%% INCIDENT FIELD / ENVIRONMENT SPECIFICATION %%%%%
%%%%%%%%%%%%%%%%%%%%%%%%%%%%%%%%%%%%%%%%%%%%%%%%%%%%%%%%%%%%%%%%%%%%%%%%%%%%%%%%

PEinc=4;                    % Laser power (W) of TE polarised component
PMinc=0;                    % Laser power (W) of TW polarised component
V=0.05;                     % Translation velocity velocity (m/s, x-direction)
w0=15;                      % Beam waist radius (micron)
lambda0=0.515;              % Beam wavelength in a vacuum (micron)
Ta=25;                      % Ambient temperature (degC)
theta=0;                    % Angle of incidence (deg)


%%%%%%%%%%%%%%%%%%%%%%%%%%%%%%%%%%%
%%%%% TARGET SPECIFICATION %%%%%
%%%%%%%%%%%%%%%%%%%%%%%%%%%%%%%%%%%

% Layer 0: Preceeding Medium
COHERENT(1)=0;
n(1)=1;
kappa(1)=0;

% Layer 1
Layer=1;                    % Layer number
COHERENT(Layer+1)=0;        % Is the interface with next layer coherent? [0=No, 1=Yes]
h(Layer+1)=7;               % Layer thickness (micron)
Aluminium                   % Layer material properties file
n(Layer+1)=interp1(lambda0lambda0,nlambda0,lambda0,'linear');          % Layer refractive index
kappa(Layer+1)=interp1(lambda0lambda0,kappalambda0,lambda0,'linear');  % Layer extinction coefficient
Ks(Layer)=Ksmat;            % Layer thermal conductivity (W/mK)
Kl(Layer)=Klmat;            % Layer thermal conductivity (W/mK)
rho(Layer)=rhomat;          % Layer density (kg/m^3)
Cps(Layer)=Cpsmat;          % Layer solid specific heat capacity (J/gK)
Cpl(Layer)=Cplmat;          % Layer liquid specific heat capacity (J/gK)
Tm(Layer)=Tmmat;            % Melting temperature (degC)
Tv(Layer)=Tvmat;            % Boiling/combustion temperature (degC)
Hf(Layer)=Hfmat;            % Heat of fusion (J/g)
Hv(Layer)=Hvmat;            % Heat of vaporisation (J/g)

% Layer 2
Layer=2;
Paper
COHERENT(Layer+1)=0;
h(Layer+1)=69;
n(Layer+1)=interp1(lambda0lambda0,nlambda0,lambda0,'linear');
kappa(Layer+1)=interp1(lambda0lambda0,kappalambda0,lambda0,'linear');
Ks(Layer)=Ksmat;
Kl(Layer)=Klmat;
rho(Layer)=rhomat;
Cps(Layer)=Cpsmat;
Cpl(Layer)=Cplmat;
Tm(Layer)=Tmmat;
Tv(Layer)=Tvmat;
Hf(Layer)=Hfmat;
Hv(Layer)=Hvmat;

% % Layer 3
% Layer=3;
% Polypropylene
% COHERENT(Layer+1)=0;
% h(Layer+1)=20;
% n(Layer+1)=interp1(lambda0lambda0,nlambda0,lambda0,'linear');
% kappa(Layer+1)=interp1(lambda0lambda0,kappalambda0,lambda0,'linear');
% Ks(Layer)=Ksmat;
% Kl(Layer)=Klmat;
% rho(Layer)=rhomat;
% Cps(Layer)=Cpsmat;
% Cpl(Layer)=Cplmat;
% Tm(Layer)=Tmmat;
% Tv(Layer)=Tvmat;
% Hf(Layer)=Hfmat;
% Hv(Layer)=Hvmat;

% Layer M: Proceeding Medium
M=Layer+2;                  % Number of layers (including pre- and proceeding)
COHERENT(M)=0;
h(M)=0;
n(M)=1;
kappa(M)=0;


%%%%%%%%%%%%%%%%%%%%%%%%%%%%%%%%%%%
%%%%% NUMERICAL PARAMETERS %%%%%
%%%%%%%%%%%%%%%%%%%%%%%%%%%%%%%%%%%

% Fundamental parameters
dstep=1000;                 % Plot resolution (steps per section)
plotw=100;                  % Plot width (+/-1*w0) in the positive direction
itmax=100;                  % Maximum number of iterations

% Output options / advanced parameters
conv=0;                     % Temporary convergence plots [0=No, 1=Yes]
tempdiff=1;                 % Maximum temperature difference at convergence (degC)
noise=1e-7;                 % Noise floor [default 1e-7]
```

B.2 Model for Nanosecond Pulsed Laser Ablation of Metals

B.2.1 Laser.m

```
%%%%%%%%%%%%%%%%%%%%%%%
%%%%% DESCRIPTION %%%%%
%%%%%%%%%%%%%%%%%%%%%%%

% 1D numerical model for nanosecond pulse laser ablation of metals.
% Adrian Lutey, University of Bologna, 2013


%%%%%%%%%%%%%%%%%%%
%%%%% INPUTS %%%%%
%%%%%%%%%%%%%%%%%%%

clear
display('Reading input file...')
Input


%%%%%%%%%%%%%%%%%%%%%%%%%%%%%%%%%
%%%%% CALCULATION CONSTANTS %%%%%
%%%%%%%%%%%%%%%%%%%%%%%%%%%%%%%%%

display('Calculating solution constants...')

% Physical constants (SI units)
avo=6.0221415e23;               % Avogadro's number
boltz=1.3806503e-23;            % Boltzman constant
c=299792458;                    % Speed of light in free space
mu00=4e-7*pi;                   % Permeability constant
omega=2*pi*c/(lambda0*1e-6);    % Angular frequency
e0=8.854187817e-12;             % Vacuum permittivity
e=1.60217646e-19;               % Electron charge
m=9.10938188e-31;               % Electron mass

% Number of divisions and coordinate generation
divsz=divsiz;
deltz=h(2)*1e-6/divsz;
zzz=0:deltz:h(2)*1e-6-h(2)*1e-6/divsz;
divst=divsit;
deltt=domaint*FWHM*1e-9/divst;
ttt=0:deltt:domaint*FWHM*1e-9-deltt;

% Integrated time constant (to multiply with peak intensity)
intt=zeros(1,divst);
for t=1:divst
    if t==1
        % Starting position is half t-domain before pulse peak (t=0)
        trel=-domaint/2*FWHM*1e-9;
    else
        % Update time position by adding time-step
        trel=trel+deltt;
        % Calculate integration constant
        intt(t)=1/4*FWHM*1e-9*sqrt(pi/log(2))*(erf(2*(trel)*sqrt(log(2))/FWHM/1e-9)-erf(2*(trel-deltt)*sqrt(log(2))/FWHM/1e-9))/(deltt);
    end
end

% Initial conditions and calculation constants
vap=0;                      % Incremental height reduction
vapcount=0;                 % Number of elements removed by vaporisation
pecount=0;                  % Number of elements removed by phase explosion
cuth1=0;                    % Total fluence gain of material
Kz=Ks.*ones(1,divsz);       % Initial thermal conductivity distribution
Kzmen=Kz;                   % Initial 'preceeding step' thermal conductivity distribution
Tz=Ta.*ones(1,divsz);       % Initial temperature distribution
Tzmen=Tz;                   % Initial 'preceeding step' temperature distribution
hz(1)=0;                    % Preceeding element height (necessary for optical calculation)
hz(2:divsz+1)=h(2)/divsz.*ones(1,divsz);    % Finite-element division of material
hz(divsz+2)=0;              % Proceeding element height (necessary for optical calculation)
COHERENTz(1)=COHERENT(1);   % Preceeding element coherence condition
COHERENTz(2:divsz+1)=COHERENT(2).*ones(1,divsz); % Proceeding element coherence condition
COHERENTz(divsz+2)=0;                            % Proceeding element coherence condition
IEinc=0.94*FPEinc*1e4/FWHM/1e-9;    % On-axis peak laser intensity (TE polarised component)
IMinc=0.94*FPMinc*1e4/FWHM/1e-9;    % On-axis peak laser intensity (TM polarised component)

% Initiate data storage variables
if stor>0
    store=1;
    storesize=ceil(divst/ceil(divst/storesize));
    Tstore=zeros(min(divst,storesize),divsz);
    tstore=zeros(1,min([divst storesize]));
end


%%%%%%%%%%%%%%%%%%%%%%%%%%%%%%%%%%%%%%%%%%%%%%%%%%%%%%%%%%%%%%%%%%%%%%%%%%%%%%%
%%%%% PHYSICAL PROPERTIES & TEMPERATURE CALCULATION %%%%%
```

```
%%%%%%%%%%%%%%%%%%%%%%%%%%%%%%%%%%%%%%%%%%%%%%%%%%%%%%%%%%%%%%%%%%%%%%%%%%%%%%%%

display('Running time-steps...')

% Main time loop
for t=1:divst;

    % Optical and thermal properties
    nz=zeros(1,divsz+2);        % Reset refractive index
    kappaz=zeros(1,divsz+2);    % Reset extinction coefficient
    for kk=1:divsz
        % Below melting point use room physical temperature properties
        if Tzmen(kk)<=Tm;
            nz(kk+1)=n(2);
            kappaz(kk+1)=kappa(2);
            Kz(kk)=Ks;
        else
            % Above melting temperature but below 80% of Tc use linear
            % interpolation/extrapolation of electrical resistivity
            if Tzmen(kk)<(Tc+273)*0.8-273
                Sigma=1/(Rescoeff(1)*Tzmen(kk)+Rescoeff(2));
                Kz(kk)=2.44e-8*(Tzmen(kk)+273)*Sigma;
            % Above 80% of Tc, use nonmetal conductivity
            else
                Sigma=1/Resht;
                Kz(kk)=2.44e-8*(Tc+273)*0.8*Sigma;
            end
            % Calculate electron collision frequency, critical frequency
            % and optical properties
            N=val*avo*rho*1e3/mol;
            Beta=N*e^2/m/Sigma;
            omegac=sqrt(c^2*mu00*N*e^2/m-Beta^2);
            B=1-(omegac^2+Beta^2)/(omega^2+Beta^2);
            C=-Beta^2*(omegac^2+Beta^2)^2/(4*omega^2*(omega^2+Beta^2)^2);
            kappaz(kk+1)=sqrt((-B+sqrt(B^2-4*C))/2);
            nz(kk+1)=Beta*(omegac^2+Beta^2)/(2*kappaz(kk+1)*omega*(omega^2+Beta^2));
        end
    end
    % Set preceeding and proceeding medium properties (vacuum)
    nz(1)=n(1);
    nz(kk+2)=n(M);
    kappaz(1)=kappa(1);
    kappaz(kk+2)=kappa(M);

    % Convert to inputs for Optics.m and run absorption calculation
    if limitabs>0
        kmax=min(divsz,round(limitabs*1e-6/(h(2)/divsz*1e-6)));
        h=[hz(1:kmax+1) 0];
        n=[nz(1:kmax+1) 1];
        kappa=[kappaz(1:kmax+1) 0];
        COHERENT=[COHERENTz(1:kmax+1) 0];
        M=kmax+2;
        Optics
        IABSEqz=[IABS zeros(1,divsz-kmax)].*intt(t);
    else
        h=hz(:)';
        n=nz(:)';
        kappa=kappaz(:)';
        COHERENT=COHERENTz(:)';
        M=kk+2;
        Optics
        IABSEqz=IABS.*intt(t);
    end

    % Reset material properties
    clear n h kappa COHERENT IABS
    Input

    % Reset heat flow calculation matrices
    Frow=zeros(1,3*divsz);
    Fcol=zeros(1,3*divsz);
    Fval=zeros(1,3*divsz);
    R=zeros(1,divsz);
    ind=1;

    % Construct linear equation matrix for heat flow problem
    for kk=1:divsz

        % Second derivative components
        if kk>1
            % Normal conditions
            if abs(Kz(kk-1)-Kz(kk))<100
                Frow(ind)=kk; Fcol(ind)=kk-1; Fval(ind)=(Kz(kk-1)+Kz(kk))/2/Cps/1000/rho/2/deltz/deltz; ind=ind+1;
                Frow(ind)=kk; Fcol(ind)=kk; Fval(ind)=-(Kz(kk-1)+Kz(kk))/2/Cps/1000/rho/2/deltz/deltz; ind=ind+1;
            % Dieletric interface
            else
                Frow(ind)=kk; Fcol(ind)=kk-1; Fval(ind)=Kz(kk-1)/Cps/1000/rho/2/deltz/deltz; ind=ind+1;
                Frow(ind)=kk; Fcol(ind)=kk; Fval(ind)=-Kz(kk-1)/Cps/1000/rho/2/deltz/deltz; ind=ind+1;
            end
            % Normal conditions
            if abs(Kzmen(kk-1)-Kzmen(kk))<100
                R(kk) = R(kk) + Tzmen(kk-1)*-(Kzmen(kk-1)+Kzmen(kk))/2/Cps/1000/rho/2/deltz/deltz;
                R(kk) = R(kk) + Tzmen(kk)*(Kzmen(kk-1)+Kzmen(kk))/2/Cps/1000/rho/2/deltz/deltz;
            % Dielectric interface
            else
                R(kk) = R(kk) + Tzmen(kk-1)*-Kzmen(kk-1)/Cps/1000/rho/2/deltz/deltz;
                R(kk) = R(kk) + Tzmen(kk)*Kzmen(kk-1)/Cps/1000/rho/2/deltz/deltz;
```

```
            end
        end
        if kk<divsz
            % Normal conditions
            if abs(Kz(kk+1)-Kz(kk))<100
                Frow(ind)=kk; Fcol(ind)=kk+1; Fval(ind)=(Kz(kk+1)+Kz(kk))/2/Cps/1000/rho/2/deltz/deltz; ind=ind+1;
                Frow(ind)=kk; Fcol(ind)=kk; Fval(ind)=-(Kz(kk+1)+Kz(kk))/2/Cps/1000/rho/2/deltz/deltz; ind=ind+1;
            % Dieletric interface
            else
                Frow(ind)=kk; Fcol(ind)=kk+1; Fval(ind)=Kz(kk)/Cps/1000/rho/2/deltz/deltz; ind=ind+1;
                Frow(ind)=kk; Fcol(ind)=kk; Fval(ind)=-Kz(kk)/Cps/1000/rho/2/deltz/deltz; ind=ind+1;
            end
            % Normal conditions
            if abs(Kzmen(kk+1)-Kzmen(kk))<100
                R(kk) = R(kk) + Tzmen(kk+1)*-(Kzmen(kk+1)+Kzmen(kk))/2/Cps/1000/rho/2/deltz/deltz;
                R(kk) = R(kk) + Tzmen(kk)*(Kzmen(kk+1)+Kzmen(kk))/2/Cps/1000/rho/2/deltz/deltz;
            % Dieletric interface
            else
                R(kk) = R(kk) + Tzmen(kk+1)*-Kzmen(kk)/Cps/1000/rho/2/deltz/deltz;
                R(kk) = R(kk) + Tzmen(kk)*Kzmen(kk)/Cps/1000/rho/2/deltz/deltz;
            end
        end

        % First derivative components
        Frow(ind)=kk; Fcol(ind)=kk; Fval(ind)=-1/deltt; ind=ind+1;
        R(kk) = R(kk) + Tzmen(kk)*(-1/deltt);

        % Laser source
        R(kk)= R(kk) - IABSEqz(kk)*exp(-peshield*pecount*h(2)*1e-6/divsz)/(Cps*1000*rho*deltz);

    end

    % Solve temperature distribution
    Tz=sparse(Frow(1:ind-1),Fcol(1:ind-1),Fval(1:ind-1))\R';

    % Restrict maximum temperature to 0.9*Tc
    for kk=1:divsz
        if Tz(kk)>(Tc+273)*0.9-273
            Tz(kk)=(Tc+273)*0.9-273;
        end
    end
    % Remove elements at 0.9*Tc
    for kk=1:divsz
        if Tz(kk)>=(Tc+273)*0.9-273
            pecount=pecount+1;
        end
    end

    % Vaporisation depth recorded and elements removed due to vaporisation
    % up until onset of phase explosion.
    if t>1 && Tz(1)>=Tv && pecount==0
        vap=vap+deltt*0.82*101.3*7.5/100/rho*1000*sqrt(mol/2/pi/boltz/avo/(Tz(1)+273.1))*exp(Hv*mol/avo/boltz*(1/(Tv+273.1)-1/(Tz(1)+273.1)));
        vapcount=vapcount+floor(vap/(h(2)/divsz*1e-6));
    end

    % Remove elements and their respective energy, shift up values to fill
    % places and extend final values to fill domain (final part simply
    % maintains stability in case of thin film heating).
    if t>1 && (pecount>pecountmen || vapcount>vapcountmen)
        Tz(1:divsz-(pecount-pecountmen+vapcount-vapcountmen))=Tz(1+(pecount-pecountmen+vapcount-vapcountmen):divsz);
        Tz(divsz-(pecount-pecountmen+vapcount-vapcountmen)+1:divsz)=Tz(divsz-(pecount-pecountmen+vapcount-vapcountmen)).*ones(1,(pecount-
pecountmen+vapcount-vapcountmen));
        Kz(1:divsz-(pecount-pecountmen+vapcount-vapcountmen))=Kz(1+(pecount-pecountmen+vapcount-vapcountmen):divsz);
        Kz(divsz-(pecount-pecountmen+vapcount-vapcountmen)+1:divsz)=Kz(divsz-(pecount-pecountmen+vapcount-vapcountmen)).*ones(1,(pecount-
pecountmen+vapcount-vapcountmen));
        % Reset incremental height reduction
        vap=0;
    end

    % Total aborbed laser energy
    cuth1=cuth1+sum(IABSEqz)*deltt;

    % Periodic data storage (automatically adjusts to storesize)
    if stor>0 && rem(t+ceil(divst/storesize)-1,ceil(divst/storesize))==0
        Tstore(store,(vapcount+pecount+1):divsz)=Tz(1:divsz-(vapcount+pecount));
        if vapcount+pecount>0
            Tstore(store,1:(vapcount+pecount))=NaN.*ones(1,vapcount+pecount);
        end
        tstore(store)=t;
        store=store+1;
    end

    % Assign variables as 'preceeding step'
    Kzmen=Kz;
    Tzmen=Tz;
    vapcountmen=vapcount;
    pecountmen=pecount;

    % Display step number
    if rem(t,500)==0
        display(['Time step ' num2str(t) '...'])
    end
end


%%%%%%%%%%%%%%%%%%
%%%%% OUTPUT %%%%%
```

```
%%%%%%%%%%%%%%%%%%%

% Line temperature plot
figure('Position',[0 0 1900 800]);
plot(zzz,Tstore(floor(0.2*storesize),:),zzz,Tstore(floor(0.3*storesize),:),zzz,Tstore(floor(0.4*storesize),:),zzz,Tstore(floor(0.5*
storesize),:),zzz,Tstore(floor(0.6*storesize),:),zzz,Tstore(floor(0.7*storesize),:),zzz,Tstore(floor(0.8*storesize),:))
xlim([zzz(1) zzz(divsz)])
xlabel('Position z (m)')
ylabel('Temperature (degC)')
legend('0.2*tmax','0.3*tmax','0.4*tmax','0.5*tmax','0.6*tmax','0.7*tmax','0.8*tmax')

% Surface temperature plot
figure('Position',[0 0 1900 800]);
surf(tstore,zzz(1:ceil(divsz/storesize):divsz),Tstore(:,1:ceil(divsz/storesize):divsz)')
shading flat
xlabel('Time')
ylabel('Position z (m)')

% Save output file and display ablation depth
display('Saving data...')
save('temperature.mat');
display('Simulation data file stored in project folder as: temperature.mat')
display(['Ablation depth ' num2str((pecount+vapcount)*deltz*1e9) ' nm, of which ' num2str(vapcount*deltz*1e9) ' nm vaporised and '
num2str(pecount*deltz*1e9) ' nm removed due to phase explosion'])
```

B.2.2 Input.m

```
%%%%%%%%%%%%%%%%%%%%%%%%
%%%%% DESCRIPTION %%%%%
%%%%%%%%%%%%%%%%%%%%%%%%

% Contains all simulation inputs.
% Adrian Lutey, University of Bologna, 2013


%%%%%%%%%%%%%%%%%%%%%%%%%%%%%%%%%%%%%%%%%%%%%%%%%%%%%%%%%%%%%%%%%%%
%%%%% INCIDENT FIELD / ENVIRONMENT SPECIFICATION %%%%%
%%%%%%%%%%%%%%%%%%%%%%%%%%%%%%%%%%%%%%%%%%%%%%%%%%%%%%%%%%%%%%%%%%%

FPEinc=20;              % Pulse fluence (J/cm^2) of TE polarised component
FPMinc=0;               % Pulse fluence (J/cm^2) of TM polarised component
FWHM=10;                % Pulse full width at half maximum (ns)
lambda0=1.064;          % Beam wavelength in a vacuum (micron)
peshield=1e6;           % Shielding coefficient (1/m)
Ta=25;                  % Ambient / departing temperature (degC)
theta=0;                % Angle of incidence (deg)


%%%%%%%%%%%%%%%%%%%%%%%%%%%%%%%%%%
%%%%% TARGET SPECIFICATION %%%%%
%%%%%%%%%%%%%%%%%%%%%%%%%%%%%%%%%%

% Layer 0: Preceeding Medium
COHERENT(1)=0;
n(1)=1;
kappa(1)=0;

% 1: Aluminium
Layer=1;                % Layer number
COHERENT(2)=0;          % Is the interface with next layer coherent? [0=No, 1=Yes]
h(2)=4;                 % Thermal layer thickness (micron)
Aluminium               % Load layer material properties file
n(2)=interp1(lambda0lambda0,nlambda0,lambda0,'linear');         % Layer refractive index
kappa(2)=interp1(lambda0lambda0,kappalambda0,lambda0,'linear'); % Layer extinction coefficient
Ks=Ksmat;               % Layer solid thermal conductivity (W/mK)
Kl=Klmat;               % Layer liquid thermal conductivity (W/mK)
rho=rhomat;             % Layer density (kg/m^3)
Cps=Cpsmat;             % Layer solid specific heat capacity (J/gK)
Cpl=Cplmat;             % Layer liquid specific heat capacity (J/gK)
Tm=Tmmat;               % Melting temperature (degC)
Tv=Tvmat;               % Boiling/combustion temperature (degC)
Hf=Hfmat;               % Heat of fusion (J/g)
Hv=Hvmat;               % Heat of vaporisation (J/g)
Tc=Tcmat;               % Critical temperature (degC)
mol=molmat;             % Molar mass (g/mol)
val=valmat;             % Number of valence electrons
Rescoeff=Resmatcoeff;  % Electrical resistance linear coefficients
Resht=Reshtmat;         % High temperature (near critical) electrical resistance

% Layer M: Proceeding Medium
M=3;                    % Number of layers (including pre- and proceeding)
COHERENT(M)=0;
h(M)=0;
n(M)=1;
kappa(M)=0;


%%%%%%%%%%%%%%%%%%%%%%%%%%%%%%%%%%
```

```
%%%%% NUMERICAL PARAMETERS %%%%%
%%%%%%%%%%%%%%%%%%%%%%%%%%%%%%%%

% Input parameters
divsit=20000;         % Number of time-steps
domaint=2;            % t-domain size (*FWHM)
divsiz=4000;          % Total number of z-divisions

% Output options / advanced parameters
stor=1;               % Full temperature data storage [0=No, 1=Yes]
storesize=500;        % Number of temperature data points stored
limitabs=0.3;         % Optical absorption calculation depth [0=No, #=Limit (micron)]
noise=1e-7;           % Numerical noise floor [default 1e-7]
```

B.3 General Time-Domain Model for Continuous-Wave and Pulsed Laser Incision and Cut of Thin Single and Multi-Layer Films

B.3.1 Laser.m

```
%%%%%%%%%%%%%%%%%%%%%%%%
%%%%% DESCRIPTION %%%%%
%%%%%%%%%%%%%%%%%%%%%%%%

% General time-domain model for continuous-wave and pulsed laser incision and cut of thin single and multi-layer films.
% Adrian Lutey, University of Bologna, 2013


%%%%%%%%%%%%%%%%%%%
%%%%% INPUTS %%%%%
%%%%%%%%%%%%%%%%%%%

clear
display('Reading input file...')
Input


%%%%%%%%%%%%%%%%%%%%%%%%%%%%%%%%%
%%%%% CALCULATION CONSTANTS %%%%%
%%%%%%%%%%%%%%%%%%%%%%%%%%%%%%%%%

display('Calculating solution constants...')

% Physical constants (SI units)
c=299792458;                    % Speed of light in free space
mu00=4e-7*pi;                   % Permeability constant
omega=2*pi*c/(lambda0*1e-6);    % Angular frequency
e0=8.854187817e-12;             % Vacuum permittivity

% Coordinates
if PULSE==0
    divst=divsit;
    deltt=tmax/divst;
    ttt=0:deltt:tmax;
else
    divst=ceil(divsit/tnum)*tnum;
    deltt=1/(RR*1e3)*tnum/divst;
    ttt=0:deltt:1/(RR*1e3)*tnum-deltt;
end
divsx=ceil(divsix/2)*2+1;
divsxmed=(divsx+1)/2;
xxx=zeros(1,divsx);
for i=1:divsxmed-1
    xxx(divsxmed+i)=xxx(divsxmed+i-1)+xcord*w0*1e-6/sum(mult.^(1:divsxmed-1))*mult^(i);
    xxx(divsxmed-i)=-xxx(divsxmed+i);
end
divsy=divsiy;
yyy=zeros(1,divsy);
for j=1:divsy-1
    yyy(1+j)=yyy(j)+ycord*w0*1e-6/sum(mult.^(1:divsy-1))*mult^(j);
end

% Forward and backward differences and integrated position constants (to
% multiply with intensity)
deltx=zeros(1,divsx);
deltxmin=zeros(1,divsx);
intx=zeros(1,divsx);
delty=zeros(1,divsy);
```

```
deltymin=zeros(1,divsy);
inty=zeros(1,divsy);
for i=1:divsx
    if i>1 && i<divsx
        deltx(i)=xxx(i+1)-xxx(i);
        deltxmin(i)=xxx(i)-xxx(i-1);
    elseif i==divsx
        deltx(i)=xxx(i)-xxx(i-1);
        deltxmin(i)=xxx(i)-xxx(i-1);
    elseif i==1
        deltx(i)=xxx(i+1)-xxx(i);
        deltxmin(i)=xxx(i+1)-xxx(i);
    end
    intx(i)=1/2*sqrt(pi/2)*w0*1e-6*(erf(sqrt(2)*(xxx(i)+deltx(i)/2)/(w0*1e-6))-erf(sqrt(2)*(xxx(i)-deltxmin(i)/2)/(w0*1e-6)))/
(deltx(i)/2+deltxmin(i)/2);
end
for j=1:divsy
    if j>1 && j<divsy
        delty(j)=yyy(j+1)-yyy(j);
        deltymin(j)=yyy(j)-yyy(j-1);
    elseif j==divsy
        delty(j)=yyy(j)-yyy(j-1);
        deltymin(j)=yyy(j)-yyy(j-1);
    elseif j==1
        delty(j)=yyy(j+1)-yyy(j);
        deltymin(j)=yyy(j+1)-yyy(j);
    end
    inty(j)=1/2*sqrt(pi/2)*w0*1e-6*(erf(sqrt(2)*(yyy(j)+delty(j)/2)/(w0*1e-6))-erf(sqrt(2)*(yyy(j)-deltymin(j)/2)/(w0*1e-6)))/
(delty(j)/2+deltymin(j)/2);
end

% Calculation constants
% For CW processing calculate intensity based on incident beam power and
% geometry. For pulsed processing set intensity as 1 so that absorption
% ratios can be determined for each layer.
if PULSE==0
    IEinc=2*PEinc/pi/(w0*1e-6)^2;
    IMinc=2*PMinc/pi/(w0*1e-6)^2;
else
    IEinc=1;
    IMinc=1;
end
IABSEq=zeros(5^(M-2),M-2);  % Total absorbed laser intensity
ht=zeros(1,5^(M-2));        % Equivalent film height
Kt=zeros(1,5^(M-2));        % Equivalent film thermal conductivity
rhot=zeros(1,5^(M-2));      % Equivalent film density
Cpt=zeros(1,5^(M-2));       % Equivalent film specific heat capacity
Hmelt=zeros(5^(M-2),M-2);   % Minimum energy density for layer melt
Hliq=zeros(5^(M-2),M-2);    % Minimum energy density for layer liquid
Hvap=zeros(5^(M-2),M-2);    % Minimum energy density for layer vaporising
Hrem=zeros(5^(M-2),M-2);    % Minimum energy density for layer removed
for o=1:5^(M-2)
    % Consider all possible layer state combinations
    % Minimum total energy density for entry into states. Add transition/heating
    % enthalpies of layer if existent (if does not exist, noting that
    % Hmen(i) does not include energy of layer, we consider only the energy
    % necessary to obtain the other layer states/temperatures equivalent to
    % condition. In the case were statemen(itrans(i),j,p)~=4 we have
    % reappearance of layer in this state due to translation).
    for p=1:M-2
        if (rem(o,5^p)>0 && rem(o,5^p)<=5^(p-1)) || (rem(o,5^p)>5^(p-1) && rem(o,5^p)<=2*5^(p-1)) || (rem(o,5^p)>2*5^(p-1) &&
rem(o,5^p)<=3*5^(p-1)) || (rem(o,5^p)>3*5^(p-1) && rem(o,5^p)<=4*5^(p-1))
            Hmelt(o,p)=Cps(p)*1000*Tm(p)*rho(p)*h(p+1)*1e-6;
            Hliq(o,p)=Hf(p)*1000*rho(p)*h(p+1)*1e-6+Cps(p)*1000*Tm(p)*rho(p)*h(p+1)*1e-6;
            Hvap(o,p)=Cpl(p)*1000*(Tv(p)-Tm(p))*rho(p)*h(p+1)*1e-6+Hf(p)*1000*rho(p)*h(p+1)*1e-6+Cps(p)*1000*Tm(p)*rho(p)*h(p+1)*1e-6;
            Hrem(o,p)=Hv(p)*1000*rho(p)*h(p+1)*1e-6+Cpl(p)*1000*(Tv(p)-Tm(p))*rho(p)*h(p+1)*1e-6+Hf(p)*1000*rho(p)*h(p+1)*1e-6+Cps(p)*
1000*Tm(p)*rho(p)*h(p+1)*1e-6;
        end
        for pp=1:M-2
            if pp~=p && ((rem(o,5^pp)>0 && rem(o,5^pp)<=5^(pp-1)) || (rem(o,5^pp)>5^(pp-1) && rem(o,5^pp)<=2*5^(pp-1)) ||
(rem(o,5^pp)>2*5^(pp-1) && rem(o,5^pp)<=3*5^(pp-1)) || (rem(o,5^pp)>3*5^(pp-1) && rem(o,5^pp)<=4*5^(pp-1)))
                if Tv(p)>Tv(pp)
                    Hrem(o,p)=Hrem(o,p)+Hf(pp)*1000*rho(pp)*h(pp+1)*1e-6+Hv(pp)*1000*rho(pp)*h(pp+1)*1e-6+Tm(pp)*Cps(pp)*1000*rho(pp)*
h(pp+1)*1e-6+(Tv(pp)-Tm(pp))*Cpl(pp)*1000*rho(pp)*h(pp+1)*1e-6;
                    Hvap(o,p)=Hvap(o,p)+Hf(pp)*1000*rho(pp)*h(pp+1)*1e-6+Hv(pp)*1000*rho(pp)*h(pp+1)*1e-6+Tm(pp)*Cps(pp)*1000*rho(pp)*
h(pp+1)*1e-6+(Tv(pp)-Tm(pp))*Cpl(pp)*1000*rho(pp)*h(pp+1)*1e-6;
                elseif Tv(p)==Tv(pp)
                    Hrem(o,p)=Hrem(o,p)+Hf(pp)*1000*rho(pp)*h(pp+1)*1e-6+Hv(pp)*1000*rho(pp)*h(pp+1)*1e-6+Tm(pp)*Cps(pp)*1000*rho(pp)*
h(pp+1)*1e-6+(Tv(pp)-Tm(pp))*Cpl(pp)*1000*rho(pp)*h(pp+1)*1e-6;
                    Hvap(o,p)=Hvap(o,p)+Hf(pp)*1000*rho(pp)*h(pp+1)*1e-6+Tm(pp)*Cps(pp)*1000*rho(pp)*h(pp+1)*1e-6+(Tv(pp)-Tm(pp))*Cpl(pp)*
1000*rho(pp)*h(pp+1)*1e-6;
                elseif Tv(p)>Tm(pp)
                    Hrem(o,p)=Hrem(o,p)+Hf(pp)*1000*rho(pp)*h(pp+1)*1e-6+Tm(pp)*Cps(pp)*1000*rho(pp)*h(pp+1)*1e-6+(Tv(p)-Tm(pp))*Cpl(pp)*
1000*rho(pp)*h(pp+1)*1e-6;
                    Hvap(o,p)=Hvap(o,p)+Hf(pp)*1000*rho(pp)*h(pp+1)*1e-6+Tm(pp)*Cps(pp)*1000*rho(pp)*h(pp+1)*1e-6+(Tv(p)-Tm(pp))*Cpl(pp)*
1000*rho(pp)*h(pp+1)*1e-6;
                elseif Tv(p)==Tm(pp)
                    Hrem(o,p)=Hrem(o,p)+Hf(pp)*1000*rho(pp)*h(pp+1)*1e-6+Tm(pp)*Cps(pp)*1000*rho(pp)*h(pp+1)*1e-6;
                    Hvap(o,p)=Hvap(o,p)+Tm(pp)*Cps(pp)*1000*rho(pp)*h(pp+1)*1e-6;
                else
                    Hrem(o,p)=Hrem(o,p)+Tv(p)*Cps(pp)*1000*rho(pp)*h(pp+1)*1e-6;
                    Hvap(o,p)=Hvap(o,p)+Tv(p)*Cps(pp)*1000*rho(pp)*h(pp+1)*1e-6;
                end
                if Tm(p)>Tv(pp)
                    Hliq(o,p)=Hliq(o,p)+Hf(pp)*1000*rho(pp)*h(pp+1)*1e-6+Hv(pp)*1000*rho(pp)*h(pp+1)*1e-6+Tm(pp)*Cps(pp)*1000*rho(pp)*
h(pp+1)*1e-6+(Tv(pp)-Tm(pp))*Cpl(pp)*1000*rho(pp)*h(pp+1)*1e-6;
                    Hmelt(o,p)=Hmelt(o,p)+Hf(pp)*1000*rho(pp)*h(pp+1)*1e-6+Hv(pp)*1000*rho(pp)*h(pp+1)*1e-6+Tm(pp)*Cps(pp)*1000*rho(pp)*
```

```
h(pp+1)*1e-6+(Tv(pp)-Tm(pp))*Cpl(pp)*1000*rho(pp)*h(pp+1)*1e-6;
                elseif Tm(p)==Tv(pp)
                    Hliq(o,p)=Hliq(o,p)+Hf(pp)*1000*rho(pp)*h(pp+1)*1e-6+Hv(pp)*1000*rho(pp)*h(pp+1)*1e-6+Tm(pp)*Cps(pp)*1000*rho(pp)*
h(pp+1)*1e-6+(Tv(pp)-Tm(pp))*Cpl(pp)*1000*rho(pp)*h(pp+1)*1e-6;
                    Hmelt(o,p)=Hmelt(o,p)+Hf(pp)*1000*rho(pp)*h(pp+1)*1e-6+Tm(pp)*Cps(pp)*1000*rho(pp)*h(pp+1)*1e-6+(Tv(pp)-Tm(pp))*Cpl(pp)*
1000*rho(pp)*h(pp+1)*1e-6;
                elseif Tm(p)>Tm(pp)
                    Hliq(o,p)=Hliq(o,p)+Hf(pp)*1000*rho(pp)*h(pp+1)*1e-6+Tm(pp)*Cps(pp)*1000*rho(pp)*h(pp+1)*1e-6+(Tm(p)-Tm(pp))*Cpl(pp)*
1000*rho(pp)*h(pp+1)*1e-6;
                    Hmelt(o,p)=Hmelt(o,p)+Hf(pp)*1000*rho(pp)*h(pp+1)*1e-6+Tm(pp)*Cps(pp)*1000*rho(pp)*h(pp+1)*1e-6+(Tm(p)-Tm(pp))*Cpl(pp)*
1000*rho(pp)*h(pp+1)*1e-6;
                elseif Tm(p)==Tm(pp)
                    Hliq(o,p)=Hliq(o,p)+Hf(pp)*1000*rho(pp)*h(pp+1)*1e-6+Tm(pp)*Cps(pp)*1000*rho(pp)*h(pp+1)*1e-6;
                    Hmelt(o,p)=Hmelt(o,p)+Tm(pp)*Cps(pp)*1000*rho(pp)*h(pp+1)*1e-6;
                else
                    Hliq(o,p)=Hliq(o,p)+Tm(p)*Cps(pp)*1000*rho(pp)*h(pp+1)*1e-6;
                    Hmelt(o,p)=Hmelt(o,p)+Tm(p)*Cps(pp)*1000*rho(pp)*h(pp+1)*1e-6;
                end
            end
        end
    end

    % Transform selected layers
    for p=1:M-2
        % Layer solid
        if rem(o,5^p)>0 && rem(o,5^p)<=5^(p-1)
            Cp(p)=Cps(p);
            K(p)=Ks(p);
        % Layer melting (take specific heat of solid)
        elseif rem(o,5^p)>5^(p-1) && rem(o,5^p)<=2*5^(p-1)
            Cp(p)=Cps(p);
            K(p)=Ks(p);
        % Layer liquid
        elseif rem(o,5^p)>2*5^(p-1) && rem(o,5^p)<=3*5^(p-1)
            Cp(p)=Cpl(p);
            K(p)=Kl(p);
        % Layer vaporising (take specific heat of solid)
        elseif rem(o,5^p)>3*5^(p-1) && rem(o,5^p)<=4*5^(p-1)
            Cp(p)=Cpl(p);
            K(p)=Kl(p);
        % Layer removed
        elseif (rem(o,5^p)>4*5^(p-1) && rem(o,5^p)<=5*5^(p-1)) || rem(o,5^p)==0
            COHERENT(p)=0;
            COHERENT(p+1)=0;
            n(p+1)=1;
            kappa(p+1)=0;
            K(p)=0;
            rho(p)=0;
            Cp(p)=0;
            h(p+1)=0;
        end
    end

    % Equivalent material properties
    ht(o)=sum(h(2:M-1));
    Kt(o)=sum(K(1:M-2).*h(2:M-1))/ht(o);
    rhot(o)=sum(rho(1:M-2).*h(2:M-1))/ht(o);
    Cpt(o)=sum(Cp(1:M-2).*rho(1:M-2).*h(2:M-1))/(ht(o)*rhot(o));

    % Optical absorption
    Optics
    IABSEq(o,:)=IABS(1:M-2);

    % Reset material properties
    clear n h kappa COHERENT IABS
    Input

end

% Initiate data storage variables
if stor>0
    store=1;
    storesize=ceil(divst/ceil(divst/storesize));
    Tstore=zeros(min(divst,storesize),divsx,divsy);
    Hstore=zeros(min(divst,storesize),divsx,divsy);
    Htstore=zeros(min(divst,storesize),divsx,divsy,M-2);
    mapstore=zeros(min(divst,storesize),divsx,divsy);
    statestore=zeros(min(divst,storesize),divsx,divsy,M-2);
    heightstore=zeros(min(divst,storesize),divsx,divsy,M-2);
    tstore=zeros(1,min(divst,storesize));
    statemenstore=zeros(min(divst,storesize),divsx,divsy,M-2);
    heightmenstore=zeros(min(divst,storesize),divsx,divsy,M-2);
    Tmenstore=zeros(min(divst,storesize),divsx,divsy);
    Hmenstore=zeros(min(divst,storesize),divsx,divsy);
    Htmenstore=zeros(min(divst,storesize),divsx,divsy,M-2);
    mapmenstore=zeros(min(divst,storesize),divsx,divsy);
    tpstore=zeros(min(divst,storesize),divsx,divsy,4);
    grainstore=zeros(min(divst,storesize),divsx,divsy);
    capphasestore=zeros(min(divst,storesize),1);
    itransstore=zeros(min(divst,storesize),divsx);
end

% Initiate video file
if vid>0
    tplot=figure('Position',[0 0 1900 800]);
    temperature=VideoWriter('temperature');
    temperature.FrameRate=min(divst,storesize)/plottime;
```

```
    open(temperature)
end


%%%%%%%%%%%%%%%%%%%%%%%%%%%
%%%%% ZONE ALLOCATION %%%%%
%%%%%%%%%%%%%%%%%%%%%%%%%%%

display('Running time-steps...')

% Main time loop
for t=1:divst;

    % Initial states
    if t==1

        % Zone mapping matrix
        map=ones(divsx,divsy);
        % Layer state (0-Solid, 1-Melting, 2-Liquid, 3-Vaporising, 4-Removed)
        state=zeros(divsx,divsy,M-2);
        % Layer heights
        for p=1:M-2
            height(:,:,p)=ones(divsx,divsy).*h(p+1).*1e-6;
        end
        % Optical absorption
        IABSEqt=zeros(divsx,divsy);
        % x-index from previous time-step equivalent to current x-index
        % (for discrete translation of removed material)
        itrans=zeros(1,divsx);
        % Differences between exact value (x+Vx) and nearest
        % data point (itrans), which is then added to exact value
        % of next calculation step to avoid accumulation errors and
        % maintain constant plot velocity
        iremainder=zeros(1,divsx);
        % x-position from previous time-step equivalent to current x-index
        % (for continuous translation of layer heights)
        transind=zeros(1,divsx);
        transdiff=zeros(1,divsx);
        for i=1:divsx
            for ii=2:divsx
                if xxx(ii)>xxx(i)+V*deltt
                    transind(i)=ii;
                    transdiff(i)=xxx(ii)-(xxx(i)+V*deltt);
                    break
                elseif ii==divsx
                    transind(i)=ii;
                end
            end
        end
        % Region type (0-Heating with no abrupt adjacent zones, 1-Heating
        % with abrupt adjacent zones in x- or y-directions, 2-Phase change,
        % 3-All layers removed)
        tp=zeros(divsx,divsy,4);
        % Grain number
        grain=zeros(divsx,divsy);
        % Grain heat capacity (vector grows with number of grains)
        capphase=0;

    else

        % Discrete mesh movement
        for i=divsxmed:divsx
            if i==divsxmed && V*deltt+iremainder(i)>(xxx(i+1)-xxx(i))/2
                itrans(i)=i+1;
                itrans(i-1)=i;
            elseif i==divsxmed
                itrans(i)=i;
                itrans(i-1)=i-1;
            elseif i==divsx
                itrans(i)=i;
            elseif itrans(i-1)==i && V*deltt+iremainder(i)>(xxx(i+1)-xxx(i))/2
                itrans(i)=i+1;
            else
                itrans(i)=i;
            end
        end
        for i=divsxmed-2-(0:divsxmed-3)
            if itrans(i+1)==i+2 && V*deltt+iremainder(i)>(xxx(i+1)-xxx(i))/2
                itrans(i)=i+1;
            else
                itrans(i)=i;
            end
        end
        % Update iremainder
        for i=1:divsx
            iremainder(i)=xxx(i)+V*deltt+iremainder(i)-xxx(itrans(i));
        end

        % Determine material states by comparing energy density to that
        % required for phase changes
        for i=1:divsx
            for j=1:divsy
                for p=1:M-2
                    if ((Hmen(i,j)~=0 && Hmen(i,j)<=Hmelt(mapmen(i,j),p)) || (Hmen(i,j)==0 && Hmen(itrans(i),j)<=
Hmelt(mapmen(itrans(i),j),p))) && statemen(itrans(i),j,p)~=4 && heightmen(itrans(i),j,p)>0 && (statemen(i,j,p)~=4 || i==1 ||
statemen(itrans(i-1),j,p)==4 || heightmen(itrans(i-1),j,p)==0)
                        state(i,j,p)=0;
```

```
                    elseif ((Hmen(i,j)~=0 && Hmen(i,j)>Hmelt(mapmen(i,j),p) && Hmen(i,j)<Hliq(mapmen(i,j),p)) ||
(Hmen(i,j)==0 && Hmen(itrans(i),j)>Hmelt(mapmen(itrans(i),j),p) && Hmen(itrans(i),j)<Hliq(mapmen(itrans(i),j),p))) &&
statemen(itrans(i),j,p)~=4 && heightmen(itrans(i),j,p)>0 && (statemen(i,j,p)~=4 || i==1 || statemen(itrans(i-1),j,p)==4 ||
heightmen(itrans(i-1),j,p)==0)
                        state(i,j,p)=1;
                    elseif ((Hmen(i,j)~=0 && Hmen(i,j)>=Hliq(mapmen(i,j),p) && Hmen(i,j)<=Hvap(mapmen(i,j),p)) ||
(Hmen(i,j)==0 && Hmen(itrans(i),j)>=Hliq(mapmen(itrans(i),j),p) && Hmen(itrans(i),j)<=Hvap(mapmen(itrans(i),j),p))) &&
statemen(itrans(i),j,p)~=4 && heightmen(itrans(i),j,p)>0 && (statemen(i,j,p)~=4 || i==1 || statemen(itrans(i-1),j,p)==4 ||
heightmen(itrans(i-1),j,p)==0)
                        state(i,j,p)=2;
                    elseif ((Hmen(i,j)~=0 && Hmen(i,j)>Hvap(mapmen(i,j),p) && Hmen(i,j)<Hrem(mapmen(i,j),p)) ||
(Hmen(i,j)==0 && Hmen(itrans(i),j)>Hvap(mapmen(itrans(i),j),p) && Hmen(itrans(i),j)<Hrem(mapmen(itrans(i),j),p))) &&
statemen(itrans(i),j,p)~=4 && heightmen(itrans(i),j,p)>0 && (statemen(i,j,p)~=4 || i==1 || statemen(itrans(i-1),j,p)==4 ||
heightmen(itrans(i-1),j,p)==0)
                        state(i,j,p)=3;
                    else
                        state(i,j,p)=4;
                    end
                end
            end
        end

        % Remove isolated elements
        for kk=1:2
            for i=1:divsx
                for j=1:divsy
                    if (i==1 || sum(state(i-1,j,:))==4*(M-2)) && (i==divsx-1 || i==divsx || sum(state(i+1,j,:))==4*(M-2) ||
sum(state(i+2,j,:))==4*(M-2))
                        state(i,j,:)=4.*ones(1,1,M-2);
                    elseif (j==1 || sum(state(i,j-1,:))==4*(M-2)) && (j==divsy-1 || j==divsy || sum(state(i,j+1,:))==4*(M-2) ||
sum(state(i,j+2,:))==4*(M-2))
                        state(i,j,:)=4.*ones(1,1,M-2);
                    end
                end
            end
        end

        % Map matrix and layer heights
        for i=1:divsx
            for j=1:divsy
                Ind=1;
                for p=1:M-2
                    if state(i,j,p)==0
                    elseif state(i,j,p)==1
                        Ind=Ind+5^(p-1);
                    elseif state(i,j,p)==2
                        Ind=Ind+2*5^(p-1);
                    elseif state(i,j,p)==3
                        Ind=Ind+3*5^(p-1);
                    elseif state(i,j,p)==4
                        Ind=Ind+4*5^(p-1);
                    end
                    % Layer height transfer
                    if state(i,j,p)~=4 && state(transind(i),j,p)~=4 && abs(xxx(i))<w0*1e-6
                        height(i,j,p)=heightmen(transind(i),j,p)-transdiff(i)/(xxx(transind(i))-xxx(transind(i)-1))*
(heightmen(transind(i),j,p)-heightmen(transind(i)-1,j,p));
                    elseif state(i,j,p)~=4 && abs(xxx(i))<w0*1e-6
                        height(i,j,p)=heightmen(transind(i)-1,j,p);
                    elseif state(i,j,p)~=4
                        height(i,j,p)=heightmen(itrans(i),j,p);
                    else
                        height(i,j,p)=0;
                    end
                end
                map(i,j)=Ind;

                % Addition or removal of layer energy density from total in case
                % of removal/arrival of layer
                for p=1:M-2
                    if statemen(i,j,p)~=4 && state(i,j,p)==4
                        Hmen(i,j)=Hmen(i,j)-Htmen(i,j,p);
                    elseif statemen(i,j,p)==4 && state(i,j,p)~=4
                        Hmen(i,j)=Hmen(i,j)+Htmen(i,j,p);
                    end
                end

                % Determine optical absorption and height reduction due to
                % laser intensity or short pulse ablation
                if PULSE==0
                    IABSEqt(i,j)=sum(IABSEq(map(i,j),:))*intx(i)*inty(j);
                else
                    if rem(t+divst/tnum-2,divst/tnum)==0
                        IABSEqt(i,j)=0;
                        for p=1:M-2
                            if state(i,j,p)~=4
                                % Effective linear absorption ratio
                                % multiplied by incident fluence (J/cm^2)
                                IrateffFP=IABSEq(map(i,j),p)/(IEinc+IMinc)*(2*EPEinc/1000/pi/(w0*1e-4)^2+2*EPMinc/1000/pi/(w0*1e-4)^2)*
intx(i)*inty(j);
                                % Interpolation of cutd and cutht
                                for kk=2:size(IratFPt,2)
                                    if IratFPt(p,kk)>IrateffFP
                                        Iratind=kk;
                                        Iratdiff=IratFPt(p,kk)-IrateffFP;
                                        break
                                    elseif kk==size(IratFPt,2)
                                        Iratind=kk;
```

```
                                    Iratdiff=0;
                                end
                            end
                            for kk=2:size(Tdepmat,2)
                                if Tdept(p,kk)>Tmen(i,j)
                                    Tdepind=kk;
                                    Tdepdiff=Tdept(p,kk)-Tmen(i,j);
                                    break
                                elseif kk==size(Tdepmat,2)
                                    Tdepind=kk;
                                    Tdepdiff=0;
                                end
                            end
                            cutd1(1)=cutdt(p,Iratind,Tdepind)-Iratdiff/(IratFPt(p,Iratind)-IratFPt(p,Iratind-1))*
(cutdt(p,Iratind,Tdepind)-cutdt(p,Iratind-1,Tdepind));
                            cutd1(2)=cutdt(p,Iratind,Tdepind-1)-Iratdiff/(IratFPt(p,Iratind)-IratFPt(p,Iratind-1))*
(cutdt(p,Iratind,Tdepind-1)-cutdt(p,Iratind-1,Tdepind-1));
                            cuth1(1)=cutht(p,Iratind,Tdepind)-Iratdiff/(IratFPt(p,Iratind)-IratFPt(p,Iratind-1))*
(cutht(p,Iratind,Tdepind)-cutht(p,Iratind-1,Tdepind));
                            cuth1(2)=cutht(p,Iratind,Tdepind-1)-Iratdiff/(IratFPt(p,Iratind)-IratFPt(p,Iratind-1))*
(cutht(p,Iratind,Tdepind-1)-cutht(p,Iratind-1,Tdepind-1));
                            cutd=cutd1(1)-Tdepdiff/(Tdept(p,Tdepind)-Tdept(p,Tdepind-1))*(cutd1(1)-cutd1(2));
                            cuth=cuth1(1)-Tdepdiff/(Tdept(p,Tdepind)-Tdept(p,Tdepind-1))*(cuth1(1)-cuth1(2));
                            % Update height and source values
                            IABSEqt(i,j)=IABSEqt(i,j)+cuth*RR*1e3;
                            height(i,j,p)=max(height(i,j,p)-cutd,0);
                        end
                    end
                end
            end

        end
    end

    % Determine region type
    tp=zeros(divsx,divsy,4);
    for j=1:divsy
        for i=1:divsx
            if min(abs(state(i,j,:)-1))==0 || min(abs(state(i,j,:)-3))==0
                tp(i,j,1)=2;
            elseif sum(state(i,j,:))==4*(M-2)
                tp(i,j,1)=3;
            end
        end
    end
    for j=1:divsy
        for i=1:divsx
            % Abrupt heating zone to the left
            if tp(i,j,1)<2 && (i>1 && tp(i-1,j,1)<2 && (max(abs(state(i,j,:)-state(i-1,j,:)))==2 || max(abs(state(i,j,:)-
state(i-1,j,:)))==4))
                tp(i,j,1)=1;
            end
            % Abrupt heating zone to the right
            if tp(i,j,1)<2 && (i<divsx && tp(i+1,j,1)<2 && (max(abs(state(i,j,:)-state(i+1,j,:)))==2 || max(abs(state(i,j,:)-
state(i+1,j,:)))==4))
                tp(i,j,2)=1;
            end
            % Abrupt heating zone below
            if tp(i,j,1)<2 && (j>1 && tp(i,j-1,1)<2 && (max(abs(state(i,j,:)-state(i,j-1,:)))==2 || max(abs(state(i,j,:)-
state(i,j-1,:)))==4))
                tp(i,j,3)=1;
            end
            % Abrupt heating zone above
            if tp(i,j,1)<2 && (j<divsy && tp(i,j+1,1)<2 && (max(abs(state(i,j,:)-state(i,j+1,:)))==2 || max(abs(state(i,j,:)-
state(i,j+1,:)))==4))
                tp(i,j,4)=1;
            end
        end
    end

    % Grouping grains of region types and calculation of
    % total heat capacity of each grain
    g=0;
    grain=zeros(divsx,divsy);
    for j=1:divsy
        for i=1:divsx
            % New grain defined as element with abrupt adjacent zone to
            % the right or above, but not to the left or below
            % (calculation proceeds left to right, bottom to top)
            if (tp(i,j,2)==1 || tp(i,j,4)==1) && tp(i,j,1)~=1 && tp(i,j,3)~=1
                % Start new grain
                g=g+1;
                grain(i,j)=g;
                capphase(grain(i,j))=Cpt(map(i,j))*1000*rhot(map(i,j))*ht(map(i,j))*(deltxmin(i)/2+deltx(i)/2)*(deltymin(j)/2+
delty(j)/2);
            % Where abrupt adjacent zone is to the left, add current
            % element to grain to the left
            elseif tp(i,j,1)==1
                grain(i,j)=grain(i-1,j);
                capphase(grain(i,j))=capphase(grain(i,j))+Cpt(map(i,j))*1000*rhot(map(i,j))*ht(map(i,j))*(deltxmin(i)/2+deltx(i)/2)*
(deltymin(j)/2+delty(j)/2);
                % Where abrupt adjacent zone is also below, convert
                % grain below to that which is current, if not already
                % the case
                if tp(i,j,3)==1 && grain(i,j-1)~=grain(i,j)
                    capphase(grain(i,j))=capphase(grain(i,j))+capphase(grain(i,j-1));
                    grain(grain==grain(i,j-1))=grain(i,j);
```

```
                end
            % Where abrupt adjacent zone is below, add current element
            % to grain below
            elseif tp(i,j,3)==1
                grain(i,j)=grain(i,j-1);
                capphase(grain(i,j))=capphase(grain(i,j))+Cpt(map(i,j))*1000*rhot(map(i,j))*ht(map(i,j))*(deltxmin(i)/2+deltx(i)/2)*
(deltymin(j)/2+delty(j)/2);
            % Phase change elements are joined in all directions
            elseif tp(i,j,1)==2
                if (i==1 || tp(i-1,j,1)~=2) && (j==1 || tp(i,j-1,1)~=2)
                    g=g+1;
                    grain(i,j)=g;
                    capphase(grain(i,j))=Cpt(map(i,j))*1000*rhot(map(i,j))*ht(map(i,j))*(deltxmin(i)/2+deltx(i)/2)*(deltymin(j)/2+
delty(j)/2);
                elseif i>1 && tp(i-1,j,1)==2
                    grain(i,j)=grain(i-1,j);
                    capphase(grain(i,j))=capphase(grain(i,j))+Cpt(map(i,j))*1000*rhot(map(i,j))*ht(map(i,j))*(deltxmin(i)/2+deltx(i)/2)*
(deltymin(j)/2+delty(j)/2);
                    if j>1 && tp(i,j-1,1)==2 && grain(i,j-1)~=grain(i,j)
                        capphase(grain(i,j))=capphase(grain(i,j))+capphase(grain(i,j-1));
                        grain(grain==grain(i,j-1))=grain(i-1,j);
                    end
                elseif j>1 && tp(i,j-1,1)==2
                    grain(i,j)=grain(i,j-1);
                    capphase(grain(i,j))=capphase(grain(i,j))+Cpt(map(i,j))*1000*rhot(map(i,j))*ht(map(i,j))*(deltxmin(i)/2+deltx(i)/2)*
(deltymin(j)/2+delty(j)/2);
                    end
                end
            end
        end

    end


%%%%%%%%%%%%%%%%%%%%%%%%%%%%%%%%%%%%%%%%%%%%%%%%%%%%%%%%%%%%%%%%%%%%%%%%%%%%%%%%
%%%%% ENERGY DENSITY & TEMPERATURE DISTRIBUTIONS %%%%%
%%%%%%%%%%%%%%%%%%%%%%%%%%%%%%%%%%%%%%%%%%%%%%%%%%%%%%%%%%%%%%%%%%%%%%%%%%%%%%%%

    % Initial conditions
    if t==1

        % Energy density solution matrix
        C=zeros(1,divsx*divsy);
        for j=1:divsy
            for i=1:divsx
                Pos=(j-1)*divsx+i;
                C(Pos)=Cpt(map(i,j))*1000*Ta*rhot(map(i,j))*ht(map(i,j))*1e-6;
            end
        end

    else

        % Reset heat flow calculation matrices
        Frow=zeros(1,10*divsx*divsy);
        Fcol=zeros(1,10*divsx*divsy);
        Fval=zeros(1,10*divsx*divsy);
        R=zeros(1,divsx*divsy);
        Pos=0;
        ind=1;

        % Construct linear equation matrix
        for j=1:divsy
            for i=1:divsx

                Pos=Pos+1;

                % No material present
                if tp(i,j,1)==3

                    Frow(ind)=Pos; Fcol(ind)=Pos; Fval(ind)=1; ind=ind+1;

                % Heat conduction WITHOUT abrupt adjacent phase-changes
                elseif max(tp(i,j,:))==0

                    % Contribution from LHS (taken only if adjacent element
                    % exists)
                    if i>1 && tp(i-1,j,1)~=3
                        % Value of conduction coefficient
                        valu=Kt(map(i,j))/Cpt(map(i,j))/1000/rhot(map(i,j))/2/deltxmin(i)/(deltxmin(i)/2+deltx(i)/2);
                        % If adjacent element is of different phase, apply
                        % boundary condition, otherwise build energy density
                        % coefficient and constant matrices
                        if max(abs(state(i,j,:)-state(i-1,j,:)))>0
                            % Input indices for bound.m
                            bini1=i-1; binj1=j;    bini2=i; binj2=j;
                            bound;
                        else
                            Frow(ind)=Pos; Fcol(ind)=Pos-1; Fval(ind)=valu; ind=ind+1;
                            R(Pos) = R(Pos) + Hmen(i-1,j)*-valu;
                        end
                        % Build energy density coefficient and constant matrices
                        % for current element
                        Frow(ind)=Pos; Fcol(ind)=Pos; Fval(ind)=-valu; ind=ind+1;
                        R(Pos) = R(Pos) + Hmen(i,j)*valu;
                    end

                    % Contribution from RHS
```

```
                if i<divsx && tp(i+1,j,1)~=3
                    valu=Kt(map(i,j))/Cpt(map(i,j))/1000/rhot(map(i,j))/2/deltx(i)/(deltxmin(i)/2+deltx(i)/2);
                    if max(abs(state(i,j,:)-state(i+1,j,:)))>0
                        bini1=i+1; binj1=j;    bini2=i; binj2=j;
                        bound;
                    else
                        Frow(ind)=Pos; Fcol(ind)=Pos+1; Fval(ind)=valu; ind=ind+1;
                        R(Pos) = R(Pos) + Hmen(i+1,j)*-valu;
                    end
                    Frow(ind)=Pos; Fcol(ind)=Pos; Fval(ind)=-valu; ind=ind+1;
                    R(Pos) = R(Pos) + Hmen(i,j)*valu;
                end

                % Contribution from below
                if j>1 && tp(i,j-1,1)~=3
                    valu=Kt(map(i,j))/Cpt(map(i,j))/1000/rhot(map(i,j))/2/deltymin(j)/(deltymin(j)/2+delty(j)/2);
                    if max(abs(state(i,j,:)-state(i,j-1,:)))>0
                        bini1=i; binj1=j-1;    bini2=i; binj2=j;
                        bound;
                    else
                        Frow(ind)=Pos; Fcol(ind)=Pos-divsx; Fval(ind)=valu; ind=ind+1;
                        R(Pos) = R(Pos) + Hmen(i,j-1)*-valu;
                    end
                    Frow(ind)=Pos; Fcol(ind)=Pos; Fval(ind)=-valu; ind=ind+1;
                    R(Pos) = R(Pos) + Hmen(i,j)*valu;
                end

                % Contribution from above
                if j<divsy && tp(i,j+1,1)~=3
                    valu=Kt(map(i,j))/Cpt(map(i,j))/1000/rhot(map(i,j))/2/delty(j)/(deltymin(j)/2+delty(j)/2);
                    if max(abs(state(i,j,:)-state(i,j+1,:)))>0
                        bini1=i; binj1=j+1;    bini2=i; binj2=j;
                        bound;
                    else
                        Frow(ind)=Pos; Fcol(ind)=Pos+divsx; Fval(ind)=valu; ind=ind+1;
                        R(Pos) = R(Pos) + Hmen(i,j+1)*-valu;
                    end
                    Frow(ind)=Pos; Fcol(ind)=Pos; Fval(ind)=-valu; ind=ind+1;
                    R(Pos) = R(Pos) + Hmen(i,j)*valu;
                end

                % Laser source
                R(Pos)= R(Pos) - IABSEqt(i,j);

                % First derivative components
                if i<divsx && tp(i+1,j,1)~=3
                    valu=V/2/deltx(i);
                    Frow(ind)=Pos; Fcol(ind)=Pos+1; Fval(ind)=valu; ind=ind+1;
                    R(Pos) = R(Pos) + Hmen(i+1,j)*-valu;
                    for p=1:M-2
                        % Layer present to left, not present in section
                        if state(i+1,j,p)~=4 && state(i,j,p)==4
                            R(Pos)=R(Pos)-2*Htmen(i+1,j,p)*-valu;
                        % Layer not present to left, present in section
                        elseif state(i+1,j,p)==4 && state(i,j,p)~=4
                            R(Pos)=R(Pos)+2*Htmen(i+1,j,p)*-valu;
                        end
                    end
                    Frow(ind)=Pos; Fcol(ind)=Pos; Fval(ind)=-1/deltt-valu; ind=ind+1;
                    R(Pos) = R(Pos) + Hmen(i,j)*(-1/deltt+valu);
                else
                    Frow(ind)=Pos; Fcol(ind)=Pos; Fval(ind)=-1/deltt; ind=ind+1;
                    R(Pos) = R(Pos) + Hmen(i,j)*-1/deltt;
                end

            % Heat conduction WITH abrupt adjacent phase-changes
            elseif max(tp(i,j,:))==1

                % All elements are scanned so that second derivative
                % contributions at all boundaries (conduction) and
                % points (laser absorption) of grain can be included
                % and averaged such that temperature change is
                % identical for all elements within grain
                for jj=1:divsy
                    for ii=1:divsx
                        if grain(ii,jj)==grain(i,j)

                            Poss=(jj-1)*divsx+ii;

                            if ii>1 && tp(ii-1,jj,1)~=3 && grain(ii-1,jj)~=grain(i,j)
                                valu=Kt(map(ii,jj))/Cpt(map(ii,jj))/1000/rhot(map(ii,jj))/2/deltxmin(ii)*(deltymin(jj)/2+delty(jj)/2)*
Cpt(map(i,j))*1000*rhot(map(i,j))*ht(map(i,j))/capphase(grain(i,j));
                                if max(abs(state(ii,jj,:)-state(ii-1,jj,:)))>0
                                    bini1=ii-1; binj1=jj; bini2=ii; binj2=jj;
                                    bound;
                                else
                                    Frow(ind)=Pos; Fcol(ind)=Poss-1; Fval(ind)=valu; ind=ind+1;
                                    R(Pos) = R(Pos) + Hmen(ii-1,jj)*-valu;
                                end
                                Frow(ind)=Pos; Fcol(ind)=Poss; Fval(ind)=-valu; ind=ind+1;
                                R(Pos) = R(Pos) + Hmen(ii,jj)*valu;
                            end

                            if ii<divsx && tp(ii+1,jj,1)~=3 && grain(ii+1,jj)~=grain(i,j)
                                valu=Kt(map(ii,jj))/Cpt(map(ii,jj))/1000/rhot(map(ii,jj))/2/deltx(ii)*(deltymin(jj)/2+delty(jj)/2)*
Cpt(map(i,j))*1000*rhot(map(i,j))*ht(map(i,j))/capphase(grain(i,j));
                                if max(abs(state(ii,jj,:)-state(ii+1,jj,:)))>0
```

```
                                    bini1=ii+1; binj1=jj; bini2=ii; binj2=jj;
                                    bound;
                                else
                                    Frow(ind)=Pos; Fcol(ind)=Poss+1; Fval(ind)=valu; ind=ind+1;
                                    R(Pos) = R(Pos) + Hmen(ii+1,jj)*-valu;
                                end
                                Frow(ind)=Pos; Fcol(ind)=Poss; Fval(ind)=-valu; ind=ind+1;
                                R(Pos) = R(Pos) + Hmen(ii,jj)*valu;
                            end

                            if jj>1 && tp(ii,jj-1,1)~=3 && grain(ii,jj-1)~=grain(i,j)
                                valu=Kt(map(ii,jj))/Cpt(map(ii,jj))/1000/rhot(map(ii,jj))/2/deltymin(jj)*(deltxmin(ii)/2+deltx(ii)/2)*
Cpt(map(i,j))*1000*rhot(map(i,j))*ht(map(i,j))/capphase(grain(i,j));
                                if max(abs(state(ii,jj,:)-state(ii,jj-1,:)))>0
                                    bini1=ii; binj1=jj-1; bini2=ii; binj2=jj;
                                    bound;
                                else
                                    Frow(ind)=Pos; Fcol(ind)=Poss-divsx; Fval(ind)=valu; ind=ind+1;
                                    R(Pos) = R(Pos) + Hmen(ii,jj-1)*-valu;
                                end
                                Frow(ind)=Pos; Fcol(ind)=Poss; Fval(ind)=-valu; ind=ind+1;
                                R(Pos) = R(Pos) + Hmen(ii,jj)*valu;
                            end

                            if jj<divsy && tp(ii,jj+1,1)~=3 && grain(ii,jj+1)~=grain(i,j)
                                valu=Kt(map(ii,jj))/Cpt(map(ii,jj))/1000/rhot(map(ii,jj))/2/delty(jj)*(deltxmin(ii)/2+deltx(ii)/2)*
Cpt(map(i,j))*1000*rhot(map(i,j))*ht(map(i,j))/capphase(grain(i,j));
                                if max(abs(state(ii,jj,:)-state(ii,jj+1,:)))>0
                                    bini1=ii; binj1=jj+1; bini2=ii; binj2=jj;
                                    bound;
                                else
                                    Frow(ind)=Pos; Fcol(ind)=Poss+divsx; Fval(ind)=valu; ind=ind+1;
                                    R(Pos) = R(Pos) + Hmen(ii,jj+1)*-valu;
                                end
                                Frow(ind)=Pos; Fcol(ind)=Poss; Fval(ind)=-valu; ind=ind+1;
                                R(Pos) = R(Pos) + Hmen(ii,jj)*valu;
                            end

                            % Laser source
                            R(Pos)= R(Pos) - IABSEqt(ii,jj)*(deltxmin(ii)/2+deltx(ii)/2)*(deltymin(jj)/2+delty(jj)/2)*Cpt(map(i,j))*
1000*rhot(map(i,j))*ht(map(i,j))/capphase(grain(i,j));

                        end

                    end
                end

                % First derivative components
                if i<divsx && tp(i+1,j,1)~=3
                    valu=V/2/deltx(i);
                    Frow(ind)=Pos; Fcol(ind)=Pos+1; Fval(ind)=valu; ind=ind+1;
                    R(Pos) = R(Pos) + Hmen(i+1,j)*-valu;
                    for p=1:M-2
                        % Layer present to left, not present in section
                        if state(i+1,j,p)~=4 && state(i,j,p)==4
                            R(Pos)=R(Pos)-2*Htmen(i+1,j,p)*-valu;
                        % Layer not present to left, present in section
                        elseif state(i+1,j,p)==4 && state(i,j,p)~=4
                            R(Pos)=R(Pos)+2*Htmen(i+1,j,p)*-valu;
                        end
                    end
                    Frow(ind)=Pos; Fcol(ind)=Pos; Fval(ind)=-1/deltt-valu; ind=ind+1;
                    R(Pos) = R(Pos) + Hmen(i,j)*(-1/deltt+valu);
                else
                    Frow(ind)=Pos; Fcol(ind)=Pos; Fval(ind)=-1/deltt; ind=ind+1;
                    R(Pos) = R(Pos) + Hmen(i,j)*-1/deltt;
                end

            % Phase change
            elseif tp(i,j,1)==2

                % All elements are scanned so that contributions at all
                % boundaries (conduction) of grain can be included and
                % averaged
                for jj=1:divsy
                    for ii=1:divsx
                        if grain(ii,jj)==grain(i,j)

                            Poss=(jj-1)*divsx+ii;

                            if ii>1 && tp(ii-1,jj,1)~=3 && grain(ii-1,jj)~=grain(i,j)
                                valu=Kt(map(ii-1,jj))/Cpt(map(ii-1,jj))/1000/rhot(map(ii-1,jj))/2/deltxmin(ii)*(deltymin(jj)/2+
delty(jj)/2)*Cpt(map(i,j))*1000*rhot(map(i,j))*ht(map(i,j))/capphase(grain(i,j));
                                Frow(ind)=Pos; Fcol(ind)=Poss-1; Fval(ind)=valu; ind=ind+1;
                                R(Pos) = R(Pos) + Hmen(ii-1,jj)*-valu;
                                bini1=ii; binj1=jj; bini2=ii-1; binj2=jj;
                                bound;
                            end

                            if ii<divsx && tp(ii+1,jj,1)~=3 && grain(ii+1,jj)~=grain(i,j)
                                valu=Kt(map(ii+1,jj))/Cpt(map(ii+1,jj))/1000/rhot(map(ii+1,jj))/2/deltx(ii)*(deltymin(jj)/2+
delty(jj)/2)*Cpt(map(i,j))*1000*rhot(map(i,j))*ht(map(i,j))/capphase(grain(i,j));
                                Frow(ind)=Pos; Fcol(ind)=Poss+1; Fval(ind)=valu; ind=ind+1;
                                R(Pos) = R(Pos) + Hmen(ii+1,jj)*-valu;
                                bini1=ii; binj1=jj; bini2=ii+1; binj2=jj;
                                bound;
                            end
```

```
                            if jj>1 && tp(ii,jj-1,1)~=3 && grain(ii,jj-1)~=grain(i,j)
                                valu=Kt(map(ii,jj-1))/Cpt(map(ii,jj-1))/1000/rhot(map(ii,jj-1))/2/deltymin(jj)*(deltxmin(ii)/2+
deltx(ii)/2)*Cpt(map(i,j))*1000*rhot(map(i,j))*ht(map(i,j))/capphase(grain(i,j));
                                Frow(ind)=Pos; Fcol(ind)=Poss-divsx; Fval(ind)=valu; ind=ind+1;
                                R(Pos) = R(Pos) + Hmen(ii,jj-1)*-valu;
                                bini1=ii; binj1=jj; bini2=ii; binj2=jj-1;
                                bound;
                            end

                            if jj<divsy && tp(ii,jj+1,1)~=3 && grain(ii,jj+1)~=grain(i,j)
                                valu=Kt(map(ii,jj+1))/Cpt(map(ii,jj+1))/1000/rhot(map(ii,jj+1))/2/delty(jj)*(deltxmin(ii)/2+
deltx(ii)/2)*Cpt(map(i,j))*1000*rhot(map(i,j))*ht(map(i,j))/capphase(grain(i,j));
                                Frow(ind)=Pos; Fcol(ind)=Poss+divsx; Fval(ind)=valu; ind=ind+1;
                                R(Pos) = R(Pos) + Hmen(ii,jj+1)*-valu;
                                bini1=ii; binj1=jj; bini2=ii; binj2=jj+1;
                                bound;
                            end

                        end

                    end
                end

                % Laser source
                R(Pos)= R(Pos) - IABSEqt(i,j);

                % First derivative components
                if i<divsx && tp(i+1,j,1)~=3
                    valu=V/2/deltx(i);
                    Frow(ind)=Pos; Fcol(ind)=Pos+1; Fval(ind)=valu; ind=ind+1;
                    R(Pos) = R(Pos) + Hmen(i+1,j)*-valu;
                    for p=1:M-2
                        % Layer present to left, not present in section
                        if state(i+1,j,p)~=4 && state(i,j,p)==4
                            R(Pos)=R(Pos)-2*Htmen(i+1,j,p)*-valu;
                        % Layer not present to left, present in section
                        elseif state(i+1,j,p)==4 && state(i,j,p)~=4
                            R(Pos)=R(Pos)+2*Htmen(i+1,j,p)*-valu;
                        end
                    end
                    Frow(ind)=Pos; Fcol(ind)=Pos; Fval(ind)=-1/deltt-valu; ind=ind+1;
                    R(Pos) = R(Pos) + Hmen(i,j)*(-1/deltt+valu);
                else
                    Frow(ind)=Pos; Fcol(ind)=Pos; Fval(ind)=-1/deltt; ind=ind+1;
                    R(Pos) = R(Pos) + Hmen(i,j)*-1/deltt;
                end

            end
        end
    end

    % Solve energy density distribution
    C=sparse(Frow(1:ind-1),Fcol(1:ind-1),Fval(1:ind-1))\R';

end

% Temperature and individual layer enthalpies
T=zeros(divsx,divsy);
Ht=zeros(divsx,divsy,M-2);
for j=1:divsy
    for i=divsx-(0:divsx-1)

        Pos=(j-1)*divsx+i;
        H(i,j)=C(Pos);

        % Range limiter locks maximum and minimum energy density
        % within range of current phase
        if filt==1
            if max(state(i,j,:))>0 || H(i,j)>min(Hmelt(map(i,j),:))
                for p=1:M-2
                    if state(i,j,p)==0 && H(i,j)>Hmelt(map(i,j),p)
                        H(i,j)=Hmelt(map(i,j),p)+noise;
                    elseif state(i,j,p)==1 && H(i,j)<=Hmelt(map(i,j),p)
                        H(i,j)=Hmelt(map(i,j),p);
                    elseif state(i,j,p)==1 && H(i,j)>=Hliq(map(i,j),p)
                        H(i,j)=Hliq(map(i,j),p);
                    elseif state(i,j,p)==2 && H(i,j)>Hvap(map(i,j),p)
                        H(i,j)=Hvap(map(i,j),p)+noise;
                    elseif state(i,j,p)==2 && H(i,j)<Hliq(map(i,j),p)
                        H(i,j)=Hliq(map(i,j),p)-noise;
                    elseif state(i,j,p)==3 && H(i,j)<=Hvap(map(i,j),p)
                        H(i,j)=Hvap(map(i,j),p);
                    elseif state(i,j,p)==3 && H(i,j)>=Hrem(map(i,j),p)
                        H(i,j)=Hrem(map(i,j),p);
                    end
                end
            end
        end

        Href=H(i,j);
        Tref=0;

        % Account for energy to arrive at and complete all phase changes
        for p=1:M-2
            if state(i,j,p)==1
                Href=Href-Tm(p)*Cps(p)*1000*rho(p)*h(p+1)*1e-6;
```

```
                    Ht(i,j,p)=Ht(i,j,p)+Tm(p)*Cps(p)*1000*rho(p)*h(p+1)*1e-6;
                    if Tm(p)>Tref
                        Tref=Tm(p);
                    end
                elseif state(i,j,p)==2
                    Href=Href-Hf(p)*1000*rho(p)*h(p+1)*1e-6-Tm(p)*Cps(p)*1000*rho(p)*h(p+1)*1e-6;
                    Ht(i,j,p)=Ht(i,j,p)+Hf(p)*1000*rho(p)*h(p+1)*1e-6+Tm(p)*Cps(p)*1000*rho(p)*h(p+1)*1e-6;
                    if Tm(p)>Tref
                        Tref=Tm(p);
                    end
                elseif state(i,j,p)==3
                    Href=Href-Hf(p)*1000*rho(p)*h(p+1)*1e-6-Tm(p)*Cps(p)*1000*rho(p)*h(p+1)*1e-6-(Tv(p)-Tm(p))*Cpl(p)*1000*rho(p)*
h(p+1)*1e-6;
                    Ht(i,j,p)=Ht(i,j,p)+Hf(p)*1000*rho(p)*h(p+1)*1e-6+Tm(p)*Cps(p)*1000*rho(p)*h(p+1)*1e-6+(Tv(p)-Tm(p))*Cpl(p)*1000*
rho(p)*h(p+1)*1e-6;
                    if Tv(p)>Tref
                        Tref=Tv(p);
                    end
                elseif state(i,j,p)==4
                    Ht(i,j,p)=Ht(i,j,p)+Hv(p)*1000*rho(p)*h(p+1)*1e-6+Hf(p)*1000*rho(p)*h(p+1)*1e-6+Tm(p)*Cps(p)*1000*rho(p)*h(p+1)*1e-6+
(Tv(p)-Tm(p))*Cpl(p)*1000*rho(p)*h(p+1)*1e-6;
                end
            end

            % Account for energy to heat to final global phase change
            for p=1:M-2
                % If layer is solid account for energy density to increase
                % temperature to final phase change (Tref)
                if state(i,j,p)==0
                    Href=Href-Tref*Cps(p)*1000*rho(p)*h(p+1)*1e-6;
                    Ht(i,j,p)=Ht(i,j,p)+Tref*Cps(p)*1000*rho(p)*h(p+1)*1e-6;
                % If layer is liquid account for energy density to increase
                % temperature from its melting temperature to final phase
                % change (Tref)
                elseif state(i,j,p)==2
                    Href=Href-(Tref-Tm(p))*Cpl(p)*1000*rho(p)*h(p+1)*1e-6;
                    Ht(i,j,p)=Ht(i,j,p)+(Tref-Tm(p))*Cpl(p)*1000*rho(p)*h(p+1)*1e-6;
                end
            end

            % If layer is melting/vaporising then temperature is set as such,
            % otherwise remaining energy density heats material, with given total
            % properties, from Tref
            if min(abs(state(i,j,:)-1))==0
                for p=1:M-2
                    if state(i,j,p)==1
                        T(i,j)=Tm(p);
                        break
                    end
                end
            elseif min(abs(state(i,j,:)-3))==0
                for p=1:M-2
                    if state(i,j,p)==3
                        T(i,j)=Tv(p);
                        break
                    end
                end
            else
                T(i,j)=Href/(Cpt(map(i,j))*1000*rhot(map(i,j))*ht(map(i,j))*1e-6)+Tref;
            end

            % Layer enthalpies. Begin by determining number of phase
            % changes occurring simultaneously (nnn).
            nnn=0;
            for p=1:M-2
                if state(i,j,p)==1 || state(i,j,p)==3
                    nnn=nnn+1;
                end
            end
            for p=1:M-2
                % If state is solid or liquid then its energy density is derived
                % from the amount that temperature is above last global
                % phase change
                if state(i,j,p)==0
                    Ht(i,j,p)=Ht(i,j,p)+(T(i,j)-Tref)*Cps(p)*1000*rho(p)*h(p+1)*1e-6;
                elseif state(i,j,p)==2
                    Ht(i,j,p)=Ht(i,j,p)+(T(i,j)-Tref)*Cpl(p)*1000*rho(p)*h(p+1)*1e-6;
                % If state is a phase change then its energy density is derived by
                % dividing remaining energy density between all layers currently
                % changing phase
                elseif state(i,j,p)==1 || state(i,j,p)==3
                    Ht(i,j,p)=Ht(i,j,p)+Href/nnn;
                % If layer is removed but others are present its
                % theoretical energy density (used where layers are reintroduced
                % due to translation) is derived based on its theoretical
                % phase (noting that Hrem etc. due not include the energy density
                % of the layer itself)
                elseif state(i,j,p)==4 && tp(i,j,1)~=3
                    if Hmen(i,j)>=Hrem(map(i,j),p)
                        Ht(i,j,p)=Hv(p)*1000*rho(p)*h(p+1)*1e-6+Cpl(p)*1000*(Tv(p)-Tm(p))*rho(p)*h(p+1)*1e-6+Hf(p)*1000*rho(p)*h(p+1)*
1e-6+Cps(p)*1000*Tm(p)*rho(p)*h(p+1)*1e-6;
                    elseif Hmen(i,j)<Hrem(map(i,j),p) && Hmen(i,j)>Hvap(map(i,j),p)
                        if nnn>0
                            Ht(i,j,p)=Ht(i,j,p)-Hv(p)*1000*rho(p)*h(p+1)*1e-6+Href/nnn;
                        else
                            Ht(i,j,p)=Ht(i,j,p)-Hv(p)*1000*rho(p)*h(p+1)*1e-6+Href;
                        end
```

```
                    elseif Hmen(i,j)>=Hliq(map(i,j),p)
                        Ht(i,j,p)=Ht(i,j,p)-Hv(p)*1000*rho(p)*h(p+1)*1e-6-(Tv(p)-Tm(p))*Cpl(p)*1000*rho(p)*h(p+1)*1e-6+(T(i,j)-Tm(p))*
Cpl(p)*1000*rho(p)*h(p+1)*1e-6;
                    elseif Hmen(i,j)>Hmelt(map(i,j),p)
                        if nnn>0
                            Ht(i,j,p)=Ht(i,j,p)-Hv(p)*1000*rho(p)*h(p+1)*1e-6-(Tv(p)-Tm(p))*Cpl(p)*1000*rho(p)*h(p+1)*1e-6-Hf(p)*1000*
rho(p)*h(p+1)*1e-6+Href/nnn;
                        else
                            Ht(i,j,p)=Ht(i,j,p)-Hv(p)*1000*rho(p)*h(p+1)*1e-6-(Tv(p)-Tm(p))*Cpl(p)*1000*rho(p)*h(p+1)*1e-6-Hf(p)*1000*
rho(p)*h(p+1)*1e-6+Href;
                        end
                    else
                        Ht(i,j,p)=Ht(i,j,p)-Hv(p)*1000*rho(p)*h(p+1)*1e-6-(Tv(p)-Tm(p))*Cpl(p)*1000*rho(p)*h(p+1)*1e-6-Hf(p)*1000*rho(p)*
h(p+1)*1e-6-Tm(p)*Cps(p)*1000*rho(p)*h(p+1)*1e-6+T(i,j)*Cps(p)*1000*rho(p)*h(p+1)*1e-6;
                    end
                elseif state(i,j,p)==4 && i<divsx
                    Ht(i,j,p)=Ht(i+1,j,p);
                end
            end
        end
    end

    % Periodic data storage (automatically adjusts to storesize)
    if stor>0 && rem(t+ceil(divst/storesize)-1,ceil(divst/storesize))==0;
        Tstore(store,:,:)=T;
        Hstore(store,:,:)=H;
        Htstore(store,:,:,:)=Ht;
        mapstore(store,:,:)=map;
        statestore(store,:,:,:)=state;
        heightstore(store,:,:,:)=height;
        tstore(store)=t;
        tpstore(store,:,:,:)=tp;
        grainstore(store,:,:)=grain;
        capphasestore(store,1:size(capphase,2))=capphase;
        itransstore(store,:)=itrans;
        if t>1
            statemenstore(store,:,:,:)=statemen;
            heightmenstore(store,:,:,:)=heightmen;
            Hmenstore(store,:,:)=Hmen;
            Tmenstore(store,:,:)=Tmen;
            Htmenstore(store,:,:,:)=Htmen;
            mapmenstore(store,:,:)=mapmen;
        end
        store=store+1;
    end

    % Assign information as 'previous step' for use in next step
    statemen=state;
    heightmen=height;
    Hmen=H;
    Tmen=T;
    Htmen=Ht;
    mapmen=map;

    if rem(t,50)==0
        display(['Time step ' num2str(t) '...'])
    end


%%%%%%%%%%%%%%%%%%
%%%%% OUTPUT %%%%%
%%%%%%%%%%%%%%%%%%

    if vid>0 && rem(t+ceil(divst/storesize)-1,ceil(divst/storesize))==0

        % Laser intensity plot
        subplot(2,2,1)
        Iplot=zeros(divsx,divsy);
        if PULSE==0
            for i=1:divsx
                for j=1:divsy
                    Iplot(i,j)=(IEinc+IMinc)*exp(-2*(xxx(i)^2+yyy(j)^2)/(w0*1e-6)^2);
                end
            end
        else
            for i=1:divsx
                for j=1:divsy
                    Iplot(i,j)=0.94*(2*EPEinc/1000/pi/(w0*1e-6)^2+2*EPMinc/1000/pi/(w0*1e-6)^2)/(FWHM*1e-9)*intx(i)*inty(j);
                end
            end
        end
        pcolor(xxx.*1e3,yyy.*1e3,Iplot')
        title('Peak Intensity Distribution');
        shading flat
        colorbar('East')
        axis([-min(xcord,plotview)*w0*1e-3 min(xcord,plotview)*w0*1e-3 0 min(ycord,plotview)*w0*1e-3])
        xlabel('Position x (mm)')
        ylabel('Position y (mm)')

        % Layer state plot
        subplot(2,2,2)
        plot3(xxx(abs(xxx)<=plotview*w0*1e-6)'*ones(1,size(yyy(abs(yyy)<=plotview*w0*1e-6),2)).*1e3,ones(size(xxx(abs(xxx)<=
plotview*w0*1e-6),2),1)*yyy(abs(yyy)<=plotview*w0*1e-6).*1e3,state(abs(xxx)<=plotview*w0*1e-6,abs(yyy)<=plotview*w0*1e-6,1),'r',
xxx(abs(xxx)<=plotview*w0*1e-6)'*ones(1,size(yyy(abs(yyy)<=plotview*w0*1e-6),2)).*1e3,ones(size(xxx(abs(xxx)<=plotview*w0*1e-6),2),1)*
yyy(abs(yyy)<=plotview*w0*1e-6).*1e3,state(abs(xxx)<=plotview*w0*1e-6,abs(yyy)<=plotview*w0*1e-6,min(2,size(state,3))),'g',xxx(abs(xxx)<=
plotview*w0*1e-6)'*ones(1,size(yyy(abs(yyy)<=plotview*w0*1e-6),2)).*1e3,ones(size(xxx(abs(xxx)<=plotview*w0*1e-6),2),1)*yyy(abs(yyy)<=
plotview*w0*1e-6).*1e3,state(abs(xxx)<=plotview*w0*1e-6,abs(yyy)<=plotview*w0*1e-6,min(3,size(state,3))),'b',xxx(abs(xxx)<=
```

```
plotview*w0*1e-6)'*ones(1,size(yyy(abs(yyy)<=plotview*w0*1e-6),2)).*1e3,ones(size(xxx(abs(xxx)<=plotview*w0*1e-6),2),1)*yyy(abs(yyy)<=
plotview*w0*1e-6).*1e3,state(abs(xxx)<=plotview*w0*1e-6,abs(yyy)<=plotview*w0*1e-6,min(4,size(state,3))),'c',xxx(abs(xxx)<=
plotview*w0*1e-6)'*ones(1,size(yyy(abs(yyy)<=plotview*w0*1e-6),2)).*1e3,ones(size(xxx(abs(xxx)<=plotview*w0*1e-6),2),1)*yyy(abs(yyy)<=
plotview*w0*1e-6).*1e3,state(abs(xxx)<=plotview*w0*1e-6,abs(yyy)<=plotview*w0*1e-6,min(5,size(state,3))),'m',xxx(abs(xxx)<=
plotview*w0*1e-6)'*ones(1,size(yyy(abs(yyy)<=plotview*w0*1e-6),2)).*1e3,ones(size(xxx(abs(xxx)<=plotview*w0*1e-6),2),1)*yyy(abs(yyy)<=
plotview*w0*1e-6).*1e3,state(abs(xxx)<=plotview*w0*1e-6,abs(yyy)<=plotview*w0*1e-6,min(6,size(state,3))),'y',xxx(abs(xxx)<=
plotview*w0*1e-6)'*ones(1,size(yyy(abs(yyy)<=plotview*w0*1e-6),2)).*1e3,ones(size(xxx(abs(xxx)<=plotview*w0*1e-6),2),1)*yyy(abs(yyy)<=
plotview*w0*1e-6).*1e3,state(abs(xxx)<=plotview*w0*1e-6,abs(yyy)<=plotview*w0*1e-6,min(7,size(state,3))),'k')
        title('Layer States');
        axis([-min(xcord,plotview)*w0*1e-3 min(xcord,plotview)*w0*1e-3 0 min(ycord,plotview)*w0*1e-3 0 4])
        view(40,30)
        xlabel('Position x (mm)')
        ylabel('Position y (mm)')
        set(gca,'ZTick',[0 1 2 3 4])
        set(gca,'ZTickLabel',{'Solid';'Melting';'Liquid';'Vaporising';'Removed'})

        % Temperature distribution plot
        subplot(2,2,3)
        pcolor(xxx.*1e3,yyy.*1e3,T')
        title('2D Temperature Distribution');
        shading flat
        caxis([0 Tmax])
        colorbar('East')
        axis([-min(xcord,plotview)*w0*1e-3 min(xcord,plotview)*w0*1e-3 0 min(ycord,plotview)*w0*1e-3])
        xlabel('Position x (mm)')
        ylabel('Position y (mm)')

        % Layer heights plot
        subplot(2,2,4)
        plot3(xxx(abs(xxx)<=plotview*w0*1e-6)'*ones(1,size(yyy(abs(yyy)<=plotview*w0*1e-6),2)).*1e3,ones(size(xxx(abs(xxx)<=
plotview*w0*1e-6),2),1)*yyy(abs(yyy)<=plotview*w0*1e-6).*1e3,height(abs(xxx)<=plotview*w0*1e-6,abs(yyy)<=plotview*w0*1e-6,1).*1e6,'r',
xxx(abs(xxx)<=plotview*w0*1e-6)'*ones(1,size(yyy(abs(yyy)<=plotview*w0*1e-6),2)).*1e3,ones(size(xxx(abs(xxx)<=plotview*w0*1e-6),2),1)*
yyy(abs(yyy)<=plotview*w0*1e-6).*1e3,height(abs(xxx)<=plotview*w0*1e-6,abs(yyy)<=plotview*w0*1e-6,min(2,size(height,3))).*1e6,'g',xxx(abs(xxx)<=
plotview*w0*1e-6)'*ones(1,size(yyy(abs(yyy)<=plotview*w0*1e-6),2)).*1e3,ones(size(xxx(abs(xxx)<=plotview*w0*1e-6),2),1)*yyy(abs(yyy)<=
plotview*w0*1e-6).*1e3,height(abs(xxx)<=plotview*w0*1e-6,abs(yyy)<=plotview*w0*1e-6,min(3,size(height,3))).*1e6,'b',xxx(abs(xxx)<=
plotview*w0*1e-6)'*ones(1,size(yyy(abs(yyy)<=plotview*w0*1e-6),2)).*1e3,ones(size(xxx(abs(xxx)<=plotview*w0*1e-6),2),1)*yyy(abs(yyy)<=
plotview*w0*1e-6).*1e3,height(abs(xxx)<=plotview*w0*1e-6,abs(yyy)<=plotview*w0*1e-6,min(4,size(height,3))).*1e6,'c',xxx(abs(xxx)<=
plotview*w0*1e-6)'*ones(1,size(yyy(abs(yyy)<=plotview*w0*1e-6),2)).*1e3,ones(size(xxx(abs(xxx)<=plotview*w0*1e-6),2),1)*yyy(abs(yyy)<=
plotview*w0*1e-6).*1e3,height(abs(xxx)<=plotview*w0*1e-6,abs(yyy)<=plotview*w0*1e-6,min(5,size(height,3))).*1e6,'m',xxx(abs(xxx)<=
plotview*w0*1e-6)'*ones(1,size(yyy(abs(yyy)<=plotview*w0*1e-6),2)).*1e3,ones(size(xxx(abs(xxx)<=plotview*w0*1e-6),2),1)*yyy(abs(yyy)<=
plotview*w0*1e-6).*1e3,height(abs(xxx)<=plotview*w0*1e-6,abs(yyy)<=plotview*w0*1e-6,min(6,size(height,3))).*1e6,'y',xxx(abs(xxx)<=
plotview*w0*1e-6)'*ones(1,size(yyy(abs(yyy)<=plotview*w0*1e-6),2)).*1e3,ones(size(xxx(abs(xxx)<=plotview*w0*1e-6),2),1)*yyy(abs(yyy)<=
plotview*w0*1e-6).*1e3,height(abs(xxx)<=plotview*w0*1e-6,abs(yyy)<=plotview*w0*1e-6,min(7,size(height,3))).*1e6,'k')
        title('Layer Heights');
        axis([-min(xcord,plotview)*w0*1e-3 min(xcord,plotview)*w0*1e-3 0 min(ycord,plotview)*w0*1e-3 0 max(h)])
        view(40,30)
        xlabel('Position x (mm)')
        ylabel('Position y (mm)')
        zlabel('Layer height (micron)')

        % Write video frame
        writeVideo(temperature,getframe(tplot));
    end
end

% Close plot and save output file
if vid>0
    display('Saving video...')
    close(tplot);
    close(temperature);
    display('Video file stored in project folder as: temperature.avi')
end
if stor>0
    display('Saving data...')
    save('temperature.mat');
    display('Simulation data file stored in project folder as: temperature.mat')
end
```

B.3.2 Input.m

```
%%%%%%%%%%%%%%%%%%%%%%%
%%%%% DESCRIPTION %%%%%
%%%%%%%%%%%%%%%%%%%%%%%

% Contains all simulation inputs.
% Adrian Lutey, University of Bologna, 2013


%%%%%%%%%%%%%%%%%%%%%%%%%%%%%%%%%%%%%%%%%%%%%%%%%%%%%%%%%%%%%%%%%%%%%%%%%%%%%%%
%%%%% INCIDENT FIELD / ENVIRONMENT SPECIFICATION %%%%%
%%%%%%%%%%%%%%%%%%%%%%%%%%%%%%%%%%%%%%%%%%%%%%%%%%%%%%%%%%%%%%%%%%%%%%%%%%%%%%%

PULSE=1;                    % Laser type (0=CW, 1=Pulsed)

% CW-specific (applicable only in case PULSE=0)
PEinc=0;                    % Laser power (W) of TE polarised component
PMinc=0;                    % Laser power (W) of TM polarised component
tmax=0;                     % Length of simulation (seconds)
```

```
% Pulsed-specific (applicable only in case PULSE=1)
EPEinc=0.126;               % Pulse energy (mJ) of TE polarised component
EPMinc=0;                   % Pulse energy (mJ) of TM polarised component
FWHM=10;                    % Pulse full width at half maximum (ns)
RR=30;                      % Repetition rate (kHz)
tnum=150;                   % Number of pulses

% Mutual
V=0.05;                     % Translation velocity (m/s, x-direction)
w0=15;                      % Beam waist radius (micron)
lambda0=0.515;              % Beam wavelength in a vacuum (micron)
Ta=25;                      % Ambient temperature (degC)
theta=0;                    % Angle of incidence (deg)


%%%%%%%%%%%%%%%%%%%%%%%%%%%%%%%%
%%%%% TARGET SPECIFICATION %%%%%
%%%%%%%%%%%%%%%%%%%%%%%%%%%%%%%%

% Layer 0: Preceeding Medium
COHERENT(1)=0;
n(1)=1;
kappa(1)=0;

% Layer 1
Layer=1;                    % Layer number
COHERENT(Layer+1)=0;        % Is the interface with next layer coherent? [0=No, 1=Yes]
h(Layer+1)=20;              % Layer thickness (micron)
Polypropylene               % Layer material properties file
n(Layer+1)=interp1(lambda0lambda0,nlambda0,lambda0,'linear');         % Layer refractive index
kappa(Layer+1)=interp1(lambda0lambda0,kappalambda0,lambda0,'linear'); % Layer extinction coefficient
Ks(Layer)=Ksmat;            % Layer thermal conductivity (W/mK)
Kl(Layer)=Klmat;            % Layer thermal conductivity (W/mK)
rho(Layer)=rhomat;          % Layer density (kg/m^3)
Cps(Layer)=Cpsmat;          % Layer solid specific heat capacity (J/gK)
Cpl(Layer)=Cplmat;          % Layer liquid specific heat capacity (J/gK)
Tm(Layer)=Tmmat;            % Melting temperature (degC)
Tv(Layer)=Tvmat;            % Boiling/combustion temperature (degC)
Hf(Layer)=Hfmat;            % Heat of fusion (J/g)
Hv(Layer)=Hvmat;            % Heat of vaporisation (J/g)
Tdept(Layer,:)=Tdepmat;     % Temperature data points for pulse calculation (degC)
IratFPt(Layer,:)=IratFPmat;% Linear absorption ratio multiplied by total fluence data points (J/cm^2)
cutdt(Layer,:,:)=cutdmat;  % Ablation depth data points (m)
cutht(Layer,:,:)=cuthmat;  % Absorbed fluence data points (J/m^2)

% Layer 2
Layer=2;
COHERENT(Layer+1)=0;
h(Layer+1)=9;
Aluminium
n(Layer+1)=interp1(lambda0lambda0,nlambda0,lambda0,'linear');
kappa(Layer+1)=interp1(lambda0lambda0,kappalambda0,lambda0,'linear');
Ks(Layer)=Ksmat;
Kl(Layer)=Klmat;
rho(Layer)=rhomat;
Cps(Layer)=Cpsmat;
Cpl(Layer)=Cplmat;
Tm(Layer)=Tmmat;
Tv(Layer)=Tvmat;
Hf(Layer)=Hfmat;
Hv(Layer)=Hvmat;
Tdept(Layer,:)=Tdepmat;
IratFPt(Layer,:)=IratFPmat;
cutdt(Layer,:,:)=cutdmat;
cutht(Layer,:,:)=cuthmat;

% Layer 3
Layer=3;
COHERENT(Layer+1)=0;
h(Layer+1)=20;
Polypropylene
n(Layer+1)=interp1(lambda0lambda0,nlambda0,lambda0,'linear');
kappa(Layer+1)=interp1(lambda0lambda0,kappalambda0,lambda0,'linear');
Ks(Layer)=Ksmat;
Kl(Layer)=Klmat;
rho(Layer)=rhomat;
Cps(Layer)=Cpsmat;
Cpl(Layer)=Cplmat;
Tm(Layer)=Tmmat;
Tv(Layer)=Tvmat;
Hf(Layer)=Hfmat;
Hv(Layer)=Hvmat;
Tdept(Layer,:)=Tdepmat;
IratFPt(Layer,:)=IratFPmat;
cutdt(Layer,:,:)=cutdmat;
cutht(Layer,:,:)=cuthmat;

% Layer M: Proceeding Medium
M=Layer+2;                  % Number of layers (including pre- and proceeding)
COHERENT(M)=0;
h(M)=0;
n(M)=1;
kappa(M)=0;


%%%%%%%%%%%%%%%%%%%%%%%%%%%%%%%%
```

```
%%%%% NUMERICAL PARAMETERS %%%%%
%%%%%%%%%%%%%%%%%%%%%%%%%%%%%%%%

% Input parameters
divsit=50000;               % Number of time-steps
xcord=400;                  % (+/-1*w0) domain
ycord=400;                  % (+1*w0) domain
divsix=100;                 % Total number of x-divisions
divsiy=50;                  % Total number of y-divisions
mult=1.153;                 % Mesh difference multiplier [default 1.153]

% Output options / advanced parameters
vid=0;                      % Video output [0=No, 1=Yes]
stor=1;                     % Data storage [0=No, 1=Yes]
plottime=30;                % Length of simulation video (s)
plotview=40;                % (+/-*w0) maximum plot domain
Tmax=2500;                  % Plot range maximum temperature (degC)
storesize=500;              % Number of video/data points stored
noise=1e-7;                 % Noise floor [default 1e-7]
filt=1;                     % Range limiter filter [0=No, 1=Yes]
```

B.3.3 bound.m

```
%%%%%%%%%%%%%%%%%%%%%%%%
%%%%% DESCRIPTION %%%%%
%%%%%%%%%%%%%%%%%%%%%%%%

% Compatibility condition sub-program.
% Adrian Lutey, University of Bologna, 2013


%%%%%%%%%%%%%%%%%%%%%%
%%%%% SOLUTION %%%%%
%%%%%%%%%%%%%%%%%%%%%%

% In the case of simultaneous compatibility conditions, the highest value
% is taken.
Hbound=0;   % Reset boundary value
for p=1:M-2
    % Higher energy state to left, solid at point of interest
    if state(bini1,binj1,p)>0 && state(bini2,binj2,p)==0
        % Check that left is actually higher energy state and not just
        % removed
        if Hbound<Hmelt(map(bini2,binj2),p) && Hmen(bini1,binj1)>Hmelt(map(bini1,binj1),p)
            Hbound=Hmelt(map(bini2,binj2),p);
        % Otherwise assign as value from previous step
        elseif Hbound<Hmelt(map(bini2,binj2),p)
            Hbound=Hmen(bini1,binj1);
            for pp=1:M-2
                if state(bini1,binj1,pp)~=4 && state(bini2,binj2,pp)==4
                    Hbound=Hbound-Htmen(bini1,binj1,pp);
                elseif state(bini1,binj1,pp)==4 && state(bini2,binj2,pp)~=4
                    Hbound=Hbound+Htmen(bini1,binj1,pp);
                end
            end
        end
    % Lower energy state to left, liquid at point of interest
    elseif state(bini1,binj1,p)<2 && state(bini2,binj2,p)==2
        if Hbound<Hliq(map(bini2,binj2),p)
            Hbound=Hliq(map(bini2,binj2),p);
        end
    % Higher energy state to left, liquid at point of interest
    elseif state(bini1,binj1,p)>2 && state(bini2,binj2,p)==2
        % Check that left is actually higher energy state and not just
        % removed
        if Hbound<Hvap(map(bini2,binj2),p) && Hmen(bini1,binj1)>Hvap(map(bini1,binj1),p)
            Hbound=Hvap(map(bini2,binj2),p);
        % Otherwise assign as value from previous step
        elseif Hbound<Hvap(map(bini2,binj2),p)
            Hbound=Hmen(bini1,binj1);
            for pp=1:M-2
                if state(bini1,binj1,pp)~=4 && state(bini2,binj2,pp)==4
                    Hbound=Hbound-Htmen(bini1,binj1,pp);
                elseif state(bini1,binj1,pp)==4 && state(bini2,binj2,pp)~=4
                    Hbound=Hbound+Htmen(bini1,binj1,pp);
                end
            end
        end
    % Lower energy state to left, removed at point of interest
    elseif state(bini1,binj1,p)<4 && state(bini2,binj2,p)==4
        % Check that current value is actually higher energy state and not
        % just removed
        if Hbound<Hrem(map(bini2,binj2),p) && Hmen(bini2,binj2)>=Hrem(map(bini2,binj2),p)
            Hbound=Hrem(map(bini2,binj2),p);
        % Otherwise assign as value from previous step
        elseif Hbound<Hrem(map(bini2,binj2),p)
            Hbound=Hmen(bini1,binj1);
            for pp=1:M-2
```

```
                if state(bini1,binj1,pp)~=4 && state(bini2,binj2,pp)==4
                    Hbound=Hbound-Htmen(bini1,binj1,pp);
                elseif state(bini1,binj1,pp)==4 && state(bini2,binj2,pp)~=4
                    Hbound=Hbound+Htmen(bini1,binj1,pp);
                end
            end
        end
    end
end

% Assign boundary value to heat flow calculation matrix
if tp(i,j,1)==2
    R(Pos) = R(Pos) + 2*Hbound*valu;
else
    R(Pos) = R(Pos) + 2*Hbound*-valu;
end
```

B.4 Common Files

B.4.1 Optics.m

```
%%%%%%%%%%%%%%%%%%%%%%%%
%%%%% DESCRIPTION %%%%%
%%%%%%%%%%%%%%%%%%%%%%%%

% Simulation of coherent and incoherent plane wave propagation and absorption
% in multi-layered medium. All layers assumed to be non-magnetic.
% Adrian Lutey, University of Bologna, 2013


%%%%%%%%%%%%%%%%%%%%%%%%%%%%%%%%
%%%%% CALCULATION CONSTANTS %%%%%
%%%%%%%%%%%%%%%%%%%%%%%%%%%%%%%%

km=omega.*(n+1i.*kappa)./c;                 % Wave number vector
sincx=sind(theta);                          % Direction vector x component
sprimez=sqrt(1-km(1)^2./km.^2*sincx^2);     % Direction vector z component
um=sqrt(km.^2-(km(1)*sincx)^2);             % Direction vector z / km


%%%%%%%%%%%%%%%%%%%%%%%%%%%%%
%%%%% SOLUTION TE WAVE %%%%%
%%%%%%%%%%%%%%%%%%%%%%%%%%%%%

% l-1 is the total number of incoherent interfaces considered. l-2 is the
% reduced number of layers.
if IEinc>0;
    qe1=0;
    l=1;
    j=1;
    for i=1:M-1
        if i>=j
            % Use coherent matrix method for reflectance and transmission coefficients
            if COHERENT(i)==1
                for j=i:M
                    if COHERENT(j)==1
                    else
                        break
                    end
                end
                TEW;
                RE(l)=abs(rE)^2;
                REprime(l)=abs(rEprime)^2;
                TE(l)=abs(tE)^2*real((n(j)+1i*kappa(j))*sprimez(j)/(sprimez(i)*(n(i)+1i*kappa(i))));
                TEprime(l)=abs(tEprime)^2*real((n(i)+1i*kappa(i))*sprimez(i)/(sprimez(j)*(n(j)+1i*kappa(j))));
            % Evaluate reflectance and transmission coefficients assuming incoherence
            else
                RE(l)=abs(((n(i)+1i.*kappa(i)).*sprimez(i)-(n(i+1)+1i.*kappa(i+1)).*sprimez(i+1))./((n(i)+1i.*kappa(i)).*sprimez(i)+
(n(i+1)+1i.*kappa(i+1)).*sprimez(i+1))).^2;
                REprime(l)=RE(l);
                TE(l)=1-RE(l);
                TEprime(l)=TE(l);
            end
            % Incoherent coefficients; transfer matrix components
            aUEm(l)=(TE(l).*TEprime(l)-RE(l).*REprime(l))./TEprime(l).*abs(exp(1i.*km(i).*sprimez(i).*h(i).*1e-6)).^2;
            bUEm(l)=REprime(l)./TEprime(l).*abs(exp(-1i.*km(i).*sprimez(i).*h(i).*1e-6)).^2;
            cUEm(l)=-RE(l)./TEprime(l).*abs(exp(1i.*km(i).*sprimez(i).*h(i).*1e-6)).^2;
            dUEm(l)=1./TEprime(l).*abs(exp(-1i.*km(i).*sprimez(i).*h(i).*1e-6)).^2;
            l=l+1;
        end
    end

    % Transfer matrix loop. Initial statement is assignment of components to
    % layer transfer matrix. First 'if' considers all transfer matrices from
```

```
    % 2nd on and constructs total transfer matrix based on current layer
    % transfer matrix and previous total transfer matrix. Second 'if' detects
    % no transmission and activates trigger q=1, leaves total transfer matrix
    % as is (unless k=1, in which case reflected field is set to 0) and zeros
    % current layer transfer matrix. Third 'if' sets initial total transfer
    % matrix equal to first layer transfer matrix. Fourth 'if' detects trigger
    % and zeros all proceeding layer transfer matrices.
    qi=0;
    for k=1:l-1;
        TUEm(1:2,2*k-1:2*k)=[aUEm(k),bUEm(k);cUEm(k),dUEm(k)];
        if qi==0 && k>1 && max(max(isnan(TUEm(1:2,2*k-1:2*k))))==0 && max(max(isnan(TUEm(1:2,2*k-1:2*k)*TUE)))==0 &&
max(max(abs(TUEm(1:2,2*k-1:2*k))))<1/noise && max(max(abs(TUEm(1:2,2*k-1:2*k)*TUE)))<1/noise
            TUE=TUEm(1:2,2*k-1:2*k)*TUE;
        elseif qi==0 && (max(max(isnan(TUEm(1:2,2*k-1:2*k))))==1 || max(max(abs(TUEm(1:2,2*k-1:2*k))))>=1/noise || (k>1 &&
max(max(isnan(TUEm(1:2,2*k-1:2*k)*TUE)))==1) || (k>1 && max(max(abs(TUEm(1:2,2*k-1:2*k)*TUE)))>=1/noise))
            qi=k;
            TUEm(1:2,2*k-1:2*k)=zeros(2,2);
            if k==1
                TUE(2,2)=1;
            end
        elseif qi==0 && k==1
            TUE=TUEm(1:2,2*k-1:2*k);
        elseif qi>0
            TUEm(1:2,2*k-1:2*k)=zeros(2,2);
        end
    end

    % Incident & reflected field
    GUE(:,1)=[IEinc;-TUE(2,1)/TUE(2,2)*IEinc];

    % Coefficient vector loop. Initial statement constructs the proceeding
    % layer coefficient vector based on current layer transfer matrix and
    % coefficient vector. 'If' statements remove small (noisy) coefficients to
    % avoid noise amplification.
    for i=1:l-1;
        GUE(1:2,i+1)=TUEm(1:2,2*i-1:2*i)*GUE(1:2,i);
        if abs(GUE(1,i+1))/abs(GUE(1,1))<noise
            GUE(1,i+1)=0;
        end
        if abs(GUE(2,i+1))/abs(GUE(2,1))<noise
            GUE(2,i+1)=0;
        end
    end

    % Evaluation of absorption for forward and backward global waves. First 'if' statement
    % proceeds for coherent cases and diverts to 'TEW'. Second 'if' evaluates
    % for all layers prior to non-transmitting layer. Final 'if' evaluates only
    % forward travelling wave in non-transmitting materials, as exponential on
    % backward travelling wave is Inf (same as in transfer matrices).
    qe1=1;
    l=1;
    j=1;
    for i=1:M-2;
        if i>=j-1
            if COHERENT(i)==1 && COHERENT(i+1)==1
                for j=i+1:M
                    if COHERENT(j)==1;
                    else
                        break
                    end
                end
                TEW
            elseif i+1<qi || qi==0
                IEABS(i)=GUE(1,l+1)*(1-abs(exp(1i.*km(i+1).*sprimez(i+1).*h(i+1).*1e-6)).^2)+GUE(2,l+1)*(abs(exp(-1i.*km(i+1).*
sprimez(i+1).*h(i+1).*1e-6)).^2-1);
                l=l+1;
            else
                IEABS(i)=GUE(1,l+1)*(1-abs(exp(1i.*km(i+1).*sprimez(i+1).*h(i+1).*1e-6)).^2);
                l=l+1;
            end
        end
    end
else
    IEABS=0;
end


%%%%%%%%%%%%%%%%%%%%%%%%%%%%%%
%%%%% SOLUTION TM WAVE %%%%%
%%%%%%%%%%%%%%%%%%%%%%%%%%%%%%

% l-1 is the total number of incoherent interfaces considered. l-2 is the
% reduced number of layers.
if IMinc>0
    qm1=0;
    l=1;
    j=1;
    for i=1:M-1
        if i>=j
            % Use coherent matrix method for reflectance and transmission coefficients
            if COHERENT(i)==1
                for j=i:M
                    if COHERENT(j)==1
                    else
                        break
                    end
                end
```

```
                TMW;
                RM(l)=abs(rM)^2;
                RMprime(l)=abs(rMprime)^2;
                TM(l)=abs(tM)^2*real((n(j)+1i*kappa(j))*sprimez(j)/(sprimez(i)*(n(i)+1i*kappa(i))));
                TMprime(l)=abs(tMprime)^2*real((n(i)+1i*kappa(i))*sprimez(i)/(sprimez(j)*(n(j)+1i*kappa(j))));
            % Evaluate reflectance and transmission coefficients assuming incoherence
            else
                RM(l)=abs(((n(i+1)+1i.*kappa(i+1)).*sprimez(i)-(n(i)+1i.*kappa(i)).*sprimez(i+1))./((n(i+1)+1i.*kappa(i+1)).*sprimez(i)+
(n(i)+1i.*kappa(i)).*sprimez(i+1))).^2;
                RMprime(l)=RM(l);
                TM(l)=1-RM(l);
                TMprime(l)=TM(l);
            end
            % Incoherent coefficients; transfer matrix components
            aUMm(l)=(TM(l).*TMprime(l)-RM(l).*RMprime(l))./TMprime(l).*abs(exp(1i.*km(i).*sprimez(i).*h(i).*1e-6)).^2;
            bUMm(l)=RMprime(l)./TMprime(l).*abs(exp(-1i.*km(i).*sprimez(i).*h(i).*1e-6)).^2;
            cUMm(l)=-RM(l)./TMprime(l).*abs(exp(1i.*km(i).*sprimez(i).*h(i)*1e-6)).^2;
            dUMm(l)=1./TMprime(l).*abs(exp(-1i.*km(i).*sprimez(i).*h(i).*1e-6)).^2;
            l=l+1;
        end
    end

    % Transfer matrix loop. Initial statement is assignment of components to
    % layer transfer matrix. First 'if' considers all transfer matrices from
    % 2nd on and constructs total transfer matrix based on current layer
    % transfer matrix and previous total transfer matrix. Second 'if' detects
    % no transmission and activates trigger q=1, leaves total transfer matrix
    % as is (unless k=1, in which case reflected field is set to 0) and zeros
    % current layer transfer matrix. Third 'if' sets initial total transfer
    % matrix equal to first layer transfer matrix. Fourth 'if' detects trigger
    % and zeros all proceeding layer transfer matrices.
    qi=0;
    for k=1:l-1;
        TUMm(1:2,2*k-1:2*k)=[aUMm(k),bUMm(k);cUMm(k),dUMm(k)];
        if qi==0 && k>1 && max(max(isnan(TUMm(1:2,2*k-1:2*k))))==0 && max(max(isnan(TUMm(1:2,2*k-1:2*k)*TUM)))==0 &&
max(max(abs(TUMm(1:2,2*k-1:2*k)))<1/noise && max(max(abs(TUMm(1:2,2*k-1:2*k)*TUM)))<1/noise
            TUM=TUMm(1:2,2*k-1:2*k)*TUM;
        elseif qi==0 && (max(max(isnan(TUMm(1:2,2*k-1:2*k))))==1 || max(max(abs(TUMm(1:2,2*k-1:2*k))))>=1/noise || (k>1 &&
max(max(isnan(TUMm(1:2,2*k-1:2*k)*TUM)))==1) || (k>1 && max(max(abs(TUMm(1:2,2*k-1:2*k)*TUM)))>=1/noise))
            qi=k;
            TUMm(1:2,2*k-1:2*k)=zeros(2,2);
            if k==1
                TUM(2,2)=1;
            end
        elseif qi==0 && k==1
            TUM=TUMm(1:2,2*k-1:2*k);
        elseif qi>0
            TUMm(1:2,2*k-1:2*k)=zeros(2,2);
        end
    end

    % Incident & reflected field
    GUM(:,1)=[IMinc;-TUM(2,1)/TUM(2,2)*IMinc];

    % Coefficient vector loop. Initial statement constructs the proceeding
    % layer coefficient vector based on current layer transfer matrix and
    % coefficient vector. 'If' statements remove small (noisy) coefficients to
    % avoid noise amplification.
    for i=1:l-1;
        GUM(1:2,i+1)=TUMm(1:2,2*i-1:2*i)*GUM(1:2,i);
        if abs(GUM(1,i+1))/abs(GUM(1,1))<noise
            GUM(1,i+1)=0;
        end
        if abs(GUM(2,i+1))/abs(GUM(2,1))<noise
            GUM(2,i+1)=0;
        end
    end

    % Evaluation of absorption for forward and backward global waves. First 'if' statement
    % proceeds for coherent cases and diverts to 'TEW'. Second 'if' evaluates
    % for all layers prior to non-transmitting layer. Final 'if' evaluates only
    % forward travelling wave in non-transmitting materials, as exponential on
    % backward travelling wave is Inf (same as in transfer matrices).
    qm1=1;
    l=1;
    j=1;
    for i=1:M-2;
        if i>=j-1
            if COHERENT(i)==1 && COHERENT(i+1)==1
                for j=i:M
                    if COHERENT(j)==1;
                    else
                        break
                    end
                end
                TMW
            elseif i+1<qi || qi==0
                IMABS(i)=GUM(1,l+1)*(1-abs(exp(1i.*km(i+1).*sprimez(i+1).*h(i+1).*1e-6)).^2)+GUM(2,l+1)*(abs(exp(-1i.*km(i+1).*
sprimez(i+1).*h(i+1).*1e-6)).^2-1);
                l=l+1;
            else
                IMABS(i)=GUM(1,l+1)*(1-abs(exp(1i.*km(i+1).*sprimez(i+1).*h(i+1).*1e-6)).^2);
                l=l+1;
            end
        end
    end
else
```

```
    IMABS=0;
end


%%%%%%%%%%%%%%%%%%%%%%%%%%%%%%%%%%%%
%%%%% TOTAL LAYER ABSORPTION %%%%%
%%%%%%%%%%%%%%%%%%%%%%%%%%%%%%%%%%%%

IABS=IEABS+IMABS;
```

B.4.2 TEW.m

```
%%%%%%%%%%%%%%%%%%%%%%%%
%%%%% DESCRIPTION %%%%%
%%%%%%%%%%%%%%%%%%%%%%%%

% Coherent TE plane-wave propagation sub-program.
% Adrian Lutey, University of Bologna, 2013


%%%%%%%%%%%%%%%%%%%%%%
%%%%% SOLUTION %%%%%
%%%%%%%%%%%%%%%%%%%%%%

% Transfer matrix components
aEm=(1+um(i:j-1)./um(i+1:j)).*exp(1i.*um(i:j-1).*[0 h(i+1:j-1)].*1e-6)./2;
bEm=(1-um(i:j-1)./um(i+1:j)).*exp(1i.*-um(i:j-1).*[0 h(i+1:j-1)].*1e-6)./2;
cEm=(1-um(i:j-1)./um(i+1:j)).*exp(1i.*um(i:j-1).*[0 h(i+1:j-1)].*1e-6)./2;
dEm=(1+um(i:j-1)./um(i+1:j)).*exp(1i.*-um(i:j-1).*[0 h(i+1:j-1)].*1e-6)./2;

% Transfer matrix loop. Initial statement is assignment of components to
% layer transfer matrix. First 'if' considers all transfer matrices from
% 2nd on and constructs total transfer matrix based on current layer
% transfer matrix and previous total transfer matrix. Second 'if' detects
% no transmission and activates trigger q=1, leaves total transfer matrix
% as is (unless k=1, in which case reflected field is set to 0) and zeros
% current layer transfer matrix. Third 'if' sets initial total transfer
% matrix equal to first layer transfer matrix. Fourth 'if' detects trigger
% and zeros all proceeding layer transfer matrices.
q=0;
for k=1:j-i;
    TEEm(1:2,2*k-1:2*k)=[aEm(k),bEm(k);cEm(k),dEm(k)];
    if q==0 && k>1 && max(max(isnan(TEEm(1:2,2*k-1:2*k))))==0 && max(max(isnan(TEEm(1:2,2*k-1:2*k)*TEE)))==0 &&
max(max(abs(TEEm(1:2,2*k-1:2*k))))<1/noise && max(max(abs(TEEm(1:2,2*k-1:2*k)*TEE)))<1/noise
        TEE=TEEm(1:2,2*k-1:2*k)*TEE;
    elseif q==0 && (max(max(isnan(TEEm(1:2,2*k-1:2*k))))==1 || max(max(abs(TEEm(1:2,2*k-1:2*k))))>=1/noise || (k>1 &&
max(max(isnan(TEEm(1:2,2*k-1:2*k)*TEE)))==1) || (k>1 && max(max(abs(TEEm(1:2,2*k-1:2*k)*TEE)))>=1/noise))
        q=k;
        TEEm(1:2,2*k-1:2*k)=zeros(2,2);
        if k==1
            TEE(2,2)=1;
        end
    elseif q==0 && k==1
        TEE=TEEm(1:2,2*k-1:2*k);
    elseif q>0
        TEEm(1:2,2*k-1:2*k)=zeros(2,2);
    end
end

rE=-TEE(2,1)/TEE(2,2);
if q==0 && isnan(det(TEE)/TEE(2,2))==0 && isnan(1/TEE(2,2))==0
    rEprime=TEE(1,2)/TEE(2,2);
    tE=det(TEE)/TEE(2,2);
    tEprime=1/TEE(2,2);
else
    rEprime=0;
    tE=0;
    tEprime=1;
end

if qe1==1

    % Incident & reflected field
    GEF(:,1)=[sqrt(2/c/e0*GUE(1,l)*abs(exp(1i.*km(i).*sprimez(i).*h(i).*1e-6)).^2);rE*sqrt(2/c/e0*GUE(1,l)*abs(exp(1i.*km(i).*
sprimez(i).*h(i).*1e-6)).^2)];
    if q==0
        GEB(:,j-i+1)=[rEprime*sqrt(2/c/e0*GUE(2,l+1));sqrt(2/c/e0*GUE(2,l+1))];
    end

    % Coefficient vector loop. Initial statement constructs the proceeding
    % layer coefficient vector based on current layer transfer matrix and
    % coefficient vector. 'If' statements remove small (noisy) coefficients
    % to avoid noise amplification. Second 'for' loop does the same with
    % the reverse wave
    for k=1:j-i;
        GEF(1:2,k+1)=TEEm(1:2,2*k-1:2*k)*GEF(1:2,k);
        if abs(GEF(1,k+1))/abs(GEF(1,1))<noise
            GEF(1,k+1)=0;
```

```
        end
        if abs(GEF(2,k+1))/abs(GEF(2,1))<noise
            GEF(2,k+1)=0;
        end
    end

    if q==0 && isnan(det(TEE)/TEE(2,2))==0 && abs(det(TEE)/TEE(2,2))<1/noise && isnan(1/TEE(2,2))==0 && abs(1/TEE(2,2))<1/noise
        for k=j-i-(0:j-i-1);
            GEB(1:2,k)=inv(TEEm(1:2,2*k-1:2*k))*GEB(1:2,k+1);
            if abs(GEB(1,k))/abs(GEB(1,j-i+1))<noise
                GEB(1,k)=0;
            end
            if abs(GEB(2,k))/abs(GEB(2,j-i+1))<noise
                GEB(2,k)=0;
            end
        end
    end

    % Evaluation of intensity at start of layers (row 1) and at end (row
    % 2) for forward (IEEF) and backward (IEEB) global waves. First 'if'
    % statement proceeds for all layers when all are transmitting. Second
    % 'if' evaluates only forward travelling global wave, to the point of
    % the non-transmitting layer (as nothing has been transmitted through
    % the material to have reflections from incoherent layers and thus
    % provide the backward global wave). Final 'if' evaluates only forward
    % travelling component of local wave in non-transmitting materials, as
    % exponential on backward travelling wave is NaN (same as in transfer
    % matrices).
    for k=1:j-i-1;
        if q==0 && isnan(det(TEE)/TEE(2,2))==0 && abs(det(TEE)/TEE(2,2))<1/noise && isnan(1/TEE(2,2))==0 && abs(1/TEE(2,2))<1/noise
            IEEF(1,k)=c*e0/2*real((GEF(1,k+1)+GEF(2,k+1))*conj((n(k+i)+1i*kappa(k+i))*sprimez(k+i)/(sprimez(i)*(n(i)+1i*kappa(i)))*
(GEF(1,k+1)-GEF(2,k+1))));
            IEEF(2,k)=c*e0/2*real((GEF(1,k+1)*exp(1i*h(k+i)*1e-6*um(k+i))+GEF(2,k+1)*exp(-1i*h(k+i)*1e-6*um(k+i)))*conj((n(k+i)+
1i*kappa(k+i))*sprimez(k+i)/(sprimez(i)*(n(i)+1i*kappa(i)))*(GEF(1,k+1)*exp(1i*h(k+i)*1e-6*um(k+i))-GEF(2,k+1)*exp(-1i*h(k+i)*1e-6*
um(k+i)))));
            IEEB(1,k)=c*e0/2*real((GEB(1,k+1)+GEB(2,k+1))*conj((n(k+i)+1i*kappa(k+i))*sprimez(k+i)/(sprimez(j)*(n(j)+1i*kappa(j)))*
(GEB(1,k+1)-GEB(2,k+1))));
            IEEB(2,k)=c*e0/2*real((GEB(1,k+1)*exp(1i*h(k+i)*1e-6*um(k+i))+GEB(2,k+1)*exp(-1i*h(k+i)*1e-6*um(k+i)))*conj((n(k+i)+
1i*kappa(k+i))*sprimez(k+i)/(sprimez(j)*(n(j)+1i*kappa(j)))*(GEB(1,k+1)*exp(1i*h(k+i)*1e-6*um(k+i))-GEB(2,k+1)*exp(-1i*h(k+i)*1e-6*
um(k+i)))));
        elseif k+1<q || q==0
            IEEF(1,k)=c*e0/2*real((GEF(1,k+1)+GEF(2,k+1))*conj((n(k+i)+1i*kappa(k+i))*sprimez(k+i)/(sprimez(i)*(n(i)+1i*kappa(i)))*
(GEF(1,k+1)-GEF(2,k+1))));
            IEEF(2,k)=c*e0/2*real((GEF(1,k+1)*exp(1i*h(k+i)*1e-6*um(k+i))+GEF(2,k+1)*exp(-1i*h(k+i)*1e-6*um(k+i)))*conj((n(k+i)+
1i*kappa(k+i))*sprimez(k+i)/(sprimez(i)*(n(i)+1i*kappa(i)))*(GEF(1,k+1)*exp(1i*h(k+i)*1e-6*um(k+i))-GEF(2,k+1)*exp(-1i*h(k+i)*1e-6*
um(k+i)))));
            IEEB(1,k)=0;
            IEEB(2,k)=0;
        else
            IEEF(1,k)=c*e0/2*real((GEF(1,k+1))*conj((n(k+i)+1i*kappa(k+i))*sprimez(k+i)/(sprimez(i)*(n(i)+1i*kappa(i)))*(GEF(1,k+1))));
            IEEF(2,k)=c*e0/2*real((GEF(1,k+1)*exp(1i*h(k+i)*1e-6*um(k+i)))*conj((n(k+i)+1i*kappa(k+i))*sprimez(k+i)/(sprimez(i)*(n(i)+
1i*kappa(i)))*(GEF(1,k+1)*exp(1i*h(k+i)*1e-6*um(k+i)))));
            IEEB(1,k)=0;
            IEEB(2,k)=0;
        end
        IEABS(i+k-1)=IEEF(1,k)-IEEF(2,k)+IEEB(1,k)-IEEB(2,k);
    end
end
```

B.4.3 TMW.m

```
%%%%%%%%%%%%%%%%%%%%%%
%%%%% DESCRIPTION %%%%%
%%%%%%%%%%%%%%%%%%%%%%

% Coherent TW plane-wave propagation sub-program.
% Adrian Lutey, University of Bologna, 2013


%%%%%%%%%%%%%%%%%%%%%
%%%%% SOLUTION %%%%%
%%%%%%%%%%%%%%%%%%%%%

% Transfer matrix components
aMm=(1+um(i:j-1)./um(i+1:j).*(2.*omega.*n(i+1:j).*kappa(i+1:j)+1i.*omega.*(kappa(i+1:j).^2-n(i+1:j).^2))./(2.*omega.*n(i:j-1).*
kappa(i:j-1)+1i.*omega.*(kappa(i:j-1).^2-n(i:j-1).^2))).*exp(1i.*um(i:j-1).*[0 h(i+1:j-1)].*1e-6)./2;
bMm=(1-um(i:j-1)./um(i+1:j).*(2.*omega.*n(i+1:j).*kappa(i+1:j)+1i.*omega.*(kappa(i+1:j).^2-n(i+1:j).^2))./(2.*omega.*n(i:j-1).*
kappa(i:j-1)+1i.*omega.*(kappa(i:j-1).^2-n(i:j-1).^2))).*exp(1i.*-um(i:j-1).*[0 h(i+1:j-1)].*1e-6)./2;
cMm=(1-um(i:j-1)./um(i+1:j).*(2.*omega.*n(i+1:j).*kappa(i+1:j)+1i.*omega.*(kappa(i+1:j).^2-n(i+1:j).^2))./(2.*omega.*n(i:j-1).*
kappa(i:j-1)+1i.*omega.*(kappa(i:j-1).^2-n(i:j-1).^2))).*exp(1i.*um(i:j-1).*[0 h(i+1:j-1)].*1e-6)./2;
dMm=(1+um(i:j-1)./um(i+1:j).*(2.*omega.*n(i+1:j).*kappa(i+1:j)+1i.*omega.*(kappa(i+1:j).^2-n(i+1:j).^2))./(2.*omega.*n(i:j-1).*
kappa(i:j-1)+1i.*omega.*(kappa(i:j-1).^2-n(i:j-1).^2))).*exp(1i.*-um(i:j-1).*[0 h(i+1:j-1)].*1e-6)./2;

% Transfer matrix loop. Initial statement is assignment of components to
% layer transfer matrix. First 'if' considers all transfer matrices from
% 2nd on and constructs total transfer matrix based on current layer
% transfer matrix and previous total transfer matrix. Second 'if' detects
% no transmission and activates trigger q=1, leaves total transfer matrix
```

```
% as is (unless k=1, in which case reflected field is set to 0) and zeros
% current layer transfer matrix. Third 'if' sets initial total transfer
% matrix equal to first layer transfer matrix. Fourth 'if' detects trigger
% and zeros all proceeding layer transfer matrices.
q=0;
for k=1:j-i;
    TMMm(1:2,2*k-1:2*k)=[aMm(k),bMm(k);cMm(k),dMm(k)];
    if q==0 && k>1 && max(max(isnan(TMMm(1:2,2*k-1:2*k))))==0 && max(max(isnan(TMMm(1:2,2*k-1:2*k)*TMM)))==0 &&
max(max(abs(TMMm(1:2,2*k-1:2*k))))<1/noise && max(max(abs(TMMm(1:2,2*k-1:2*k)*TMM)))<1/noise
        TMM=TMMm(1:2,2*k-1:2*k)*TMM;
    elseif q==0 && (max(max(isnan(TMMm(1:2,2*k-1:2*k))))==1 || max(max(abs(TMMm(1:2,2*k-1:2*k))))>=1/noise ||
(k>1 && max(max(isnan(TMMm(1:2,2*k-1:2*k)*TMM)))==1) || (k>1 && max(max(abs(TMMm(1:2,2*k-1:2*k)*TMM)))>=1/noise))
        q=k;
        TMMm(1:2,2*k-1:2*k)=zeros(2,2);
        if k==1
            TMM(2,2)=1;
        end
    elseif q==0 && k==1
        TMM=TMMm(1:2,2*k-1:2*k);
    elseif q>0
        TMMm(1:2,2*k-1:2*k)=zeros(2,2);
    end
end

rM=TMM(2,1)/TMM(2,2);
if q==0 && isnan(det(TMM)/TMM(2,2))==0 && isnan(1/TMM(2,2))==0
    rMprime=-TMM(1,2)/TMM(2,2);
    tM=det(TMM)/TMM(2,2)*(n(i)+1i*kappa(i))/(n(j)+1i*kappa(j));
    tMprime=1/TMM(2,2)*(n(j)+1i*kappa(j))/(n(i)+1i*kappa(i));
else
    rMprime=0;
    tM=0;
    tMprime=1;
end

if qm1==1

    % Incident & reflected field
    GMF(:,1)=[sqrt(2*c*e0*GUM(1,l)*abs(exp(1i.*km(i).*sprimez(i).*h(i).*1e-6)).^2);-rM*sqrt(2*c*e0*GUM(1,l)*abs(exp(1i.*km(i).*
sprimez(i).*h(i).*1e-6)).^2)];
    if q==0
        GMB(:,j-i+1)=[-rMprime*sqrt(2*c*e0*GUM(2,l+1));sqrt(2*c*e0*GUM(2,l+1))];
    end

    % Coefficient vector loop. Initial statement constructs the proceeding
    % layer coefficient vector based on current layer transfer matrix and
    % coefficient vector. 'If' statements remove small (noisy) coefficients
    % to avoid noise amplification. Second 'for' loop does the same with
    % the reverse wave
    for k=1:j-i;
        GMF(1:2,k+1)=TMMm(1:2,2*k-1:2*k)*GMF(1:2,k);
        if abs(GMF(1,k+1))/abs(GMF(1,1))<noise
            GMF(1,k+1)=0;
        end
        if abs(GMF(2,k+1))/abs(GMF(2,1))<noise
            GMF(2,k+1)=0;
        end
    end

    if q==0 && isnan(det(TMM)/TMM(2,2))==0 && abs(det(TMM)/TMM(2,2))<1/noise && isnan(1/TMM(2,2))==0 && abs(1/TMM(2,2))<1/noise
        for k=j-i-(0:j-i-1);
            GMB(1:2,k)=inv(TMMm(1:2,2*k-1:2*k))*GMB(1:2,k+1);
            if abs(GMB(1,k))/abs(GMB(1,j-i+1))<noise
                GMB(1,k)=0;
            end
            if abs(GMB(2,k))/abs(GMB(2,j-i+1))<noise
                GMB(2,k)=0;
            end
        end
    end

    % Evaluation of intensity at start of layers (row 1) and at end (row
    % 2) for forward (IMMF) and backward (IMMB) global waves. First 'if'
    % statement proceeds for all layers when all are transmitting. Second
    % 'if' evaluates only forward travelling global wave, to the point of
    % the non-transmitting layer (as nothing has been transmitted through
    % the material to have reflections from incoherent layers and thus
    % provide the backward global wave). Final 'if' evaluates only forward
    % travelling component of local wave in non-transmitting materials, as
    % exponential on backward travelling wave is NaN (same as in transfer
    % matrices).
    for k=1:j-i-1;
        if q==0 && isnan(det(TMM)/TMM(2,2))==0 && abs(det(TMM)/TMM(2,2))<1/noise && isnan(1/TMM(2,2))==0 && abs(1/TMM(2,2))<1/noise
            IMMF(1,k)=1/2/c/e0*real((GMF(1,k+1)+GMF(2,k+1))*conj((n(i)+1i*kappa(i))*sprimez(k+i)/(sprimez(i)*(n(k+i)+1i*kappa(k+i)))*
(GMF(1,k+1)-GMF(2,k+1))));
            IMMF(2,k)=1/2/c/e0*real((GMF(1,k+1)*exp(1i*h(k+i)*1e-6*um(k+i))+GMF(2,k+1)*exp(-1i*h(k+i)*1e-6*um(k+i)))*conj((n(i)+
1i*kappa(i))*sprimez(k+i)/(sprimez(i)*(n(k+i)+1i*kappa(k+i)))*(GMF(1,k+1)*exp(1i*h(k+i)*1e-6*um(k+i))-GMF(2,k+1)*exp(-1i*h(k+i)*1e-6*
um(k+i)))));
            IMMB(1,k)=1/2/c/e0*real((GMB(1,k+1)+GMB(2,k+1))*conj((n(j)+1i*kappa(j))*sprimez(k+i)/(sprimez(j)*(n(k+i)+1i*kappa(k+i)))*
(GMB(1,k+1)-GMB(2,k+1))));
            IMMB(2,k)=1/2/c/e0*real((GMB(1,k+1)*exp(1i*h(k+i)*1e-6*um(k+i))+GMB(2,k+1)*exp(-1i*h(k+i)*1e-6*um(k+i)))*conj((n(j)+
1i*kappa(j))*sprimez(k+i)/(sprimez(j)*(n(k+i)+1i*kappa(k+i)))*(GMB(1,k+1)*exp(1i*h(k+i)*1e-6*um(k+i))-GMB(2,k+1)*exp(-1i*h(k+i)*1e-6*
um(k+i)))));
        elseif k+1<q || q==0
            IMMF(1,k)=1/2/c/e0*real((GMF(1,k+1)+GMF(2,k+1))*conj((n(i)+1i*kappa(i))*sprimez(k+i)/(sprimez(i)*(n(k+i)+1i*kappa(k+i)))*
(GMF(1,k+1)-GMF(2,k+1))));
            IMMF(2,k)=1/2/c/e0*real((GMF(1,k+1)*exp(1i*h(k+i)*1e-6*um(k+i))+GMF(2,k+1)*exp(-1i*h(k+i)*1e-6*um(k+i)))*conj((n(i)+
```

```
1i*kappa(i))*sprimez(k+i)/(sprimez(i)*(n(k+i)+1i*kappa(k+i)))*(GMF(1,k+1)*exp(1i*h(k+i)*1e-6*um(k+i))-GMF(2,k+1)*exp(-1i*h(k+i)*1e-6*
um(k+i)));
            IMMB(1,k)=0;
            IMMB(2,k)=0;
        else
            IMMF(1,k)=1/2/c/e0*real((GMF(1,k+1))*conj((n(i)+1i*kappa(i))*sprimez(k+i)/(sprimez(i)*(n(k+i)+1i*kappa(k+i)))*(GMF(1,k+1))));
            IMMF(2,k)=1/2/c/e0*real((GMF(1,k+1)*exp(1i*h(k+i)*1e-6*um(k+i)))*conj((n(i)+1i*kappa(i))*sprimez(k+i)/(sprimez(i)*(n(k+i)+
1i*kappa(k+i)))*(GMF(1,k+1)*exp(1i*h(k+i)*1e-6*um(k+i)));
            IMMB(1,k)=0;
            IMMB(2,k)=0;
        end
        IMABS(i+k-1)=IMMF(1,k)-IMMF(2,k)+IMMB(1,k)-IMMB(2,k);
    end
end
```

B.4.4 Typical Material File (Aluminium.m)

```
%%%%%%%%%%%%%%%%%%%%%%%%
%%%%% DESCRIPTION %%%%%
%%%%%%%%%%%%%%%%%%%%%%%%

% Material data file: aluminium.
% Adrian Lutey, University of Bologna, 2013


%%%%%%%%%%%%%%%%%%%%%%%%%%%%%%%%
%%%%% PHYSICAL PROPERTIES %%%%%
%%%%%%%%%%%%%%%%%%%%%%%%%%%%%%%%

Ksmat=220;          % Solid thermal conductivity (W/mK)
Klmat=100;          % Liquid thermal conductivity (W/mK)
rhomat=2700;        % Density (kg/m^3)
Cpsmat=0.904;       % Solid specific heat capacity (J/gk)
Cplmat=0.904;       % Liquid specific heat capacity (J/gk)
Tmmat=650;          % Melting temperature (degC)
Tvmat=2519;         % Vaporisation temperature (degC)
Hfmat=390;          % Enthalpy of fusion (J/g)
Hvmat=10875;        % Enthalpy of vaporisation (J/g)
Tcmat=6427;         % Critical temperature (degC)
molmat=26.9815386;  % Molar mass (g/mol)
valmat=3;           % Number of valence electrons

% Room temperature optical properties
lambda0lambda0=[0
1.3776E+01
1.2398E+01



    .
    .
    .


1.7711E-01
1.6531E-01
1.5498E-01];

nlambda0=[3.9651E+01
3.9651E+01
3.4464E+01



    .
    .
    .



9.5000E-02
8.2000E-02
7.2000E-02];

kappalambda0=[1.1410E+02
1.1410E+02
1.0560E+02



    .
    .
    .


1.9830E+00
1.8140E+00
1.6630E+00];

% Electrical conductivity above melting temperature
Tmat=[933.521
```

```
1000
1100
1200
1300
1400
1500
1600
1700
1800
1900
2000] - 273.*ones(12,1);

Resmat=[24.77
25.88
27.46
28.95
30.38
31.77
33.11
34.40
35.69
36.93
38.18
39.34].*1e-8;

Resmatcoeff=polyfit(Tmat,Resmat,1);

Reshtmat=(Resmatcoeff(1)*0.792*Tcmat+Resmatcoeff(2))/2.5e-2;

% Ablation rates and laser absorption functions
Tdepmat=[25 500 1000 1500 2000];    % Data temperature distribution
cutdmat=zeros(49,5);                % Ablation depth matrix
cuthmat=zeros(49,5);                % Absorbed fluence matrix
if lambda0>=1 && lambda0<=1.1 && FWHM<=0.5

    IratFPmat=4.39E-002.*[0:10 15:5:200];

    % Cut depth
    cutdmat=[0  0   0   0   0
    0.00E+000 0.00E+000 4.70E-008 9.90E-008 1.37E-007
    1.45E-007 1.91E-007 2.22E-007 2.49E-007 2.79E-007




                                .
                                .
                                .


    1.09E-006 1.10E-006 1.13E-006 1.15E-006 1.18E-006
    1.09E-006 1.11E-006 1.13E-006 1.16E-006 1.19E-006
    1.10E-006 1.12E-006 1.14E-006 1.16E-006 1.19E-006];

    % Absorbed fluence
    cuthmat=[0  0   0   0   0
    8.80E+002 1.66E+003 2.52E+003 3.19E+003 3.65E+003
    5.95E+003 7.36E+003 7.95E+003 8.40E+003 8.83E+003




                                .
                                .
                                .


    8.93E+005 9.06E+005 9.13E+005 9.27E+005 9.42E+005
    9.17E+005 9.28E+005 9.41E+005 9.50E+005 9.68E+005
    9.40E+005 9.52E+005 9.60E+005 9.74E+005 9.93E+005];

elseif lambda0>=1 && lambda0<=1.1 && FWHM<=1



    .
    .
    .


elseif ...



    .
    .
    .


else

    IratFPmat=0:48;
    if PULSE>0
        display('!!Missing aluminium absorption data!!')
    end

end
```

Bibliography

[1] Von Allmen M. *Laser-Beam Interactions with Materials.* Springer-Verlag, Germany, 1987.

[2] Ready J.F., editor. *LIA Handbook of Laser Materials Processing.* Laser Insitute of America Magnolia Publishing, United States of America, 2001.

[3] Kannatey-Asibu E. *Principles of Laser Materials Processing.* John Wiley & Sons, United States of America, 2009.

[4] Dowden J., editor. *The Theory of Laser Materials Processing: Heat and Mass Transfer in Modern Technology.* Springer Science+Business Media B.V., Netherlands, 2009.

[5] Biot M.A. and Daughaday H. Variational analysis of ablation. *Journal of the Aerospace Sciences*, 29(2):228–229, 1962.

[6] Schulz W., Kostrykin V., Zefferer H., Petring D., and Poprawe R. A free boundary problem related to laser beam fusion cutting: ODE approximation. *International Journal of Heat and Mass Transfer*, 40(12):2913–2928, 1997.

[7] Schulz W., Kostrykin V., Nießen M., Michel J., Petring D., Kreutz E.W., and Poprawe R. Dynamics of ripple formation and melt flow in laser beam cutting. *Journal of Physics D: Applied Physics*, 32(11):1219–1228, 1999.

[8] Kaplan A.F.H. An analytical model of metal cutting with a laser beam. *Journal of Applied Physics*, 79(5):2198–2208, 1996.

[9] Solana P., Kapadia P., Dowden J.M., and Marsden P.J. An analytical model for the laser drilling of metals with absorption within the vapour. *Journal of Physics D: Applied Physics*, 32(8):942–952, 1999.

[10] Duan J., Man H.C., and Yue T.M. Modelling the laser fusion cutting process: I. Mathematical modelling of the cut kerf geometry for laser fusion cutting of thick metal. *Journal of Physics D: Applied Physics*, 34(14):2127–2134, 2001.

[11] Lampa C., Kaplan A.F.H., Powell J., and Magnusson C. An analytical thermodynamic model of laser welding. *Journal of Physics D: Applied Physics*, 30(9): 1293–1299, 1997.

[12] Kim M.J., Chen Z.H., and Majumdar P. Finite element modelling of the laser cutting process. *Computers & Structures*, 49(2):231–241, 1993.

[13] Picasso M. and Hoadley A.F.A. Finite element simulation of laser surface treatments including convection in the melt pool. *International Journal of Numerical Methods for Heat & Fluid Flow*, 4(1):61–83, 1994.

[14] Modest M.F. Three-dimensional, transient model for laser machining of ablating/decomposing materials. *International Journal of Heat and Mass Transfer*, 39 (2):221–234, 1996.

[15] Kim M.J. and Zhang J. Finite element analysis of evaporative cutting with a moving high energy pulsed laser. *Applied Mathematical Modelling*, 25(3):203–220, 2001.

[16] Solana P. and Ocaña J.L. A mathematical model for penetration laser welding as a free-boundary problem. *Journal of Physics D: Applied Physics*, 30(9):1300–1313, 1997.

[17] Ki H., Mohanty P.S., and Mazumder J. Modeling of laser keyhole welding: Part I. Mathematical modeling, numerical methodology, role of recoil pressure, multiple reflections, and free surface evolution. *Metallurgical and Materials Transactions A*, 33(6):1817–1830, 2002.

[18] Cho W.-I., Na S.-J., Thomy C., and Vollertsen F. Numerical simulation of molten pool dynamics in high power disk laser welding. *Journal of Materials Processing Technology*, 212(1):262–275, 2012.

[19] Braisted W. and Brockman R. Finite element simulation of laser shock peening. *International Journal of Fatigue*, 21(7):719–724, 1999.

[20] Ocaña J.L., Morales M., Molpeceres C., and Torres J. Numerical simulation of surface deformation and residual stresses fields in laser shock processing experiments. *Applied Surface Science*, 238(1-4):242–248, 2004.

[21] Tani G., Orazi L., Fortunato A., Ascari A., and Campana G. Warm laser shock peening: New developments and process optimization. *CIRP Annals - Manufacturing Technology*, 60(1):219–222, 2011.

[22] Tani G., Fortunato A., Ascari A., and Campana G. Laser surface hardening of martensitic stainless steel hollow parts. *CIRP Annals - Manufacturing Technology*, 59(1):207–210, 2010.

[23] Edwardson S.P., Griffiths J., Edwards K.R., Dearden G., and Watkins K.G. Laser forming: Overview of the controlling factors in the temperature gradient mechanism. *Proceedings of the Institution of Mechanical Engineers, Part C: Journal of Mechanical Engineering Science*, 224(5):1031–1040, 2010.

[24] Ding H., Shen N., and Shin Y.C. Thermal and mechanical modeling analysis of laser-assisted micro-milling of difficult-to-machine alloys. *Journal of Materials Processing Technology*, 212(3):601–613, 2012.

[25] Arif A.F.M. and Yilbas B.S. Thermal stress developed during the laser cutting process: Consideration of different materials. *The International Journal of Advanced Manufacturing Technology*, 37(7-8):698–704, 2008.

[26] Shidfar A., Alinejadmofrad M., and Garshasbi M. A numerical procedure for estimation of the melt depth in laser material processing. *Optics & Laser Technology*, 41(3):280–284, 2009.

[27] Otto A., Koch H., Leitz K.-H., and Schmidt M. Numerical simulations - A versatile approach for better understanding dynamics in laser material processing. *Physics Procedia*, 12(A):11–20, 2011.

[28] Lunau F.W., Paine E.W., and Richardson M. Wijetunge M.D.S.P. High-power laser cutting using a gas jet. *Optics Technology*, 1(5):255–258, 1969.

[29] Chen S.-L. The effects of gas composition on the CO_2 laser cutting of mild steel. *Journal of Materials Processing Technology*, (73):147–159, 1998.

[30] Man H.C., Duan J., and Yue T.M. Analysis of the dynamic characteristics of gas flow inside a laser cut kerf under high cut-assist gas pressure. *Journal of Physics D: Applied Physics*, 32(13):1469–1477, 1999.

[31] Chen K., Yao Y.L., and Modi V. Gas dynamic effects on laser cut quality. *Journal of Manufacturing Processes*, 3(1):38–49, 2001.

[32] Rajaram N., Sheikh-Ahmad J., and Cheraghi S.H. CO_2 laser cut quality of 4130 steel. *International Journal of Machine Tools & Manufacture*, 43(4):351–358, 2003.

[33] Stournaras A., Stavropoulos P., Salonitis K., and Chryssolouris G. An investigation of quality in CO_2 laser cutting of aluminium. *CIRP Journal of Manufacturing Science and Technology*, 2(1):61–69, 2009.

[34] Quintino L., Costa A., Miranda R., Yapp D., Kumar V., and Kong C.J. Welding with high power fiber lasers – a preliminary study. *Materials and Design*, 28(4): 1231–1237, 2007.

[35] Salminen A., Piili H., and Purtonen T. The characteristics of high power fibre laser welding. *Proceedings of the Institution of Mechanical Engineers, Part C: Journal of Mechanical Engineering Science*, 224(5):1019–1029, 2010.

[36] Kratky A., Schuöcker D., and Liedl G. Processing with kW fibre lasers - advantages and limits. In *XVII International Symposium on Gas Flow, Chemical Lasers, and High-Power Lasers*, volume 7131, page 71311X. SPIE, 2009.

[37] Sobih M., Crouse P.L., and Li L. Elimination of striation in laser cutting of mild steel. *Journal of Physics D: Applied Physics*, 40(22):6908–6916, 2007.

[38] Sobih M., Crouse P.L., and Li L. Striation-free fibre laser cutting of mild steel sheets. *Applied Physics A*, 90(1):171–174, 2008.

[39] Powell J., Al-Mashikhi S.O., Kaplan A.F.H., and Voisey K.T. Fibre laser cutting of thin section mild steel: An explanation of the 'striation free' effect. *Optics and Lasers in Engineering*, 49(8):1069–1075, 2011.

[40] Wandera C., Salminen A., and Kujanpaa V. Inert gas cutting of thick-section stainless steel and medium-section aluminium using a high power fiber laser. *Journal of Laser Applications*, 21(3), 2009.

[41] Born M. and Wolf E. *Principles of Optics*. Pergamon Press Ltd., England, 6th edition, 1986.

[42] Palik E.D., editor. *Handbook of Optical Constants of Solids*, volume I. Academic Press Limited, England, 1998.

[43] Palik E.D., editor. *Handbook of Optical Constants of Solids*, volume II. Academic Press Limited, England, 1998.

[44] Atanasov P.A. Laser welding of plastics: Theory and experiments. *Optical Engineering*, 34(10):2976–2980, 1995.

[45] Kneip J.C., Martin B., Loredo A., Mattei S., and Grevey D. Heat transfer in semi-transparent materials during laser interaction. *Journal of Materials Processing Technology*, 155-156:1805–1809, 2004.

[46] Ilie M., Cicala E., Grevey D., Mattei S., and Stoica V. Diode laser welding of ABS: Experiments and process modeling. *Optics & Laser Technology*, 41(5):608–614, 2009.

[47] Ilie M., Kneip J.-C., Matteï S., Nichici A., Roze C., and Girasole T. Through-transmission laser welding of polymers – temperature field modeling and infrared investigation. *Infrared Physics & Technology*, 51(1):73–79, 2007.

[48] Ilie M., Kneip J.-C., Matteï S., Nichici A., Roze C., and Girasole T. Laser beam scattering effects in non-absorbent inhomogenous polymers. *Optics and Lasers in Engineering*, 45(3):405–412, 2007.

[49] Caiazzo F., Curcio F., Daurelio G., and Minutolo F.M.C. Laser cutting of different polymeric plastics (PE, PP and PC) by a CO_2 laser beam. *Journal of Materials Processing Technology*, 159(3):279–285, 2005.

[50] Choudhury I.A. and Shirley S. Laser cutting of polymeric materials: An experimental investigation. *Optics & Laser Technology*, 42(3):503–508, 2010.

[51] Eltawahni H.A., Olabi A.G., and Benyounis K.Y. Effect of process parameters and optimization of CO_2 laser cutting of ultra high-performance polyethylene. *Materials and Design*, 31(8):4029–4038, 2010.

[52] Mingareev I., Weirauch F., Olowinsky A., Shah L., Kadwani P., and Richardson M. Welding of polymers using a 2μm thulium fiber laser. *Optics & Laser Technology*, 44(7):2095–2099, 2012.

[53] Kelly R. and Miotello A. Contribution of vaporization and boiling to thermal-spike sputtering by ions or laser pulses. *Physical Review E*, 60(3):2616–2625, 1999.

[54] Martynyuk M.M. Vaporization and boiling of liquid metal in an exploding wire. *Soviet Physics - Technical Physics*, 19(6):793–797, 1974.

[55] Miotello A. and Kelly R. Critical assessment of thermal models for laser sputtering at high fluences. *Applied Physics Letters*, 67(24):3535–3537, 1995.

[56] Kelly R. and Miotello A. Comments on explosive mechanisms of laser sputtering. *Applied Surface Science*, 96-98:205–215, 1996.

[57] Miotello A. and Kelly R. Laser-induced phase explosion: New physical problems when a condensed phase approaches the thermodynamic critical temperature. *Applied Physics A*, 69:S67–S73, 1999.

[58] Peterlongo A., Miotello A., and Kelly R. Laser-pulse sputtering of aluminium: Vaporization, boiling, superheating, and gas-dynamic effects. *Physical Review E*, 50(6):4716–4727, 1994.

[59] Bulgakova N.M. and Bulgakov A.V. Pulsed laser ablation of solids: Transition from normal vaporization to phase explosion. *Applied Physics A*, 73(2):199–208, 2001.

[60] Bulgakova N.M., Bulgakov A.V., and Babich L.P. Energy balance of pulsed laser ablation: Thermal model revised. *Applied Physics A*, 79(4-6):1323–1326, 2004.

[61] Porneala C. and Willis D.A. Effect of the dielectric transition on laser-induced phase explosion in metals. *International Journal of Heat and Mass Transfer*, 49 (11-12):1928–1936, 2006.

[62] Prokhorov A.M., Batanov V.A., Bunkin F.V., and Fedorov V.B. Metal evaporation under powerful optical radiation. *IEEE Journal of Quantum Electronics*, 9(5):503–510, 1973.

[63] Zhuang H.-Z., Zou X.-W., Jin Z.-Z., and Tian D.-C. Metal-nonmetal transition of fluid Cs along the liquid-vapour coexistence curve. *Physica B*, 253(1-2):68–72, 1998.

[64] Gragossian A., Tavassoli S.H., and Shokri B. Laser ablation of aluminium from normal evaporation to phase explosion. *Journal of Applied Physics*, 105(10):103304, 2009.

[65] Porneala C. and Willis D.A. Observation of nanosecond laser-induced phase explosion in aluminium. *Applied Physics Letters*, 89(21):211121, 2006.

[66] Colina M., Molpeceres C., Morales M., Allens-Perkins F., Guadaño G., and Ocaña J.L. Laser ablation modelling of aluminium, silver and crystalline silicon for applications in photovoltaic technologies. *Surface Engineering*, 27(6):414–423, 2011.

[67] Porneala C. and Willis D.A. Time-resolved dynamics of nanosecond laser-induced phase explosion. *Journal of Physics D: Applied Physics*, 42(15):155503, 2009.

[68] Stafe M., Vlădoiu I., Neguţu C., and Popescu I.M. Experimental investigation of the nanosecond laser ablation rate of aluminium. *Romanian Reports in Physics*, 60(3):789–796, 2008.

[69] Horn I., Guillong M., and Günther D. Wavelength dependant ablation rates for metals and silicate glasses using homogenized laser beam profiles – implications for LA-ICP-MS. *Applied Surface Science*, 182(1-2):91–102, 2001.

[70] Anisimov S.I., Kapeliovich B.L., and Perel'man T.L. Electron emission from metal surfaces exposed to ultrashort laser pulses. *Soviet Physics - JETP*, 39(2):375–377, 1974.

[71] Hohlfeld J., Wellershoff S.-S., Güdde J., Conrad U., Jähnke V., and Matthias E. Electron and lattice dynamics following optical excitation of metals. *Chemical Physics*, 251(1-3):237–258, 2000.

[72] Yilbas B.S. Electron kinetic theory approach – one- and three-dimensional heating with pulsed laser. *International Journal of Heat and Mass Transfer*, 44(10):1925–1936, 2001.

[73] Zhigilei L.V. and Garrison B.J. Microscropic mechanisms of laser ablation of organic solids in the thermal and stress confinement irradiation regimes. *Journal of Applied Physics*, 88(3):1281–1298, 2000.

[74] Yang J., Zhao Y., and Zhu X. Transition between nonthermal and thermal ablation of metallic targets under the strike of high-fluence ultrashort laser pulses. *Applied Physics Letters*, 88(9):094101, 2006.

[75] Schäfer C., Urbassek H.M., and Zhigilei L.V. Metal ablation by picosecond laser pulses: a hybrid simulation. *Physical Review B*, 66(11):115404, 2002.

[76] Perez D. and Lewis L.J. Molecular-dynamics study of ablation of solids under femtosecond laser pulses. *Physical Review B*, 67(18):184102, 2003.

[77] Bouilly D., Perez D., and Lewis L.J. Damage in materials following ablation by ultrashort laser pulses: A molecular-dynamics study. *Physical Review B*, 76(18): 184119, 2007.

[78] Lewis L.J. and Perez D. Laser ablation with short and ultrashort laser pulses: Basic mechanisms from molecular-dynamics simulations. *Applied Surface Science*, 255(10):5101–5106, 2009.

[79] Nedialkov N.N., Imamova S.E., Atanasov P.A., Berger P., and Dausinger F. Mechanism of ultrashort laser ablation of metals: Molecular dynamics simulation. *Applied Surface Science*, 247(1-4):243–248, 2005.

[80] Zhang N., Zhu X., Yang J., Wang X., and Wang M. Time-resolved shadowgraphs of material ejection in intense femtosecond laser ablation of aluminum. *Physical Review Letters*, 99(16):167602, 2007.

[81] Sonntag S., Paredes C.T., Roth J., and Trebin H.-R. Molecular dynamics simulations of cluster distribution from femtosecond laser ablation in aluminium. *Applied Physics A*, 104(2):559–565, 2011.

[82] Pronko P.P., Dutta S.K., Squier J., Rudd J.V., Du D., and Mourou G. Machining of sub-micron holes using a femtosecond laser at 800nm. *Optics Communications*, 114(1-2):106–110, 1995.

[83] Momma C., Nolte S., Chichkov B.N., Von Alvensleben F., and Tünnermann A. Precise laser ablation with ultrashort pulses. *Applied Surface Science*, 109-110: 15–19, 1997.

[84] Nolte S., Momma C., Jacobs H., Tünnermann A., Chichkov B.N., Wellegehausen B., and Welling H. Ablation of metals by ultrashort laser pulses. *Journal of the Optical Society of America B*, 14(10):2716–2722, 1997.

[85] Semerok A., Chaléard C., Detalle V., Lacour J.-L., Mauchien P., Meynadier P., Nouvellon C., Sallé B., Palianov P., Perdrix M., and Petite G. Experimental investigations of laser ablation efficiency of pure metals with femto, pico and nanosecond pulses. *Applied Surface Science*, 138-139:311–314, 1999.

[86] Zhao J., Huettner B., and Menschig A. Microablation with ultrashort laser pulses. *Optics & Laser Technology*, 33(7):487–491, 2001.

[87] Yalizay B., Ersoy T., Soylu B., and Akturk S. Fabrication of nanometer-size structures in metal thin films using femtosecond laser bessel beams. *Applied Physics Letters*, 100(3):031104, 2012.

[88] Lippert T. Interaction of photons with polymers: From surface modification to ablation. *Plasma Processes and Polymers*, 2(7):525–546, 2005.

[89] Lippert T. and Dickinson J.T. Chemical and spectroscopic aspects of polymer ablation: Special features and novel directions. *Chemical Reviews*, 103(2):453–485, 2003.

[90] Dyer P.E. Excimer laser polymer ablation: Twenty years on. *Applied Physics A*, 77(2):167–173, 2003.

[91] Bityurin N., Luk'yanchuk B.S., Hong M.H., and Chong T.C. Models for laser ablation of polymers. *Chemical Reviews*, 103(2):519–552, 2003.

[92] Sohn I.-B., Noh Y.-C., Kim Y.-S., Ko D.-K., Lee J., and Choi Y.-J. Laser ablation of polypropylene films using nanosecond, picosecond, and femtosecond laser. *Journal of the Optical Society of Korea*, 12(1):38–41, 2008.

[93] Leme F.O., Godoi Q., Kiyataka P.H.M., Santos D., Agnelli J.A.M., and Krug F.J. Effect of pulse repetition rate and number of pulses in the analysis of polypropylene

and high density polyethylene by nanosecond infrared laser induced breakdown spectroscopy. *Applied Surface Science*, 258(8):3598–3603, 2012.

[94] Hahn Ch., Lippert T., and Wokaun A. Comparison of the ablation behavior of polymer films in the IR and UV with nanosecond and picosecond pulses. *Journal of Physical Chemistry B*, 103(8):1287–1294, 1999.

[95] Luk'yanchuk B., Bityurin N., Himmelbauer M., and Arnold N. UV-laser ablation of polyimide: from long to ultra-short laser pulses. *Nuclear Instruments and Methods in Physics Research B*, 122(3):347–355, 1997.

[96] Baudach S., Bonse J., and Kautek W. Ablation experiments on polyimide with femtosecond laser pulses. *Applied Physics A*, 69(1S):S395–S398, 1999.

[97] Baudach S., Bonse J., Krüger J., and Kautek W. Ultrashort pulse laser ablation of polycarbonate and polymethylmethacrylate. *Applied Surface Science*, 154-155: 555–560, 2000.

[98] Coelho J.M.P., Abreu M.A., and Rodrigues F.C. Thermal modeling CO_2 laser radiation transmission welding of superposed thermoplastic films. *Optical Engineering*, 42(11):3365–3373, 2003.

[99] Coelho J.M.P., Abreu M.A., and Rodrigues F.C. High-speed laser cutting of superposed thermoplastic films: Thermal modeling and process characterization. *Optics and Lasers in Engineering*, 42(1):27–39, 2004.

[100] Engelhart P., Hermann S., Neubert T., Plagwitz H., Grischke R., Meyer R., Klug U., Schoonderbeek A., Stute U., and Brendel R. Laser ablation of SiO_2 for locally contacted Si solar cells with ultra-short pulses. *Progress in Photovoltaics: Research and Applications*, 15(6):521–527, 2007.

[101] Halbwax M., Sarnet T., Delaporte P., Sentis M., Etienne H., Torregrosa F., Vervisch V., Perichaud I., and Martinuzzi S. Micro and nano-structuration of silicon by femtosecond laser: Application to silicon photovoltaic cells fabrication. *Thin Solid Films*, 516(20):6791–6795, 2008.

[102] Lee B.G., Lin Y.-T., Mazur E., Sher M.-J., and Branz H.M. Light trapping for thin silicon solar cells by femtosecond laser texturing. In *IEEE Photovoltaic Specialists Conference (PVSC)*, 2012.

[103] Smith M.J., Sher M.J., Franta B., Lin Y.-T., Mazur E., and Gradečak S. The origins of pressure-induced phase transformations during the surface texturing of silicon using femtosecond laser irradiation. *Journal of Applied Physics*, 112(8): 083518, 2012.

[104] Müller-Meskamp L., Kim Y.H., Roch T., Hofmann S., Scholz R., Eckardt S., Leo K., and Lasagni A.F. Efficiency enhancement of organic solar cells by fabricating periodic surface textures using direct laser interference patterning. *Advanced Materials*, 24(7):906–910, 2012.

[105] Selleri S., Cucinotta A., Poli F., and Passaro D. High brilliance fiber lasers for the scribing of photovoltaic modules. In *Transparent Optical Networks (ICTON)*, number 11, pages 1–4, 2009.

[106] Selleri S., Bosio A., Cucinotta A., Sozzi M., Menossi D., Hernandez Y., Bertrand A., and Duterte C. Optimization of pulsed fiber laser scribing for CdTe and CIGS solar cells. In *Transparent Optical Networks (ICTON)*, volume 14, pages 1–4, 2012.

[107] Hernandez Y., Bertrand A., Selleri S., Salin F., Leick L., Hueske M., Petkovsek R., Ferrario F., and Lichtenstein N. Recent progress on the ALPINE (Advanced Lasers for Photovoltaic INdustrial Processing Enhancement) FP7 integrated project. In *Fiber Laser Applications*, 2011.

[108] Gečys P., Račiukaitis G., Gedvilas M., and Selskis A. Laser structuring of thin-film solar cells on polymers. *The European Journal of Applied Physics*, 46(1):12508, 2009.

[109] Schoonderbeek A., Schütz V., Haupt O., and Stute U. Laser processing of thin films for photovoltaic applications. *Journal of Laser Micro/Nanoengineering*, 5 (3):248–255, 2010.

[110] Bovatsek J., Tamhankar A., Patel R.S., Bulgakova N.M., and Bonse J. Thin film removal mechanisms in ns-laser processing of photovoltaic materials. *Thin Solid Films*, 518(10):2897–2904, 2010.

[111] Wait J.R. *Electromagnetic Waves in Stratified Media.* Pergamon Press Ltd., England, 1962.

[112] Yeh P., Yariv A., and Hong C.-S. Electromagnetic propagation in periodic stratified media. I. General theory. *Journal of the Optical Society of America*, 67(4): 423–438, 1977.

[113] Prentice J.S.C. Coherent, partially coherent and incoherent light absorption in thin-film multilayer structure. *Journal of Physics D: Applied Physics*, 33(24): 3139–3145, 2000.

[114] Prentice J.S.C. Optical generation rate of electron-hole pairs in multilayer thin-film photovoltaic cells. *Journal of Physics D: Applied Physics*, 32(17):2146–2150, 1999.

[115] Centurioni E. Generalized matrix method for calculation of internal light energy flux in mixed coherent and incoherent multilayers. *Applied Optics*, 44(35):7532–7539, 2005.

[116] Singh R.K. and Viatella J. Estimation of plasma absorption effects during pulsed laser ablation of high-critical-temperature superconductors. *Journal of Applied Physics*, 75(2):1204–1206, 1994.

[117] Desai P.D., James H.M., and Ho C.Y. Electrical resistivity of aluminium and manganese. *Journal of Physical and Chemical Reference Data*, 13(4):1131–1172, 1984.

[118] Morel V., Bultel A., and Chéron B.G. The critical temperature of aluminium. *International Journal of Thermophysics*, 30(6):1853–1863, 2009.

[119] Wu B. and Shin Y.C. Absorption coefficient of aluminium near the critical point and the consequences on high-power nanosecond laser ablation. *Applied Physics Letters*, 89(11):111902, 2006.

[120] Tannehill J.C., Anderson D.A., and Pletcher R.H. *Computational Fluid Mechanics and Heat Transfer*. Taylor & Francis, United States of America, 2nd edition, 1997.

[121] Herman M.A., Richter W., and Sitter H. *Epitaxy: Physical Principles and Technical Implementation*. Springer-Verlag, Germany, 2004.

[122] Xu Y. and Yan X. *Chemical Vapour Deposition: An Integrated Engineering Design for Advanced Materials*. Springer-Verlag, England, 2010.

[123] Summonte C. and Menin A. Caratterizzazioni ottiche UV-visibile-NIR-MIR su materiali vari. Technical report, CNR IMM, Italy, 2010.

[124] Hatch J.E., editor. *Aluminium: Properties and Physical Metallurgy*. American Society for Metals, United States of America, 1984.

[125] Kurek M., Klepac D., Ščetar M., Galić K., Valić S., Liu Y., and Yang W. Gas barrier and morphology characteristics of linear low-density polyethylene and two different polypropylene films. *Polymer Bulletin*, 67(7):1293–1309, 2011.

[126] Passaglia E. and Kevorkian H.K. Specific heat of atactic and isotactic polypropylene and the entropy of the glass. *Journal of Applied Physics*, 34(1):90–97, 1963.

[127] Kutz M., editor. *Handbook of Materials Selection*. John Wiley & Sons, United States of America, 2002.

[128] Askeland D.R., Fulay P.P., and Wright W.J. *The Science and Engineering of Materials*. Cengage Learning, United States of America, 6th edition, 2011.

[129] Beyler C.L. and Hirschler M.M. Thermal decomposition of polymers. In *SFPE Handbook of Fire Protection Engineering*, pages 110–131, United States of America, 2001. National Fire Protection Association.

[130] Maier C. and Calafut T. *Polypropylene: The Definitive User's Guide and Databook*. Plastics Design Library, United States of America, 1998.

[131] Shivadev U.K. Thermal degradation and spontaneous ignition of paper sheets in air by irradiation. *Combustion and Flame*, 22(2):223–236, 1974.

[132] Ashby M.F. *Materials and the Environment*. Elsevier, United States of America, 2013.